ABSTRACT

Title of dissertation: HIGHLY-CHARGED IONS ISOLATED IN UNITARY PENNING TRAPS FOR PRECISION MEASUREMENTS

Samuel M. Brewer, Doctor of Philosophy, 2012

Dissertation directed by: Dr. Joseph N. Tan
National Institute of Standards and Technology

Recently, highly–charged ions have been isolated in a novel compact Penning trap designed to capture ions extracted from the NIST electron beam ion trap (EBIT), opening a new avenue of manipulating ions isolated in a controlled environment for a variety of studies. The unique architecture of this extremely compact Penning trap facilitates optical experiments with stored ions, as well as ion counting via position-sensitive or time-of-flight micro-channel plate (MCP) detectors. As a first demonstration, Ar^{13+} ions are captured in one of the two fine structure levels forming the lowest lying states. The lifetime of the metastable $1s^2 2s^2 2p\ ^2P_{3/2}$ state is measured by counting the 441 nm photons emitted in the spin-flipping (M1) decay to the ground state. This work presents the novel Penning trap, the apparatus deployed at the NIST EBIT, techniques employed for ion capture and storage, and a new measurement of the lifetime of the metastable $^2P_{3/2}$ state.

HIGHLY-CHARGED IONS ISOLATED IN UNITARY PENNING TRAPS FOR PRECISION MEASUREMENTS

by

Samuel M. Brewer

Dissertation submitted to the Faculty of the Graduate School of the
University of Maryland, College Park in partial fulfillment
of the requirements for the degree of
Doctor of Philosophy
2012

Advisory Committee:
Dr. Joseph N. Tan
Professor Steven L. Rolston, Chair
Dr. Peter J. Mohr
Professor Amy S. Mullin
Professor Richard F. Ellis
Professor Luis A. Orozco, Dean's Representative

Acknowledgments

I am grateful for the tremendous support and guidance I have received during my time in graduate school and wish to thank those who have helped to make this thesis possible.

I would like to thank my advisor, Dr. Joseph N. Tan, for giving me the rare opportunity to work on an exciting and challenging project from its inception. His support has been genuine and consistent in all aspects of our work together, and I am thankful for his willingness to discuss every issue, whether great or small. During my time at NIST he has trusted me with every aspect of this project, and has shown me what it takes to do precision measurements. He has taught me to approach experimental physics with a sense of honesty and humility that I hope to emulate throughout the rest of my career.

I would like to thank Dr. Nicholas D. Guise for his continuous contribution to this project. His dedication and patience in the design, construction, and operation of both generations of ion traps has been unparalleled. I am fortunate to have been able to work with Nick and I am thankful for all of his help and support.

I wish to thank my co-advisor and examining committee chair, Prof. Steven L. Rolston for his support and guidance throughout my time at UMD. I wish to thank Dr. Peter J. Mohr, Prof. Amy S. Mullin, Prof. Richard F. Ellis, and Prof. Luis A. Orozco, for their willingness to serve on my thesis examining committee and for helpful comments to improve my thesis manuscript.

My colleagues at NIST, in the Atomic Spectroscopy Group and the Quantum

Measurement Division, have helped to shape my graduate career and I am grateful for all of their support. I wish to thank the group leader, Dr. John J. Curry, and division chief, Dr. Carl J. Williams, for the generous support and resources to pursue this project. I would also like to thank the Layla Armitage for all of her administrative assistance at NIST, in particular, her willingness to process a seemingly endless list of purchase orders during the construction phase of this project.

Many people have provided me with the expertise and technical guidance needed to carry out the experiments presented here. I would like to thank Dr. John D. Gillaspy for his guidance in EBIT operations, willingness to train me as an EBIT operator, and enthusiasm for the physics of highly-charged ions. I also wish to thank Dr. Joshua M. Pomeroy for his instruction and support in operation of the EBIT and ion extraction beamline, as well as many helpful discussions regarding machining techniques and general aspects of experimental physics. I would like to thank Dr. Craig J. Sansonetti for his support in a variety of laser experiments that took place early on during my time at NIST.

I have benefitted from the support of the faculty and staff of the UMD Chemical Physics Program. I wish to thank the director, Prof. Michael A. Coplan, for his support of my research interests and Debbie Jenkins for her generous administrative assistance. In addition, I would like to thank Dr. Charles W. Clark for his willingness to offer his time and expertise to help me, and others, prepare for our qualifying examination. I wish to thank the Joint Quantum Institute for support during my graduate career.

There are many people who have supported me outside of work. I would like to thank Craig and Jean Sansonetti, and Bill and Jane Phillips for their incredible support of both me and my family. I wish to thank the many friends and family members who have supported me during the writing of this thesis.

I wish to thank my wife Kristen for her love, support, prayers, and continued patience during my time in graduate school. I love you. Your support and understanding during all aspects of this experience has been extraordinary. You constantly remind me of the person that I want to be and I can't thank you enough for that. I am truly blessed to call you my family. Above all, thanks be to God.

Table of Contents

List of Tables

List of Figures

List of Abbreviations

HCI	Highly Charged Ion
NIST	National Institute of Standards and Technology
EBIT	Electron Beam Ion Trap
FEM	Finite Element Method
BEM	Boundary Element Method
FFT	Fast Fourier Transform
MCP	Micro-Channel Plate
OFHC	Oxygen-Free-High-Conductivity
TOF	Time-of-Flight
PMT	Photomultiplier tube

Chapter 1

Introduction

1.1 Overview

Highly-charged ions (HCI) are of interest in the study of atomic structure, astrophysics, and plasma diagnostics for fusion science [1]. The high nuclear charge, Z, tends to amplify relativistic effects in atoms, such as fine and hyperfine structure splitting [2]. For example, the fine structure energy splitting, the energy difference between atomic states in the same electronic manifold with differing total angular momentum, is proportional to $(Z\alpha)^4$, where $\alpha \approx 1/137$ is the fine structure constant. Hence, the fine structure splitting of an electronic manifold can be so large for some highly-charged ions that the transition energy can be increased from the microwave to the visible domain of the electromagnetic spectrum [3] – a useful feature for studying remote astrophysical objects.

Highly-charged ions are typically found in extreme environments containing strong electric and magnetic fields and a range of temperatures. These include astrophysical objects such as the solar corona [4] and a variety of laboratory light sources including high current plasma discharges [5]. The temperature of the solar corona is about one million K – hot enough to produce ions ranging from fully stripped light atoms, such as C^{6+}, to multiply charged metal atoms, like Fe^{13+} [6]. Arc sources are cooler, about 1000 – 10,000 K and generally produce lower (single, double, or triple) ionized atoms. Spectroscopic measurements of the relative abundance of high charge states of iron in the solar corona have been used to investigate the solar wind (see Ref. [6] and references therein) while measurements of emission lines in discharge lamps have been used to test the theory of atomic structure in plasmas [7].

Spectroscopic measurements of highly-charged ions are important for many disciplines. Experiments typically involve the study of the radiation emitted when an HCI beam collides with a metal or gas target. For example, hydrogen-like U^{91+} provides a system for testing quantum electrodynamics (QED) in the strong electric field regime, and recent measurements of the Lamb shift in U^{91+} [8, 9] have been carried out at the GSI accelerator in Darmstadt, Germany. Moreover, radioactive ions have also been made available at the ISOLDE mass separator at CERN for the purpose of precision mass measurements of heavy ions, cooled in a radio frequency quadrupole (RFQ) Paul trap [10].

Isolation of highly-charged ions in precision traps is of wide interest. Ongoing efforts at the Max-Planck-Institut für Kernphysik (MPI-K) in Heidelberg, Germany seek to capture highly-charged ions in Penning traps [11] with meter-long electrode structures surrounded by multi-tesla solenoid magnets [12, 13]. These planned experiments for highly-charged ion capture will employ many of the techniques developed at CERN for ISOLDE and the study of trapped antiprotons [14] and antihydrogen (see Ref. [15] and references therein). Recently, an experiment at the TITAN facility, located at TRIUMF in Canada demonstrated capture of high-charge, short-lived nuclides in a high-field Penning trap [16]. A survey of trap types and high energy ion sources, relevant to HCI capture, can be found in the review article by Kluge, *et. al.* [17].

The advent of small-scale laboratory sources of highly-charged ions has enabled a wider variety of experimental investigations. In particular, the electron beam ion trap [18] or EBIT has enabled a tunable source of highly-charged ions by controlling electron impact ionization, to optimize the production of a particular charge state of interest [2]. The charge state tuning of EBIT sources has been exploited for in-EBIT spectroscopy experiments [19], ion extraction for HCI-surface bombardment [20] (and references therein), and charge-exchange (CX) experiments [21].

EBIT ion sources are roughly one meter in length, including the vacuum envelope, and can be housed in a single room of a laboratory. This reduction in size allows for the deployment of a variety of spectrometers to observe the light source [2] as well as the addition of ion transport elements for use in ion capture investigations. Previous experiments to capture and isolate a particular charge state of interest have been carried out using an EBIT source coupled to a high-field, cryogenic Penning trap (RETRAP) at the Lawrence Livermore National Laboratory (LLNL) [22]. More recently, SMILETRAP II demonstrated capture and cooling of Ar^{16+} in a Penning trap utilizing a room-temperature 1.1 T solenoid magnet [23].

Penning traps previously developed for ion capture from EBIT sources have largely relied on designs with magnetic fields greater than 1 T for radial confinement of ions. Due to the use of large, cryogenic, solenoid magnets surrounding the trap electrodes, optical access to stored ions generally requires elaborate design and construction of the apparatus. The work presented here addresses the challenge of optical and atomic beam access to stored ions using a new approach for isolating highly-charged ions, which reduces the necessary space requirements. It discusses the first capture of ions extracted from the NIST EBIT using a novel, unitary Penning trap [24], and demonstrates the usefulness of this approach with the observation of radiative decay of ions in metastable states. In contrast to high-field solenoids, a unitary Penning trap occupies a volume of ≈ 100 cm^3, which is small compared to high-field solenoid traps which typically occupy several m^3 of space. The demonstration of capture in such a compact trap offers a new tool for studying isolated highly-charged ions, as well as for the development of miniaturized Penning traps. Initial optical experiments have focused on observation of a forbidden magnetic dipole (M1) transition in the ground electronic manifold of Ar^{13+}. This ion is of interest in benchmarking few electron atomic theory. The experimental techniques employed, as well as measurements for a new determination of the lifetime of the 1s^{2}2s^{2}2p ^{2}P$_{3/2}$ metastable state, are the subject of Chapter 7.

The experimental breakthrough that has enabled new experiments with isolated ions extracted from the NIST EBIT is the development of novel Penning traps for the capture and isolation of highly-charged ions. The design of electric and magnetic field structures in small traps with optical access to stored ions, as well as the production of temporally narrow, HCI pulses for ion capture are addressed in Chapter 2 and Chapter 3. Efficient ion capture depends upon the optimization of the arrival time of ions at the Penning trap, and the slowing of incoming beams, which are presented in Chapter 4. Characterization of the ion confinement, such as ion number, temperature, and storage lifetime are discussed in Chapter 5. The dynamics of stored ions affects fluorescence detection. A numerical model of the stored ion cloud, obtained by solving Poisson's equation for a thermalized ensemble of ions, is used to address ion transport and explain time-of-flight data in Chapter 6. Moreover, a ray-tracing calculation of the optical detection is presented in Chapter 7 to further constrain the parameters of the model. Chapter 7 also discusses the "first light" experiment to measure the lifetime of the metastable $^2P_{3/2}$ state in Ar^{13+}, including a discussion of ion loss, systematic effects due to quenching of the metastable state, and trap stability. Conclusions and suggestions for future work are presented in Chapter 8.

1.2 Metastable States of Highly-Charged Ions

Forbidden transitions play important roles in atomic and particle physics [25], frequency metrology [26], and laboratory astrophysics [27, 28]. An atomic configuration of particular interest is the boronlike isoelectronic sequence (a set of atoms with the same number of electrons and differing nuclear charge, Z). Boronlike atoms have five electrons with a ground electronic configuration of $1s^2 2s^2 2p$; consisting of one valence electron and a core of two closed electronic s-shells. The ground configuration is split into an upper $^2P_{3/2}$ state and lower $^2P_{1/2}$ state. A forbidden, spin-flipping, magnetic dipole (M1) transition can occur between these two states and the theoretical wavelength [29] of this transition is shown in Fig. 1.1 for ions ranging from neutral boron (B I) to Fe^{21+} (Fe XXII). Due to the high nuclear charge, the transition wavelength for many of these ions is found in the optical domain, making them accessible for spectroscopy using commercially available solid-state lasers.

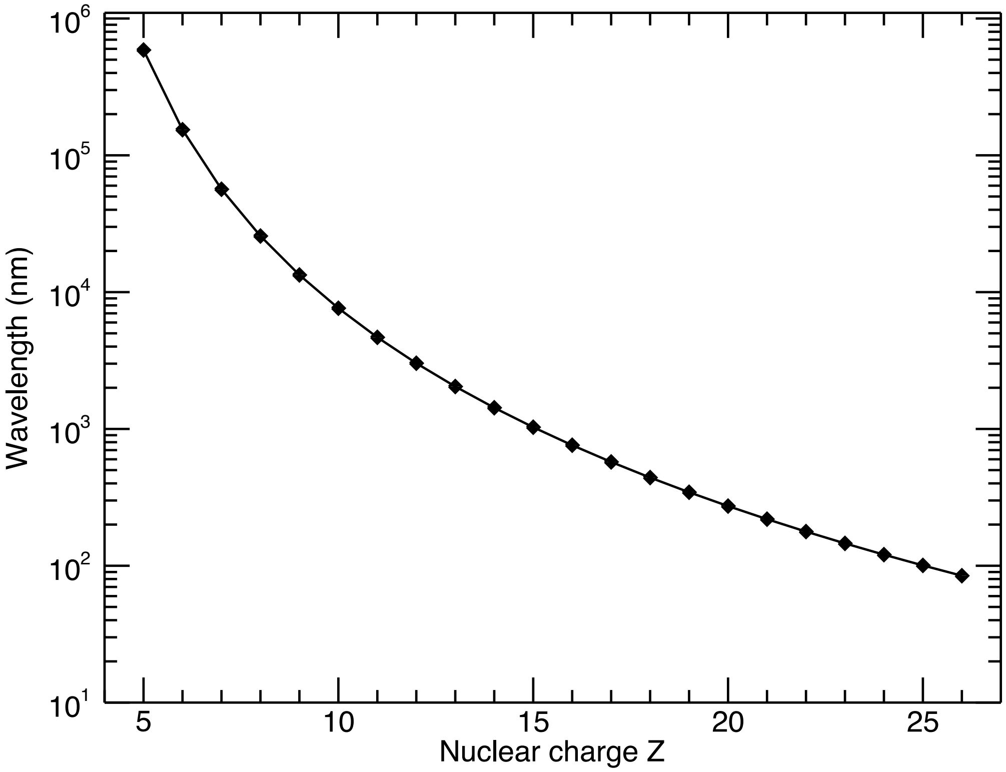

Figure 1.1: Calculated transition wavelength for the 2p $^2P_{3/2} - {}^2P_{1/2}$ M1 transition in the B-like isoelectronic sequence. Data taken from [29].

An apparatus is currently being developed at the HITRAP facility to capture and cool highly-charged B-like ions for the purpose of performing laser spectroscopy [12], and recently, laser-induced fluorescence was demonstrated on Ar^{13+} (Ar XIV) ions inside the Heidelberg EBIT [30], where the transition occurs at a wavelength of $\lambda \approx 441$ nm.

A recent measurement of the radiative lifetime of the $^2P_{3/2}$ state in Ar^{13+}, performed inside the Heidelberg EBIT in 2005 [31], has been reported to attain a precision of 0.1 %. All other published results have at least 15 times larger uncertainty [32]. To attain accuracies of order 0.1 %, theory must include, among other corrections, QED effects such as the anomalous magnetic moment of the electron. The $^2P_{3/2}$ lifetime was first measured inside the NIST EBIT in 1998 [33]. Three of the four reported measurements were performed inside EBIT sources. Until this work, only a single measurement has been done on isolated ions, using an electrostatic Kingdon trap to capture ions created in an electron cyclotron resonance (ECR) ion source [34]. A mild discrepancy of ≈ 5 %, at the $\approx 2\sigma$ (combined uncertainty) level exists among the published measurements [33, 34, 32, 31]. A new measurement with different systematic effects is desirable to corroborate higher levels of precision [35].

A new measurement of the radiative lifetime of the $^2P_{3/2}$ state in Ar^{13+} is reported here, using a novel compact Penning trap. This is an important milestone, by itself, towards precision measurements on isolated highly-charged ions in general. The simpler dynamics of isolated ions, namely the presence of a single captured charge state, in contrast to the plasma conditions inside an EBIT, should contribute to better accuracy.

While the focus of this work is on a transition of interest in atomic structure theory, metastable states of highly-charged ions are also of interest in astrophysics. A classic example is the “green coronal line” arising from the forbidden electric quadrupole (E2) transition in the ground electronic configuration of Fe^{13+}. This transition occurs at a wavelength of $\lambda \approx 530$ nm with a radiative lifetime of $\tau \approx 17$ ms [27]. Additional ions of interest with long lived metastable states are discussed in [28], many of which could potentially be studied in the newly deployed Penning trap apparatus.

1.3 Precision Measurements in Single-electron Atoms

The most familiar single-electron atom is hydrogen with a single electron bound to a single proton. It is neutral and the most abundant in nature. The isoelectronic sequence of hydrogen also consist of single electron atoms. These systems consist of atoms with one electron which make them candidates for high precision measurements of atomic properties (transitions, masses, nuclear size effects, etc) and determination of physical constants of nature. For instance, the current CODATA recommended value for the Rydberg constant, R_∞, [36] is determined by precision spectroscopic measurements on atomic hydrogen and deuterium.

The determination of the Rydberg constant has reached such high precision that it has been limited since 1997 by the uncertainty in the proton charge radius [37]. Recently, a high precision measurement of the proton charge radius, using muonic hydrogen [38] was carried out by a team from the Max-Planck-Institut für Quantenoptik (MPQ), at the Paul Scherrer Institute (PSI) accelerator facility in Switzerland. The team measured the Lamb shift in muonic hydrogen (a muon bound to a proton) which was combined with state of the art QED calculations to extract the proton rms charge radius, and subsequently, determine a new value for the Rydberg constant. The surprising result from the muonic hydrogen experiment is that the value extracted for the proton radius and Rydberg constant differs by

$\approx 7\sigma$ (combined uncertainty) from the 2010 CODATA value.

In addition to the low-lying state measurements, hydrogen has been studied in high angular momentum (high-L) circular states where the size of the proton plays little role in the determination of the Rydberg constant [39]. This investigation took place at MIT under the direction of Prof. D. Kleppner. Radio frequency spectroscopy was used to probe the maximum angular momentum states, (where $l = n - 1$) and measure transition frequencies between adjacent Rydberg states. In this regime finite nuclear size effects essentially disappear.

The recent discrepancy between the muonic hydrogen measurement and the CODATA recommended value for the Rydberg constant has been a subject of much discussion, as evidenced by the over 150 citations of the recent publication [38]. A comparison of the Rydberg frequency, cR_∞, from CODATA, muonic hydrogen, and the previous circular state measurement in neutral hydrogen is shown in Fig. 1.2. While the circular state measurement is less precise than both the CODATA value and the new muonic hydrogen value, the assigned uncertainty is comparable to the level of the discrepancy. To date, the precise value of the proton radius remains an open question, and the discrepancy casts doubt on the current precision of the Rydberg constant.

It has recently become possible to calculate the circular state energy levels of any hydrogen-like ion to very high accuracy [3, 40, 41, 42]. In some cases, the accuracy of the calculated transitions between levels is now comparable to the precision which can be obtained using commercial laser frequency combs. The great simplification in the theory for Rydberg states is due to the low probability for the electron

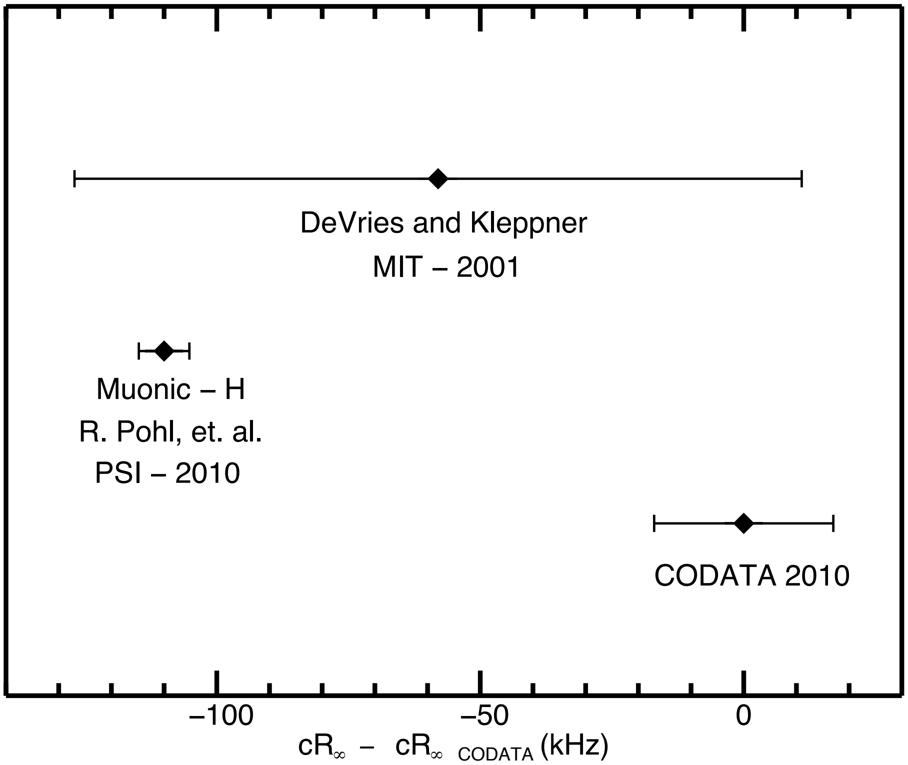

Figure 1.2: Discrepancy in the determinations of the Rydberg frequency. Difference are with respect to the CODATA 2010 recommended value. The two spectroscopic measurements presented are the recent Lamb shift measurement in muonic hydrogen, and the circular state measurement in atomic hydrogen.

to be found inside the radius of the nucleus. Consequently, the nuclear size effects are very small compared to the QED effects in Rydberg states. The properties of high angular momentum states can be illustrated by considering the hydrogen-like wave functions [1]

$$\psi_{nlm}(\theta, \phi, r) = Y_{lm}(\theta, \phi) R_{nl}(r) \tag{1.1}$$

where the angular part, $Y_{lm}(\theta, \phi)$, are spherical harmonics and the radial part of the wave function is $R_{nl}(r)$. The familiar hydrogen wave functions are shown in Fig 1.3. The low lying 1s (a), 2p (b), and 3d (c) states are shown for the case of low angular momentum where $l = 0$ and $m_l = 0$. The circular state, $n = 10$, $l = 9$, $m_l = 9$ in Ne^{10+} is shown in Fig. 1.3 (d).

Laser excitation of hydrogen-like ions, starting from the ground state, for $Z > 1$, is generally not feasible. Although the experimental details are beyond the scope of this work, a few schemes are being considered. One method for preparing cold hydrogen-like ions in Rydberg states is to charge exchange bare nuclei in a trap with a neutral beam of atoms in high n states. Experimental studies with fast ion beams [43, 44] demonstrated that charge exchange with excited atoms preferentially results in a final state of the ion with large angular momentum. Recent theoretical work [45] indicates that the main decay mechanism (E1 radiative cascade) popluates circular states. This can be advantageous when trying to create cold hydrogen-like ions in circular Rydberg states. This technique has proven to be successful in a similar system involving anti-protons undergoing charge exchange with a cloud of cool positronium [46]. Another possibility would involve three-body recombination

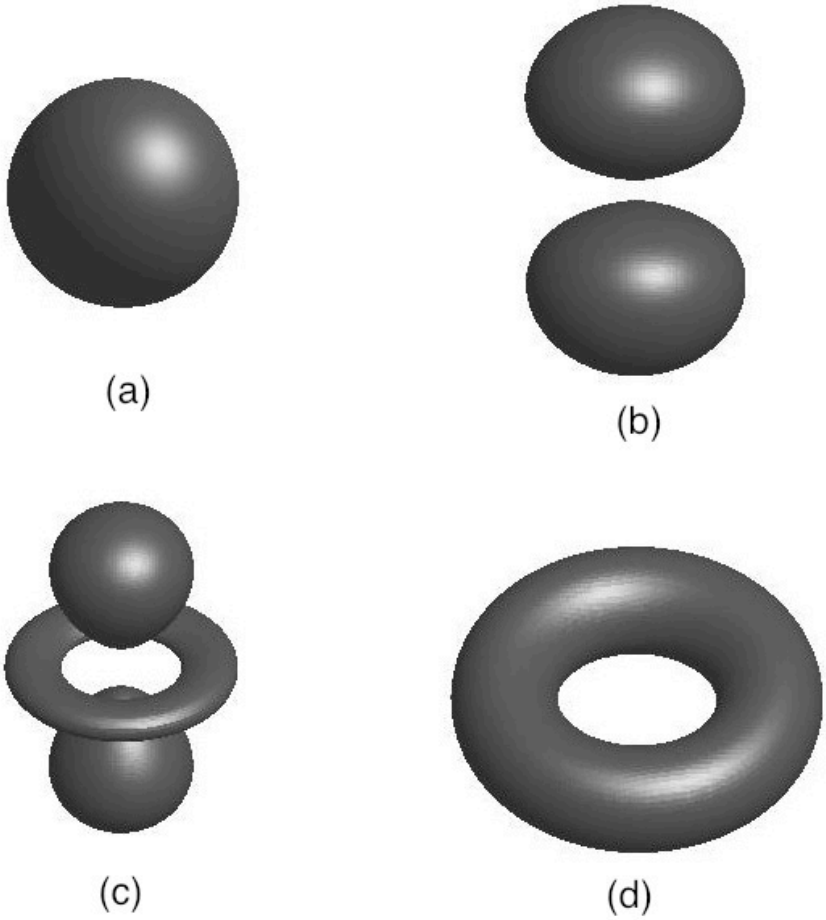

Figure 1.3: Calculated H-like wave functions for the familiar 1s, 2p, and 3d states with $m_l = 0$ in neutral hydrogen. The 1s state is shown in (a), the 2p state is shown in (b), and the 3d state is shown in (c). The circular state; $n = 10$, $l = 9$, $m_l = 9$ in Ne^{9+} is shown in (d).

when bare nuclei in a trap overlap with a cloud of cool electrons.

1.4 Summary

Highly-charged ions are of interest for investigations in the areas of astronomy and laboratory astrophysics, atomic structure theory, and tests of QED. Examples include the study of high charge states of iron in the solar corona (the "coronal green line" of Fe^{13+}), the atomic structure and metastable $^2\mathrm{P}_{3/2}$ state of B-like Ar^{13+}. Single-electron ions are of interest in QED, and may have important applications in fundamental metrology and determination of the constants of nature.

This work presents the first experiments in a broader effort to study highly-charged ions in an isolated environment. Novel ion trap architectures are designed to facilitate ion capture from the NIST EBIT, with the potential for studying a wide variety of atomic systems. The feasibility of extremely compact traps (unitary Penning traps) for isolating highly-charged ions may be useful for the development of ion cooling techniques and charge-exchange experiments that are difficult to do in high temperature ion sources. The "first light" experiments on metastable Ar^{13+} demonstrated in this work have proven the effectiveness of these novel, compact Penning traps to carry out lifetime measurements with precision rivaling some previous experiments at high energy facilities and inside EBITs. The new ways enabled by unitary Penning traps to control and investigate systematic effects in the radiative lifetimes of metastable states are a major improvement over previous works [33, 34, 32, 31].

The new tools and techniques developed here are useful for future experiments investigating single-electron systems. Planned experiments to combine recent improvements in frequency metrology with ion capture and storage techniques to probe the structure of highly-charged ions in the high angular momentum regime are motivated by the possibility of refining some constants of nature important in fundamental metrology [3].

Chapter 2

Unitary Penning Traps

2.1 Overview

To enable better control and spectroscopic measurements on highly-charged ions, this work has focused largely on capturing and confining ions extracted from the NIST EBIT. Penning traps have been selected for the first demonstration of ion capture at the NIST EBIT. A Penning trap consists of a stack of cylindrically symmetric, coaxial electrodes which provide an electric potential well used for ion confinement. Radial confinement is provided by a superimposed, axial magnetic field. Traditionally, Penning traps consist of electric and magnetic field sources with fully separable electrode and magnet structures; allowing for independent modifications of either system. The theory and operation of Penning traps is well understood, with much experimental insight into the subtleties associated with high-field (multi-Tesla) trapping [47].

It is experimentally advantageous to have easier access to the isolated ions to facilitate the control or manipulation of stored ions by laser or atomic beams. In addition, space constraints at the NIST EBIT, a multi-user facility, prevent the immediate use of a high-field Penning trap. Therefore, compact, Penning trap designs with non-traditional architecture employing rare-earth (NdFeB) axisymmetric magnets have been explored [24]. These traps are referred to as unitary Penning traps. While previous work has relied on arrays of rare-earth magnets [48, 49], the unitary architecture is characterized by the full integration of electric and magnetic field sources; making it impossible to separate the electrode and magnet structures. This novel architecture has lead to the development of extremely compact traps. The simplest realization utilizes a single NdFeB (N42 grade) magnet to generate the axial trapping magnetic field. A slightly more complex design has been developed which relies on two coaxial, separated magnets. Both the one-magnet Penning trap and two-magnet Penning trap are conceptually similar to a traditional Penning trap [11]. Here, broad design challenges in unitary Penning trap development are addressed including the generation of electric and magnetic fields for trapping, optical and atomic beam access to stored ions, and numerical estimates of expected trap performance.

2.2 One-magnet Penning trap design

A simple Penning ion trap has been developed using a single permanent magnet to generate the axial magnetic field necessary for ion confinement. A schematic of the one-magnet trap is shown in Fig. 2.1. The trap consists of three main electrodes; a central ring electrode and two endcap electrodes. The central ring electrode is made up of an axially magnetized rare-earth magnet with two oxygen-free-high-conductivity (OFHC) copper discs which are press fit to the ends of the magnet. The trap magnet has dimensions of length, inner diameter (I.D.), and outer diameter (O.D.) of 38.10 mm, 19.05 mm, and 19.05 mm, respectively. These copper discs are

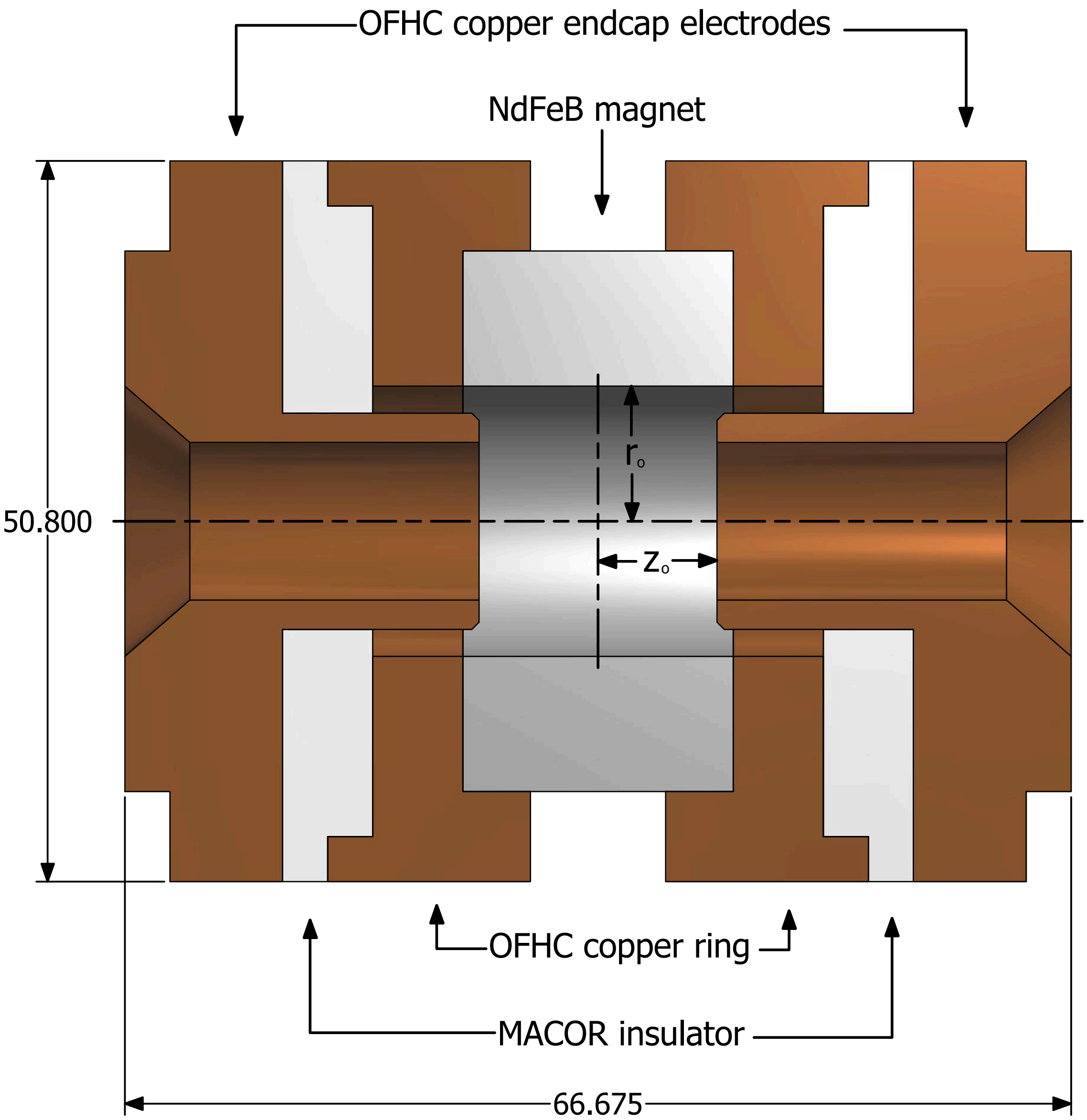

Figure 2.1: Schematic of the one-magnet Penning trap. Dimensions are in mm.

used to make electrical contacts for the ring magnet and provide structural support for the trap assembly. The ring electrode is electrically isolated from the endcaps via MACOR insulators which also provide the endcap alignment along the trap axis. The trap endcaps are made of OFHC copper and are fit to the ring assembly using compression discs. The characteristic dimensions for the one-magnet ion trap are $z_0 = 8.382$ mm and $r_0 = 9.525$ mm.

Since the physics of the Penning trap has been well studied [47], it is convenient to use its description to understand the permanent magnet Penning trap that has been designed. A charged particle moving perpendicular to a uniform magnetic field will undergo circular motion with a frequency, commonly called the cyclotron frequency, given by

$$\omega_c = \frac{Qe|B|}{m}, \tag{2.1}$$

where Qe is the charge of the particle, $|B|$ is the magnitude of the magnetic field, and m is the mass of the particle. For a bare Ne nucleus in a magnetic field of $\approx$ 0.3 T, the cyclotron frequency $\omega_c/2\pi \approx 2.3$ MHz. Under the right circumstances, (particle kinetic energy and magnetic field) the charged particle will orbit inside the trapping volume without hitting the electrode wall, and is considered to be trapped radially.

In order to trap the particle axially, an electrical potential is applied to the endcaps. Near the center of the trap, ion motions approximate the ideal case in which electrode surfaces are hyperboloids of revolution. Here the electric potential is given by

$$V = \lambda V_0 \frac{z^2 - r^2/2}{2d^2}. \tag{2.2}$$

The field coordinates z and r are defined from the center of the trap; V_0 is the applied potential difference between the endcaps and the central ring electrode, and d is a geometric factor

$$d^2 \equiv \frac{1}{2}(z_0^2 + r_0^2/2). \tag{2.3}$$

The dimensionless parameter λ (typically referred to as C_2) is of order unity. The case of $\lambda = 1$ corresponds to a perfect hyperbolic trap. The minimum distances r_0 and z_0 are from the center of the trap to the ring, and to the endcap electrodes, respectively. For small amplitudes, the ion motion in the trap approximates the ideal case in which the radial and axial motions of the particle are independent. The axial motion is described by a simple harmonic oscillator with frequency

$$\omega_z^2 = \lambda \frac{QeV_0}{md^2}. \tag{2.4}$$

For example, with $V_0 = 10$ V, a $^{20}\mathrm{Ne}^{10+}$ ion oscillates with $\omega_z/2\pi \approx 414.8$ kHz. For the trap described here $\lambda \approx 0.814$.

A third component of the ion motion, the magnetron motion, arises from the $\mathbf{E}\times\mathbf{B}$ interaction inside the trap [47]. This mechanism gives rise to a slow precession of the cyclotron orbit, with frequency given by

$$\omega_m = \frac{1}{2}[\omega_c - \sqrt{\omega_c^2 - 2\omega_z^2}]. \tag{2.5}$$

Considering a bare Ne nucleus with the trapping parameters described above, $\omega_m/2\pi \approx 38.03$ kHz. Typically, $\omega_m << \omega_z << \omega_c$; the relative magnitudes within this hierarchy of frequencies depend on trapping conditions, charge state of the ion, and trap geometry.

The region of stable ion orbits in a trap is determined by the trap magnetic field, ion charge, mass, and the axial potential well. As shown in [47], the condition for stable ion orbits is given by

$$\omega_c^2 - 2\omega_z^2 > 0. \tag{2.6}$$

This condition translates to ω_m being purely real. In the case of a hyperbolic trap in a uniform magnetic field, if an ion orbit is stable in one location in the trap, then it will be stable over the entire trap volume. However, in the case of the single permanent magnet, spatial magnetic field variations lead to orbits being stable only in certain locations within the trap. Hence, a narrower range of potential well depths is available for ion confinement. This issue is addressed in §5.5.1.

2.2.1 Magnetic Field

To approximate an ideal Penning trap, the uniform magnetic field is typically generated using a large superconducting solenoid magnet. The unitary architecture presented here relies heavily on knowledge of the magnetic field produced by permanent magnets. As shown in [50], the magnetic field produced by an axially magnetized, cylindrical permanent magnet can be treated as a pair of solenoids located at the inner and outer surfaces of the magnet with counter propagating currents. While the two solenoid description is elegant, it is not practical for the design of magnetic circuits which involving magnetically soft materials; such as the two-magnet Penning trap presented in §2.3. Therefore, numerical calculations of the magnetic fields produced by the one and two-magnet traps have been carried out. These calculations were done using QuickField, a commercially available software package designed for magnetic circuit calculations [51]. The software employes a finite-element method (FEM) [52] to calculate the magnetic field in regions containing magnetic and non-magnetic materials, as well as free space. The calculated magnetic flux density for a single N42 grade NdFeB magnet is shown in Fig. 2.2.

The magnetic field is calculated for a cylindrically symmetric model which specifies the location of magnetic material and free space. The magnetic field has a saddle-point at the center, decreasing on-axis, and increasing towards the magnet walls. The field strength is 0.317 T at the magnet center and 0.381 T at the inner wall. On-axis, the field decreases to zero at $z = \pm$ 12.94 mm and has a field-reversed, local maximum of 0.089 T at $z = \pm$ 20.75 mm.

The magnetization curve for the N42 material is an important input for the calculation. Near room temperature, and near zero magnetizing field H, the magnetic field has the form

$$B = \mu_o H + B_r \tag{2.7}$$

where B is the magnetic field, μ_o is the permeability of free space, and B_r is the remnant magnetization of the material. The grade of the magnet largely determines the field produced. In the case of N42 grade, $B_r \approx 1.31$ T. In addition to the remnant magnetization, permanent magnets are also specified by a coercive force, H_c. This is the field needed to de-magnetize a material. For N42 grade magnets,

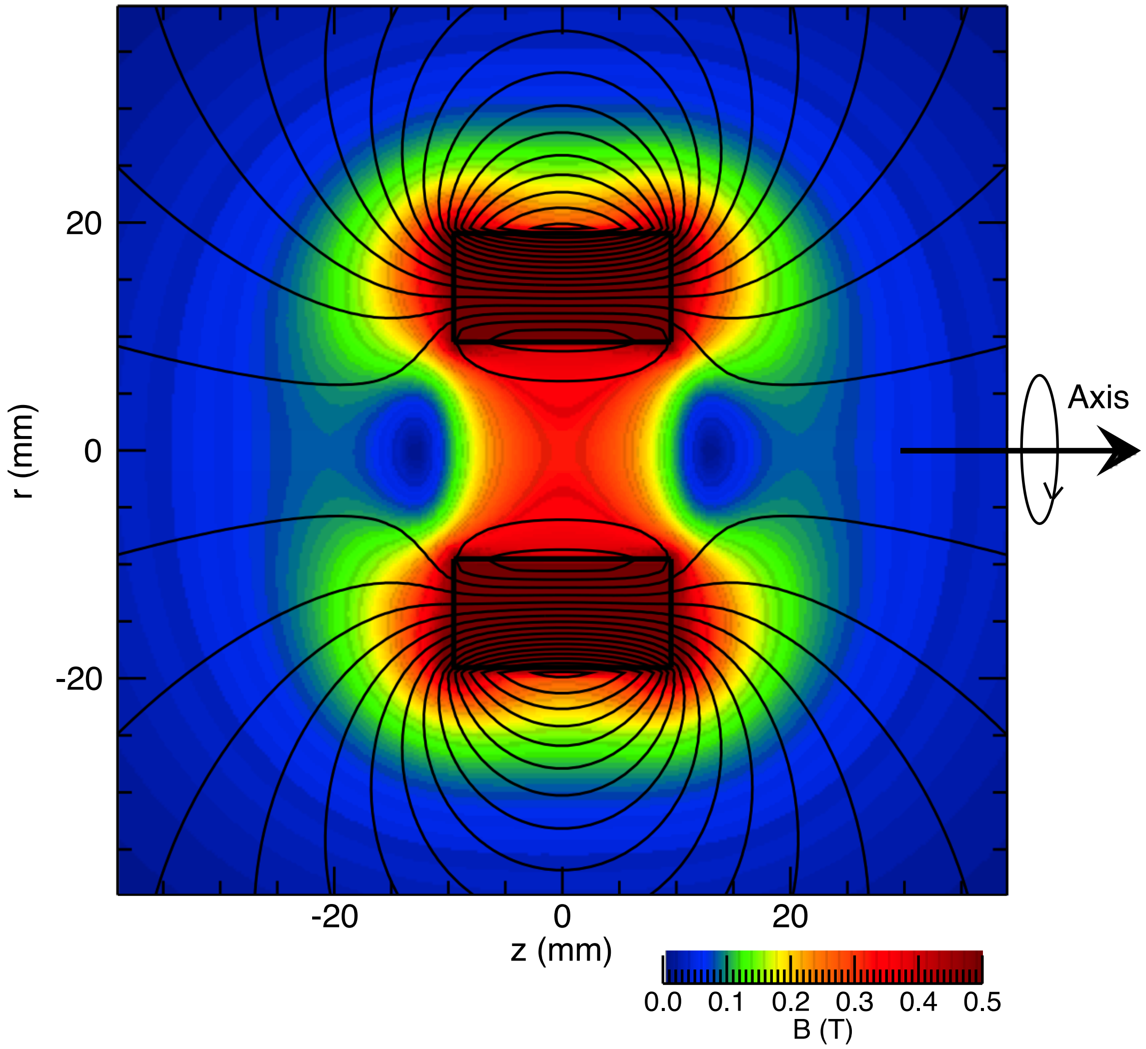

Figure 2.2: Calculated magnetic flux density for a single N42 neodymium (NdFeB) magnet.

$H_c \approx 98 \times 10^3$ A/m. Typically, these values are determined by a statistical analysis of many magnets, and have a precision of 5 % for B_r and 8 % for H_c [53]. A linear approximation for a particular grade of magnet has the form

$$B = \mu_a H + B_r \tag{2.8}$$

where μ_a is the slope of the operating line as is given by

$$\mu_a = \frac{B_r}{H_c}. \tag{2.9}$$

Given the variation in production of sintered rare-earth magnets, it is necessary to adjust the magnetization curve in order to optimize the agreement between the calculated and measured magnetic field produced by a given trap magnet. In the case of the one-magnet trap, the magnetization curve was scaled to 95 % of the specified value in both B_r and H_c. The specified and optimized magnetization curves are shown in Fig. 2.3.

A comparison of the calculated and measured magnetic field on-axis is shown in Fig. 2.4. The magnetic field measurements were made using an axial Hall probe with dimensions 1.9 mm wide, 2.3 mm long, and $\approx$ 0.5 mm thick. The probe has a calibration accuracy of 2 % and a magnetic field resolution of $\delta B/B = 1/300$. Measurements of the a batch of trap magnets revealed that the magnetic field at the center of the magnet ranged from 0.314 T – 0.320 T.

A comparison between the calculated and measured field at the center of the magnet shows an agreement of $\approx$ 0.3 %. Given this level of agreement, it is possible to design a simple trap using FEM calculations to model the permanent magnets.

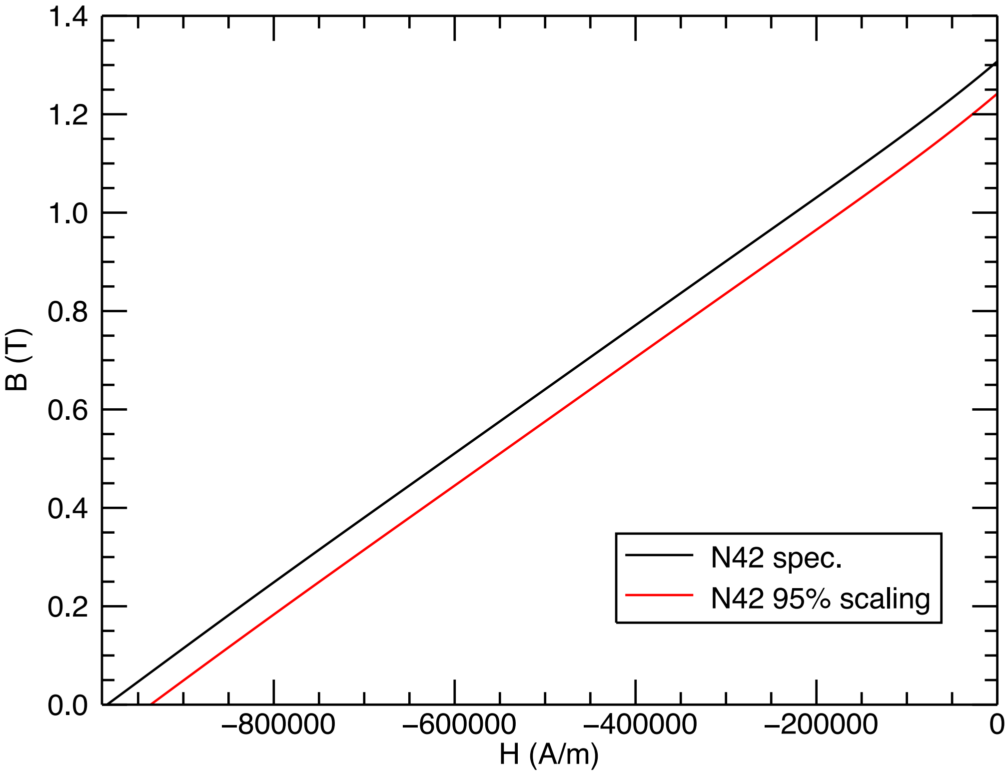

Figure 2.3: Magnetization curves for a typical N42 grade magnet.

2.3 Two-magnet Penning trap design

While the one-magnet design is the simplest realization of a unitary Penning trap, it is limited in beam access to the trapped ions. There is no direct line of sight to the trap region, other than along the magnetic field axis. A slightly more sophisticated trap design based on the use of two axially magnetized permanent magnets was developed. Two magnets, separated by a common soft iron ring (yoke piece) form a structure which allows holes to be cut in the central ring for beam

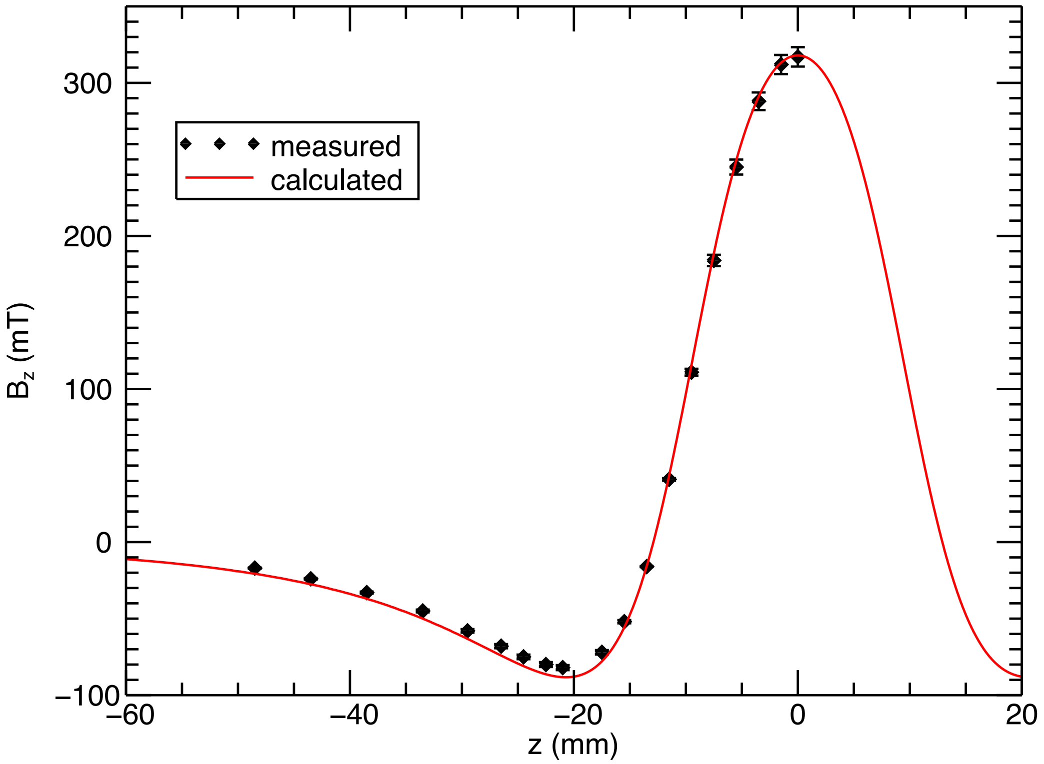

Figure 2.4: Measured and calculated magnetic flux density along the symmetry axis for a single N42 neodymium (NdFeB) magnet.

access. As in the case of the one-magnet trap, near the center of the two-magnet trap, the electric potential approximates a quadrupole with characteristic trap dimensions of $z_0 = 4.736$ mm and $r_0 = 8.500$ mm. Consequently, in the example taken for the one-magnet trap, with $V_0 = 10$ V, a $^{20}\mathrm{Ne}^{10+}$ ion oscillates with $\omega_z/2\pi \approx 597.04$ kHz. Here $\lambda \approx 0.854$.

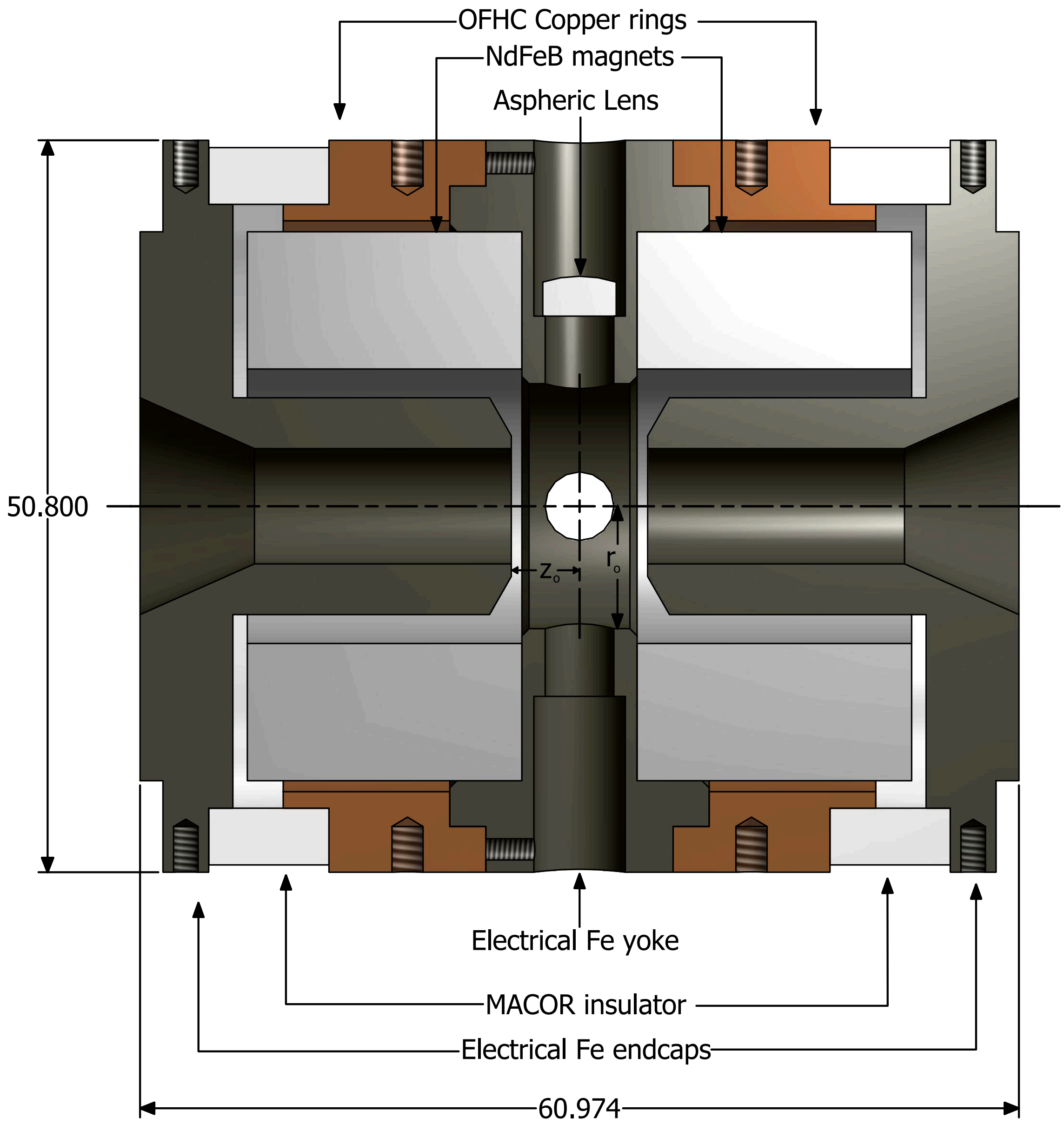

Figure 2.5: Schematic of the two-magnet Penning trap. Dimensions are given in mm.

2.3.1 Magnetic Field

The availability and low cost of N42 grade magnets makes them a logical choice for initial trap designs and investigations. However, N42 grade magnets have a low maximum operating temperature of ≈ 80° C. It is desirable to obtain the lowest possible vacuum pressure in the ion trap apparatus. The lowest possible pressure is often achieved by raising the temperature of the vacuum chamber to greater than 100° C to accelerate the outgassing rate of elements in the apparatus. Water vapor tends to adhere to electrode surfaces and porous glass insulators during assembly. The constraint to keep the operating temperature below 100° C ultimately limits the base pressure that can be achieved using room-temperature UHV pumps. Therefore, in the two-magnet trap design, N40UH (a high-temperature grade) magnets were chosen for the trap design.

As in the case of the N42 grade magnets, within manufacturing tolerances, the N40UH grade magnetization curve has been scaled to achieve close agreement between the measured and calculated magnetic field on-axis. The N40UH magnetization curve has been scaled to 97% of the specified value. A comparison of the measured and calculated magnetic field on-axis for the N40UH case is shown in Fig. 2.7, with an agreement of ≈ 0.2 % at the center of the magnet.

The field produced by two magnets separated by a distance of 8 mm is plotted in Fig. 2.8. It is assumed that the magnets could be kept separated by the use of a copper electrode similar to the central iron electrode shown in Fig. 2.5. Copper, being non-magnetic, and a good electrical conductor, is a natural choice for structural

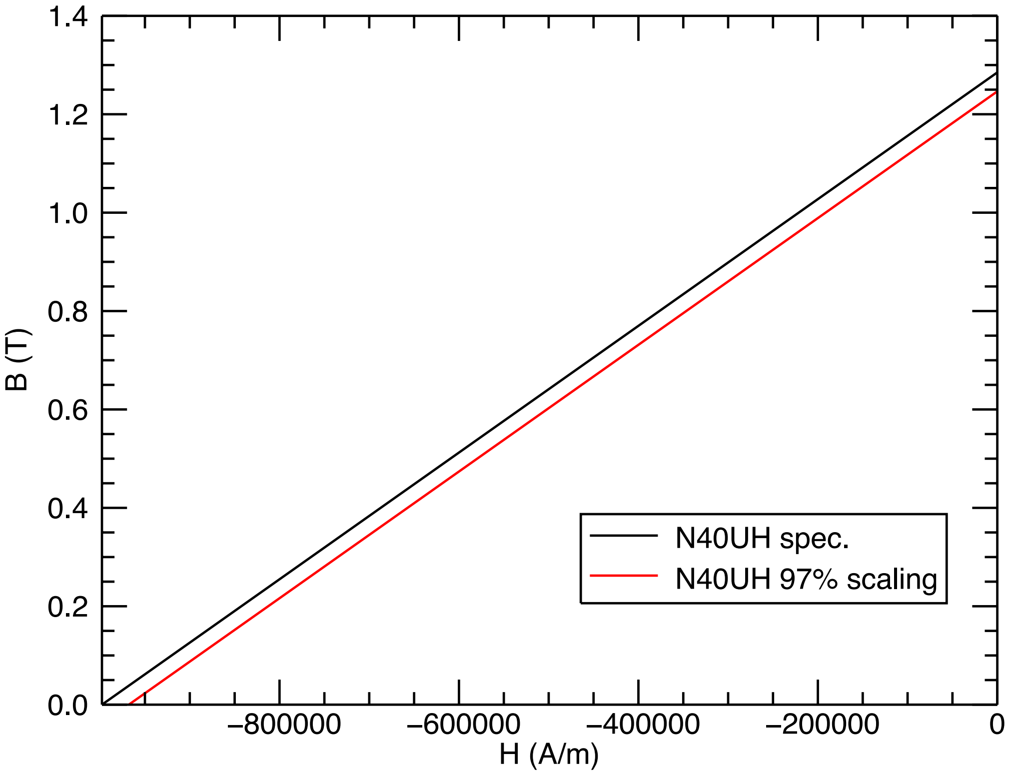

Figure 2.6: Magnetization curves for a typical N40UH grade magnet.

parts, as well as electrodes in the trap.

Sintered NdFeB magnets are brittle and easily corrode in high humidity. Commercial magnets are formed in a mold to create the desired geometry. The tolerance on custom-made magnet dimensions is typically ± 0.010 in, which is not nearly as precise as what can be achieved with modern CNC machines. The magnet surfaces are given three layers of plating (nickel-copper-nickel) to make them corrosion-resistant. The fabrication process has a tendency to produce irregular surfaces, which can lead to patch effects in the electric field produced by the surface when

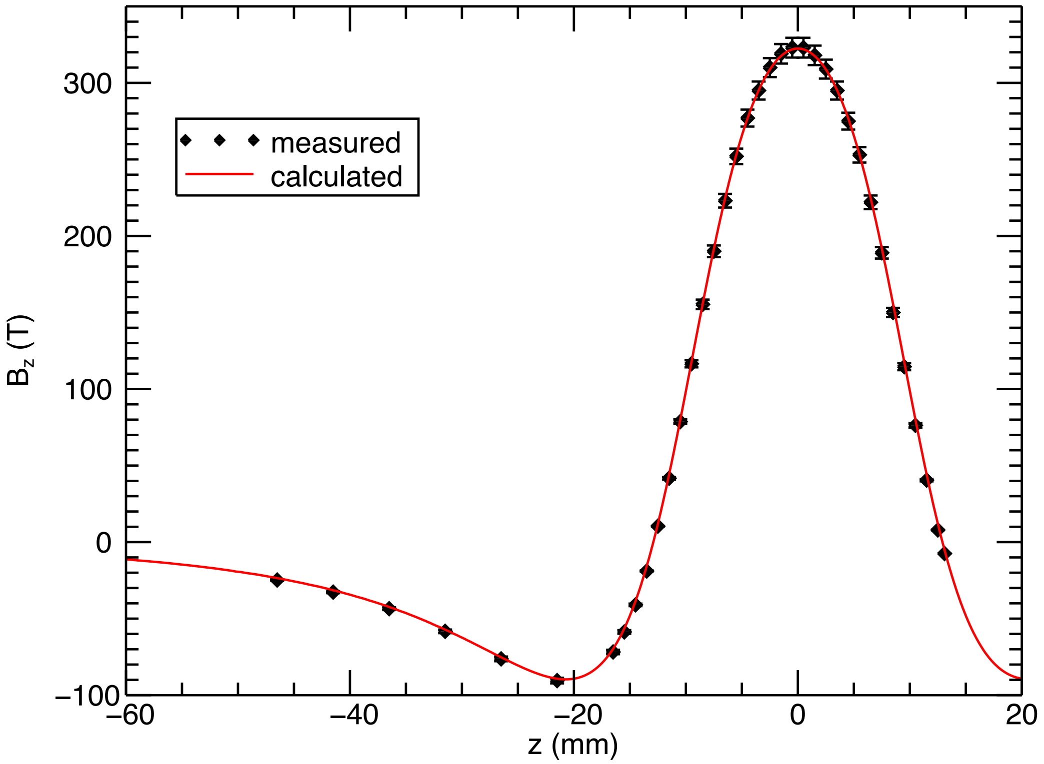

Figure 2.7: Measured and calculated on-axis magnetic flux density for a single N40UH neodymium (NdFeB) magnet.

biased at high voltage. It is more desirable to have precision-machined electrodes that conceal the two magnets, minimizing the role of the magnets in shaping the electric potential in the trap region.

As shown in Fig 2.8, the field between the two magnets drops rapidly to well below that of a single magnet, which is not useful for ion trapping. This calculation represents the starting point for a trap design based on multiple magnets. We now show that the introduction of "magnetically soft" electrical iron yoke pieces allows

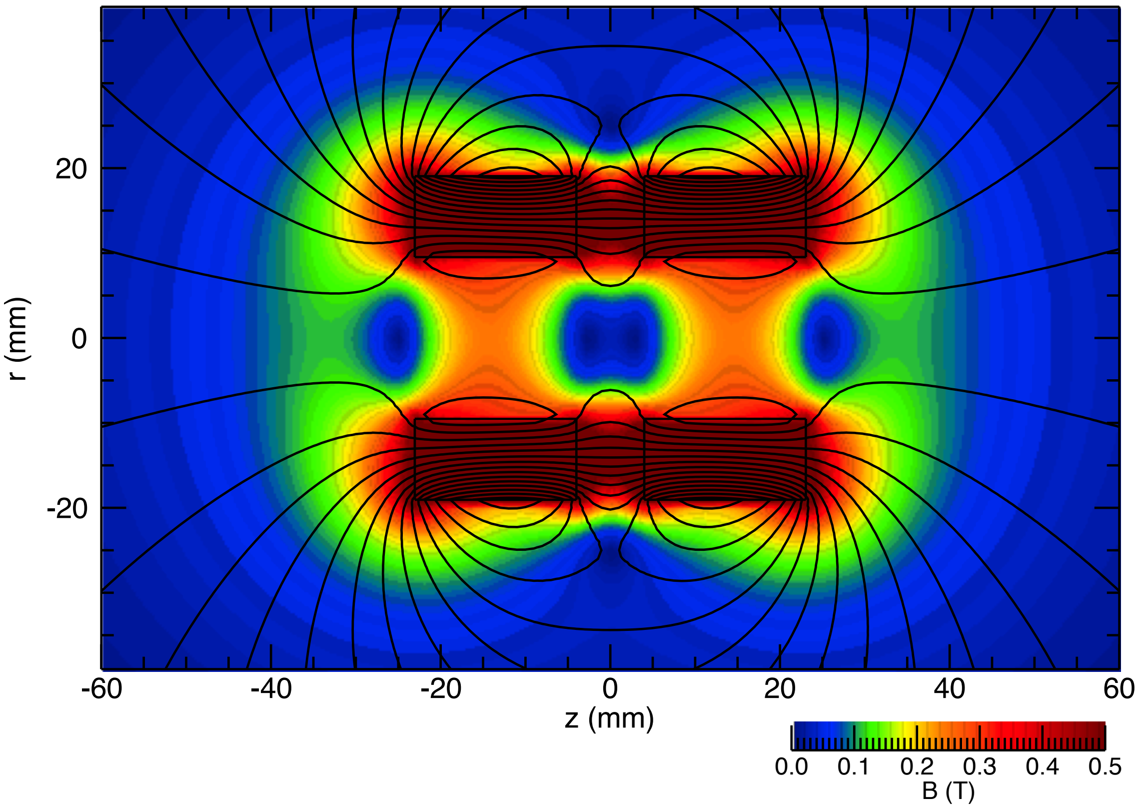

Figure 2.8: Magnetic field calculation of two-magnet trap with Cu spacer.

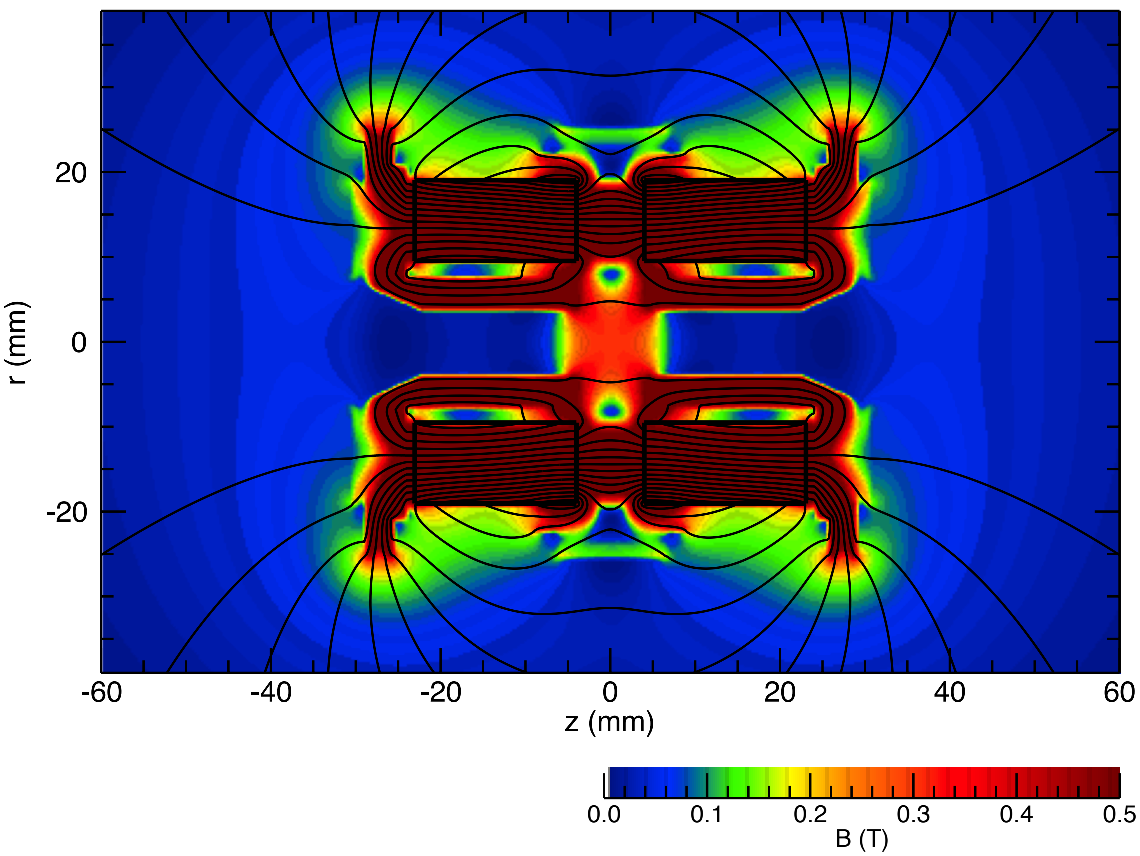

Figure 2.9: Magnetic field calculation of two-magnet trap with Fe yoke pieces shown in Fig. 2.5.

for the magnetic field to be re-directed towards the center of the assembly in such a way that the central trap region will coincide with the region of strongest magnetic field. The calculated magnetic field of the two-magnet trap with soft iron electrodes is shown in Fig. 2.9. The influence of electrical iron in shaping the magnetic field is evident when comparing the Cu spacer design (Fig. 2.8) and this final design.

The magnetization curve for the chosen electrical iron is shown in Fig. 2.10. There are various grades of electrical iron commercially available. For the construction of the two-magnet trap we chose the Class 1 grade manufactured by Carpenter.

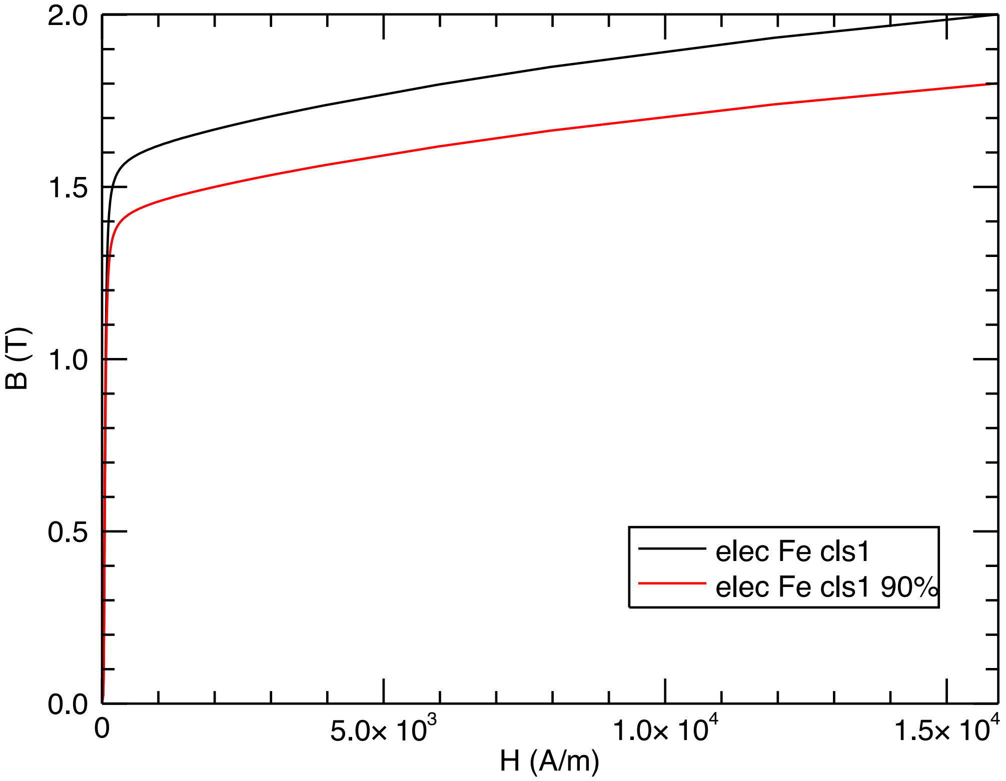

Figure 2.10: Magnetization curves for a Class 1 electrical iron.

This class has the highest field permeability of available electrical iron. As in the case of single magnet calculations, the magnetization curve of the electrical iron has been adjusted within known tolerances to obtain the closest agreement possible between measurement and calculation. The electrical iron magnetization curve has been scaled by multiplying the magnetic field by a proportionality factor. As shown in Fig. 2.10, the magnetic field has been scaled to 90% of the specified value. An enlarged plot highlighting the lower H region is shown in Fig 2.11

A comparison between the calculated and measured magnetic field on-axis is

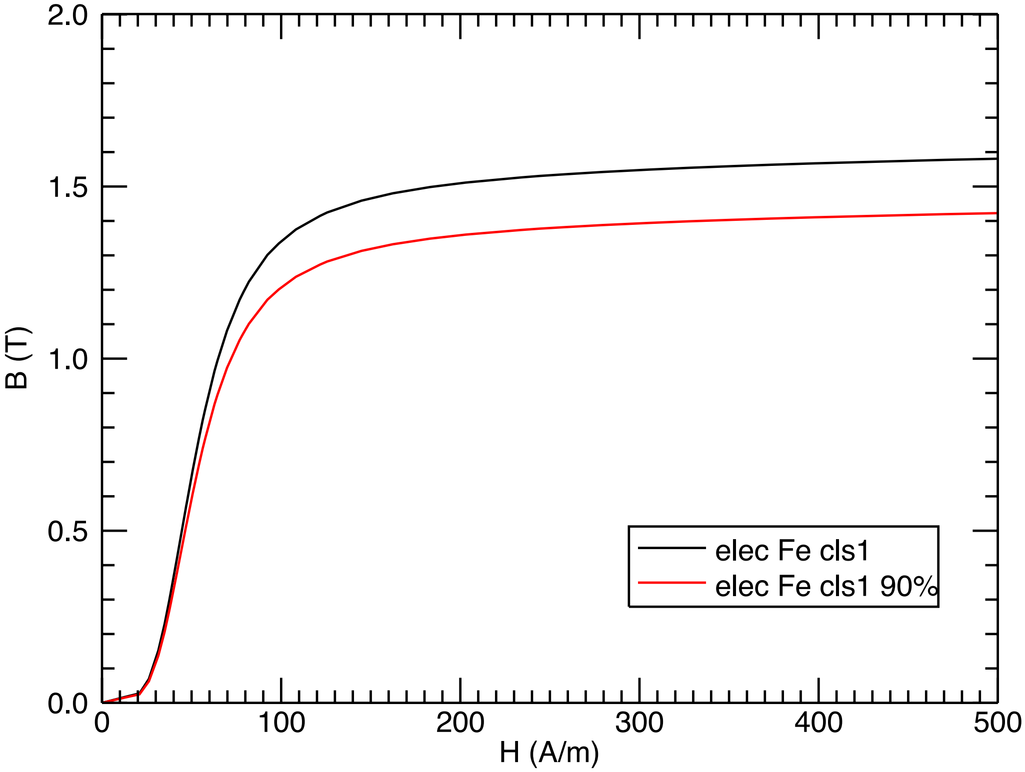

Figure 2.11: Zoomed in view of magnetization curves for Class 1 electrical iron.

shown in Fig. 2.12. A plot highlighting the trapping region is shown in Fig. 2.13. Here we present measurements of the trap magnetic field for assemblies using both N42 grade and N40UH grade magnets. The trap magnets were carefully selected and matched so that the central field of each magnet is equal within the Hall probe resolution of $\delta B/B = 1/300$. The uncertainties in the magnetic field measurements are estimated to be

$$\delta B_z = \sqrt{(\delta B_m)^2 + \left(\delta z \frac{dB_z}{dz}\right)^2} \tag{2.10}$$

where δB_m is the uncertainty in the magnetic field measurement, δz is the uncertainty of the probe position ≈ 0.1 mm, and dB_z/dz is the derivative of the calculated magnetic field on-axis. Based on these measurements, the field uniformity in the trapping region within ± 2 mm of the trap center is estimated to be better than $\delta B/B = 1/300$.

2.3.2 Ion storage calculations

Ion trajectories in a unitary Penning trap were investigated in numerical calculations to obtain the dynamical properties of the traps. In order to study trapping dynamics, the electric field inside the trapping region must be calculated in addition to the magnetic field. The electric field in the trap is simulated numerically using a commercial software package named Charged Particle Optics (CPO). This software employs a Boundary Element Method (BEM) [54] originally developed for calculating properties of electrostatic lenses. In relaxation methods, a three dimensional grid is defined, upon which Laplace's equation is solved numerically using

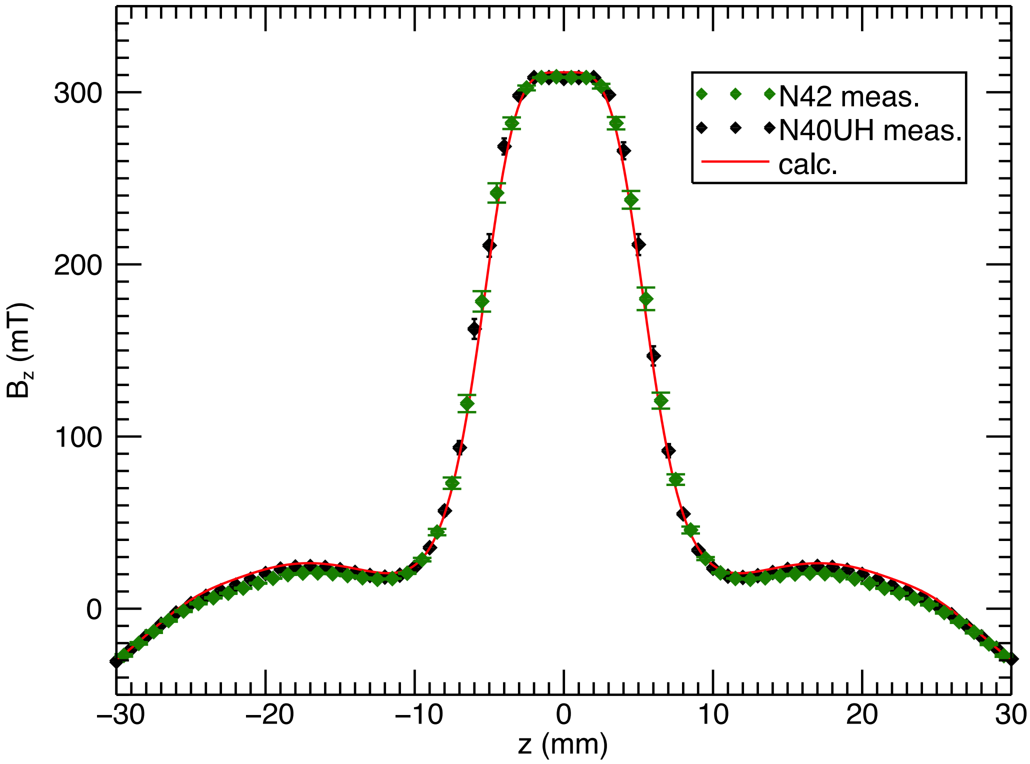

Figure 2.12: Measured and calculated on-axis magnetic flux density for the two-magnet Penning trap.

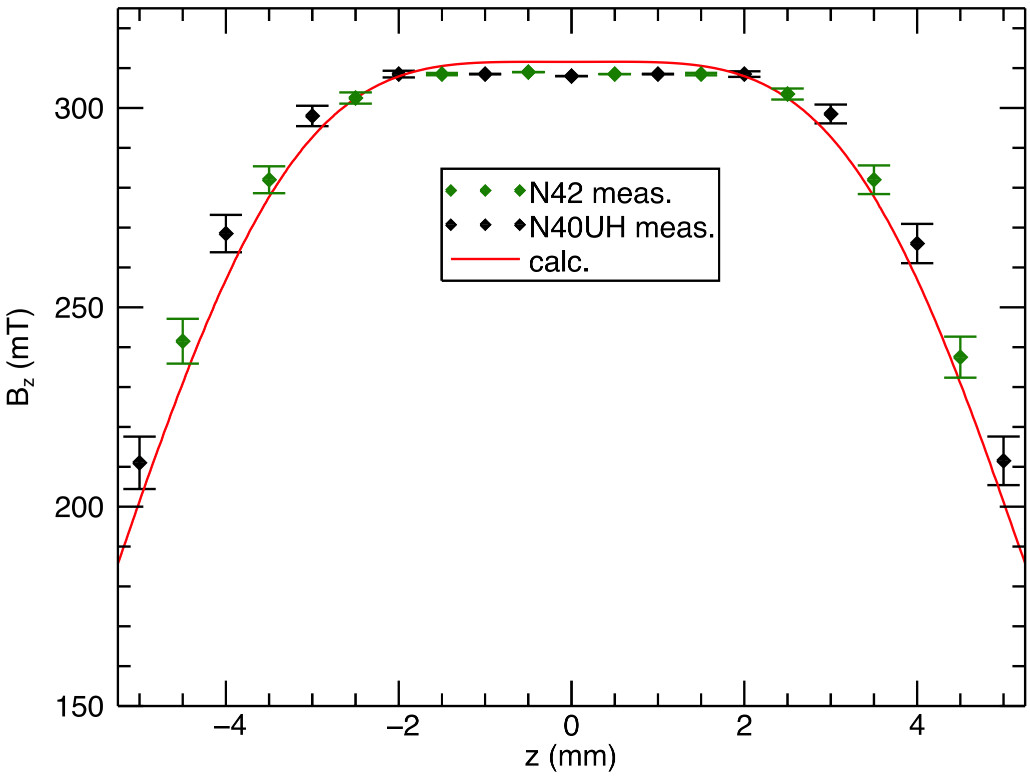

Figure 2.13: Measured and calculated on-axis magnetic flux density for the two-magnet Penning trap.

iterative algorithms. In contrast, BEM calculations are done by defining electrode surfaces as a system of segments and then calculating the field in the space around the electrode when a voltage is applied to the surface. The electric field around the electrode is calculated by first dividing the electrode surface into many small segments of electric charge and then summing the Coulomb field produced from the charge residing on each segment. In a BEM calculation, the electric field is given as

$$\mathbf{E}(\mathbf{r}) = \sum_{i}^{N} \tilde{\mathbf{E}}_i(\mathbf{r} - \mathbf{r}_i). \tag{2.11}$$

Here i is each charge segment, N is the total number of charge segments, and $\tilde{\mathbf{E}}_i(\mathbf{r} - \mathbf{r}_i)$ is given by

$$\tilde{\mathbf{E}}_i(\mathbf{r} - \mathbf{r}_i) = \frac{1}{4\pi\epsilon_0} \frac{q_i}{|\mathbf{r} - \mathbf{r}_i|^2}, \tag{2.12}$$

where q_i is the charge on each electrode segment. An example of the numerically calculated on-axis potential of the two-magnet trap is shown in Fig. 2.14. The calculated BEM potential agrees with the quadrupole potential given in Eq. (2.2) to within $\approx$ 0.1 V for $z = \pm$ 2 mm, and agrees to within $\approx$ 0.01 V for $z = \pm$ 1 mm. A detailed discussion of the electric potential during ion capture and storage will be presented in Ch. 4. Given the calculated electric and magnetic fields, it is possible to calculate an ion trajectory in the trap by integrating the equations of motion using standard Runge-Kutta techniques [55]. An example of a calculated ion trajectory is given in Fig. 2.15.

The ion trajectory (black) is shown in the mid-plane of the trap. The initial conditions are chosen such that the ion orbits in the most uniform region of the magnetic field. Here the ion exhibits a fast cyclotron motion due to the magnetic

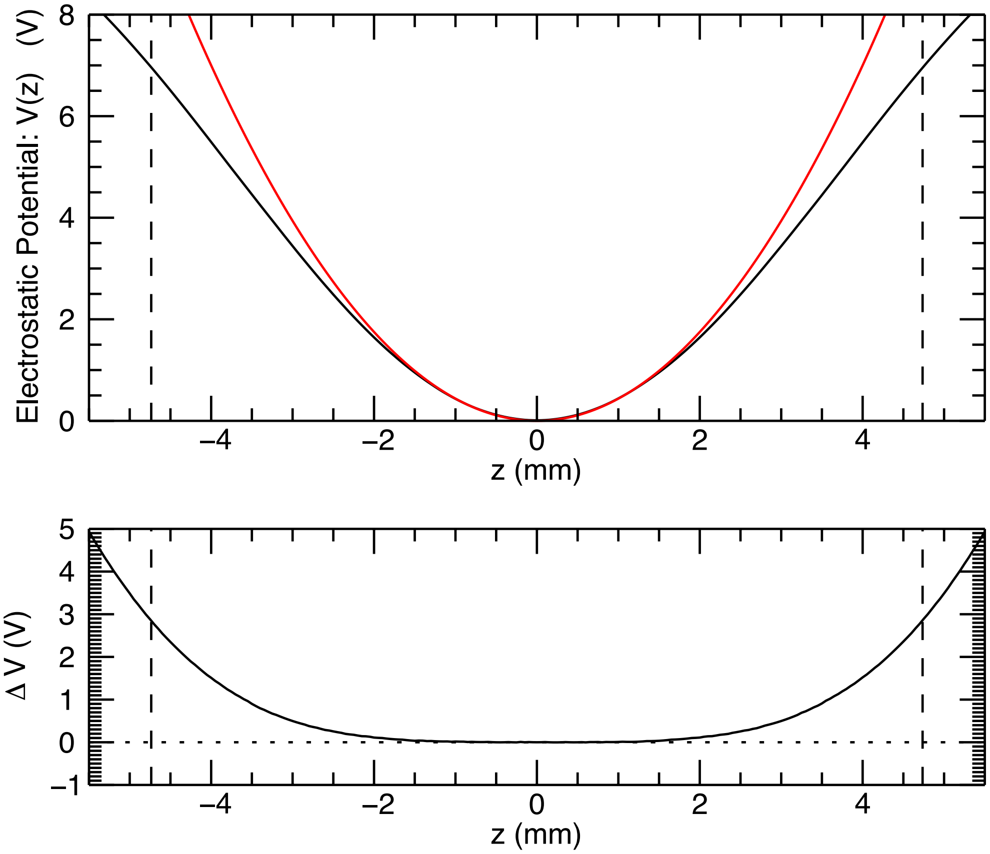

Figure 2.14: Calculated on-axis potential for the two-magnet trap. The applied potential difference V_o = 30V. Dashed lines show the position of the endcap electrodes at $z_o = \pm$ 4.736 mm. Top: Comparison of full BEM calculation (black) and approximate potential (V_{app}) calculated using Eq. (2.2) (red). Bottom: $\Delta V = V_{app} - V_{BEM}$ shows agreement of $\approx$ 0.1 V for $z = \pm$ 2 mm and agreement of $\approx$ 0.01 V for $z = \pm$ 1 mm.

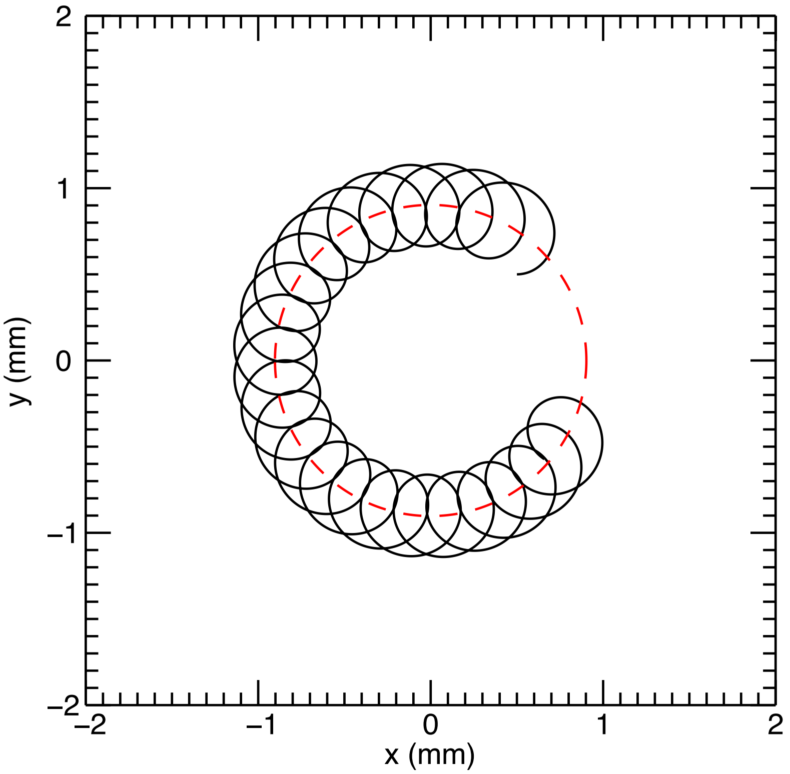

Figure 2.15: Calculated trajectory for a stored NeXI ion in the designed operating conditions of the two-magnet Penning trap.

field, while the slow magnetron precession is shown with a radius of ≈ 1mm (red dashed line). A fast Fourier transform (FFT) of the ion trajectory shown in Fig. 2.16 reveals the cyclotron (inset) and magnetron components of the motion. Since the trap is azimuthally symmetric the x-component of the trajectory is sufficient for the FFT. The cyclotron frequency and magnetron frequency are, $\omega_c/2\pi \approx 2.3$ MHz and $\omega_m/2\pi \approx 80$ kHz.

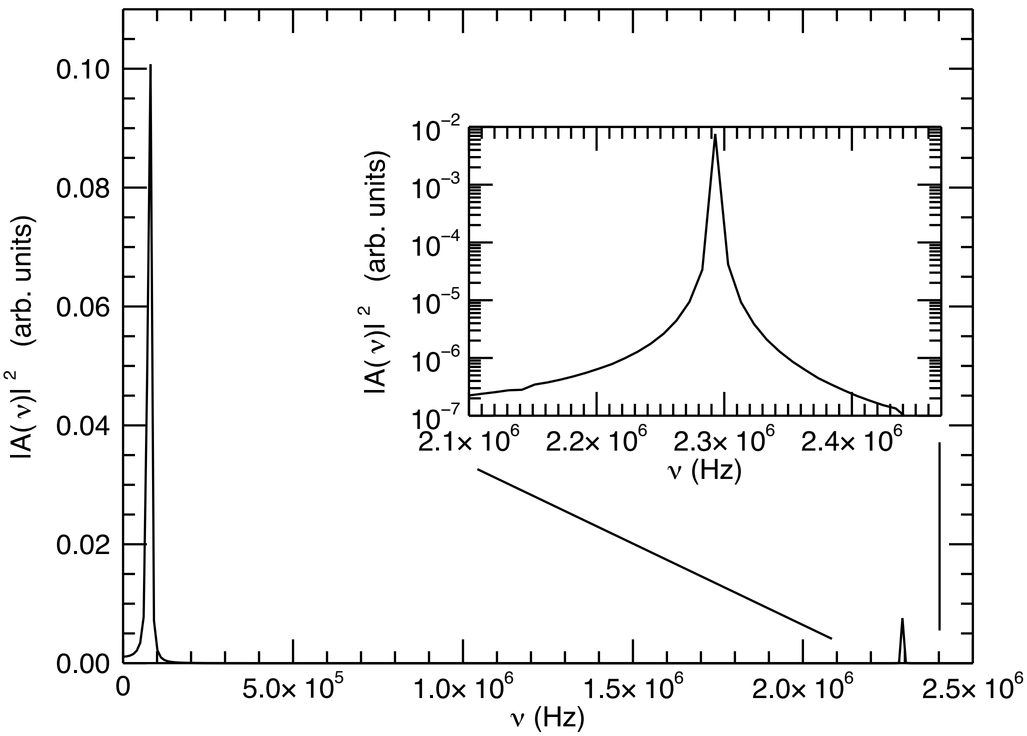

Figure 2.16: Fast Fourier Transform (FFT) spectrum of a calculated trajectory for a NeXI ion in a unitary Penning trap.

2.4 Discussion

Unitary Penning traps with fully integrated electric and magnetic components have been developed for the purpose of capture and storage of highly-charged ions. The use of rare-earth permanent magnets can be advantageous for applications with severe space constraints. We shall demonstrate that the magnetic field produced by small cylindrical magnets is sufficient for ion storage. Calculations using the QuickField software of the magnetic field from both a single magnet trap and a two-magnet design agree with measurements, within uncertainty. The field uniformity in the two-magnet trap is better than $\delta B/B = 1/300$. For small amplitude orbits, frequencies of ion motions are in good agreement with estimates using an ideal Penning trap.

The unitary traps presented here represent a limit in the compactization of a Penning trap. The ability to fully integrate the magnets and electrodes into a single structure opens a new possibility for miniaturized traps for a wide variety of applications.

Chapter 3

Special Facilities, Tools, and Techniques

The previous chapter gives an account of the development of unitary Penning traps. Here we discuss the specialized facilities needed for the production of highly-charged ions, ion extraction and transport, and the new apparatus for slowing and capture of extracted ions is also described. In §3.1 the NIST EBIT is introduced along with the ion beamline that serves to transport ions from the source to the unitary Penning trap. The one-magnet Penning trap apparatus used in the first experiments is described in §3.2, with details about the high vacuum requirements and auxiliary electrode structure to optimize ion transport and capture. The two-magnet Penning trap apparatus employed in the second generation experiments is introduced in §3.3. The two-magnet Penning trap apparatus replaced the one-magnet apparatus, occupying the same region of space despite the increased complexity and number of trap elements. The detection systems for both set-ups are presented in §3.4, highlighting the improvements implemented in the two-magnet Penning trap apparatus to overcome limitations in the one-magnet Penning trap. These improvements include the addition of a faster ion detector, and a photon counting system for observing light emitted from stored ions. Techniques used to minimize residual gases in the vacuum chamber are described in §3.5.

3.1 Electron Beam Ion Trap (EBIT)

The electron beam ion trap (EBIT) is an ion source capable of producing and storing highly-charged ions. The ions can be stored in the trap as a light source for atomic spectroscopy; or alternatively, selected ions can be extracted from the trap and used in ion-surface and charge-exchange (CX) experiments. The EBIT is an apparatus capable of producing plasma conditions typically found in astrophysical sources, such as the solar corona, and Tokamak fusion reactors. Typical plasma temperatures are on the order of 1-2 million Kelvin. Recently, the EBIT was used to measure the familiar D_1 and D_2 lines in sodium-like heavy metal ions [56]. The metals included tungsten (W), tantalum (Ta), hafnium (Hf), and gold (Au).

3.1.1 EBIT Operation

A review of the EBIT at NIST can be found in the article by Gillaspy *et al.* [19]. The EBIT works by using a high energy, high current density electron beam to both create and store highly-charged ions. A representation of the EBIT is given in Fig. 3.1. Atoms undergo multiple collisions with the electron beam which ionizes the atoms to high charge states. Three cylindrical electrodes, called drift tubes, are positioned in a region with a strong axial magnetic field ($\approx$ 3 T), generated by a pair of superconducting Helmholtz coils. The electron beam comes from an electron gun, is accelerated to high energies, and is steered through the drift tube region where it ionizes neutral atoms and provides the radial trapping potential for the ions. Ions can be loaded in the EBIT in two ways; either by electron impact

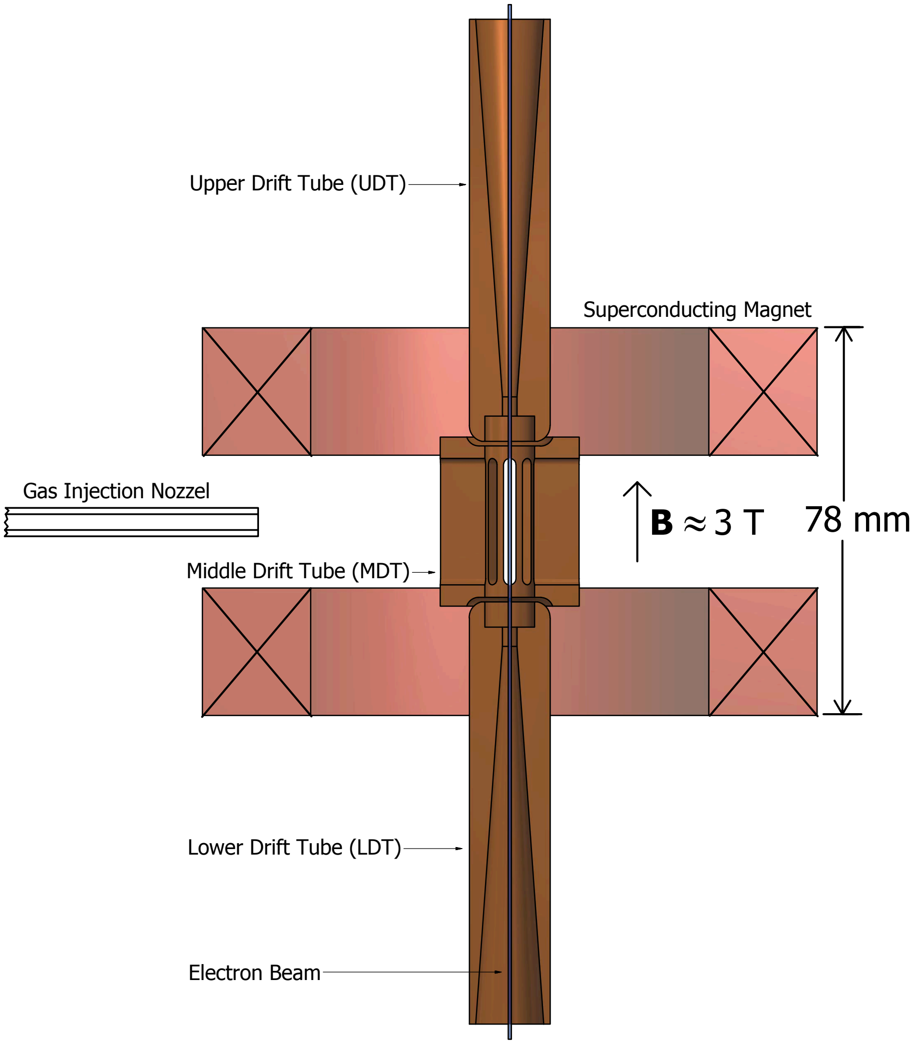

Figure 3.1: A uniform axial magnetic field is used to compress the electron beam along the axis of the trap. A radial potential well is generated by the space charge of the electron beam. The upper and lower drift tubes are biased relative to the central drift tube to provide an axial potential well. The combination of the axial and radial potential wells provides the trapping volume for the ions.

ionization of neutral gases injected through a gas nozzle, or low charge state metal ions can be loaded into the trap from an external ion source. Subsequently, ions become highly ionized through successive electron impact. The external ion source is a metal vapor vacuum arc (MeVVA) type source [57] and is mounted above the EBIT for loading along the axis of the trap.

The electron impact ionization rate is given by

$$\Gamma = n\sigma v \tag{3.1}$$

where n is the particle density, σ is the ionization cross section, and v is the electron velocity. The ionization cross section is given as a function of energy in the NIST data tables [58]. The particle density can be estimated from the measured background pressure in the trap and is given by

$$n = \frac{N_A}{V_m}\frac{P}{P_{atm}} \tag{3.2}$$

where N_A is Avogadro's number, V_m is the molar volume of the (ideal) target gas, P is the measured pressure in the trap, and P_{atm} is atmospheric pressure. The speed v is given in terms of energy by

$$v = \sqrt{\frac{2E}{m_e}} \tag{3.3}$$

where E and m_e are the kinetic energy and mass of the electron, respectively. Given the equations above, we can calculate the number of ionization events per second per electron. Since we are interested in rates of production inside the trap for a given electron beam current, we must include the trap size and number of electrons in order to get to a rate that is useful. The time taken for one electron to pass through the trap is given by

$$t = \frac{2z_o}{v} = z_o\sqrt{\frac{2m_e}{E}} \tag{3.4}$$

where z_o is the typical distance from the trap center to the endcap. The number of electrons passing through the trap during time t is given by

$$N_e = \frac{I_e}{e}t = \frac{I_e}{e}z_o\sqrt{\frac{2m_e}{E}} \tag{3.5}$$

where I_e is the measured electron beam current, and e is the charge of the electron. Substituting Eqs. (3.2) and (3.3) into Eq. (3.1) and multiply by N_e we are left with

$$\Gamma = \frac{N_A}{V_m}\frac{P}{P_{atm}}\frac{I_e}{e}2z_o\sigma. \tag{3.6}$$

The NIST EBIT is capable of operating at an electron beam energy ranging from a few hundred eV to ≈ 30 keV. The electron beam current can be greater than 150 mA. For typical ion capture experiments, an electron beam energy of ≈ 2.5 keV and electron beam current of ≈ 14.4 mA is used.

3.1.2 Ion beam extraction

The EBIT facility at NIST has been used for a variety of investigations [59]. The ion extraction capability of the NIST EBIT enables ion-surface experiments [20] and, most recently, ion capture experiments [24] that are the focus of this work. The ion extraction can be operated in a steady-state mode and a pulsed mode. In the case of ion-surface experiments, the EBIT is operated in a steady-state extraction mode which produces a constant current of highly-charged ions for bombardment of target surfaces. For the ion capture experiments, of interest here, the EBIT is

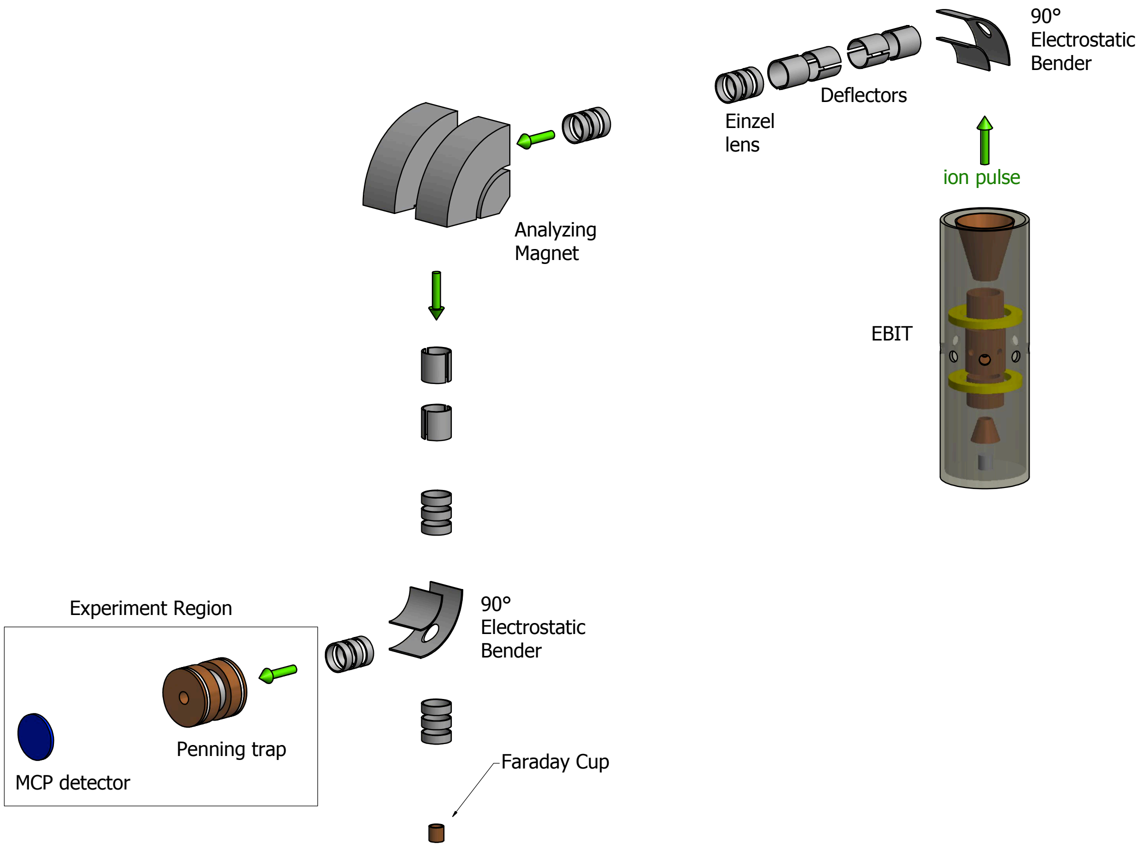

Figure 3.2: Schematic of the NIST ion extraction beamline (not to scale). Ions extracted from the EBIT are guided using electrostatic ion optics to an analyzing magnet where the charge state of interest is selected for capture or bombardment.

operated in the pulsed extraction mode which produces a periodic pulse train of ions. This pulse width in time can range from $\approx$ 100 ns - 1 μs, depending on the EBIT operating conditions. A schematic of the NIST ion beamline is shown in Fig. 3.2. The details of the ion beamline are presented in [60, 61].

The EBIT produces many charge states for a given electron beam energy, current, and ionization (or “cooking”) time. In the case of pulsed extraction, the ionization time is also the duration in which the EBIT is filled with ions before the extraction pulse is applied to the middle drift tube (MDT) electrode. As shown in [60], the electrostatic ion optics in the NIST ion beamline are charge-to-mass insensitive for all charge states accelerated through a common potential. Ions extracted from the EBIT enter the ion beamline with an energy of $E_{ion} \approx QU_{e-beam}$, where Q is the ion charge state and U_{e-beam} is the electron beam energy. Ions leave the EBIT and undergo a 90° bend through an electrostatic bender and are transported to an analyzing magnet. All ion charge states present in the EBIT are extracted from the trap and are guided via electrostatic ion optics, which includes two einzel lenses and two sets of four-quadrant deflectors before entering the analyzing magnet. The analyzing magnetic field is tuned to allow a single ion charge to mass ratio to make the 90° bend and pass through the magnet while all other charge states are deflected to the chamber walls. After filtering out unwanted charge states, the ions of interest are guided to a second electrostatic bender and either enter the ion capture apparatus, or proceed downwards to a Faraday cup located in the ion-surface target chamber.

3.2 One-magnet Penning trap apparatus

The one-magnet Penning trap is the first ion capture apparatus to be deployed at the NIST EBIT. Severe space constraints necessitated the compactization of the Penning trap for integration with ion optics, and detection systems within the ≈ 1 m space available at the ion extraction port. Experiments with this simple trap were intended to demonstrate the basic principles and techniques employed in designing unitary Penning traps for capturing ions with high kinetic energy. As another result, the EBIT and extraction beamline are optimized to produce ion pulses suitable for slowing and capture. The details of the assembly and trap geometry are discussed in §3.2.1 and §3.2.2.

3.2.1 Full assembly and vacuum chamber

The one-magnet trap apparatus was designed to be the simplest realization of the unitary Penning trap presented in Ch. 2 and therefore consists of the bare essential components for initial ion transport, capture, and detection. A simplified schematic of the apparatus is shown in Fig. 3.3. The key components consist of the one-magnet Penning trap, three sets of electrostatic steering plates, two faraday cups (FC), and a position-sensitive micro-channel-plate (MCP) ion detector (PSD).

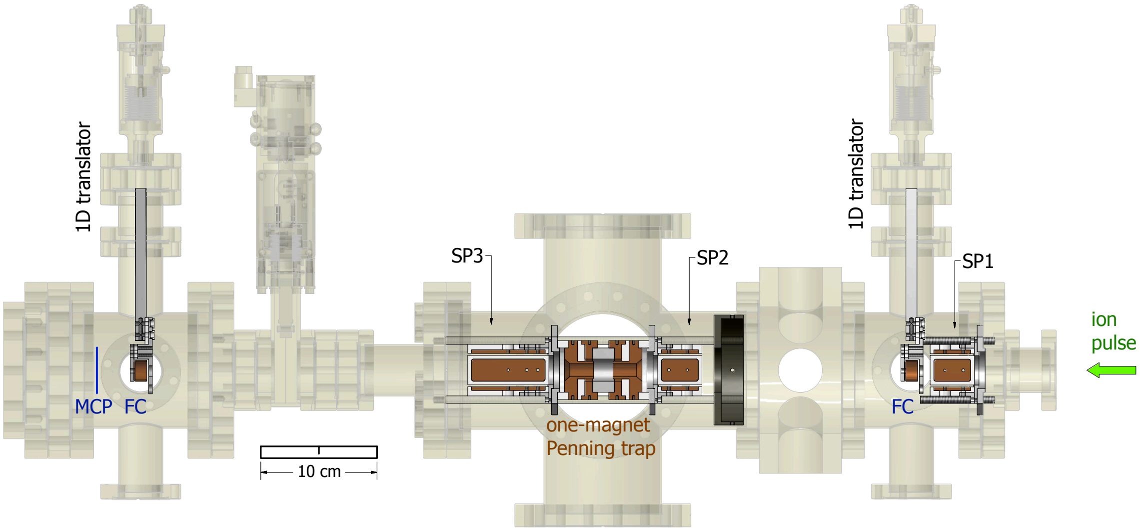

Figure 3.3: Simplified schematic of the one-magnet trap apparatus. The vacuum chamber components are shown in light grey. The one-magnet Penning trap is centered on the central six-way cross.

As shown in Ch. 2, the one-magnet Penning trap is designed with open endcaps to allow ions to enter along the trap axis of symmetry, coincident with the magnetic field axis. The right-most set of steering plates (SP1) was used to guide incoming ions towards the trap axis upon exiting the EBIT beamline. The second set of short steering plates (SP2) is used to further correct the incoming ion trajectories to ensure that ions enter the trap as close to the trap axis as possible.

As ions approach the trap and begin to slow down, if the initial velocity is not along the trap axis, the ion pulse tends to scatter and is not trappable. The sets of right-angle plates for beam steering have proven to be indispensable for ion capture. The incoming ion beam is not guaranteed to be aligned with the Penning trap axis. In fact initial tests revealed a significant misalignment. To correct the misalignment, potentials on the order of 100 V needed to be applied to SP1; for diagnostics, the ion beam was guided through the Penning trap and onto the PSD. Without the ability to tune the ion beam through the trap, ion capture is nearly impossible.

The vacuum chamber used for the one-magnet Penning trap assembly was constructed from commercially available parts. The ion trap chamber was evacuated using a turbomolecular pump (Varian V301) with a pumping speed of 250 l/s for nitrogen, 220 l/s for helium, and 200 l/s for hydrogen gases and an ion pump (Varian Vacion *Plus* 55) with a pumping speed of 50 l/s for nitrogen. The turbomolecular pump was backed using a two-stage, oil-free, vacuum pump system (Varian TPS-compact). The trap magnet, MACOR insulators, and structural parts were all air baked prior to assembly in order to remove hydro-carbons and water-vapor. All copper electrodes were polished to near optical flatness and were not subjected to air baking. After assembly, the chamber was baked, under vacuum, at an average temperature of ≈ 100° C for a total of 13 days to accelerate the overall outgassing rate of the system and reduce the final achievable base pressure. The magnetic field strength at the chamber wall closest to the trap was measured to be ≈ 5 mT. This field strength was monitored during the baking procedure and remained constant, indicating no degradation of the trap magnet.

The minimum base vacuum pressure achieved in the one-magnet Penning trap vacuum system was $\approx 8.6 \times 10^{-10}$ torr measured with a hot filament ion gauge (Granville-Phillips 274) while the ion extraction port gate valve was closed. During EBIT operation, when gate valves between the ion source and the one-magnet Penning trap were opened and source gas was injected to the EBIT, the operating trap base pressure was $\approx 1.3 \times 10^{-9}$ torr.

3.2.2 Trap configuration and construction

The Penning trap was located at the center of an ultra-high vacuum (UHV) chamber evacuated with a combination of turbomolecular and ion pumps as discussed above. A schematic of the trap electrodes and support structure is shown in Fig. 3.4. The Penning trap is located in the center of the assembly, supported by two compression plates connected with threaded rods (not shown in Fig. 3.4). The ion trap is electrically isolated from the supporting structure using MACOR rings. The short set of steering plates (SP2) is attached to the first (up-stream) compression plate on the entrance side of the trap. The long set of steering plates (SP3) is attached to the second (down-stream) compression plate on the exit side of the trap. This configuration was chosen to maximize the control of ion trajectories both entering and exiting the trap. The dimensions of the short set of steering plates (SP1 and SP2) are 31.75 mm long, and the plate separation is 31.75 mm. All steering plate electrodes are made of 3.175 mm thick OFHC copper. The long set of plates have dimensions of 63.5 mm long and a plate separation of 31.75 mm. All sets of steering plates are designed to operate at voltages up to 5 kV. To ensure adequate protection against arcing, all steering plate electrodes are encased in MACOR insulating supports as shown in Fig. 3.4. The insulating supports are attached to aluminum alignment discs using alumina (Al_2O_2) insulating screws. The alignment discs are in turn attached to the trap compression plates. To improve axial symmetry and minimize patch effects, all electrodes have been polished on a lathe to a near-mirror finish. The polishing of the electrodes also helps to keep the copper surfaces clean before being vacuum baked in the full assembly.

All high voltage connections inside the vacuum were made by attaching copper wires to tapped holes on the electrodes. As shown in Fig. 3.3, the trap electrode structure was attached to a flange via 4 threaded rods at the down-stream end of the chamber. The electrode alignment of the Penning trap was constrained during assembly by using a jig that kept the trap endcaps coaxial with the magnet and the compression plates. This jig also kept the trap centered on the assembly flange and aligned coaxially with the chamber axis. The trap was centered along the chamber axis using setup blocks that indexed the down-stream compression plate

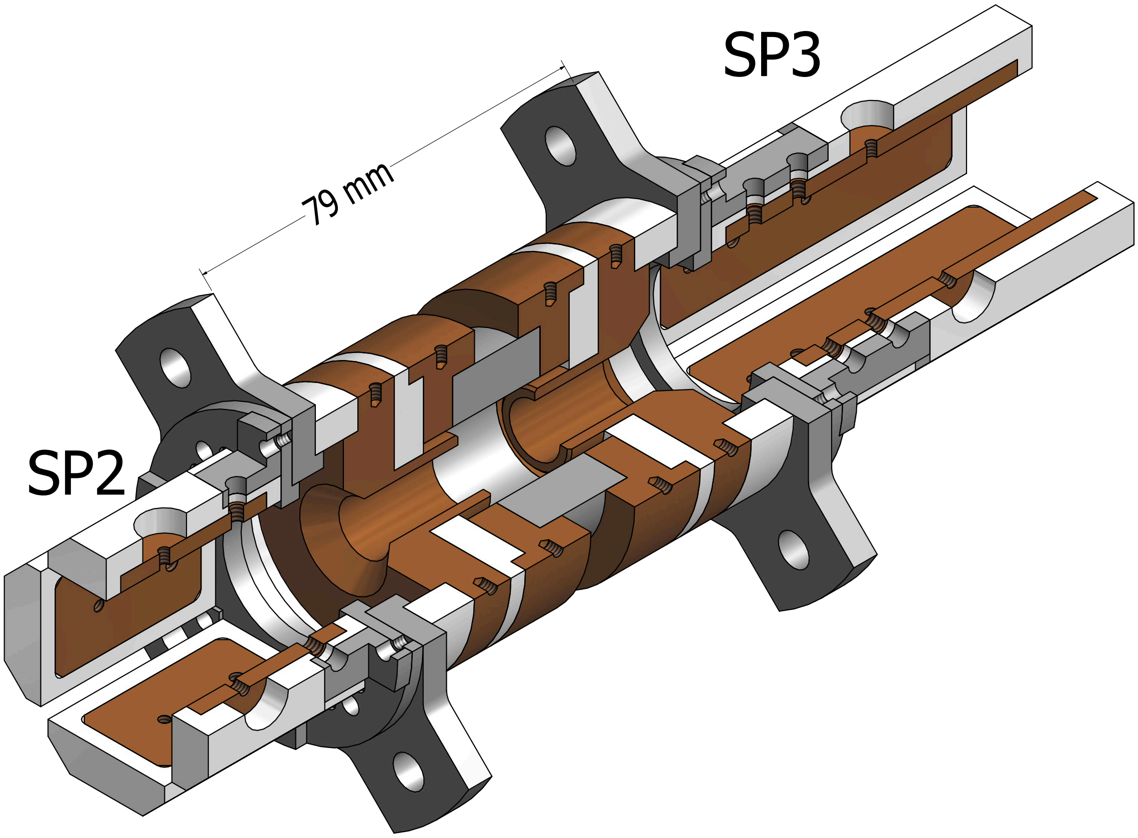

Figure 3.4: Cut-away schematic of the one-magnet trap electrode structure. The Penning trap is shown in the center of the assembly with the entrance and exit sets of steering plates.

to a distance of 92.0 mm from the inner flange surface. A centering ring was used on the up-stream portion of the supporting four-rods, near SP2, to keep the trap assembly from shifting in the chamber. This centering ring has four tapped holes for set screws that are used to align the ring by adjusting the extents of these screws to the inner chamber wall.

3.3 Two-magnet Penning trap apparatus

The two-magnet Penning trap apparatus was designed using the same basic principles and techniques tested in the first generation one-magnet trap apparatus, with the added insight gained in the initial ion capture experiments. Several improvements in the two-magnet trap design have been highlighted in §2.3: in particular, optical and atomic beam access. The ion optics is also refined to include decelerating electrodes directly in front of the entrance endcap, two einzel lenses on the exiting end of the trap, as well as the relocation of the one-magnet trap to serve as an up-stream einzel lens for beam focusing into the new Penning trap. A fast, retractable time-of-flight MCP detector is added to address pile-up issues experienced in the one-magnet trap assembly. A lower base pressure is attained by adding more vacuum pumps (§3.5) and increasing the bake out temperature and time.

3.3.1 Full assembly and vacuum chamber

The two-magnet Penning trap is the second generation realization of unitary Penning traps. As shown in Ch. 2, the two-magnet trap has greater magnetic field uniformity than the one-magnet trap, even with holes for beam access to the trapped ions. Beam access for lasers, light collection, and charge exchange experiments with neutral atoms was a key consideration in the final configuration of the two-magnet trap apparatus. A simplified schematic of the apparatus is shown in Fig. 3.5.

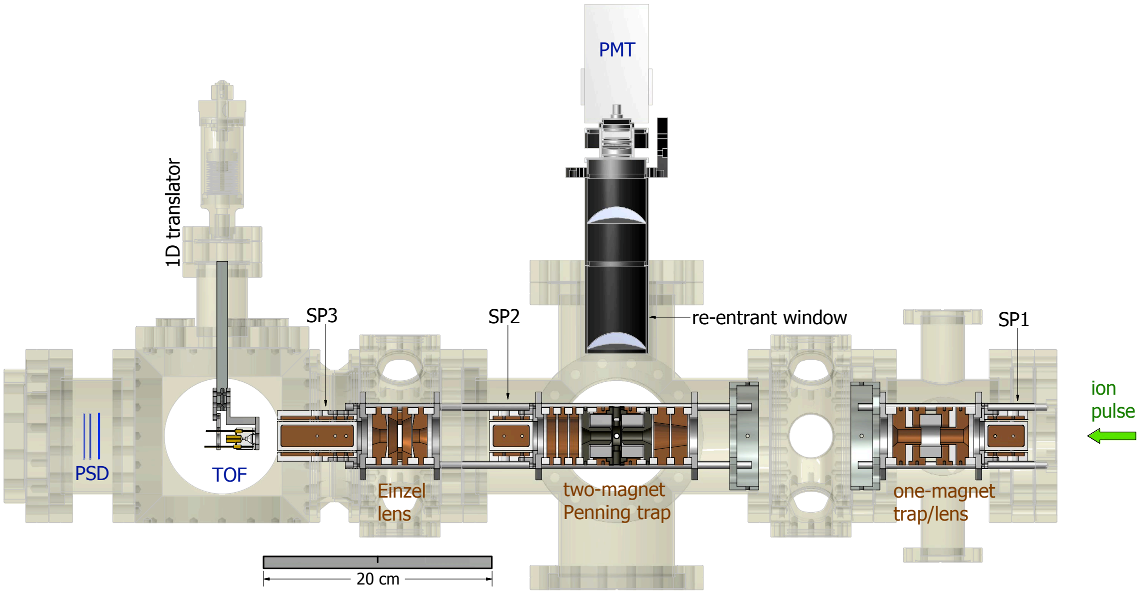

Figure 3.5: Simplified schematic of the two-magnet trap apparatus. A light-collection system (lenses and photomultiplier) is inserted into the re-entrant window above the two-magnet Penning trap.

The two-magnet Penning trap has enabled the first optical experiments with isolated ions extracted from the NIST EBIT. The apparatus consists of the two-magnet Penning trap at the center of the assembly with various ion optics on both the entrance and exit sides of the trap. The up-stream ion optics include: steering plate set 1 (SP1), the one-magnet trap, configured as an einzel lens, and two decelerating electrodes. Also, not shown in Fig. 3.5 is a Faraday cup between the one-magnet trap and the two-magnet trap. The down-stream ion optics includes:

an einzel lens, steering plate set 2 (SP2), a prototype radio frequency (RF) ion trap, configured as an einzel lens, and steering plate set 3 (SP3). The two-magnet trap apparatus uses a fast time-of-flight (TOF) MCP ion detector, in addition to the position-sensitive MCP detector previously used in the one-magnet trap apparatus. To collect light emitted by stored ions, a photon counting system was installed above the aspheric lens embedded in the trap; it consists of a lens assembly, optical filter, and a photomultiplier (PMT) detector capable of performing single photon counting. The details of the optical setup will be presented in §3.4.3.

The vacuum chamber used for the two-magnet Penning trap assembly was constructed from commercially available parts. The ion trap chamber was evacuated using two turbomolecular pumps, an ion pump, and a non-evaporative getter (NEG) pump. The turbomolecular pumps, one (Varian V301) located near the main trap region and another (Varian V81) located near the ion detectors have nominal pumping speeds of 250 l/s and 77 l/s, respectively. An ion pump (Varian Vacion *Plus* 55) with a nominal pumping speed of 50 l/s is located near the large turbomolecular pump. The turbomolecular pumps were backed simultaneously using a two-stage, oil-free, vacuum pump system (Varian TPS-compact). The NEG pump (SAES GP-50 ST-707) was heat activated under vacuum. It was operated at room temperature and has a nominal pumping speed of 200 l/s for H_2.

The trap magnets, MACOR insulators, and structural parts were all air baked prior to assembly. All copper electrodes were polished to near optical flatness and were not subjected to air baking. After assembly, the chamber was baked, under vacuum, at an average temperature of $\approx 110^o$ C for a total of 18 days to accelerate the overall outgassing rate of the system and reduce the final achievable base pressure. The magnetic field strength at the chamber wall closest to the trap was measured to be ≈ 4 mT. This field strength was monitored during the baking procedure and remained constant, indicating no degradation of the trap magnets.

The minimum base vacuum pressure achieved in the two-magnet Penning trap vacuum system was $\approx 7.6 \times 10^{-10}$ torr measured with a cold-cathode, inverted magnetron gauge (MKS 423–I–MAG), while the ion extraction port gate valve was closed. During EBIT operation, when gate valves between the ion source and the one-magnet Penning trap were opened, and source gas was injected to the EBIT, the operating trap base pressure remained unchanged.

3.3.2 Trap configuration and construction

A schematic of the trap electrodes and support structure is shown in Fig. 3.6. The Penning trap is located in the center of the assembly, supported by two compression plates fastened with threaded rods (not shown). The ion trap is electrically isolated from the supporting structure via MACOR rings. The up-stream side of the trap features two decelerating electrodes designed to remove axial kinetic energy from ions entering the trap. The decelerating electrodes are made of OFHC copper. The geometry of the decelerating rings is chosen to minimize the transverse kinetic energy of incoming ions by minimizing fringing fields and thus generating equipotential surfaces as parallel as possible. Each of the decelerating electrodes can be biased independently and the electrodes are insulated from each other and

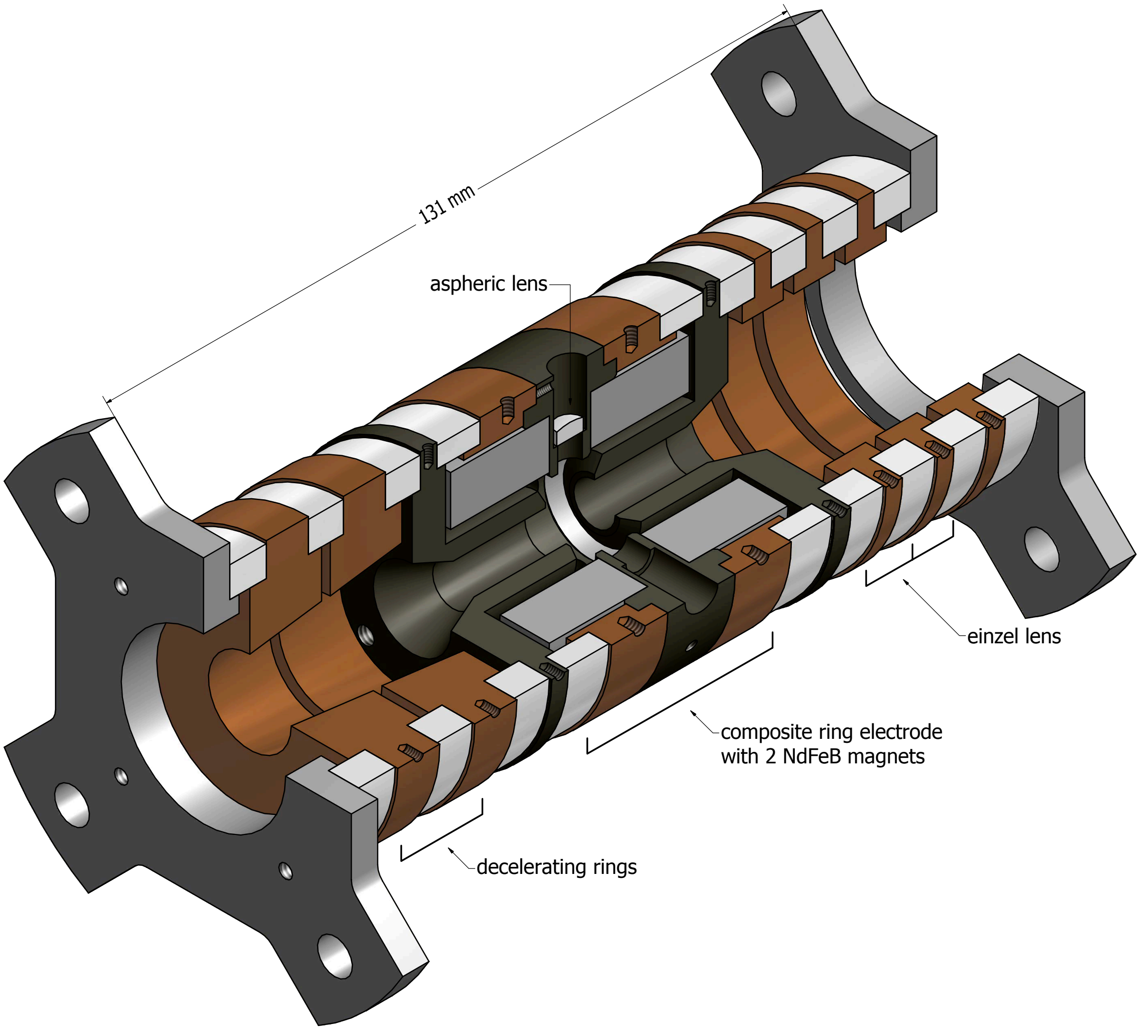

Figure 3.6: Cut-away schematic of the two-magnet trap electrode structure. The Penning trap is shown in the center of the assembly with the entrance and exit ion optics.

the rest of the trap and supporting structure by MACOR rings. On the downstream section of the trap assembly is an einzel lens for focusing and collimation of the ejected ions from the trap traveling towards the hyperbolic einzel lens, which focuses the ions onto ion detectors. The einzel lens electrodes are made of OFHC copper. All OFHC copper electrodes are polished to near-mirror finish. As with the one-magnet trap, MACOR and stainless steel components are air baked to a temperature of $\approx 230^o$ C.

3.4 Detection Systems

A variety of detectors have been incorporated into the one-magnet and two-magnet Penning trap experimental setups. Faraday cups are used in tuning the ion extraction beamline. Micro-channel plate (MCP) detectors are ideal for small signals and short pulses and are the primary diagnostic tool used in the Penning traps. Micro-channel plates are charge amplifiers which rely on micro-capillaries for electron multiplication initiated by an energetic or charged particle striking the surface of the plate. The first operational MCP detectors were built in the 1960s and reviews by Leskovar [62] and Wiza [63] discuss the details of MCP detector operation.

MCP detectors have the useful feature of providing high gain ($\approx 10^6$ electrons / incident charge) in a wide variety of geometries. A particular type of MCP design, the "chevron" [64], (sometimes referred to as a "V-stack") has been chosen for the ion detectors used here. The chevron design relies on a pair of micro-channel plates which are pressed together with the angle of the micro-capillaries opposing each other, forming a “V” shape when shown in cross-section [64]. The main advantage of this design over a single MCP, or parallel oriented plates, is that the secondary electron gain is increased while secondary ion production from the electron avalanche is suppressed. This leads to more accurate ion count rates.

In addition to ion detection, photon detection has been used to study ions in the Penning trap. Charged particle detection relies on ions being ejected from the Penning trap. However, detection of photons emitted from stored ions has the advantage of making it possible to study ions while stored inside the Penning trap.

3.4.1 Position-sensitive detector

A position-sensitive micro-channel plate detector (PSD) has been used for reliable beam diagnostics as the beamline optics are tuned to optimize ion capture. The PSD ion detector (Quantar Technology 3395A) consists of three MCPs mounted in a “chevron-plus-one” arrangement for charge amplification in front of a resistive anode encoder (RAE) [65] for position measurements. This configuration provides a gain of $\approx 10^7$ electrons/incident particle.

The PSD is operated in a fully saturated mode, in which an incident particle creates an electron avalanche. The resulting electron pulse is then accelerated towards the RAE. The RAE has a circular arc terminated geometry [65]. Each of the four corners of the RAE are connected to independent current pre-amplifiers. When the electron pulse strikes the RAE, the charge flows towards the four corners of the anode. The relative current measured at each corner is linearly proportional to the incident position of the electron pulse on the RAE [65]. Therefore, it is possible to reconstruct the spatial distribution of the incoming current pulse.

After each event, the electron pulse is shaped to produce a fast ($\approx$ 500 ns) transistor-transistor-logic (TTL) pulse that can easily be counted using a fast analog-to-digital converting (ADC) counter. The active diameter of the PSD is 40 mm. The spatial resolution of the PSD is $\delta x/x \approx 1/320$, or $\approx 125\mu$m. The dark count rate is ≈ 8 s^{-1} in continuous operation. When used in Penning trap ion detection, the detector is gated in time such that the background count rate is essentially zero. Due to the overhead associated with position calculations, ion count rates greater than 10^5 s^{-1} tend to cause detector pile-up leading to unreliable ion count data.

3.4.2 Time-of-flight MCP

Experiments revealed that ion capture efficiency is sufficiently high to cause ion count rates on the PSD detector to exceed 10^5 s^{-1} when ejected from the trap in a pulse $\approx 20-40$ ns wide. The charge-state separation of ejected ions is $\approx 100-500$ ns when a typical trap float voltage of 2.9 kV is used. To accommodate these features of ion capture experiments, a fast time-of-flight (TOF) MCP detector has been added to the two-magnet Penning trap apparatus. The TOF MCP is mounted on a linear 1D translator upstream from the PSD, allowing easy selection of each detector.

The time-of-flight MCP detector (Photonis AP-TOF 51003) is a chevron type with a disc head and an 8 mm active diameter. It can be operated in either a proportional, charge-amplifying mode, or in a fully-saturated, event-counting mode. In the event-counting mode, a pulse has a rise/fall time $\approx$ 350 ps, with a gain of $> 10^6$. The applied detector bias voltage (between the front and back MCP) is typically 1500 V in the proportional mode and 1700 V in the event-counting mode. For ion detection, the front MCP is biased negative to allow the signal to be measured near ground potential. The gain curve is shown in Fig. 3.7. The solid black points are the gain specifications provided by the manufacturer. The red curve is a fourth-order polynomial fit to the data. The use of the TOF detector for ion beam tuning is discussed in §4.3.4; and for charge state evolution in §5.1.2.

3.4.3 Light collection setup

The two-magnet trap apparatus is equipped with an optical setup to allow collection of light emitted by ions stored in the trap. The optical setup discussed here is the initial configuration for studying fluorescence from weak forbidden transitions in stored highly-charged ions. As shown in Fig. 2.5, there is an embedded aspheric lens (Edmond Optics NT46-342) with a numerical aperture of NA = 0.18 and focal length of FL = 13.9 mm to collect light emission from the ion cloud. A schematic of the optical setup is shown in Fig. 3.8. Light from the aspheric lens is focused towards the detector by two 50.8 mm concave lenses (Thorlabs LE1076-A) mounted in a lens tube, followed by one 25.4 mm convex lens (Thorlabs LB1471-A) mounted in a reducing lens tube. The fixed distance between the concave lenses is 110 mm, and the distance from the second concave lens to the convex lens is 71 mm. An optical

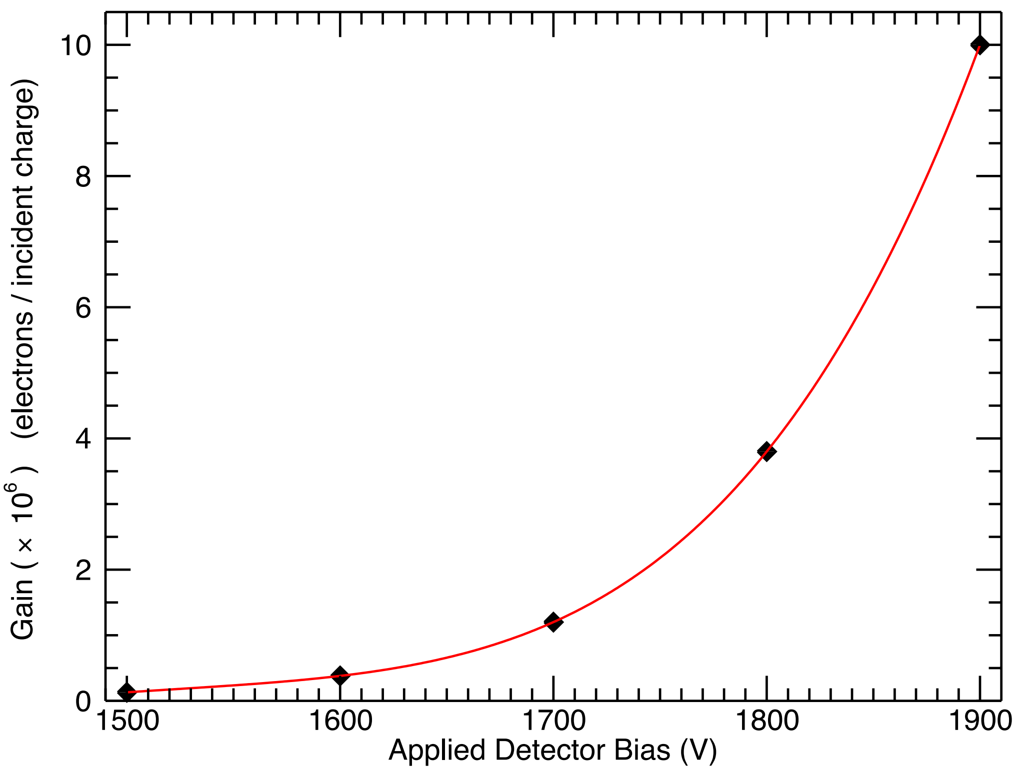

Figure 3.7: TOF micro-channel plate gain curve (Photonis).

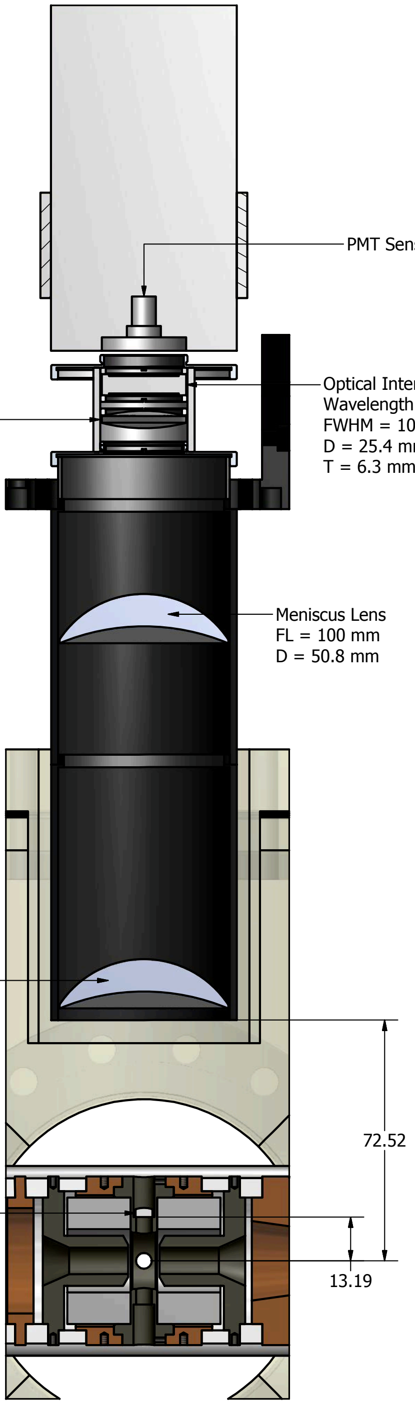

Figure 3.8: Schematic view of the optical setup. Distances are shown in mm. The distance between the concave lenses is 110 mm and the distance from the second concave lens to the convex lens is 71 mm. The optical interference filter has a central wavelength of $\lambda_o = 440 \pm 2$ nm with a bandwidth of 10 nm (FWHM).

interference filter is mounted in front of the photon counting detector (Hamamatsu H7421-40). The photon detector is a solid-state GaAsP photocathode with a 5 mm active diameter and a quantum efficiency (QE) of ≈ 40 % at the peak wavelength $\lambda = 580$ nm. The lens tube assembly is mounted on an XYZ linear translator with micrometer control to allow for the alignment and adjustment of the optical setup. The lens tube is inserted into a re-entrant window on the top flange of the ion trap vacuum chamber, with its axis aligned with the embedded aspheric lens in the Penning trap ring electrode. The interference filter can be changed to select a transition of interest. For example, a narrow band filter with a central wavelength, $\lambda_o = 440$ nm and a FWHM = 10 nm (Thorlabs FB440-10) was used for fluorescence measurements of Ar^{13+} ions, where the transition of interest occurs at $\lambda = 441.2556(1)$ nm [66].

Ray tracing calculations were performed to guide the optical design using a commercial simulation package, *OpticsLab*. To illustrate, a ray tracing calculation is shown in Fig. 3.9. Rays radiating from the source located at the center of the trap are traced through the lens system, assuming BK7 glass for all elements. The optical filter is not included due to limitations in the software, but is not thought to greatly influence the path. However, the angle of incidence of the rays through the filter can cause a shift in the transmission wavelength and has been investigated. This effect is discussed in §7.5.1. Filters used in initial experiments have specified operating lifetimes of ≈ 2 years. The active surface of the photon detector is located at the center of the image screen at the rightmost end of the model.

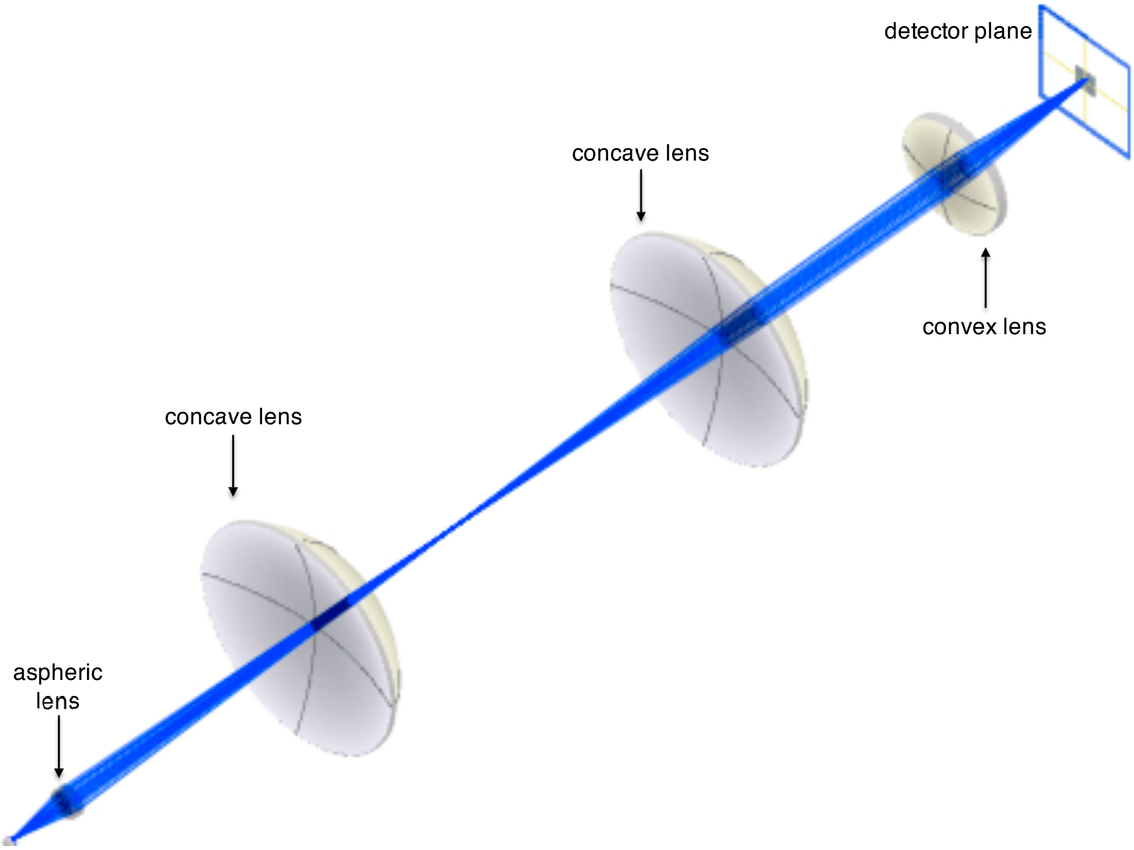

Figure 3.9: Ray tracing calculation with a light source at the center of the trap. The solid angle of the aspheric lens is the limiting factor for transmission. The photon detector is located in the center of the image screen. An interference filter located between the convex lens and image screen is omitted.

3.5 Data Acquisition Equipment

The data acquisition equipment used in ion capture experiments is discussed here. All high voltage potentials applied to electrodes and detectors are controlled via remote, low voltage input signals. These low voltage control signals are set using digital-to-analog (D/A) boards (NI PCI–6703) which are adjusted using control programs written in LabView. A variety of high-voltage power supplies have been employed depending on voltage and current requirements. For example, the two-magnet Penning trap ring electrode potential is set using a supply with a 5 mV ripple at an output voltage of 5 kV (Canberra 3125).

Experiment timing is controlled using a set of gate / delay generators (Stanford Model DG535, DG645) to arrange control signals for ion capture, storage, and ejection to a detector. Timing control signals are referenced to the EBIT extraction pulse signal and are sent to high-voltage pulse generators (Directed Energy PVX–4130), or a high-voltage amplifier (Trek 601B–2). The delay generators are also used to gate ion and photon detectors.

Ion detection is the primary diagnostic tool used in ion capture experiments. The PSD system relies on a commercial set of electronics and control programs (Quantar Technology 2401B) to count ions and analyze spatial information during an experiment. The PSD ion signal has been coupled to a multi-channel scalar (Ortec - MCS-PCI) to provide ion count rate data. The TOF ion signal is capacitively coupled to a pre-amp (Stanford SR445A) in order to detect the ion pulse while protecting both the electronics and the detector form unintended electrical events.

A schematic of the TOF detection scheme is shown in Fig. 3.10. In the event-counting mode, the TOF signal is coupled to an MCS (Stanford SR430) with a minimum bin width of 5 ns and a timing accuracy of 1 ns + 20 ppm of the bin width. In the proportional mode, the TOF signal is coupled to a digital oscilloscope (Tektronix TDS5054) which is triggered using a gate / delay generator. The detected ion number is given by

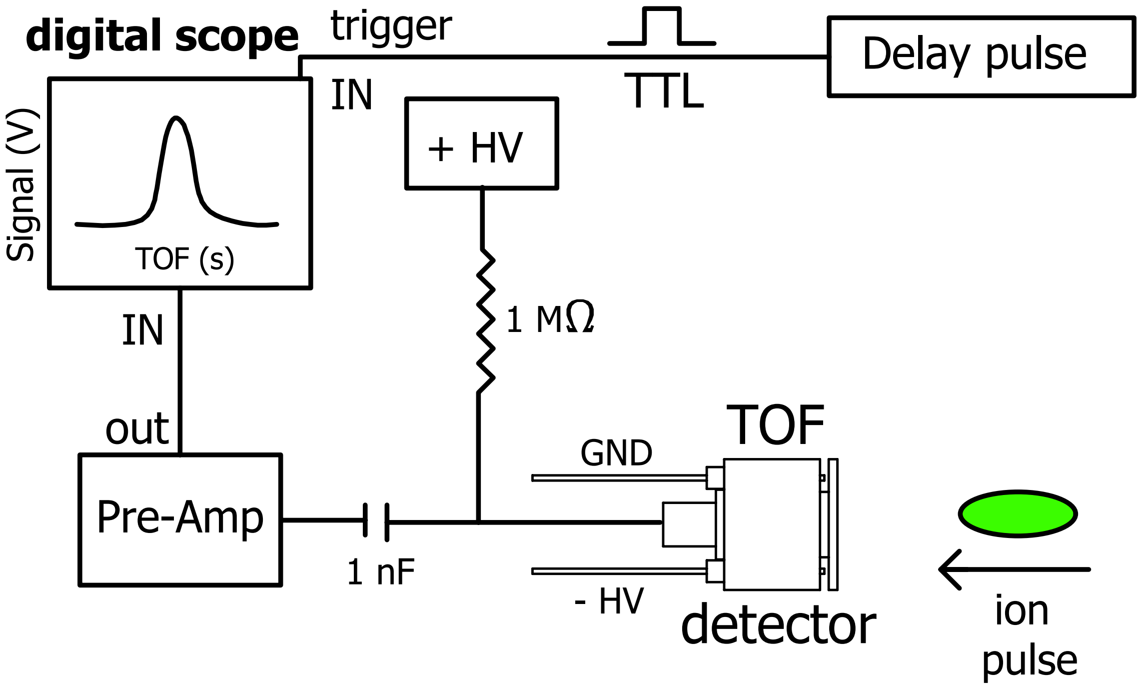

Figure 3.10: Schematic of the TOF detection system.

$$N = \frac{1}{QG_{TOF}R_{pre}G_{pre}} \int_{t_1}^{t_2} V(t)\, dt \tag{3.7}$$

where $V(t)$ is the detected ion signal, t_1 and t_2 are the limits of integration window, Q is the ion charge, G_{TOF} is the gain of the TOF detector, and R_{pre} and G_{pre} are the impedance and the gain of the pre-amplifier, respectively.

3.6 Vacuum Production

Perturbations from collisions with background gas play an important role in both ion storage performance and quenching of ion populations. Care has been taken in the production of the vacuum environment for both the one-magnet and two-magnet Penning traps to reduce the influence of such perturbations. As discussed in §3.2.1 and §3.3.1, trap electrodes have been cleaned and baked to help produce the best possible vacuum environment. Here the process of electrode preparation, assembly construction, and vacuum production is addressed, with a focus on the two-magnet Penning trap apparatus.

3.6.1 Cleaning process

Cleaning of parts inserted into the vacuum space is an important step in the assembly of the two-magnet Penning trap. The vast majority of parts in the trap assembly have been custom made. Following fabrication, each part is inspected for use in the apparatus. In the case of electrodes, a procedure in which the electrode is polished either by hand, or on a lathe is applied. The electrode surface is initially polished using increasingly finer grains of sand / lapping paper (7 grades in all). This helps to remove any gross irregularities and tool marks which remain after fabrication. Next, the electrode is polished using two grades of lapping compound. The compound helps to penetrate regions that are difficult to access using lapping papers or cloths. This polishing procedure yields electrodes that have a mirror-like finish. Electrodes are then inspected again to ensure a proper fit with each other and structural pieces. The polishing procedure has been applied to the NdFeB trap magnets as well. Care has been taken not to remove the thin Ni-Cu-Ni plating that is used to protect the magnet surface.

After inspection and polishing, the following cleaning process is applied. All grease / oil is removed through hand washing using detergents. Next, each part is inserted into a sonicating bath for further cleaning: first using detergent, then acetone, and finally isopropanol to remove any residue left behind by the acetone. For temporary storage before assembly, each part is placed in a container of clean isopropanol. This procedure is repeated for all parts in the trap apparatus.

3.6.2 Vacuum system and bake-out method

The volume of the vacuum chamber ($\approx 35,000$ cc) and high number of electrodes (26) requires a variety of vacuum pumps to create a suitable environment for ion capture experiments. These include two turbomolecular pumps, an ion pump, and a NEG pump. A schematic of the vacuum system and location of pumps is shown in Fig. 3.11.

Specified Vacuum Pumping Speeds (l/s)				
Pump	H_2	N_2	He	CO
Varian V301 turbomolecular pump	200	250	220	–
Varian V81 turbomolecular pump	50	77	65	–
Varian Vacion *Plus* 55 ion pump	–	50	–	–
SAES GP-50 ST-707 NEG getter	200	–	–	100

Table 3.1: Specified vacuum pumping speeds for the various pumps used in both the one-magnet trap and two-magnet trap chambers.

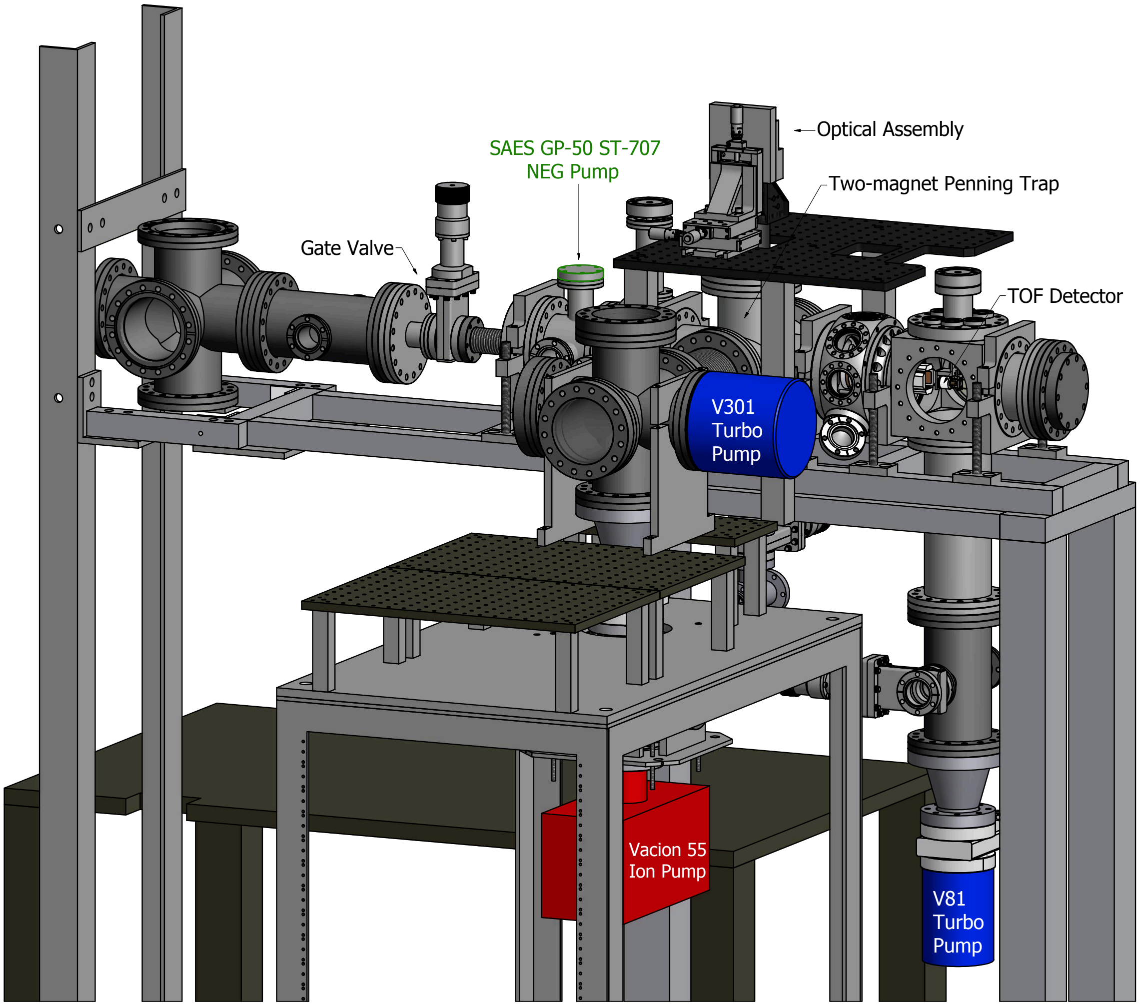

Figure 3.11: Schematic view of the two-magnet Penning trap vacuum chamber. The locations of the two-magnet Penning trap, the optical assembly, and the TOF detector are shown for reference. The locations of the various pumps are also indicated. The highlighted gate valve separates the ion extraction beamline from the two-magnet Penning trap apparatus. The distance from the gate valve to the TOF detector is approximately 80 cm.

Just prior to assembly, parts are baked in air, when appropriate, at a temperature of ≈ 230^o C for 30 – 60 minutes. Larger parts require a longer time to reach full temperature. The trap magnets are rated to an operational temperature of 180^o C and are baked at a temperature of ≈ 110^o C for a similar duration. This procedure leads to the formation of a thin oxide layer on the parts which reduces the diffusion of hydrogen from the bulk material into the vacuum space [67].

3.7 Discussion

Some important details about special tools and facilities employed in experiments with the one-magnet trap and the two-magnet trap, are presented in this chapter. The main elements used in ion capture experiments are highlighted. Modifications, improvements, and additions as the apparatus evolved are noted. For instance, initial tests with captured highly-charged ions have guided improvements in the two-magnet trap assembly. In particular, the high ion count rates observed in the one-magnet trap necessitated the addition of the fast TOF detector. Some details about the vacuum production are also provided since perturbations from residual background gas is an important consideration for some measurements.

Chapter 4

Capture of Highly-Charged Ions

As discussed in Chapter 2, the stability condition for confinement of ions in a unitary Penning trap is more stringent than high-field Penning traps. Efficient ion capture and storage in such compact traps therefore requires careful choice of design parameters, as well as optimization of ion pulse characteristics. Here the techniques for ion extraction, slowing, and capture are presented for the case of the two-magnet Penning trap because better diagnostics have been added following initial experiments with the one-magnet trap.

The full system configuration, from the ion source through the extraction beamline to the ion capture apparatus, are presented in §4.1. To guide the design of the ion capture trap and beam conditioning components, numerical simulations are presented in §4.2. An important issue is the electrostatic slowing of fast ($\approx$ 40 keV) beams of ions within an $\approx$ 0.5 cm long region of space prior to entering the trap. The necessary voltages and switching times for controlling electrodes have been guided by these simulations, as well as the estimated radial size of a trappable incoming ion pulse. Section 4.3 addresses charge state selection and ion pulse optimization, with emphasis on the time width of the extracted ion pulse, and on matching of the EBIT extraction energy with the Penning trap decelerating potential. Ion capture timing, TOF pulse narrowing, and capture efficiency are discussed in §4.4.

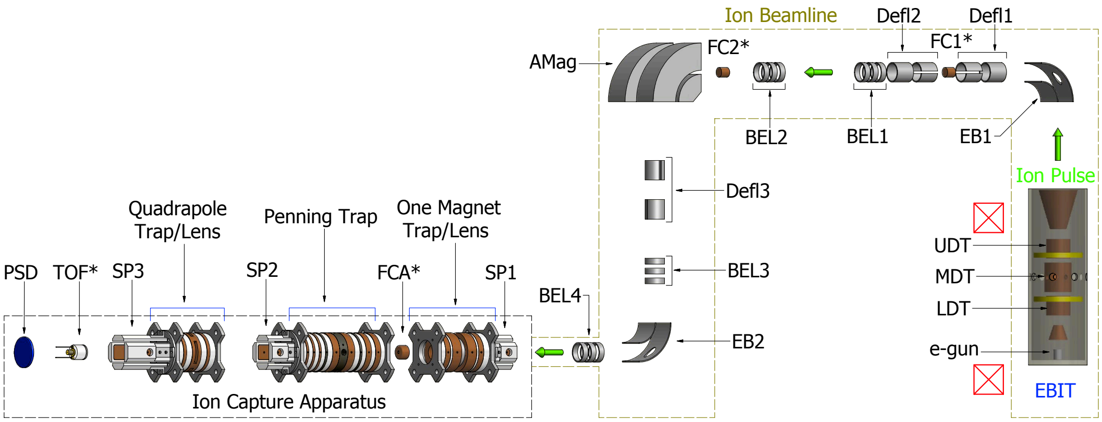

Figure 4.1: Schematic overview of the experimental set-up at the NIST EBIT (NOTE: Not to scale). The main elements of the ion source include the EBIT and ion optics in the beamline including an analyzing magnet (AMag). Elements labeled with (*) indicate mounting on retractable translators. The experiment region containing the Penning trap and detectors is also shown. Broken lines represent the boundary of evacuated space; pumps are not shown.

4.1 System Configuration

The production of highly-charged ions and ion transport to the trapping apparatus is schematically illustrated in Fig. 4.1. A brief overview of the EBIT is given in §3.1.1; a more complete description of the capabilities and previous experiments can be found in the review article by Gillaspy *et al.* [19]. The EBIT uses a high energy, high current density electron beam to both create and store highly charged ions. Ions are extracted from the EBIT by pulsing the voltage on the middle drift tube (MDT) higher than the upper drift tube (UDT). The details of the NIST EBIT ion beamline are presented in [59, 60, 68].

The EBIT in combination with the ion beamline is a source of highly-charged ions. It is a set of electrostatic and magnetic ion optics for transport and analysis of continuous and pulsed ion beams. The elements in Fig. 4.1 are grouped into two main sections of the ion beamline. Section (1), shown from right to left, consists of the following elements: the first 90° electrostatic bender (EB1), the first set of four-quadrant electrostatic deflectors (Defl1), a retractable Faraday cup (FC1), the second set of deflectors (Defl2), the first electrostatic einzel lens (BEL1), the second einzel lens (BEL2), and the second Faraday cup (FC2). Section (2), shown from top to bottom, consists of the analyzing electromagnet (AMag), the third set of deflectors (Defl3), the third einzel lens (BEL3), the second 90° bender (EB2), and the fourth einzel lens (BEL4). The ion beamline vacuum space is isolated from the capture apparatus via a UHV gate valve and has a base pressure of 2.0×10^{-9} torr. The total path length from the center of the EBIT to the center of the two-magnet Penning trap is ≈ 8 meters.

The ion capture region consists of four main sections. Section (1) consists of a set of four electrostatic steering plates (SP1), a one magnet trap/einzel lens, and a retractable Faraday cup (FCA) for ion beam current measurements. Section (2) makes up the main Penning trap region, and is described below. Section (3) consists of quadrupole trap/lens (QL1,QL2, and QL3), and a long set of steering plates (SP3) for focusing and deflection of ions extracted from the Penning trap. Section (4) consists of a retractable, fast time-of-flight (TOF) micro-channel plate (MCP) ion detector and a position-sensitive MCP ion detector (PSD). These detectors are described in §3.4.

The trap electrode stack consists of two decelerating electrodes (DR 1 and DR 2), and a two-magnet, unitary Penning trap (FEC, RING, and BEC), followed

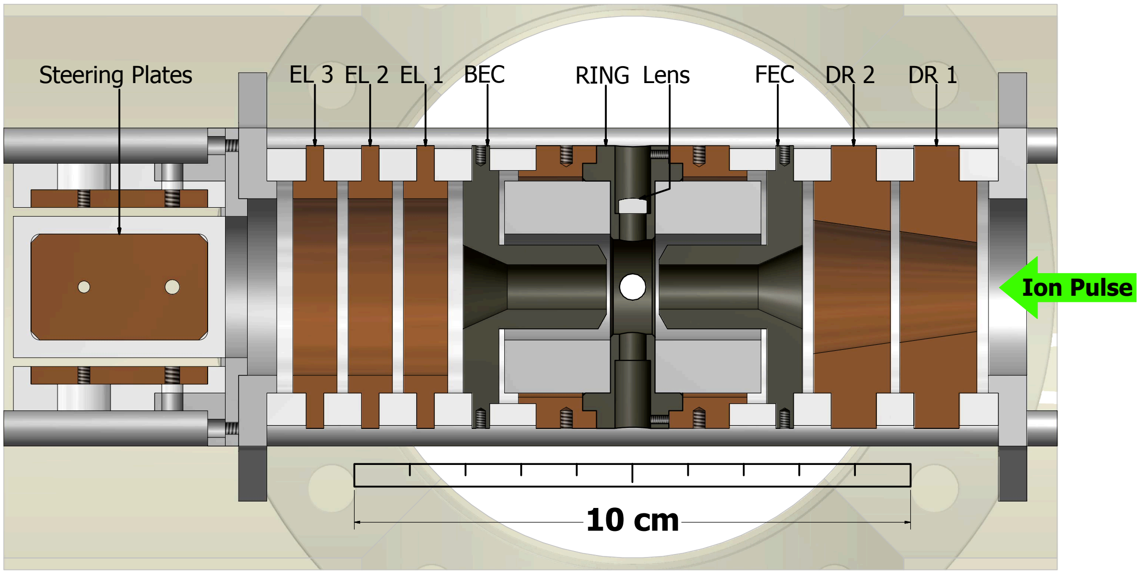

Figure 4.2: Simplified schematic diagram of ion capture trap. Ions enter the trap from the right hand side of the diagram; they are slowed and focused using the decelerating electrodes (DR1 and DR2) before entering the Penning trap. Upon ejection, ions are transported through an einzel lens (EL 1, EL 2, and EL 3) and a set of electrostatic steering plates which guide toward a time-of-flight (TOF) detector.

by an einzel lens consisting of three cylindrical electrodes (EL 1, EL 2, and EL 3), as well as a set of electrostatic steering plates. A simplified schematic of the ion trap electrode stack is shown in Fig. 4.2. The trap is designed based on a unitary architecture utilizing rare-earth (NdFeB) permanent magnets and soft iron yoke pieces to generate and shape the magnetic field required for radial ion confinement.

The details of the Penning trap, including broad design considerations are presented in [24]. Three trap electrodes, a front endcap (FEC) electrode, ring electrode, and back endcap (BEC) electrode are used to generate the electrostatic potential necessary for axial ion confinement. In the mid-plane of the ring electrode are four equidistant holes to enable atomic and laser beam access. For example, an aspheric lens is located in one of the holes of the ring electrode for collecting light from stored ions.

The ion trap, ion optics, and associated support structures are housed in a room-temperature ultra-high vacuum (UHV) chamber with an operating base pressure of 7.6×10^{-10} torr. High voltage connections are made via commercially available SHV vacuum feedthroughs rated to 5 kV. All applied potentials, both static and time-varying, are controlled through a computer interface, the details of which are provided in §4.4.

4.2 Ion capture simulations

To aid trap construction and system optimization, numerical simulations have been carried out for a variety of ions with a wide range of initial energies to investigate the capability of a compact Penning trap apparatus to slow, capture, and store ions extracted from the NIST EBIT. Ion capture simulations involve calculations of the magnetic field in the trap as well as the electrostatic potential of the ion optics and trap electrodes. The details of the magnetic field calculations, including comparisons with measured trap fields, are presented in §2.3.1 and [24]. The magnetic field in the trap is calculated with QuickField [51], a commercial software package which uses a finite element method (FEM) [52] commonly used for magnetic circuit analysis. The measured magnetic field strength is ≈ 310 mT in the trapping region and is in good agreement with the calculated field. The electric field in the trap assembly is calculated numerically using a Boundary Element Method (BEM), the details of which are presented in [54]. Briefly, calculations using the CPO sofware are done by defining electrode surfaces, dividing the surface into individual regions of charge, and then summing the electric field from each charge segment. The resulting electric field is given by Eqs. (2.11) and (2.12). An example of the calculated on-axis electrostatic potential for ion capture and storage is shown in Fig. 4.4. The "open" condition is shown in (a) and the "closed" condition is shown in (b). The applied voltages for each electrode and the critical EBIT parameters are listed in Table 4.1. For comparison, the typical EBIT shield voltage and MDT high voltage pulse levels are shown in Fig. 4.4a. An analytic quadrupole potential, shown in Fig. 4.4b, takes the form [47, 24]

$$V = \lambda V_0 \frac{z^2 - r^2/2}{2d^2} + V_C. \tag{4.1}$$

The field coordinates z and r are defined from the center of the trap; V_0 is the applied potential difference between the endcaps and the central ring electrode, V_C is the overall capture potential, and d is a geometric factor given by Eq. (2.3). The minimum distances r_0 and z_0 are from the center of the trap to the ring and endcap electrodes, respectively. As discussed in §2.3, for the two-magnet Penning trap, $r_o = 8.5$ mm, $z_o = 4.736$ mm, and $\lambda = 0.854$. The on-axis potential defines an axial well depth that is determined by the potential difference between the value at the center of the trap and the axial maximum near the endcaps and is defined as ΔV. The axial well depth can be determined in terms of the applied potential difference V_o by fitting the calculated value, ΔV as a function of V_o. An example of the calculated on axis well depth is shown in Fig. 4.3.

The two decelerating electrodes, DR1 and DR2, provide a potential gradient which removes axial kinetic energy from ions entering the trap. In order to capture ions extracted from the EBIT over a broad range of conditions and with the lowest possible thermal energy after capture it is important to minimize the amount of transverse energy added to injected ions. The geometry of the decelerating electrodes has been chosen to produce electrostatic equipotentials which are as uniform as possible, minimizing fringing fields which tend to add transverse energy to trapped ions. Figure 4.5 illustrates the equipotential surface in the decelerating region. The ion capture apparatus is designed to operate at high voltage, compatible with slowing and capturing ions entering with energy up to 5 keV/Q.

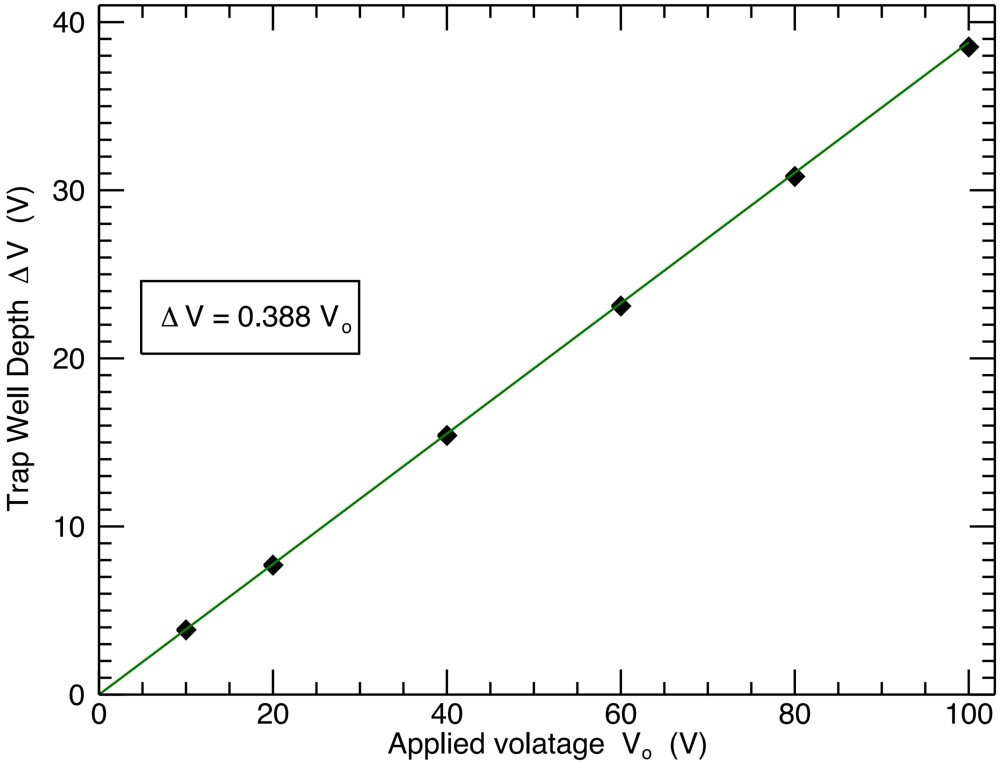

Figure 4.3: Calculated on-axis potential as a function of the applied trap potential V_o. Solid points show specific cases of calculated trap potential wells. The green line is a linear fit to the calculations.

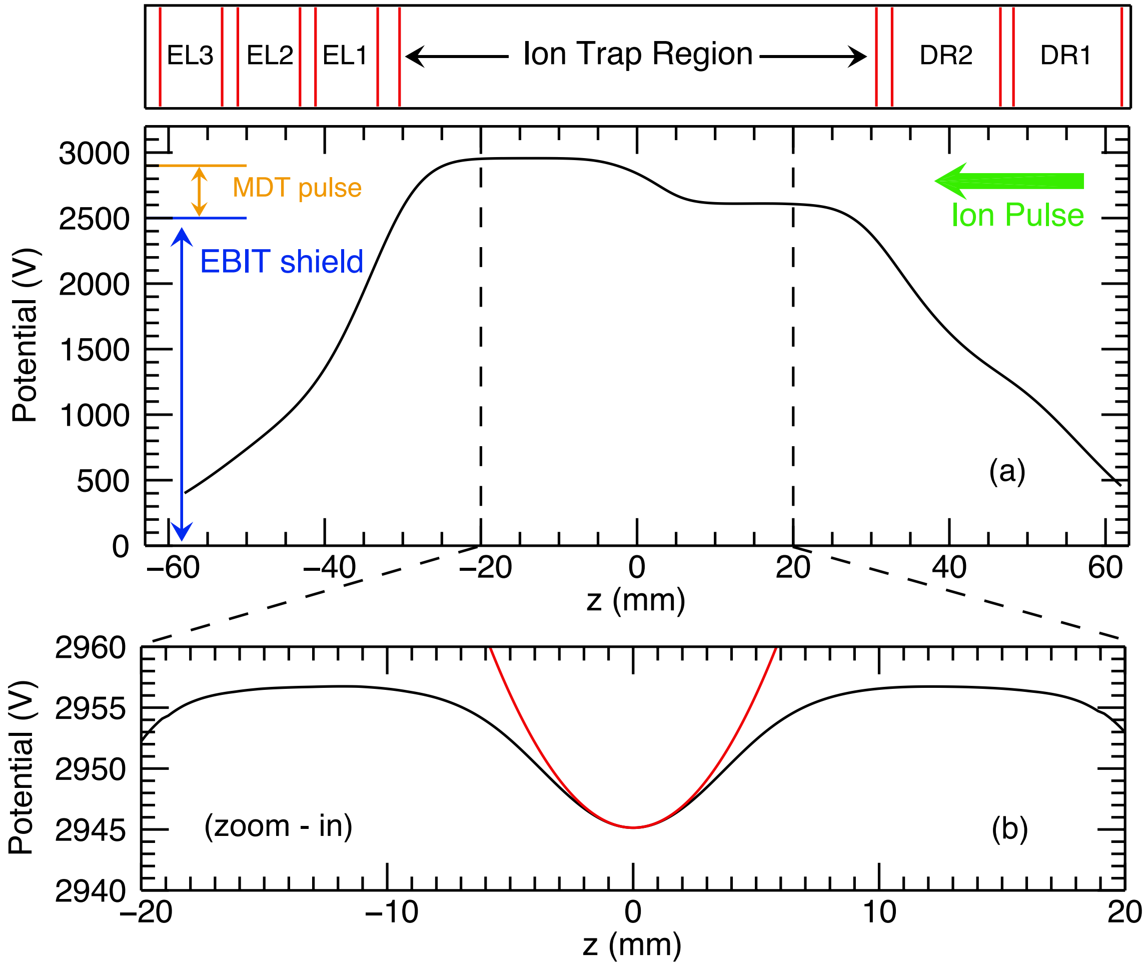

Figure 4.4: Calculated on-axis electrostatic potential for the Penning trap electrode stack. The locations of the electrodes are shown in the upper most figure, the "open" trapping condition in (a) and the "closed" condition in (b). The trap center is located at z = 0 mm. The applied potentials for each electrode are given in Table 4.1. For reference, the EBIT shield voltage and MDT pulse voltage are shown in (a) along with the ion pulse entering the apparatus from the right. The BEM calculated "closed" potential (black) and an analytic quadrupole potential (red) are shown in (b). The applied trap potential difference is 30 V; corresponding to an axial well depth of 11.61 eV/Q.

Trap Parameters	
Trap Electrode	Applied Potential (V)
DR1	1300.0
DR2	1600.0
FEC	(Low) 2610.0
	(High) 2956.8
Ring	2926.8
BEC	(Low) 2956.8
	(High) 2460.0
EL1	500.0
EL2	1500.0
EL3	500.0

EBIT Parameters	
e^- beam Energy	2.5 keV
e^- beam Current	14.4 mA
LDT	500 V
MDT	Trap Dump = 400 V
UDT	220 V
Ionization Time	76.0 ms
Analyzing B-field	66.22 mT

Table 4.1: Typical applied trap potentials and corresponding EBIT parameters for Ar^{13+} ion production and capture. The EBIT conditions have been chosen to both maximize ion production and minimize the ion pulse width.

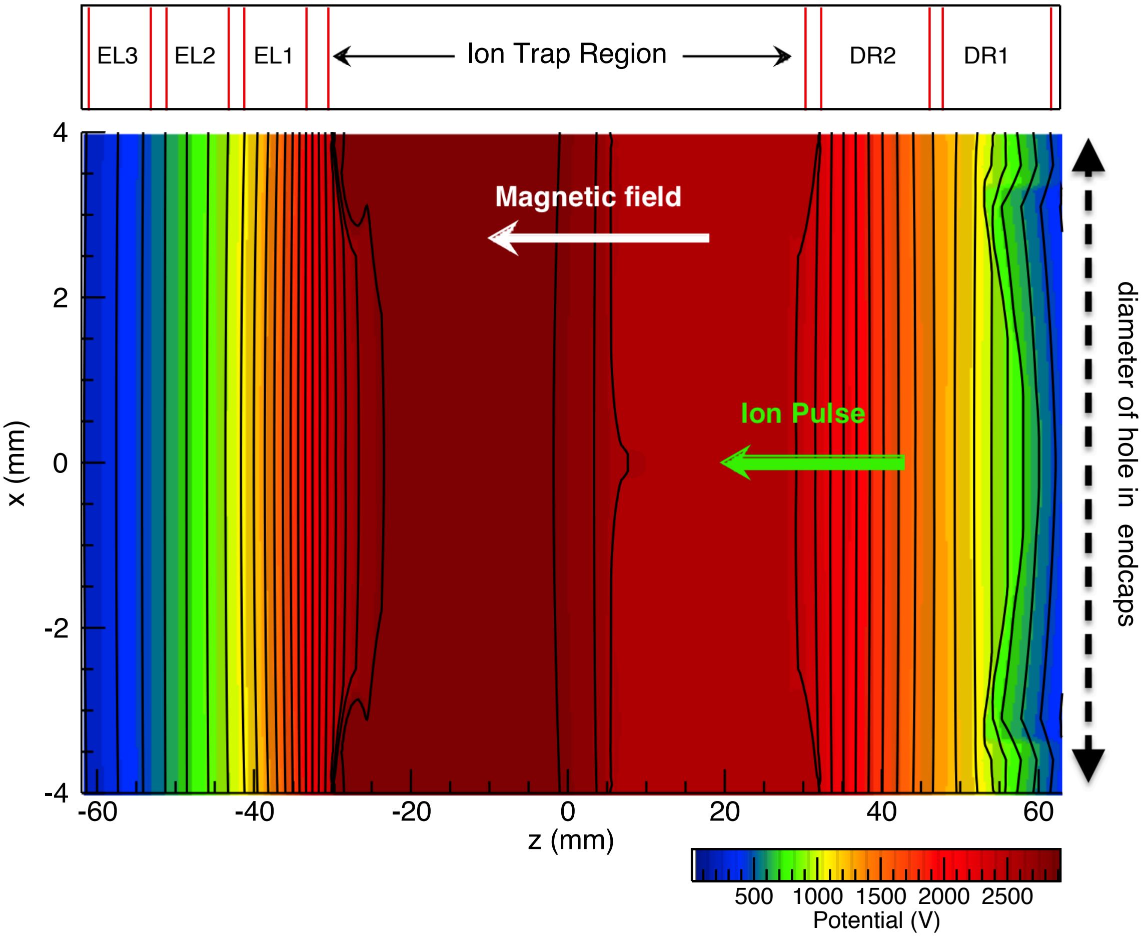

Figure 4.5: Calculated electrostatic potential in the mid-plane of the trap for the "open" state in Fig 4.4 (a). In the open state, the front endcap potential is set below the trap ring electrode potential to allow ions to enter the trap. The electric field used for slowing ions is shaped by the decelerating rings to be as uniform as possible so as not to add transverse energy to captured ions.

The equation of motion is given by:

$$m\ddot{\mathbf{r}} = Qe\mathbf{E}(\mathbf{r}) + Qe\dot{\mathbf{r}} \times \mathbf{B}(\mathbf{r}) \tag{4.2}$$

where $\mathbf{r}$ is the ion position from the center of the trap, Qe is the ion charge, m is the ion mass, $\mathbf{E}(\mathbf{r})$ is the applied electric field and $\mathbf{B}(\mathbf{r})$ is the applied magnetic field. Given the numerically calculated electric and magnetic fields, as well as initial conditions for both the ion position and velocity, an ion trajectory is computed by integrating the equations of motion using an adaptive step-size Runge-Kutta technique [55].

An instructive example is presented in Fig. 4.6, wherein ion trajectories are calculated as a function of impact parameter, a_i (distance from trap axis). Ions are given initial velocity entirely in the z direction (parallel to the trap axis), representing the zero emittance beam condition. In this case, the initial transverse kinetic energy equals zero. Calculated trajectories such as those shown in Fig. 4.6 have been used to analyze the necessary ion beam conditions for successful ion capture. For example, the ion kinetic energy after capture is an important quantity which will determine if ion trajectories will be stable or unstable. The maximum ion kinetic energy after capture is shown as a function of impact parameter in Fig. 4.7. It is clear that the deceleration is most effective on-axis, where the initial ion kinetic energy is removed more completely. As the impact parameter increases, the energy of the stored ion increases. The potentials on DR1 and DR2 have been optimized to minimize stored ion amplitudes.

Among the parameters optimized in simulation are: capture timing ($t_{capture}$),

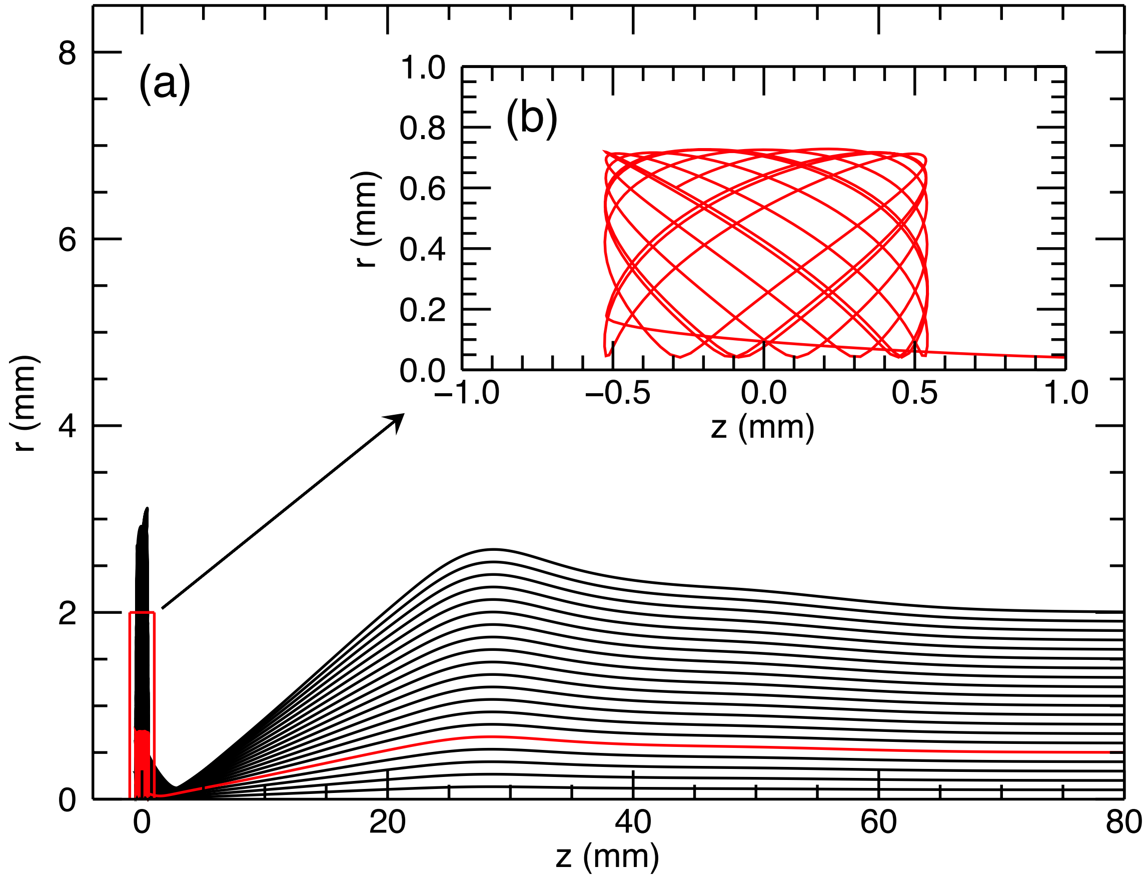

Figure 4.6: Calculated ion trajectories as a function of impact parameter, a_i. The ion trap center is located at z = 0 mm. For the case of a zero emittance beam, captured ion orbits increase with increasing a_i. The trajectory in red corresponds to an impact parameter of 0.5 mm.

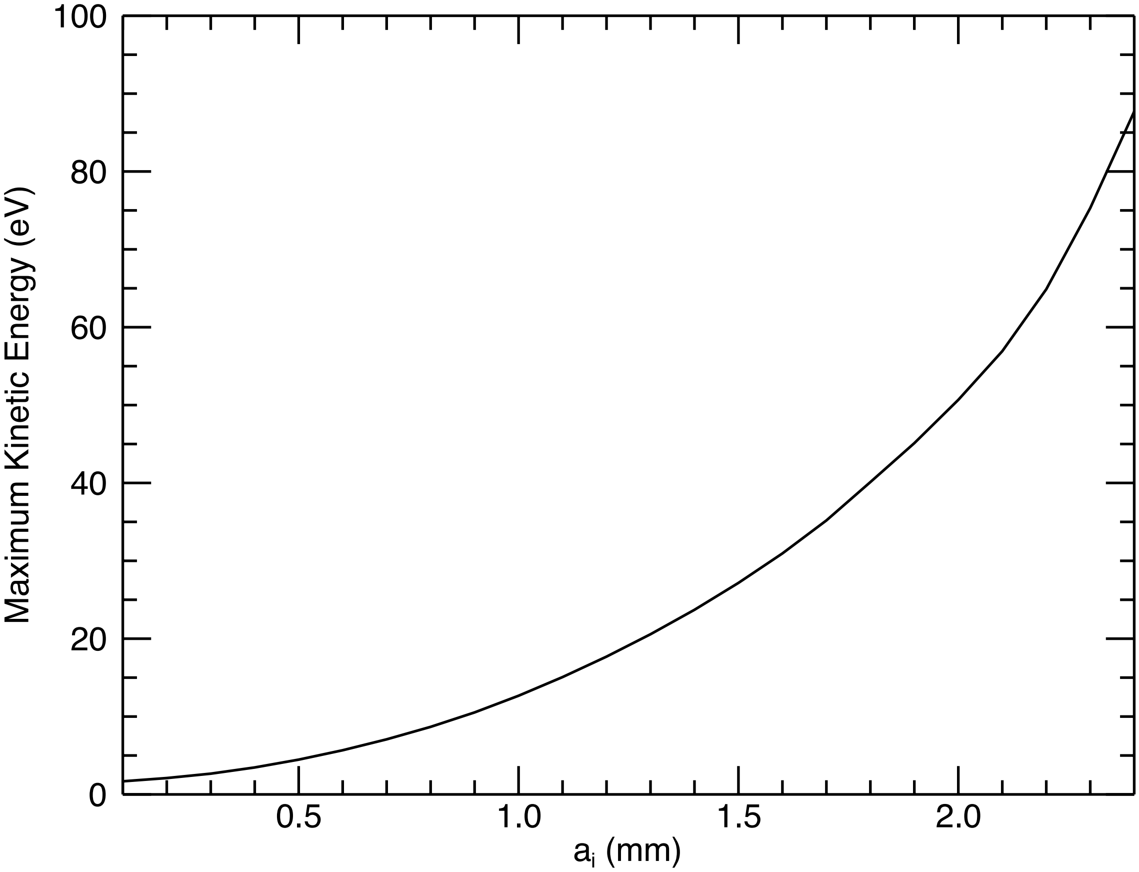

Figure 4.7: Calculated maximum kinetic energy of captured Ar^{13+} ions as a function of impact parameter, a_i. The calculation assumes that ions enter the capture apparatus with no transverse kinetic energy.

stored ion kinetic energy, and axial and radial amplitudes of trapped ions. An important calculated quantity is the acceptance range of arrival time for trapping ions entering the capture apparatus along the trap axis. Ion capture relies on the precise timing of pulsing up the voltage on the FEC electrode to close the trap. If the FEC is closed too early, before ions enter the trapping region, they will scatter off of the trap and not be captured. If the FEC is closed too late, ions will have entered the trap, turned around, and exited out the FEC, and therefore not be captured. For a given initial energy and trap well depth, there is a range of arrival times wherein the trap FEC can be switched closed to confine the ions that have entered the trap. This quantity is referred to here as the capture time width (CTW) and can be estimated by calculating ion trajectories with equal initial kinetic energy and different FEC switching times. For each ion, the capture time is varied in 10 ns steps, and the trajectory is calculated both before and after the FEC switching occurs. If the ion orbit inside the trap is stable, bound within the trapping volume for some time set in the calculation, then the ion is considered to be trapped. For ions injected on-axis, the capture time profile is a flat-top function with a width defined as the capture time width (CTW). For the case of ArXIV given above, CTW $\approx$ 80 ns. This is short compared to high-field Penning traps where the CTW can range from $\approx$ 300 ns [69] to $\approx 2\mu$s [22], or RFQ traps, CTW $\approx 100\mu$s [10].

Ions that arrive at the trap in a time spread within this time window have the best chance of being captured and stored together. The calculated CTW imposes the important constraint: the experimental time for switching the FEC potential should be significantly less than the CTW. Therefore, the timing delay between the

EBIT extraction pulse and the FEC switch should be well controlled. Otherwise, ions arriving within the calculated CTW would be lost.

4.3 Ion Extraction from the EBIT

For the experiments in this work, highly-charged ions are created using an electron beam ion trap (EBIT) operated at an electron beam energy, E_{e-}, ranging from 2.0 keV to 4.0 keV and an electron beam current, I_{e-}, ranging from 6 mA to 150 mA. The NIST ion beamline is optimized for high ion flux [59], necessary in ion-surface bombardment experiments [20]. In ion-surface experiments, the EBIT is typically operated in a continuous, high-current mode with $I_{e-} = 150$ mA. In ion capture experiments, on the other hand, it is very important to obtain tight bunching of the extracted ions in both space and time; therefore, the EBIT is operated in a low-current, pulsed extraction mode. The electron beam energy and current are chosen to optimize the production and capture of the ion of interest. As an example we now present the case of Ar^{13+} extracted at an electron beam energy of $\mathrm{E}_{e-} = 2.50$ keV and electron beam current $\mathrm{I}_{e-} = 14.4$ mA.

Ions of interest are created by injecting a gas into the EBIT. Electron-impact ionization to proceeds for a specified ionization time, before the ions are ejected by applying a fast voltage pulse. A commercial high voltage switch (Directed Energy PVX – PVX–4140) is used to rapidly change the applied potential on the EBIT middle drift tube (MDT) from 0 V to 400 V in $\approx$ 50 ns of rise time. This voltage pulse causes the ions to spill out of the trap entering the ion beamline. The EBIT ionization time, the time between ion extraction pulses, also referred to as the "cooking time", is typically between 25 ms and 200 ms, depending on the charge state of interest; lower charge states take less time to produce. The EBIT produces all possible charge states for a given electron beam energy, current, and ionization time. As shown in [60], the electrostatic ion optics in the NIST ion beamline are charge-to-mass insensitive.

When the EBIT ion beam is operated in the continuous extraction mode, ions enter the beamline with an energy of $E_{ion} \approx QU_{e-beam}$, where Q is the ion charge and U_{e-beam} is the electron beam energy. However, during pulse extraction, the extracted ions are given an additional $\sim$ 400 eV/Q of kinetic energy due to the fast switching of the EBIT MDT. Ions leave the EBIT and undergo a 90 degree bend through an electrostatic bender above the EBIT. All ion charge states present in the EBIT are extracted from the trap and are guided via electrostatic ion optics toward an analyzing magnet.

Here, we focus on pulse extraction. Figure 4.8 (a) shows a typical signal of the extracted ions striking FC2 immediately in front of the analyzing magnet. The analyzing magnetic field is tuned to allow only a single ion charge state to pass through the magnet while deflecting all other charge states to the chamber walls. After filtering out unwanted charge states, the ions of interest are guided to a second electrostatic bender below the analyzing magnet, which directs the ions into the capture apparatus. A detailed schematic of the ion capture apparatus is given in Fig. 3.5.

The ion capture apparatus is equipped with a set of 4 electrostatic steering

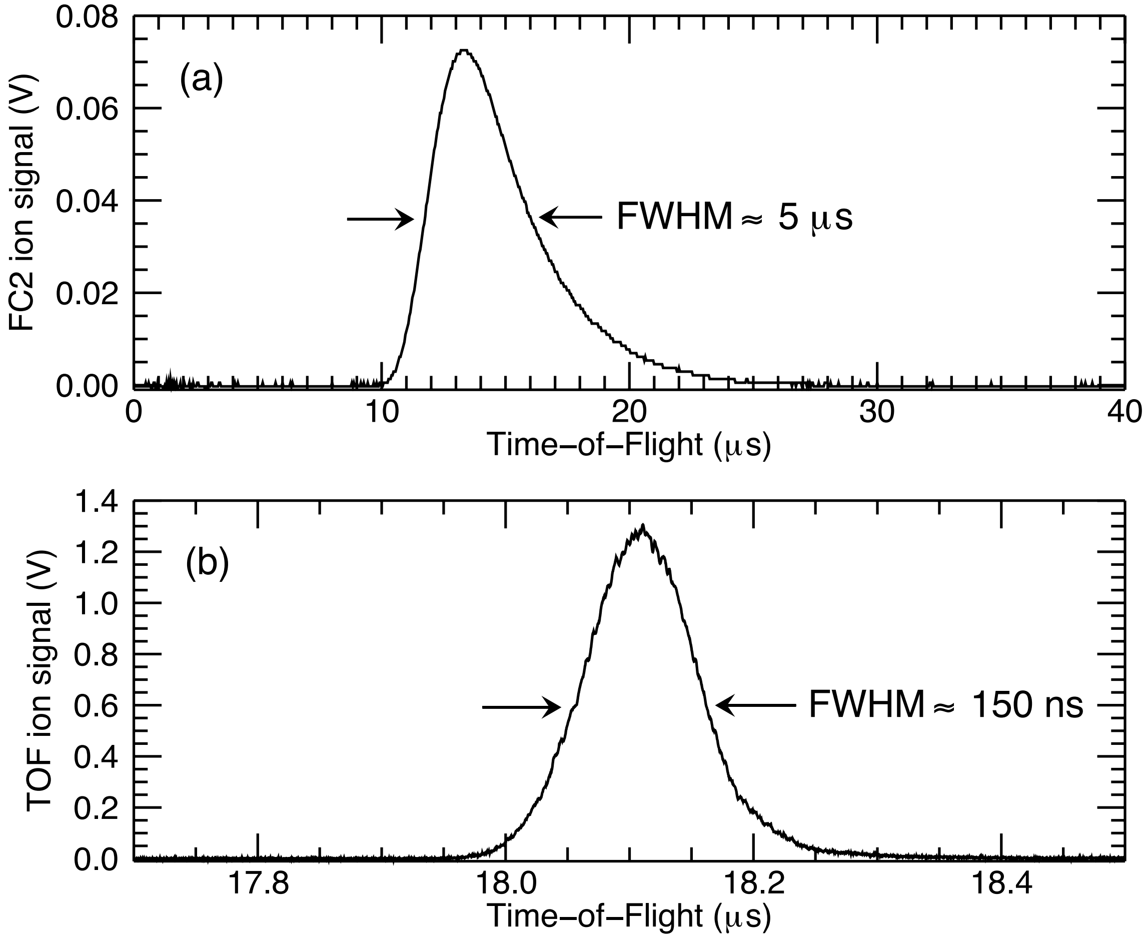

Figure 4.8: Argon ion extraction pulse from the EBIT at NIST for electron beam energy (E_{e-}) and current I_{e-} were 2.50 keV and 14.4 mA, respectively: (a) before charge state selection, on FC2, and (b) after ArXIV charge state selection on the fast TOF detector.

plates and an einzel lens to fine tune the ion beam for the final approach into the trap. With the remaining elements of the capture trap grounded, the extracted ion pulse passes through the trap and is detected using a fast time-of-flight (TOF) micro-channel plate detector. Using the ion signal on the TOF detector, the beamline and EBIT settings are optimized to get both maximum ion number and minimum pulse width (s). As illustrated in Fig 4.8 (b), the charge-state-selected ion signal amplitude is $\approx$ 1.3 V and has a full width at half maximum (FWHM) of $\approx$ 120 ns, corresponding to $\approx$ 1400 ions / extraction pulse passing through the trap. The TOF signal amplitude and FWHM are optimized by tuning all of the electrostatic elements in the ion beamline and capture apparatus, as well as by fine tuning the analyzing magnetic field. It is also important to fine tune the ion optics to match the EBIT ion extraction energy: this is necessary to get the narrowest possible ion pulse while maintaining a large amplitude ($\geq$ 0.5 V) ion signal.

4.3.1 Coarse ion beam tuning

Since all charge states produced in the EBIT are transported by the beamline, it is necessary to optimize the extracted ion pulse prior to charge state selection. As illustrate in Fig. 4.1, the EBIT beamline is equipped with multiple Faraday cups which can be used for tuning the extracted ion beam. The tuning of the ion beam is performed using the second Faraday cup (FC2) in the ion beamline. FC2 is located approximately half way between the EBIT trap center and the ion capture trap. FC2 is also located $\approx$ 20 cm from the entrance aperture of the analyzing magnet.

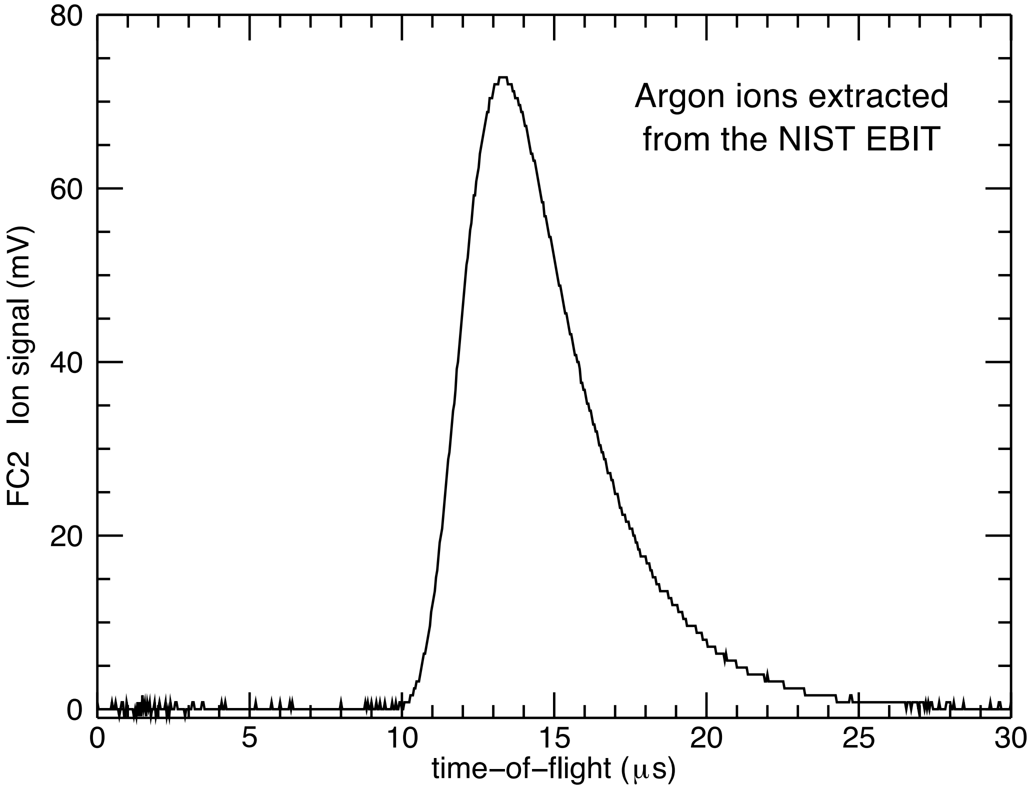

Figure 4.9: Signal on Faraday cup # 2 (*) during pulsed extraction of argon ions created in the EBIT.

Since the distance from the EBIT to FC2 is long compared to the distance from FC2 to the analyzing magnet, optimizing the ion signal on FC2 ensures that the ion beam is aligned with the entrance of the analyzing magnet. The ion signal is monitored using a low-noise current pre-amplifier (Stanford SR570) connected to a digital oscilloscope (Tektronix TDS 2024B). In the pulsed extraction mode, the current pre-amplifier is operated on the 2 μA/V scale, which has a bandwidth of 1 MHz, to avoid lineshape distortion from saturating the instrument. An example of an FC2 ion signal is shown in Fig. 4.9

The signal on Faraday cup # 2 (*) is sensitive to the tuning of the ion optics

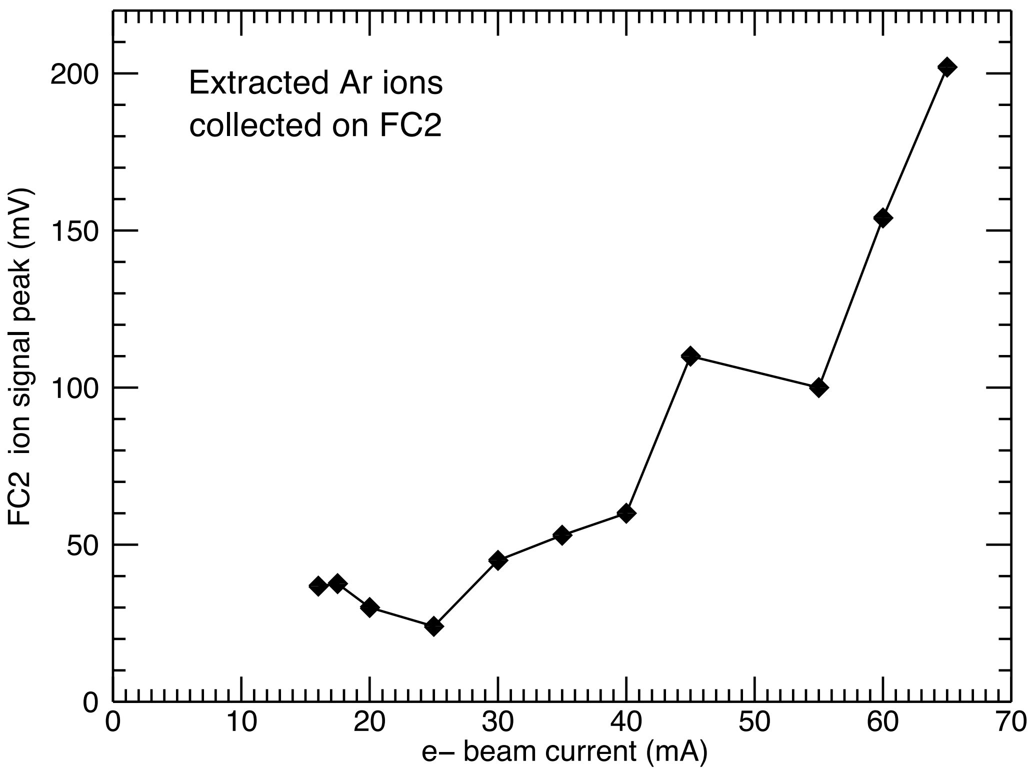

Figure 4.10: EBIT ion extraction FC2 signal strength as a function of the electron beam current

in the beamline, as well as the conditions inside the EBIT. The FC2 ion signal is optimized for high signal amplitude (overall ion number) and narrow pulse width. In particular, the signal amplitude is sensitive to the electron beam current. The ion signal dependence on the EBIT electron beam current is shown in Fig. 4.10 for argon ions extracted at an electron beam energy of ≈ 4.0 keV/Q. As the electron beam current is increased, the ion signal increases, which is to be expected since the electron impact ionization rates are proportional to the electron current density. However, given the fact that all ion charge states are transported to FC2, it is important to note that the highest electron beam current regime is not necessarily the desired regime for ion production of a particular charge state. The issue of charge state production inside the EBIT is addressed in [19, 1].

4.3.2 Single charge state selection: mass scan

After pulsed extraction, charge state selection is an the next step in isolating a single charge state for storage in a trap. The ion pulse extracted from the EBIT is guided to an analyzing magnet which bends the trajectory of an ion with a specific charge-to-mass ratio (q/m) around a 90° bend. A charged particle will undergo uniform circular motion in a uniform magnetic field. For a given bend radius r, set by the beamline geometry, ion beam velocity v, and charge state q/m, the magnetic field is given by

$$B = \frac{m}{q}\frac{v}{r} \tag{4.3}$$

where the ion velocity v is given by

$$v = \sqrt{\frac{2E}{m}}. \tag{4.4}$$

In the approximation that the ion energy $E = qU_{e-}$, where U_{e-} is the EBIT shield potential, the analyzing magnetic field needed for ion transport through the 90° bend is given by

$$B = \frac{1}{r}\sqrt{\frac{2mU_{e-}}{q}}. \tag{4.5}$$

The magnetic bend radius is nominally 20.3 cm [59]. The magnetic field is fine adjusted by either measuring the ion beam current on a faraday cup in the ion capture apparatus, FCA, or by using the TOF detector down-stream from the two-magnet trap (see Fig. 4.1. During the one-magnet trap experiments, FCA was

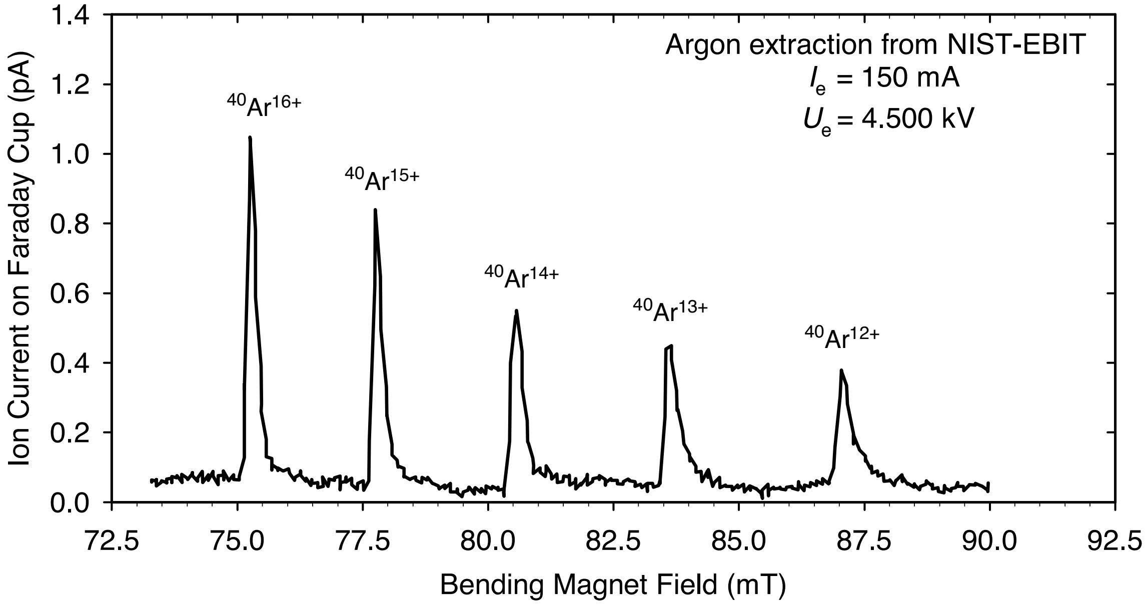

Figure 4.11: Charge-state selection mass scan - Argon 4.5kV/Q.

primarily used for magnetic field tuning, because the fast TOF detector was not yet installed. An example of a magnetic field "mass scan" is shown in Fig. 4.11.

The FCA signal has been measured in a pulse detection mode in order to determine the number of ions entering the trap apparatus. The incident ion pulse striking the Faraday cup (FCA) is measured using a fast transimpedance amplifier (Femto HCA-200M-20K-C) with a gain of 20 kV/A and a frequency bandwidth of 200 MHz. The output signal is further amplified by a factor of 5 before being measured on a digital storage scope. An example of the detected Ar^{13+} signal is shown in Fig. 4.12. The detected number of ions is $\approx$ 5300 ions / EBIT pulse with a pulse width of $\approx$ 120 ns.

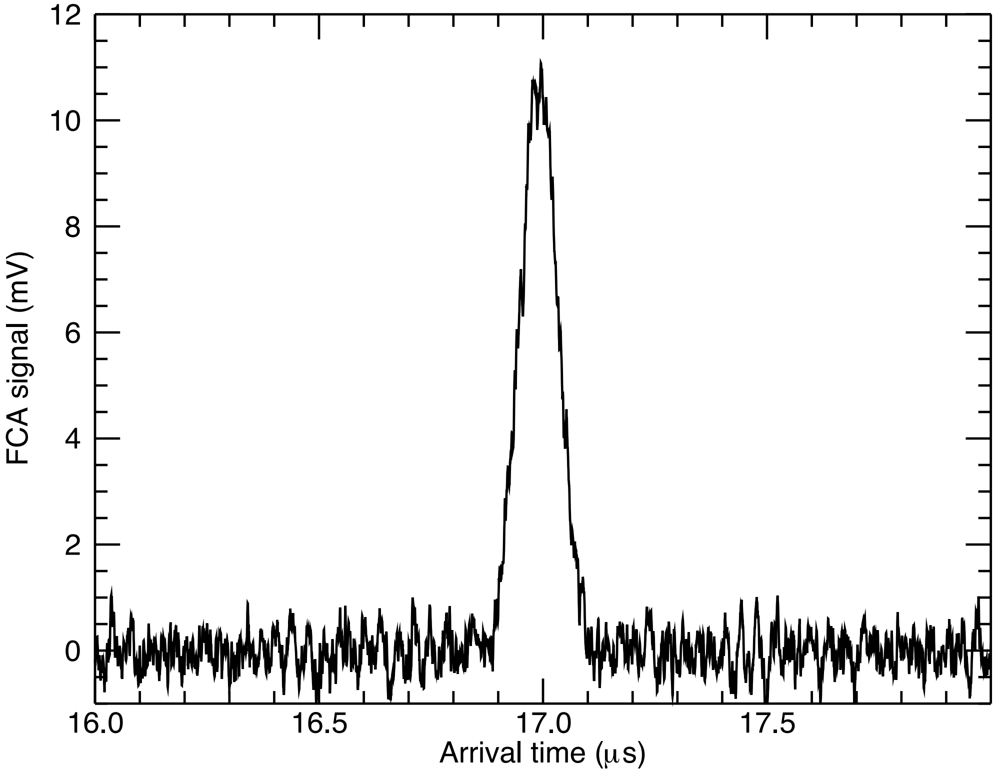

Figure 4.12: ArXIV ion extraction pulse observed on the upstream Faraday cup FCA. The detected pulse converts to an extracted ion number of $N_{FCA} \approx 5300$ ions / pulse.

4.3.3 Ion beam imaging: minimizing spot size

The ion beam entering the Penning trap apparatus is not guaranteed to be aligned with the trap axis. Given the three 90 degree turns and a total flight path of nearly 8 m, small misalignment of the ion beam can become significant when propagated to the Penning trap. In early tests with the one-magnet trap, ion beam detection was performed using a position-sensitive MCP detector (PSD) on the down-stream side of the trap. The details of the detector are presented in §3.4.1. This beam imaging capability was useful in studying the beam conditioning by the various beamline elements, including possible space charge effects that are not easily modeled.

The one-magnet trap apparatus also served to optimize the extracted ion pulse before entering the two magnet trap. An example of the ability of the one magnet trap to act as an einzel lens is shown in Fig. 4.13. A tight focus is obtained by applying 160 V on the ring electrode relative to the endcap electrodes. The spot size in the focused condition is ≈ 2 mm round. In the de-focused and over-focused conditions, the ion beam spot has a diameter of ≈ 10 mm, which is the size of the endcap holes along the trap axis.

4.3.4 Optimizing the ion beam TOF signal

Prior to capture, in addition to minimizing the beam spot near the capture trap, the ion signal on the TOF detector is optimized to obtain maximum ion number and minimum pulse width (s). With the capture trap and neighboring electrodes

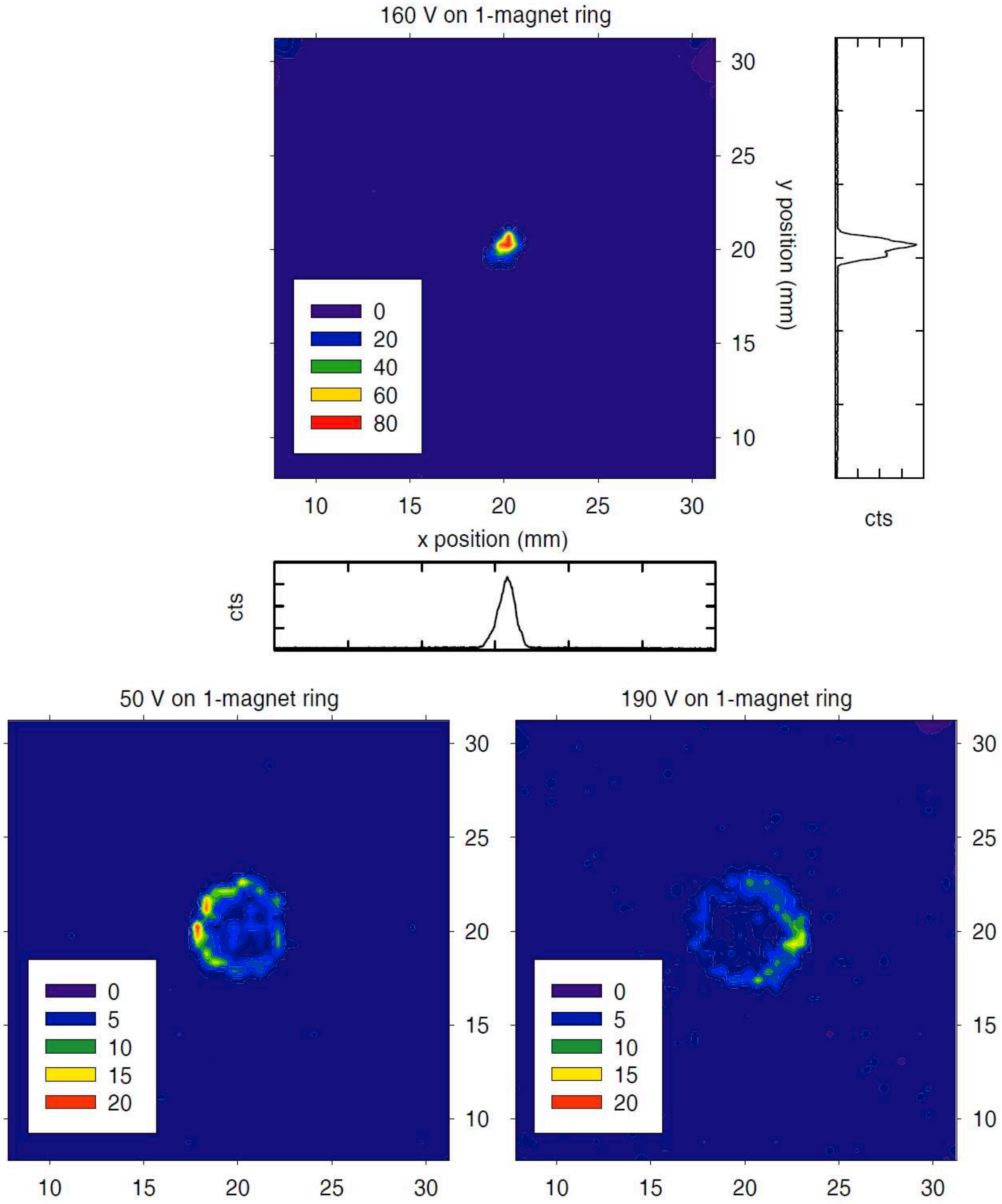

Figure 4.13: Ion beam imaging using an MCP detector backed by a resistive anode for X–Y position encoding (PSD). Bare neon nuclei (Ne^{10+}) passing through the one-magnet ring electrode can be focused to a beam diameter of $\approx$ 2 mm (top). A larger spot size results if the ring potential is too low (bottom left) or too high (bottom right).

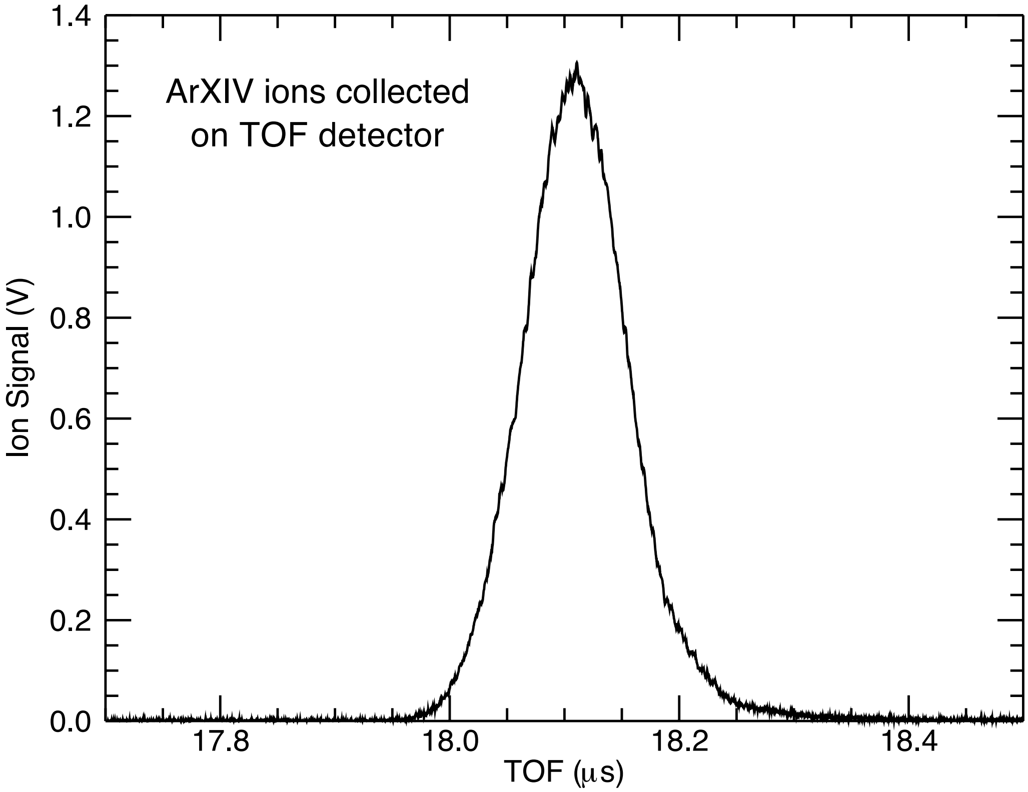

Figure 4.14: ArXIV ion extraction pulse passing through the Penning trap observed on a TOF detector. The electron beam energy (E_{e-}) and current (I_{e-}) were 2.50 keV and 14.4 mA, respectively.

grounded, the extracted ion pulse passes through the trap and is detected using a fast time-of-flight (TOF) micro-channel plate detector. Figure 4.14 is an example where the optimized ion pulse has a TOF pulse amplitude of $\approx$ 1.2 V and a full width at half maximum (FWHM) of $\approx$ 120 ns. The ion signal amplitude and FWHM are optimized by tuning all of the electrostatic elements in the ion beamline and capture apparatus, as well as fine tuning the analyzing magnetic field. Significant pulse degradation results if the ion optics are not matched to the EBIT ion extraction energy. In order to obtain the narrowest possible ion pulse while maintaining a strong (≥ 0.5 V) ion signal, the capture trap electrodes must be floated to mach the EBIT floating potential. Capture efficiency will be low if the ion TOF pulse width is large compared to the transit time in the capture trap.

4.4 Capturing the ion pulse

Ions are captured by applying a time-varying potential (≈ 10 V/ns) to the front endcap trap electrode, with magnitudes and timing guided by simulation as discussed in §4.2. Table 4.1 lists the typical potentials applied to the front endcap electrode before and after capturing Ar^{13+} ions. The timing sequence for ion extraction and capture is shown in Fig. 4.15. A schematic showing the triggers and high voltage pulses for various electrodes is shown in Fig. 4.16.

Initially, the front endcap potential is set below the ring electrode (FECL) to allow ions to enter the trap. As ions enter the trap, they are decelerated between the ring and back endcap electrode. The back endcap is set at a potential greater than the ring (BECH). Ions entering the trap will stop and then turn around, heading towards the front endcap. As the ions slow in the trap, the front endcap potential is switched from the low voltage (FECL) to the high voltage (FECH) with a slew rate of ≈ 10 V/ns. The "capture time," the time at which the entrance endcap electrode is switched to close the trap, is varied experimentally to maximize the amount of ions captured per pulse. A measurement of the optimal ion capture time is shown in Fig. 4.17. Ions are captured and stored for 1 ms before being counted by ejection to the TOF detector.

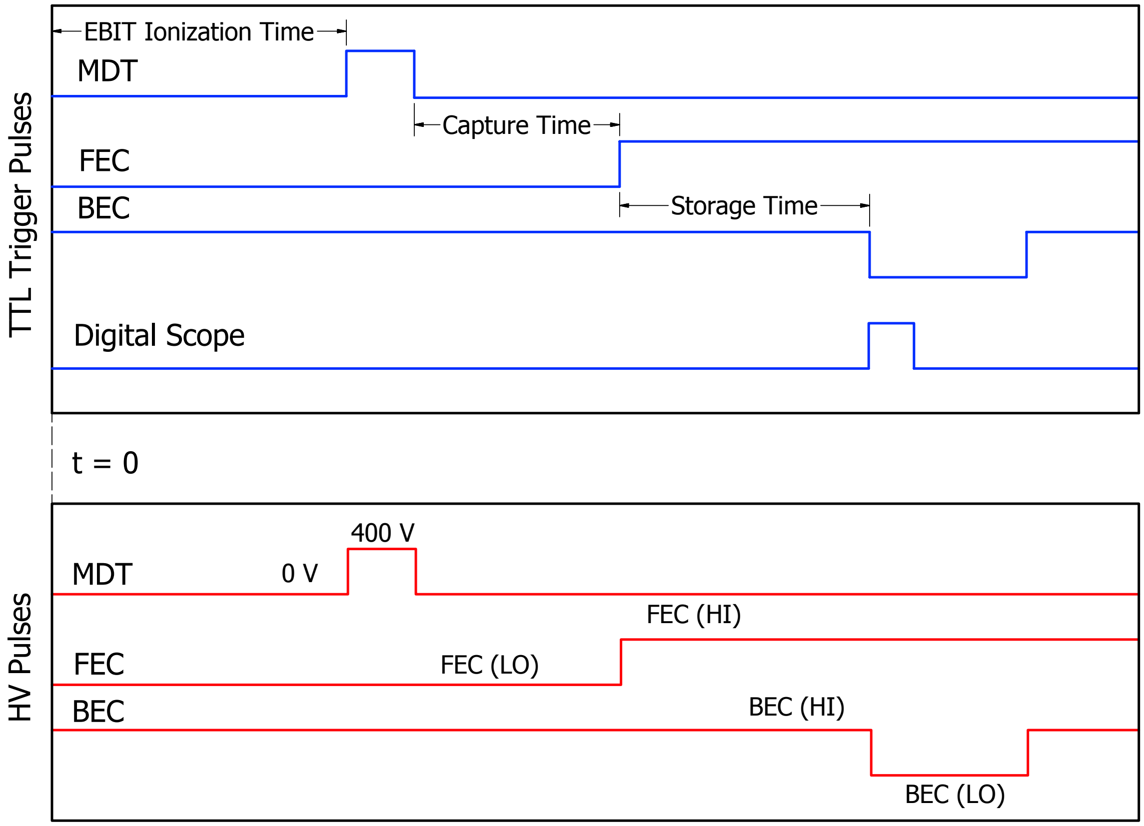

Figure 4.15: Timing pulse diagram for ion capture and detection. Low voltage TTL pulse generators are shown in blue and high voltage controls are shown in red.

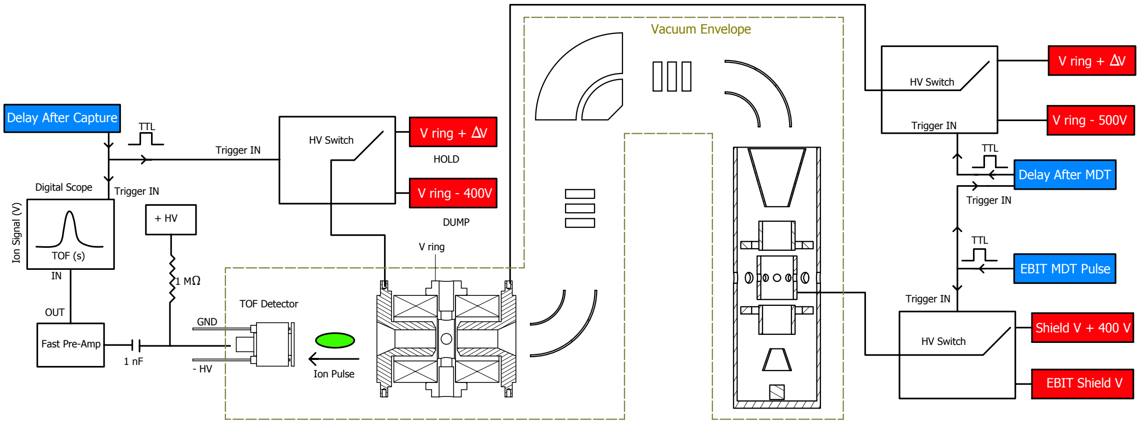

Figure 4.16: Highly simplified diagram highlighting key elements in the detection scheme. Low voltage TTL pulse generators are shown in blue and high voltage controls are shown in red.

The shape of the ion capture time profile is largely attributed to the extracted ion pulse. As described in §4.2, in the case of an infinitely narrow pulse of ions entering the Penning trap on-axis, the capture profile takes the shape of a flat-top function with a width of 50 ns to 110 ns depending on the trapping conditions. Typically, the capture time is chosen at the peak of the profile. In the case of Ar^{13+} at an electron beam energy of 2.50 keV, the optimal capture time occurs at 17.48 μs after EBIT extraction.

The optimal capture time is related to the transit time between the EBIT and the two-magnet Penning trap. An ion of charge q and mass m, extracted through the beamline, will move a distance L, in a time t given by

$$t = \int_0^L \frac{dx}{v(x)} = \sqrt{\frac{m}{q}} \int_0^L \frac{dx}{\sqrt{2(V_o - V(x))}}, \tag{4.6}$$

where $v(x)$ is the ion velocity and $V(x)$ is the electric potential at each position along the flight path. Accept for close to beamline elements (lenses, etc.), $V(x) \approx 0$.

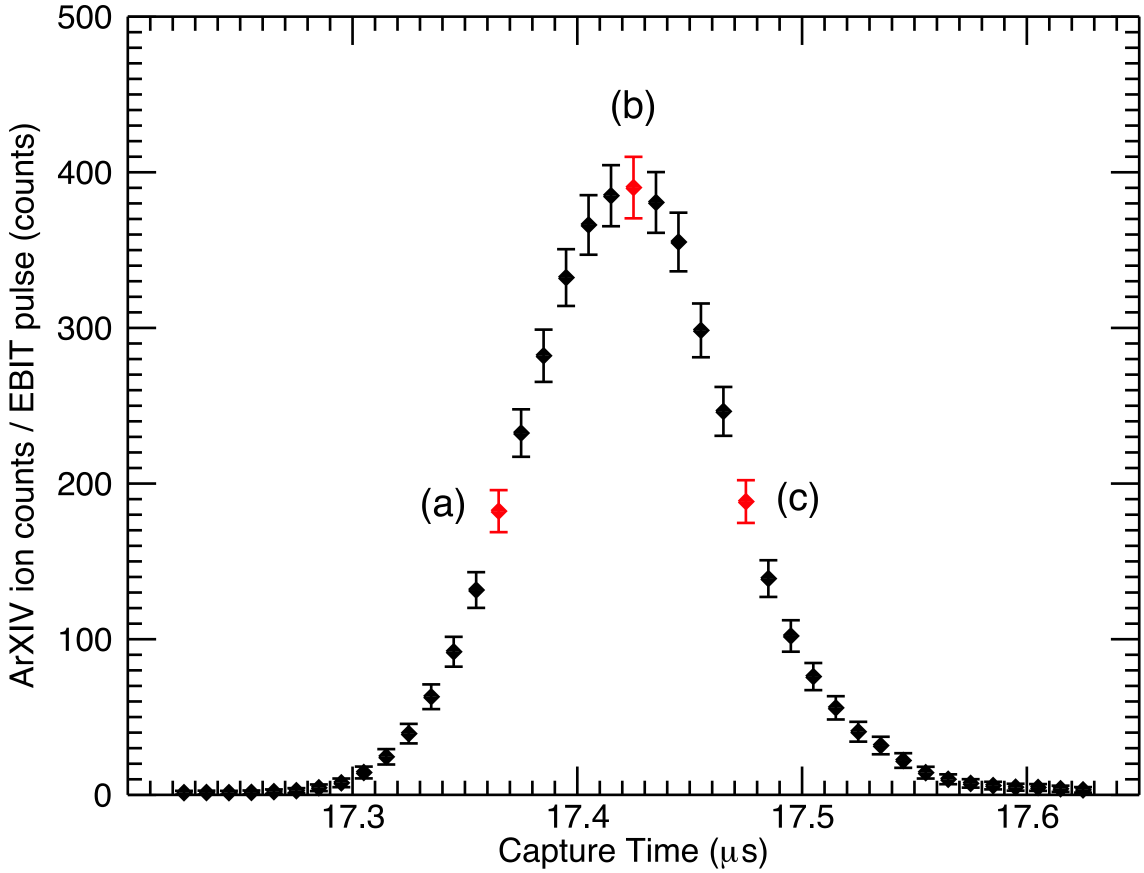

Figure 4.17: Stored ion counts for various capture times obtained from the integrated TOF signals. The associated TOF signals for the points in red, (a), (b), and (c) are shown in Figure 4.18. Ions were stored for 1 ms. The data points represent the average of 64 trials each.

In this approximation, Eq. (4.6) reduces to

$$t = L\sqrt{\frac{m}{2qV_o}}. \tag{4.7}$$

The arrival time for a variety of captured charge states is shown in Fig. 4.19. Here the expected dependance is observed and used as a confirmation of the captured ion charge state at a given extraction energy.

Another important parameter for optimizing ion capture is the overall float

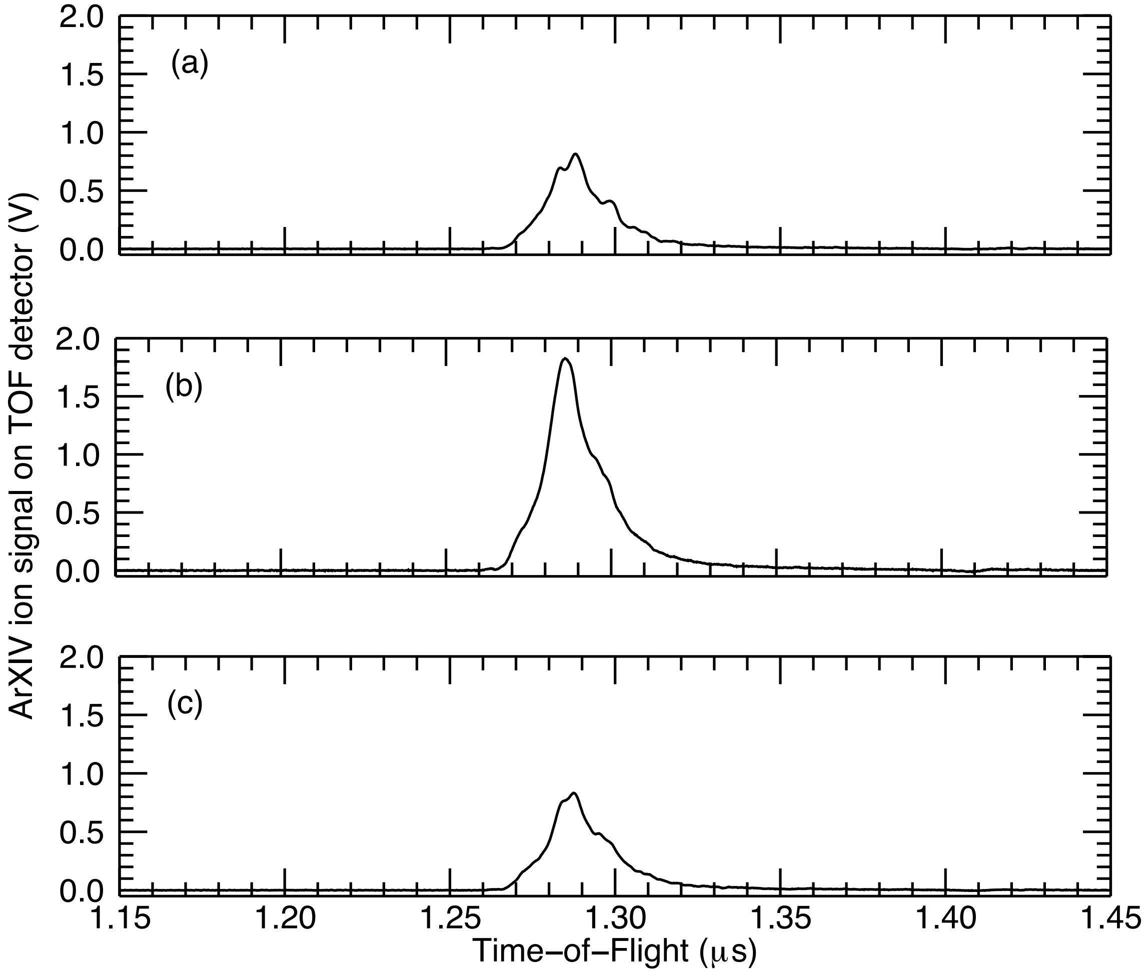

Figure 4.18: Associated TOF signals from points in Figure 4.17: (a) before the optimal capture time, (b) at the optimal capture time, and (c) after the optimal capture time.

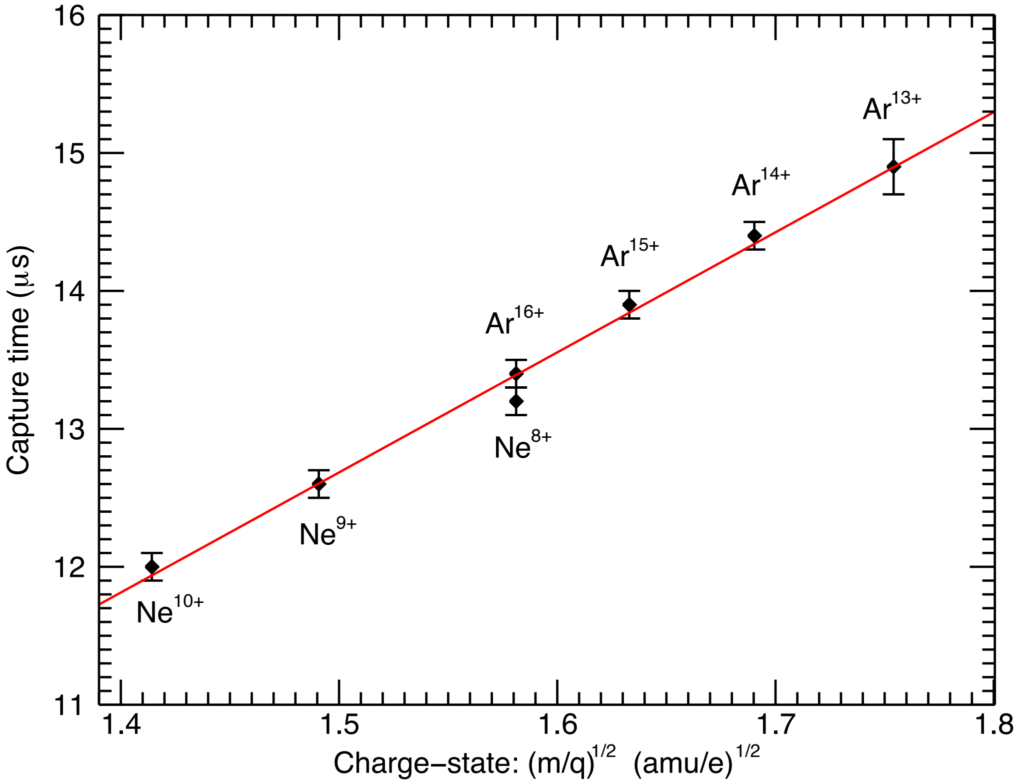

Figure 4.19: Arrival times for different charge states captured in the two-magnet Penning trap. The electron beam energy was 4.5 keV.

voltage, V_C, applied as an offset to all electrodes in the trap assembly. The float voltage is used to match the incoming ion energy, setting the amount of energy that is removed from the ion pulse during capture. The importance of energy matching in ion capture is illustrated in Figures 4.20 and 4.21. The trap float voltage, V_C is optimized to obtain a high capture rate and narrow TOF signal of ejected ions. The number of ions stored, after 1 ms, is measured as a function of the trap float voltage. There is a broad maximum between 2880 V and 2940 V wherein the number of detected ions per EBIT ion pulse is greater than 350. However, the width of the TOF signal drops steadily over that same voltage interval. The narrowing of the TOF width as a function of the float voltage indicates that as V_C is increased, the energy matching is improving between the Penning trap and the energy distribution of the incoming ion pulse. At a certain point, V_C becomes too great and the number of captured ions begins to decrease significantly. This decrease of captured ions occurs simply because some of the incoming ions do not have enough kinetic energy to reach the trapping region.

A comparison of the TOF signal for two float voltages in Fig. 4.21 further illustrates the importance of energy matching in ion capture. In the case of low float voltage, the ions enter with energy higher than the trap well minumum and a double peak structure is observed in the TOF signal, with FWHM $\approx$ 31 ns. In contrast, when the floating voltage is optimized, the TOF signal is stronger by over a factor of 3, single peaked, and narrower, with FWHM $\approx$ 18.5 ns. The dramatic difference depicted in Fig. 4.21, can be attributed to the ion pulse kinetic energy relative to the potential responsible for slowing the ions. It is important for the TOF

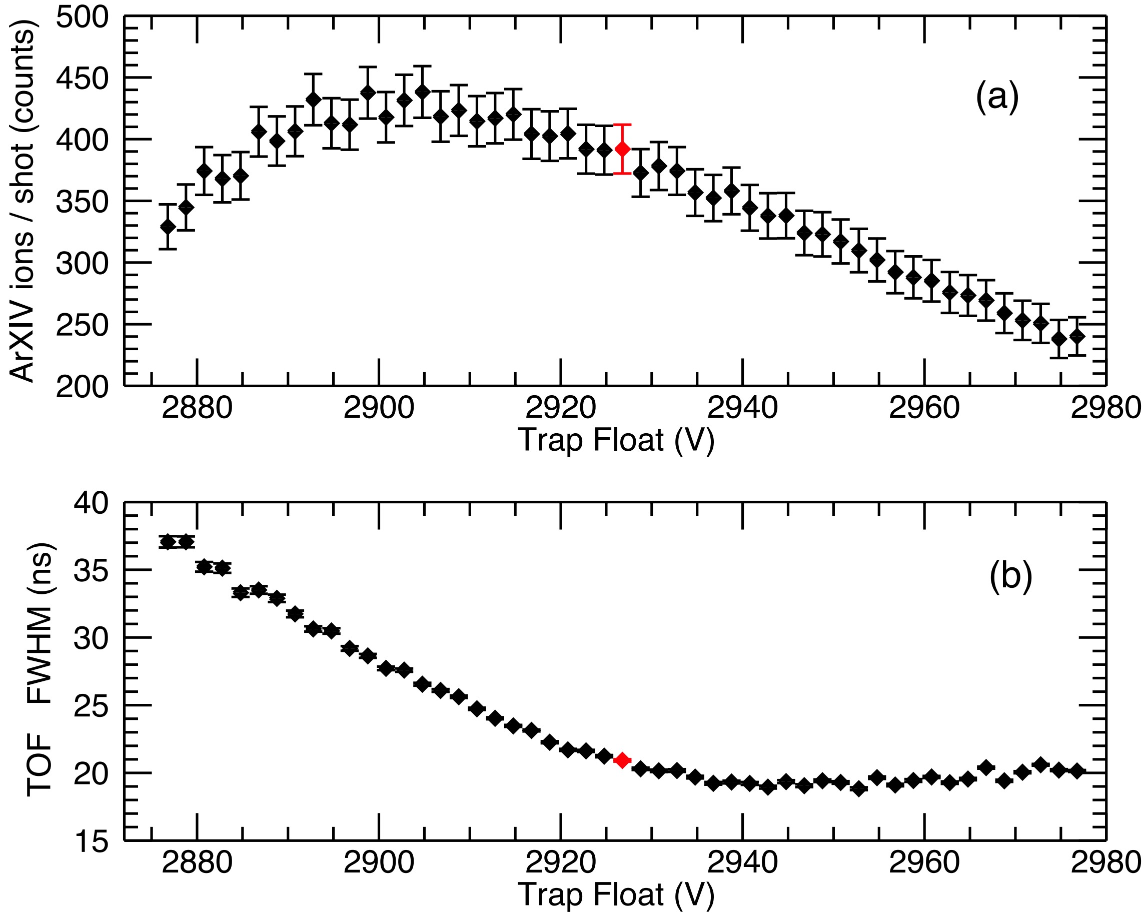

Figure 4.20: Penning trap float voltage, V_C, optimization. Figure (a) shows the number of ions detected, per EBIT ion pulse, averaged over 64 pulses, after 1 ms of storage. Figure (b) shows the TOF width of the ejected ion pulse. The applied trap well, $V_o = 30$ V, and optimal capture time $t_{capture} = 17.43\mu$s.

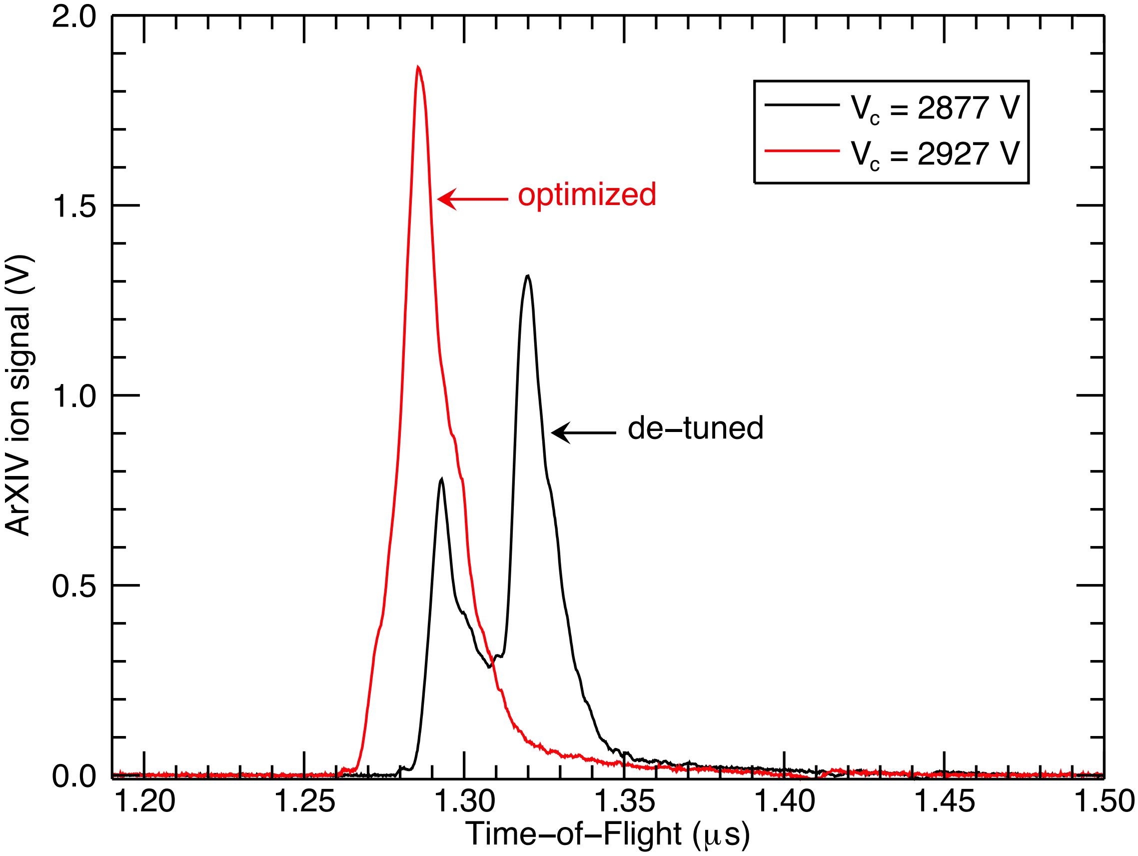

Figure 4.21: TOF signal of stored ions ejected after 1 ms of storage in the Penning trap for two trap float voltages. The trap is closed at the optimal capture time ≈ 17.43μs (see Figure 4.17). The $V_c = 2927$ V trace corresponds to the same point in Figure 4.20.

signal to be single peaked because if it is not, lower charge states detected after long storage times [24] can be misinterpreted as being part of the initial captured charge state. The narrower and higher amplitude TOF signal at optimal float voltage suggests that the captured ions are colder than those captured with mismatched float voltage. A hotter cloud will tend to have a broader axial spatial distribution inside the trap. The ion cloud distribution will tend to be concentrated at the axial turning points in the trap upon ejection. This effect can be large enough to observe a double peak structure when the capture float voltage is mismatched. In addition, there is a shift in the TOF arrival time between the optimized and mismatched extraction pulse due to the kinematic energy imparted to ejected ions at different float voltages. Ions ejected at a higher trap float voltage will arrive at the TOF detector sooner than those ejected at a lower float voltage. Details of ion ejection to the TOF detector are discussed in §6.3.

4.4.1 Ion capture efficiency

Simulations show that ions in a zero emittance beam entering the trap, neglecting space-charge effects, and arriving at a common time, can be captured with 100 % efficiency provided the beam radius is less than 2 mm. Observed capture efficiency is less than 100 % because ions are extracted from an EBIT in pulses wherein the ions have a velocity spread. We have discussed some ways of reducing the velocity spread to maximize capture efficiency.

The ion capture efficiency can be estimated from the detected number of ions after 1 ms of storage, compared with the number of ions in the extracted EBIT pulse that entered the Penning trap. The number of extracted ions entering the trap can be estimated using three numbers: (a) the number of extracted ions measured on FCA, N_{FCA}; (b) the number of extracted ions measured on the TOF detector when the trap is grounded, N_{0V}; and (c) the number of extracted ions measured when the trap is biased statically with the front endcap set for capture, the ring set for storage, and the back endcap set for extraction, N_{HV}. The measured ion number from each of these methods is shown in Table 4.2.

Ar^{13+} ions detected per EBIT pulse		
Method	Measurement	Dectected Ion number
FCA (before trap)	N_{FCA}	5275
TOF, grounded trap	N_{0V}	1418
TOF, biased trap	N_{HV}	687

Table 4.2: Measurement of the number of Ar^{13+} ions in the EBIT extraction pulse under three conditions. N_{FCA} is the number of ions measured on a Faraday cup before the trap. N_{0V} and N_{HV} are the number of ions measured on the TOF detector when the Penning trap is fully grounded and biased for capture, respectively.

These measurements of ion transport can be compared with results of simulations. Calculations of the ion beam transport have been carried out assuming both a uniform spatial beam profile and a Gaussian spatial beam profile. Trajectories have been calculated for ions entering the one magnet Penning trap lens and terminating at the TOF detector. The case of a uniform incoming beam assumes a sharp cutoff at the beam edge with a radius defined as R_B. The incoming beam is assumed to have zero emittance, meaning that the ion's velocity is entirely along the Penning trap axis. The results of the uniform case are shown in Table 4.3. Here

Uniform beam: Calculated Ar^{13+} ions detected per EBIT pulse		
Method	Calculation	Detected Ion number
TOF, grounded trap	N_{0V}	673
TOF, biased trap	N_{HV}	282

Table 4.3: Calculation of the Ar^{13+} ion detection efficiency for the two through beam cases. The incoming beam is uniform with a radius of $R_B = 5.025$ mm. The total number of ions in the incoming beam calculation is 5275.

the calculated ion detection efficiency is lower than measured, indicating that the EBIT beam profile is most likely non-uniform. There is experimental evidence for the non-uniform profile shown in Fig. 4.13. In the case of a tightly focused beam, the radial density profile is roughly Gaussian and takes the form

$$\sigma(r) = \frac{N_o}{2\pi R_B^2} \exp\left(-\frac{r^2}{2R_B^2}\right) \tag{4.8}$$

where N_o is the total number of ions and R_B is the half-width of the beam. The number of ions in a particular section of the beam is given by

$$N = \int_{r_1}^{r_2} 2\pi r \sigma(r)\, dr \tag{4.9}$$

where r_1 and r_2 define the radial limits of the beam of interest and the $2\pi r$ factor accounts for azimuthal weighting. The Gaussian description assumes zero emittance, and the results are presented in Table 4.4.

The Gaussian profile is in closer agreement with the measured ion throughput in both the grounded and biased case. The effect of ion beam emittance has been investigated and could account for the remaining discrepancy between measurement and calculation. The number of detected ions is really a lower limit of the number of ions in the trap because it is not guaranteed that the ion detection efficiency is

Gaussian beam: Calculated Ar^{13+} ions detected per EBIT pulse		
Method	Calculation	Detected Ion number
TOF, grounded trap	N_{0V}	1637
TOF, biased trap	N_{HV}	709

Table 4.4: Calculation of the Ar^{13+} ion detection efficiency for the two through beam cases. The incoming beam is Gaussian with a radius of $R_B = 2.0$ mm. The total number of ions in the incoming beam calculation is 5214.

100 %. This effect is discussed in detail in Ch. 6. Therefore, we estimate that the number of captured Ar^{13+} ions is between 300 and 700 per EBIT cycle.

Based on comparisons between measurements (see Table 4.2) and calculations (see Table 4.3 and Table 4.4) of the ion transport through the Penning trap, we estimate that the number of ions entering the Penning trap is ≈ 1500 per EBIT cycle. The capture efficiency is estimated by taking the ratio of the number of captured ions to the number of ions entering the Penning trap. The ion capture efficiency is estimated to be $\approx 20 - 45$ % for a typical ion capture experiment.

4.5 Discussion

The capture of highly-charged ions in a compact Penning trap is demonstrated for the first time, using a novel unitary architecture. This provides a new method in the continuous effort to study atomic systems in a well controlled, isolated environment. The techniques developed and presented here are anticipated to make possible other planned experiments. These techniques include the optimization of extracted ion beams from the EBIT, capture timing, and energy matching to obtain the lowest possible energy clouds.

Ion capture simulations have guided the apparatus design and ion capture operation. Specialized electrostatic lenses and decelerators near the unitary Penning trap are used to focus and slow the incoming ion pulse. Simulations provide a good approximation for the timing, energy, and radial extent of the incoming pulse that can be captured. For example, incoming ion pulses with a diameter of < 5 mm, and arriving within 80 ns of the front endcap closing time, can be captured in the two-magnet trap.

The operation of the EBIT in a low electron beam current mode is crucial for the optimization of the extracted ion pulse. With the lower electron beam current, the space charge influence on the energy distribution is reduced significantly. This produces a pulse that is more sensitive to energy matching of the ion beamline optics. With greater sensitivity to the ion optics it has become possible to fine tune the pulse alignment with the Penning trap axis and timing for capture.

Ion capture timing and energy matching of the Penning trap are the two major parameters which determine the run-to-run performance of the ion capture apparatus. The ability to select a narrow arrival time and kinetic energy of the incoming ion pulse allows for the control of the captured ion number and ion cloud temperature. Finally, the ion capture efficiency has been shown to depend not only on the properties and control of the Penning trap, but also on the characteristics of the incoming ion pulse.

Chapter 5

Ion Confinement in a Unitary Penning Trap: Empirical Characterization

Both the one-magnet and two-magnet Penning traps have proven to be effective in capturing highly-charged ions extracted from an EBIT. As discussed in Chapter 2, the stability criterion for such compact architecture is more restrictive than for multi-Tesla traps. In this chapter, observed behaviors of stored ions are presented to characterize ion confinement and highlight salient features. The ion confinement time, charge-state evolution, and the temperature of captured ions have been investigated. Some factors affecting ion confinement, such as electron capture from residual gas atoms, are discussed.

Fully stripped neon (Ne^{10+}), which could be used to synthesize one-electron ions in Rydberg states, is used to study the one-magnet and two-magnet traps. The ion confinement time in the one-magnet trap for Ne^{10+} is presented in §5.1.1. The ion confinement time in the two-magnet trap is presented in §5.1.2 using the fully resolved TOF signal of Ne^{10+} ions; the unresolved TOF signal of Ar^{13+} is also analyzed in §5.1.3. Charge exchange is an important loss mechanism. The charge-state evolution is clearly observed without the need for lineshape fitting when the TOF peaks for each charge state are fully resolved. For Ar^{13+}, for which the TOF peaks are not fully resolved, it is necessary to fit the TOF lineshape to obtain an accurate ion count.

In §5.2 the temperature of captured ions is obtained by analyzing data from a slow ion ejection technique similar to the technique used in previous high-field Penning trap experiments [14], except that ion optics are needed where the magnetic field is weak. The slow ion ejection measurements are presented in §5.2.1 for the case of Ar^{13+} ions. The ion cloud temperature is related to the ion mobility and size of the plasma. The ion cloud temperature dependence on the storage time and background gas pressure is investigated in §5.2.2 and §5.2.3, respectively. Initial observations provide evidence for buffer gas cooling of the ion cloud, suggesting that the ion cloud temperature obtained in the slow-ejection measurement can be the starting point for experiments to further cool the highly-charged ions.

5.1 Ion Storage Lifetime

A variety of highly-charged ions have been captured and stored in both the one-magnet and two-magnet Penning traps. The techniques used in ion capture have been discussed in Ch. 4. In the interests of evaluating the trap design and construction, and of evaluating the new Penning trap for precision measurement, a study on the ion storage lifetime has been carried out for a variety of trapped ions.

The storage lifetime of an ion can be influenced by processes such as charge exchange, as well as elastic and inelastic collisions with residual neutral gas molecules that lead to loss from the trap. These effects are pressure-dependent and are related to the neutral gas density in the trap. In addition, there are pressure-independent factors that influence the ion stability in general, such as trap imperfections and the relative alignment of the electrode structure, as well as ion charge state and trapping fields in a unitary Penning trap. The measurement technique and results from ion capture and storage experiments are shown for select ions in the one-magnet and two-magnet trap. Results revealing charge exchange in the two-magnet trap are also presented to demonstrate the usefulness of the apparatus for ion collision investigations.

5.1.1 Ion Storage in the One-magnet Trap

The measurement technique for determining the characteristic storage lifetime is similar to that found in Suess *et. al.* [49]. In short, ions are captured in the Penning trap, confined for a given "storage time", and then ejected and counted on an ion detector located downstream. An example of a measurement with captured NeXI ions is shown in Fig. 5.1. Ions are counted using the position-sensitive detector (PSD) discussed in §3.4.1.

The ion storage lifetime is determined by fitting a single exponential, with zero background, to the ion count data as a function of the storage time. The number of ions in the trap as a function of time is given by

$$N(t) = N_o e^{-t/\tau} \tag{5.1}$$

where N_o is the initial number of ions in the trap and τ is the ion storage lifetime. For the case of Ne^{10+} capture, the characteristic storage lifetime is $\approx$ 1 s at a background pressure of 1.3×10^{-9} torr. The reduced chi-square goodness-of-fit,

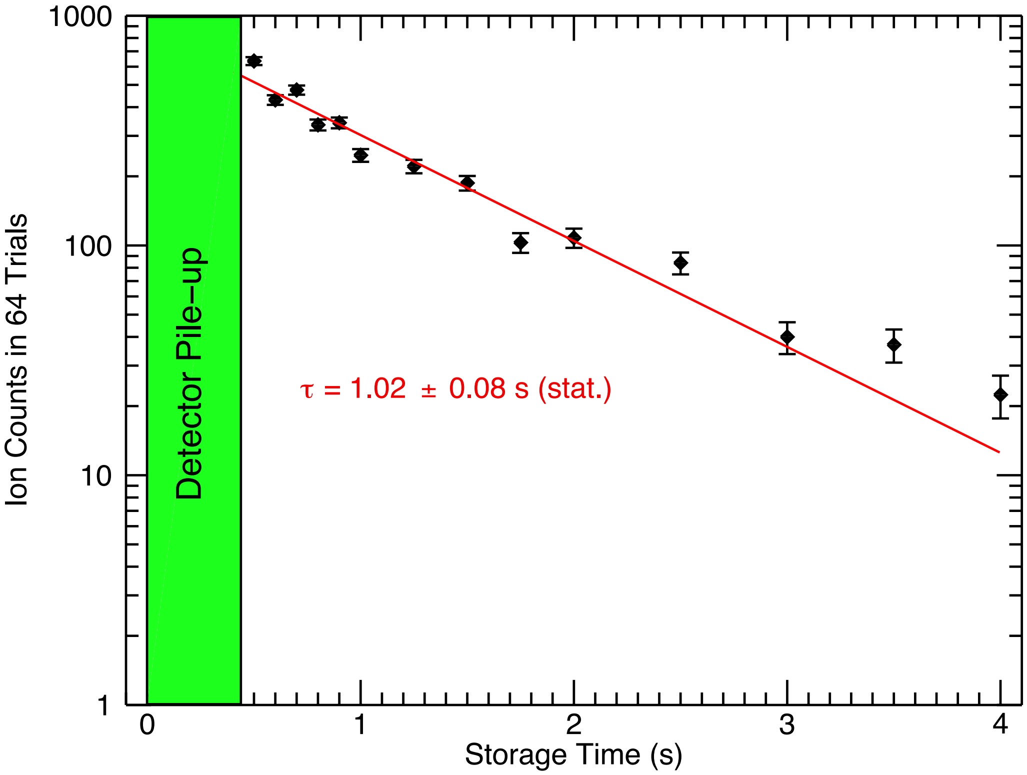

Figure 5.1: Storage lifetime measurement for NeXI ions captured in a one-magnet Penning trap. Ions are detected with the position-sensitive MCP detector (PSD). Data before 500 ms is rejected due to detector saturation effects caused by high ion count rates in the ion dump signal. The background pressure in the system was 1.3 $\times 10^{-9}$ torr. The data is fit using Eq. (5.1); here $\chi^2/\nu = 1.20$.

$\chi^2/\nu = 1.20$. A storage lifetime of order 1 s is sufficiently long to be useful in spectroscopic experiments. In addition, the observed storage lifetime indicates that the trap electrode structure is well aligned and co-axial with the magnetic field. Misalignment of the trap electrode structure produces a torque on the ion cloud, causing the ions to be driven out of the trap radially.

The ion storage lifetime can be affected not only by pressure-dependent loss processes, but also by the trapping conditions used in a unitary Penning trap. In order to investigate some of these pressure-independent effects, ion storage data was taken at different trapping conditions. One example is the dependence on the applied potential difference between the ring and endcap electrodes, V_o. Results from an ion storage measurement at two different well depths is shown in Fig. 5.2.

The two well-depth operating conditions used were $V_o = 40$ V and $V_o = 120$ V yielding storage lifetimes of 1.02 ± 0.08 s and 0.58 ± 0.02 s, respectively; the reported uncertainties are purely statistical. The fitted storage lifetime results have $\chi^2/\nu = 1.20$ and $\chi^2/\nu = 0.9$, respectively. This result is counter-intuitive when contrasted to the traditional Penning trap in a uniform magnetic field, where one would expect the storage lifetime to be longer for a deeper axial well depth and shorter for a shallower well. One possible explanation arises from the non-uniform magnetic field in a unitary Penning trap. In a uniform field trap, if the stability condition (see Eq. (2.6)) is satisfied at one point, then an ion can be confined anywhere in the trapping volume. However, in the case of the one-magnet trap, the non-uniform magnetic field gives rise to a position dependence in the stability condition.

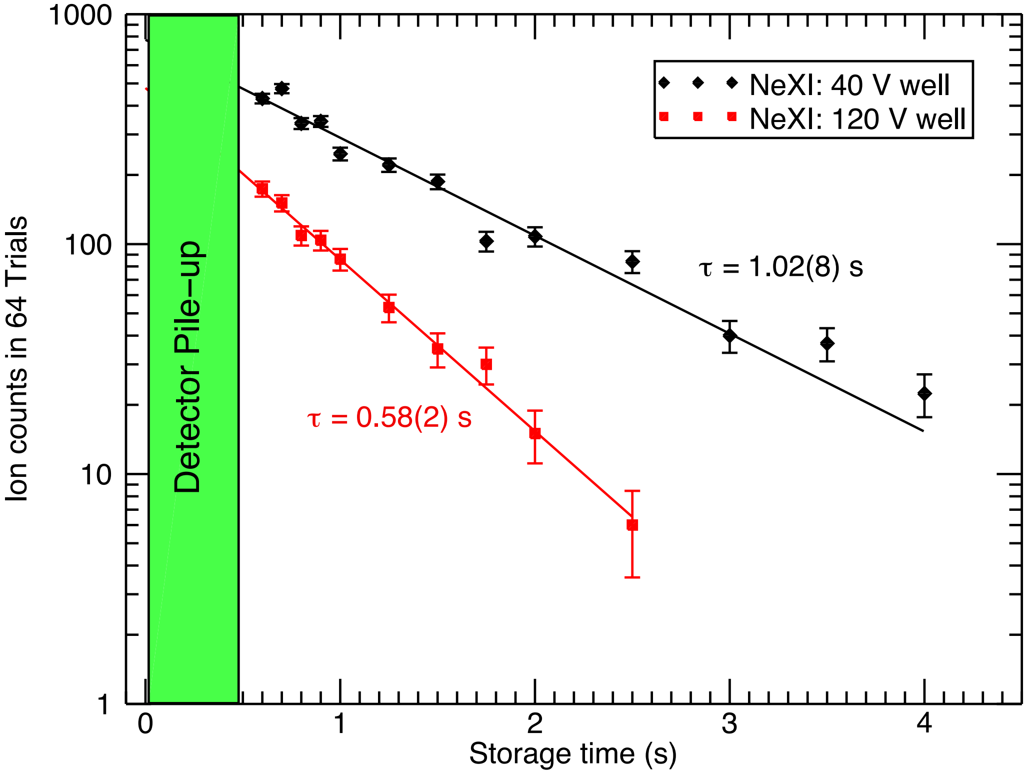

Figure 5.2: Storage lifetime measurement for NeXI ions captured in a one-magnet trap, for two different well depths. Ions are detected with the position-sensitive MCP detector (PSD). Data before 500 ms is rejected due to detector saturation effects caused by high ion count rates in the ion dump signal. The background pressure in the system was 1.3 $\times 10^{-9}$ torr.

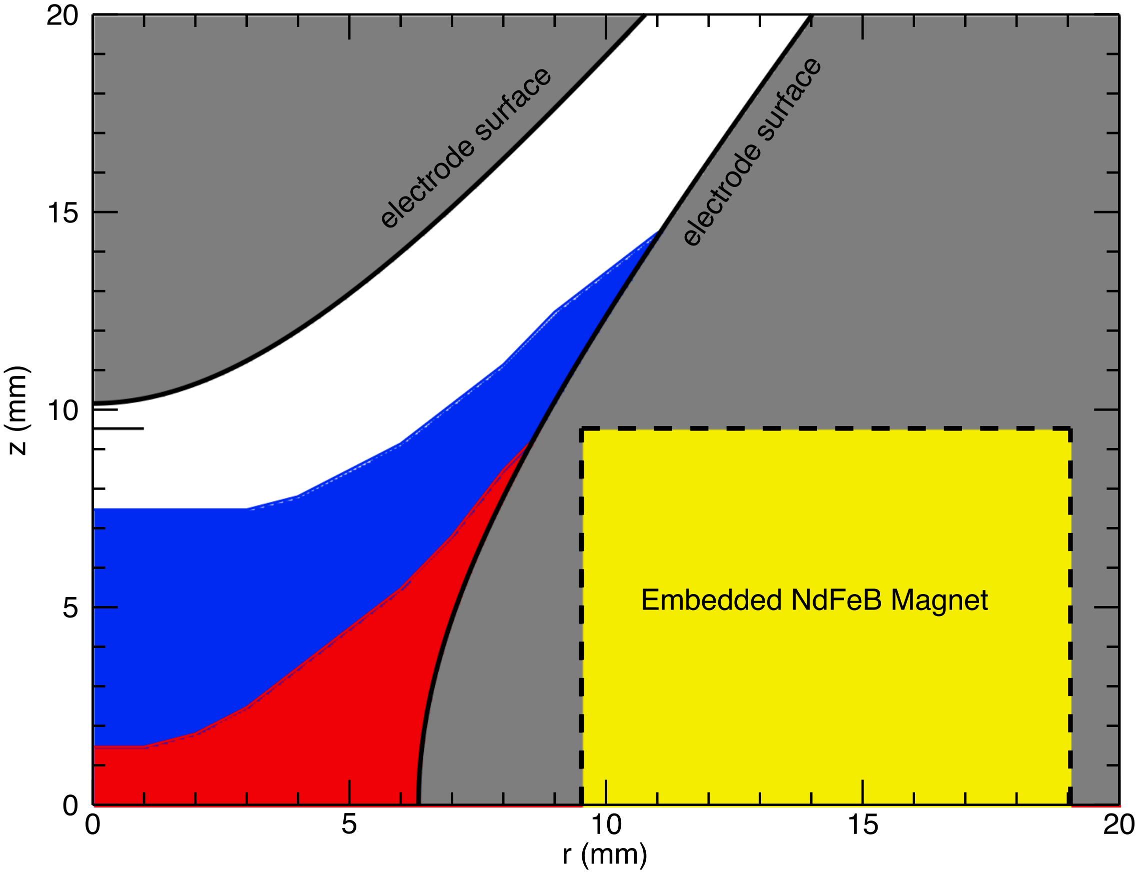

Figure 5.3: Stability diagram for a trap with hyperbolic electrodes and an cylindrical magnet embedded in the ring electrode. The boundary of stable ion orbits is shown for well depths of 45 V (blue) and 125 V (red). Ion orbits where z is less than the boundary are stable.

A simple model wherein a single magnet trap embedded in a hyperbolic ring electrode illustrates this dependence. Figure 5.3 shows a calculated stability boundary for a single magnet trap embedded in a hyperbolic electrode geometry for well depths of 45 V shown in blue and 125 V shown in red. When z is less than the value of the boundary, an ion orbit can be stable in the trapping volume, and for $V_o = 45$ V, the stability region is larger than for $V_o = 125$ V.

Qualitatively, the stability region is pushed towards the ring electrode as V_o

is increased. This occurs because the Lorentz force due to the magnetic field near the center of the trap can not balance the radial outward push of a potential well that is too steep. Since the magnetic field actually increases towards the magnet walls, the trap is better able to support ion orbits that are farther from the center of the trap. Another possible explanation for the improved storage at lower applied potential well depths has to do with the ion energy and is addressed later in this chapter using the two-magnet Penning trap.

5.1.2 Ion Storage in the Two-magnet Trap: Fully Resolved TOF

Simulations suggested that the two-magnet trap design should help improve the capture and storage capabilities, compared to the one-magnet trap. The most notable improvements are in electrode design and magnetic field uniformity, the details of which are presented in Chapters 3 and 4 [24]. The storage capabilities of the two-magnet trap were investigated by measuring the ion storage lifetime, using the technique presented in the previous section. In the two-magnet apparatus, to avoid saturation from high count rates, the ion detection was upgraded to include a fast TOF detector that is capable of resolving different charge states ejected from the trap. The ability to resolve individual charge states has enabled measurements of the injected-ion loss rate, as well as the total ion loss rate in the trap.

Measurements of the ion storage lifetime reveal an improvement in the two-magnet apparatus, in part due to lower vacuum base pressure and the better alignment of precision machined electrodes. Two charge states of interest are shown as examples. In this section ion capture studies involve Ne^{10+}, for which the TOF signal is fully resolved. In §5.1.3 we study another interesting ion, Ar^{13+}, for which the TOF is mostly, but not entirely resolved. It will be evident that the two-magnet trap apparatus is very useful for investigating both trapping dynamics and charge exchange (CX) reactions (charge state evolution) at low energies.

We briefly summarize the concept of time-of-flight (TOF) mass spectroscopy, by considering the kinematic TOF for an ion transported from a trap at a high potential, V, to a detector at ground potential. For a detector at a distance x from the trap, the TOF, t, is given by

$$t = \frac{x}{v}. \tag{5.2}$$

For and ion of charge Q and mass m, v is given by

$$v = \sqrt{\frac{2VQ}{m}}. \tag{5.3}$$

Substituting Eq. (5.3) into Eq. (5.2) the ion TOF for a given charge to mass is given by

$$t = \frac{x}{\sqrt{2V}}\sqrt{\frac{m}{Q}}. \tag{5.4}$$

Considering two ions of the same mass and different ionization, the charge state separation for these 2 ions leaving the trap is given by

$$\Delta t = x\sqrt{\frac{m}{2V}}\left(\frac{1}{\sqrt{Q_2}} - \frac{1}{\sqrt{Q_1}}\right), \tag{5.5}$$

where Q_1 is the first charge state to arrive at the detector and Q_2 is a lower charge state, arriving at the detector later in time. Depending on the charge-to-mass ratio and the applied trap potential, the charge state separation may or may not be large enough for successive charge states to be fully resolved in time.

The case of Ne^{10+} illustrates the situation where ejected charge states are fully resolved. As shown in Ch. 3, the TOF detector signal is capacitively coupled to a pre-amplifier and then recorded on a digital storage scope. The TOF detector is typically operated in the proportional mode wherein the detected ion number is determined by integrating the voltage signal obtained on the storage scope over a time window bracketing the charge state of interest. An example of the TOF signal obtained 1 ms after capture of Ne^{10+} is shown in Fig. 5.4. Here the EBIT was operated at an electron beam energy $E_{e-} = 2.5$ keV and the Penning trap applied potential well $V_o = 10$ V.

The number of ions detected is calculated using Eq. (3.7). In the case shown in Fig. 5.4, $Q = 10e$, where e is the elementary charge and the TOF gain was 1.3×10^5. The pre-amp has a fixed impedance $R_{pre} = 50\ \Omega$ and a fixed gain $G_{pre} = 5$. The integration limits are $t_1 = 1.09\ \mu$s and $t_2 = 1.45\ \mu$s. This yields a detected ion number of $N \approx 85$ ions.

The EBIT and Penning trap are operated in a pulsed extraction and capture mode; therefore, the integrated ion number, N, is the “per shot” average in 64 shots. To count ions of a different charge state, the integration window and ion charge are adjusted such that the integration is performed over the arrival time of the charge state of interest. An example of detected lower ion charge is shown in Fig 5.5. After a storage time of 1 s, TOF peaks are observed for charge states as low as Ne^{7+}.

The stored ions can capture electrons from the background gas atoms and molecules. The charge state evolution in time can be studied by counting the number of ions of each charge state as a function of the storage time. An example of the

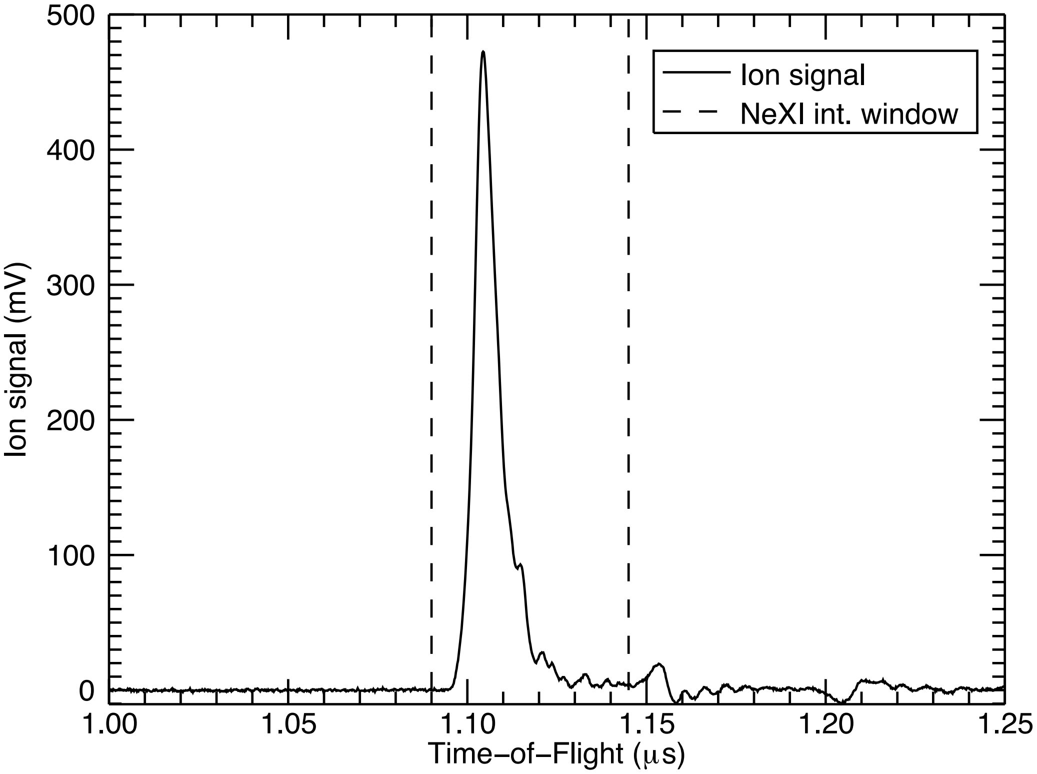

Figure 5.4: TOF ion signal average in 64 EBIT pulses. Bare neon nuclei (Ne^{10+}) were ejected to the TOF detector 1 ms after capture. The background pressure in the system was 1.3×10^{-9} torr. The integration window for the arrival of Ne^{10+} is shown by the dashed vertical lines.

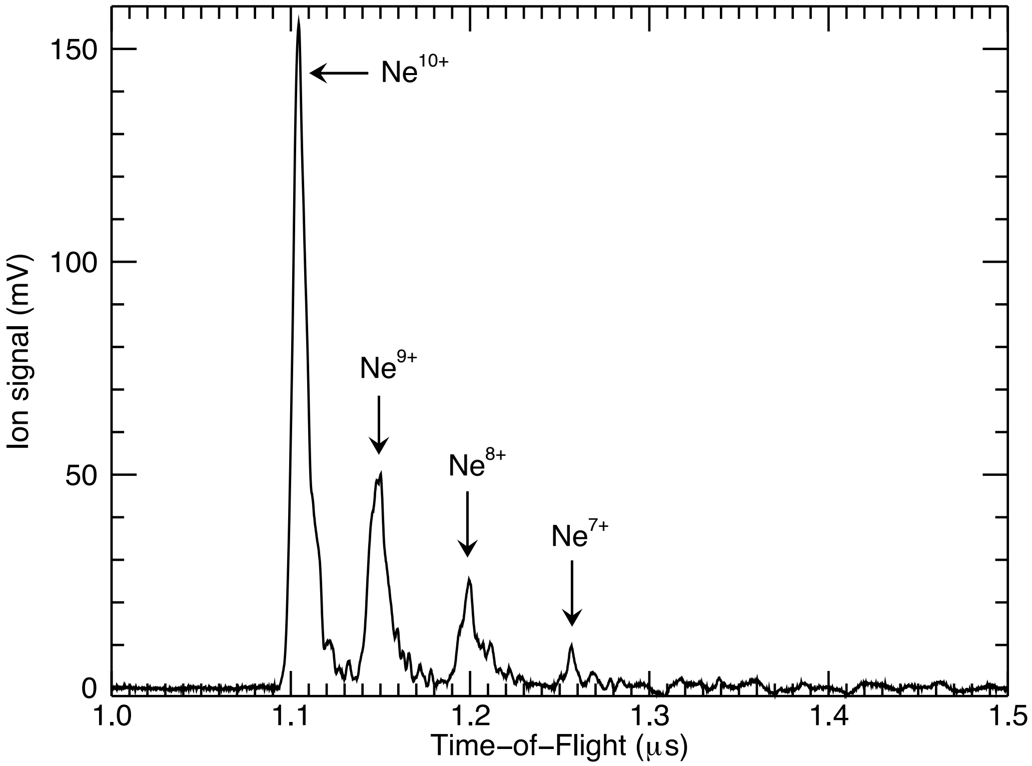

Figure 5.5: Electron capture by Ne^{10+} ions during 1 s confinement. The background pressure in the system was 1.3 $\times 10^{-9}$ torr. After 1 s of ion storage, charge states as low as Ne^{7+} are seen in the trap. TOF ion signal average in 64 EBIT pulses.

charge state evolution in the trap is shown in Fig. 5.6. Shortly after capture, only Ne^{10+} ions exist in the trap. However, since the background gas pressure is non-zero, the bare neon has a probability of undergoing a collision or charge exchange reaction with the residual neutral gas present in the trap region. See Chapter 3 for a discussion of the vacuum production and background gas composition.

The dacay in the Ne^{10+} ion number fits the exponential function shown in

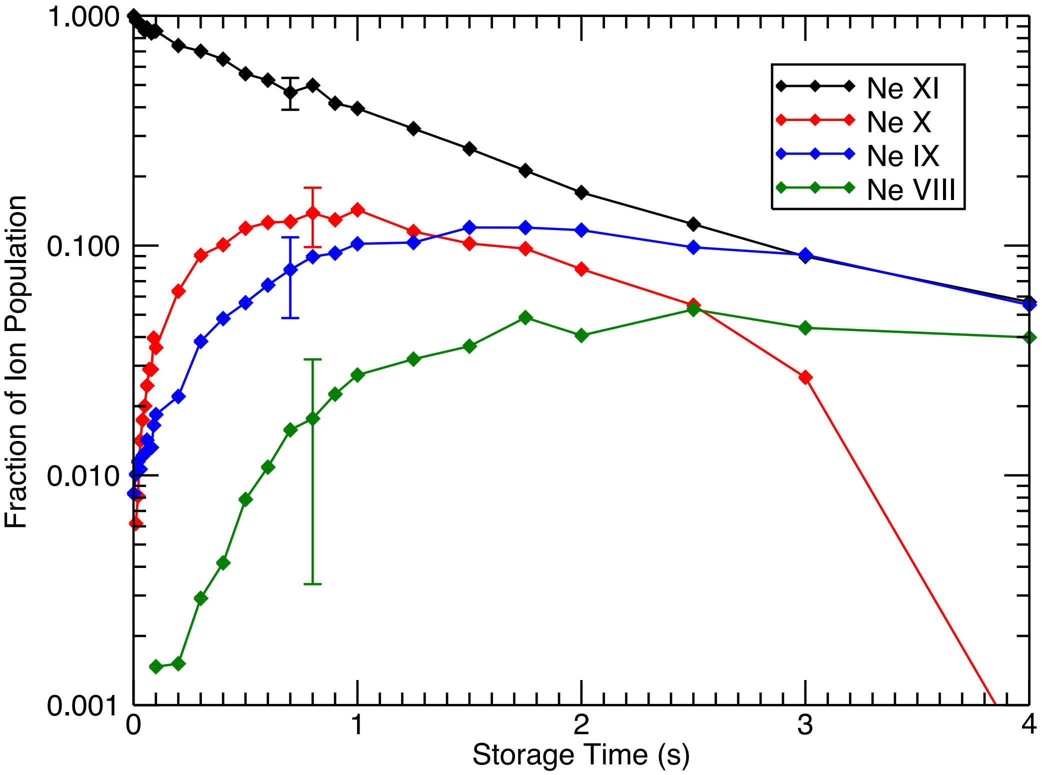

Figure 5.6: Charge state evolution upon capture of Ne^{10+}. Representative uncertainties are plotted on each charge state curve. Solid lines are shown for clarity and are not fitted results. The background pressure in the system was 1.3 $\times 10^{-9}$ torr.

Eq. (5.1). As the Ne^{10+} population decreases, the low charge state ion populations increase, up to a point; but eventually, the lower charge state ions are also lost from the trap. The total detected number of ions ejected from the trap is obtained by adding the measured ion number from each charge state.

The ion stability in the trap has been studied for both the captured charge state and the sum of charge states. The Ne^{10+} storage lifetime and the sum of

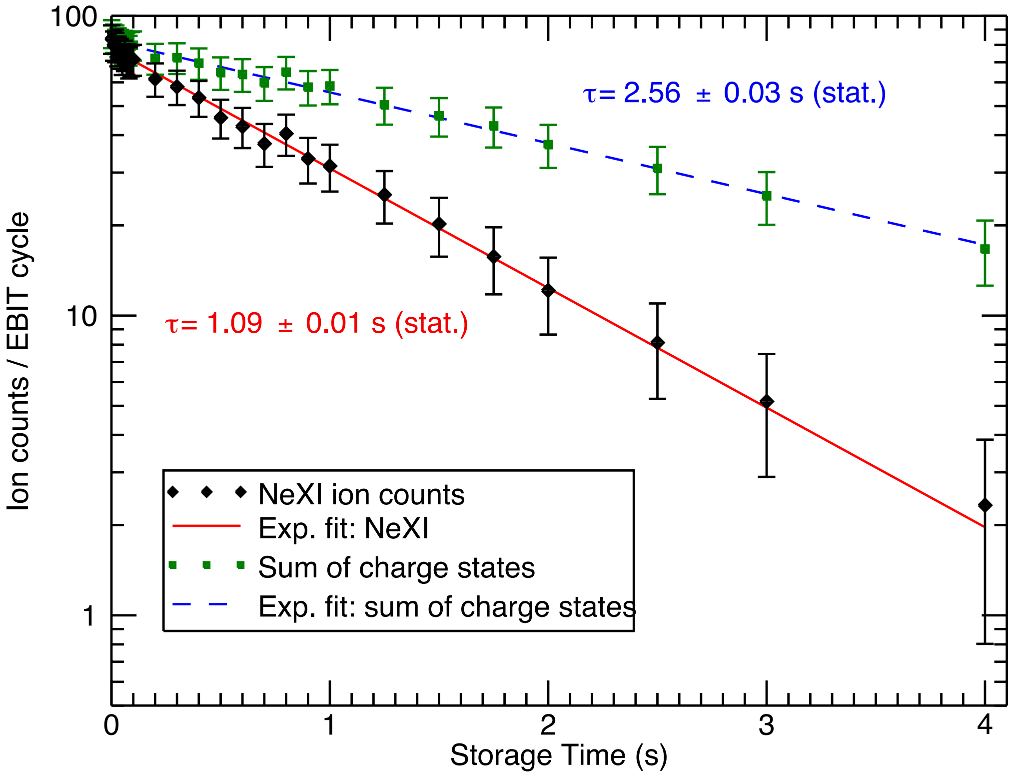

Figure 5.7: Measured storage lifetime for Ne^{10+} and the sum of detected charge states. The background pressure in the system was 1.3×10^{-9} torr.

charge states storage lifetime are shown in Fig. 5.7. The Ne^{10+} storage lifetime at a background pressure of 1.3×10^{-9} torr is measured to be $\tau = 1.09 \pm 0.01$ s and the storage lifetime of the sum of charge states is $\tau = 2.56 \pm 0.03$ s.[1] Here $\chi^2/\nu = 0.95$ for both exponential fits. The Ne^{10+} storage lifetime represents the lifetime due to all collisional processes, including charge exchange, and any heating (radial acceleration) due to trap imperfections in the electrode structure or magnets.

---

[1] Uncertainty shown is entirely statistical.

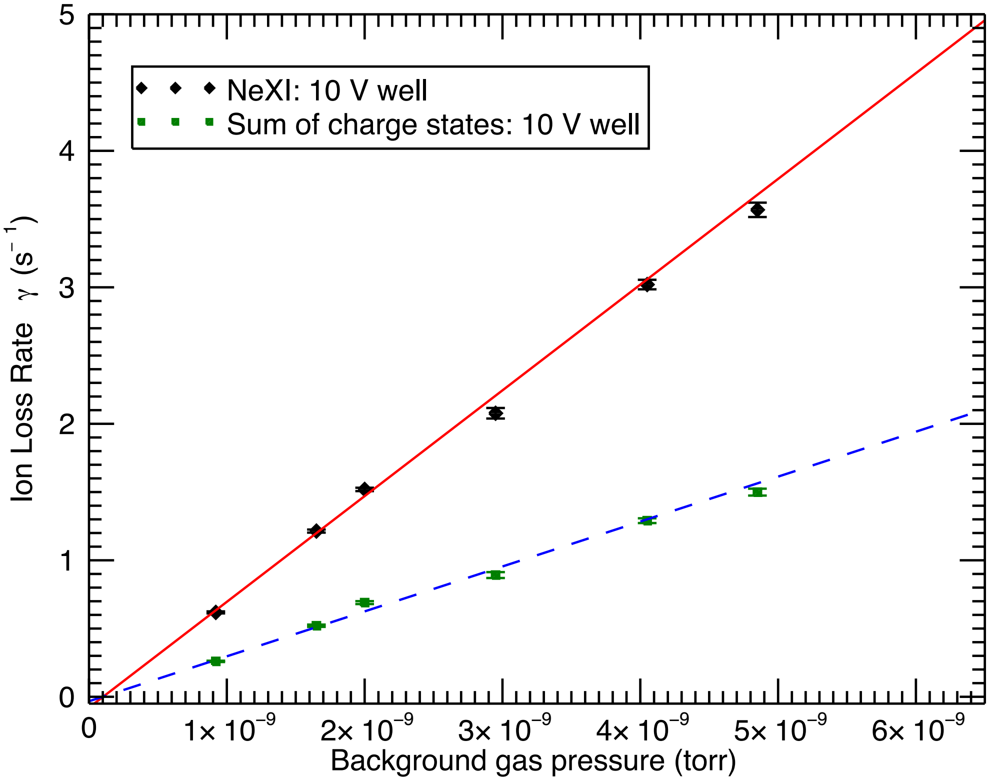

Figure 5.8: Pressure dependent ion loss measurement for NeXI ions. An applied potential well of $V_o = 10$ V was used.

The ion storage lifetime of the sum of charge states is an estimate of the characteristic ion cloud expansion rate at a given pressure.

The pressure dependence of the ion storage lifetime has been studied and a linear relationship has been observed. The results of the pressure dependent ion loss measurement at a potential well depth of $V_o = 10$ V are shown in Fig. 5.8. The Ne^{10+} ion loss rate is systematically higher at each pressure than loss due to ion cloud expansion. The charge exchange rate is approximated by the difference between the total Ne^{10+} loss rate and the loss rate due to ion cloud expansion. At the base pressure in this measurement of 9.2×10^{-10} torr, the Ne^{10+} storage lifetime is $\tau = 1.62 \pm 0.02$ s and the sum of charge states storage lifetime is $\tau = 3.85 \pm 0.07$ s. As shown in Chapter 7, ion storage lifetimes of order 1 s are useful for various spectroscopic measurements.

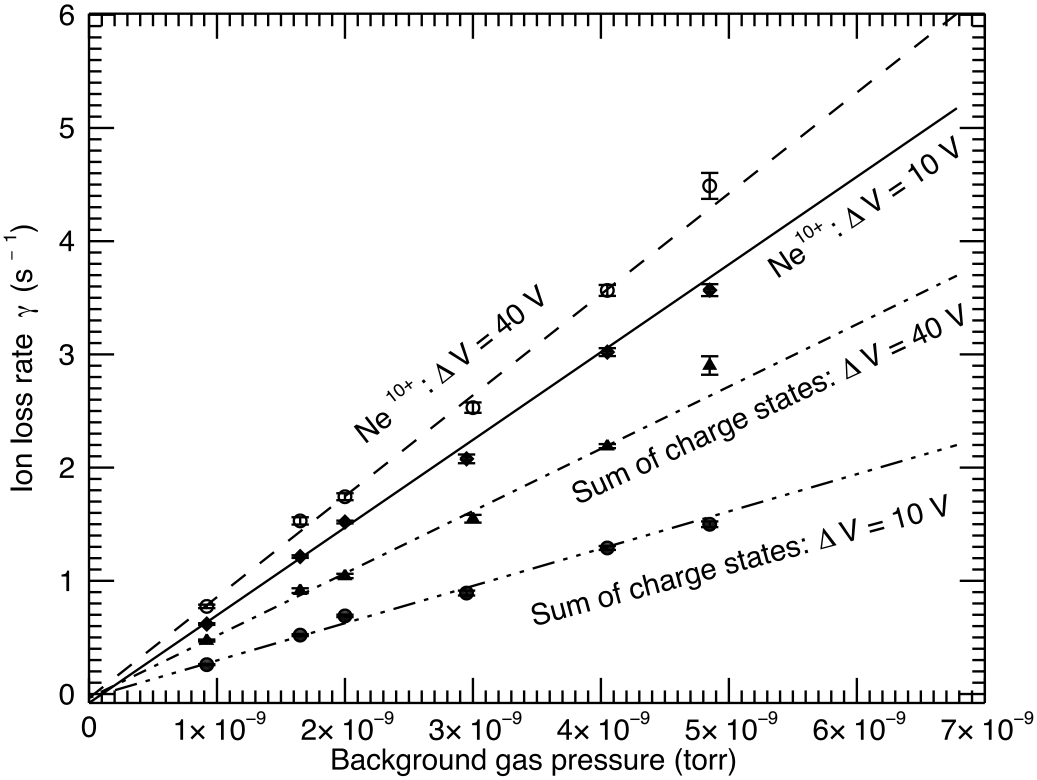

Figure 5.9: Pressure dependent ion loss measurement at two potential wells. Ne^{10+} ions captured and stored in an applied potential well of $V_o =$ 10 V and $V_o = 40$ V. The results for Ne^{10+} include all loss mechanisms. The results for the sum of charge states represent loss due to ion cloud expansion.

As in the one-magnet trap, the applied potential well has significant influence on the storage lifetime, due to change in the size of the stability region. The pressure dependence suggests another mechanism. The results of a pressure dependent measurement of the storage lifetime for the case of $\Delta V = 10$ V and $\Delta V = 40$ V are shown in Fig. 5.9. As in the case of the one-magnet trap, the ion storage lifetime is longer in the lower axial well depth. One possible explanation, in addition to the trap stability, is that ion energy is important, as suggested by Fig. 5.23 which suggests that the ions in the 10 V axial well are colder. Here, the ion stability region in the trap is important, but the non-uniform magnetic field dependence has been significantly suppressed, by design, in the two-magnet trap. Also, the electrode alignment is presumed to be improved because all indexing of the electrode assembly has been done using precision machined components.

5.1.3 Ion Storage in the Two-magnet Trap: Unresolved TOF

The case of capture and storage of Ar^{13+} illustrates the situation wherein ejected charge states are not fully resolved in time. The relative charge-to-mass ratio in the case of Ar^{13+} and Ar^{12+} is smaller than the case of Ne^{10+} and Ne^{9+}, which makes the charge state separation smaller in time for Argon ions. In fact, the charge state separation is such that the Ar^{13+} TOF peaks can not be fully resolved in time. Therefore, the technique for determining the ion number for each charge state presented above yields results which underestimate the ion number at early times. In the case of neon, it is possible to define a fixed integration window in time, because any small changes in the TOF lineshape, for example, narrowing of the line due to a decrease in the axial ion temperature, is small compared to the width of the peak and small compared to the charge state separation. However, in the case of Argon, the TOF lineshape plays an important role in the determination of the number of ions of each charge state, especially at short (< 100 ms) storage times. An example of the evolution of the TOF lineshape for capture of Ar^{13+} and production of lower charge states is shown in Fig. 5.10. The first peak corresponds to Ar^{13+}, and the successive peaks correspond to production of lower charge states from Ar^{12+} to Ar^{10+} by charge exchange with the residual background gas. As the storage time is increased, the minimum between the Ar^{13+} and Ar^{12+} shifts to a lower time as the Ar^{13+} peak becomes more narrow. In fact, at long storage times, the charge states become more resolved. This suggests that the deduced ion number will be artificially low if a fixed time window is chosen based on an upper time limit located at the minimum between the Ar^{13+} and Ar^{12+} for a storage time of ≈ 1 s; when this integration window is also applied to the early storage time signals, some truncation of the longer time signal results.

The solution to the issue of overlapping charge states in the TOF signal is to fit the lineshape to an analytic function and integrate the function in order to get a better measurement of the actual detected number of ions for each charge state. A variety of lineshapes, both symmetric and asymmetric, were considered and tested; finally, a lineshape described in [70] was selected. The lineshape used takes the form of an asymmetric Lorentzian and has been used to interpret molecular ro-vibrational spectra [70]. The lineshape is obtained by starting with a symmetric

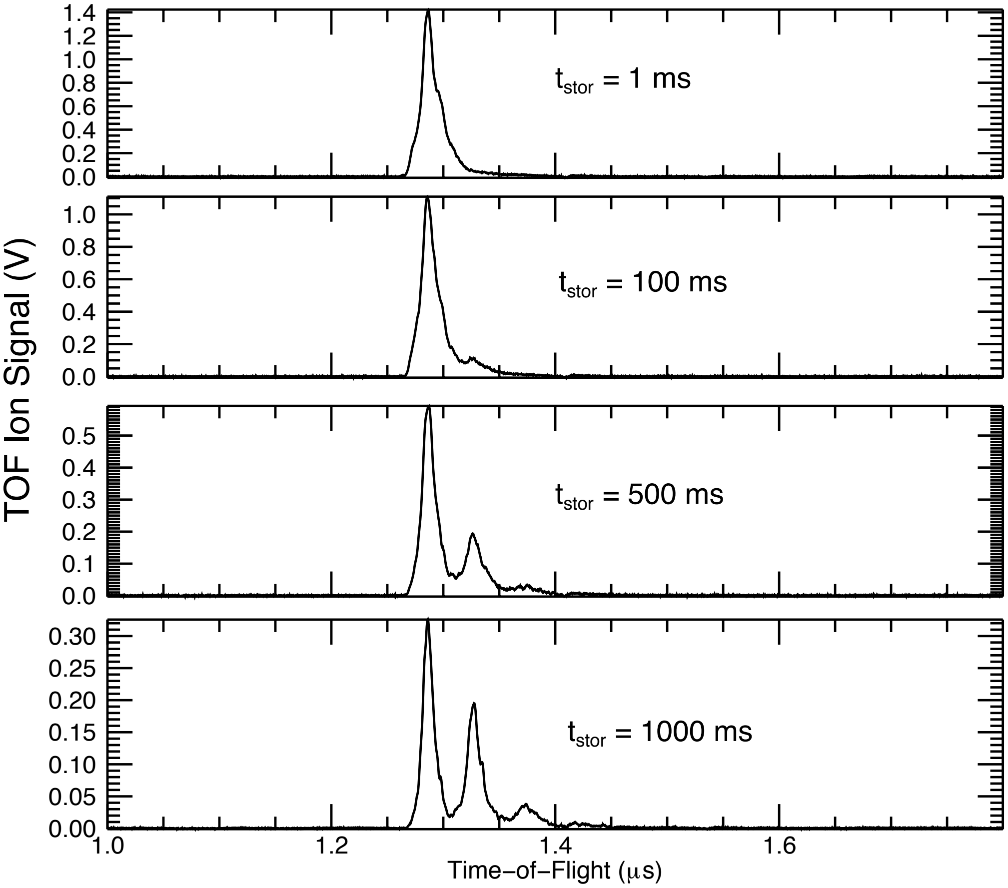

Figure 5.10: Ar^{13+} ion capture and charge state separation for storage times of 1 ms, 100 ms, 500 ms, and 1 s. Here the trap chamber pressure was $P = 8.1 \times 10^{-10}$ torr.

Lorentzian function given by

$$L(t) = \frac{A\gamma_o}{2\left[(t - t_o)^2 + \left(\frac{\gamma_o}{2}\right)^2\right]} + B, \tag{5.6}$$

where $A\pi$ is the area under the function, t_o is the location of the line center, γ_o is the full width at half maximum (FWHM), and B is a constant background level. The symmetric lineshape assumes a time-independent width, which is not in agreement with the observed lineshape on the TOF detector. The symmetric lineshape can be modified by allowing the line width to be time-dependent. With the following substitution for γ_o,

$$\gamma(t) = \frac{2\gamma_o}{1 + e^{c(t-t_o)}} \tag{5.7}$$

where γ_o is the symmetric linewidth and c is a parameter setting the degree of asymmetry in the line. The time-dependent linewidth ranges from 0 to $2\gamma_o$. For $c = 0$, the symmetric linewidth is recovered. For $c \to -\infty$, the linewidth becomes shifted entirely towards long times; and for $c \to +\infty$, the linewidth is shifted entirely towards short times. The time-dependent linewidth for the case of $c = 0$ and $c = \pm\ 0.4/\gamma_o$ is shown in Fig. 5.11. The slope of the time-dependent linewidth is given by

$$\frac{d\gamma}{dt} = -\frac{ce^{c(t-t_o)}}{1 + e^{c(t-t_o)}}\gamma(t), \tag{5.8}$$

and near the line center, t_o, the slope can be expanded as

$$\frac{d\gamma}{dt} \approx -\frac{c\gamma_o}{2} + \frac{1}{8}\gamma_o c^3 (t - t_o)^2 + \mathcal{O}(t - t_o)^3. \tag{5.9}$$

Here it is clear that the degree to which the line is asymmetric is determined by the magnitude of c. The full form of the lineshape is obtained by substituting Eq. (5.7)

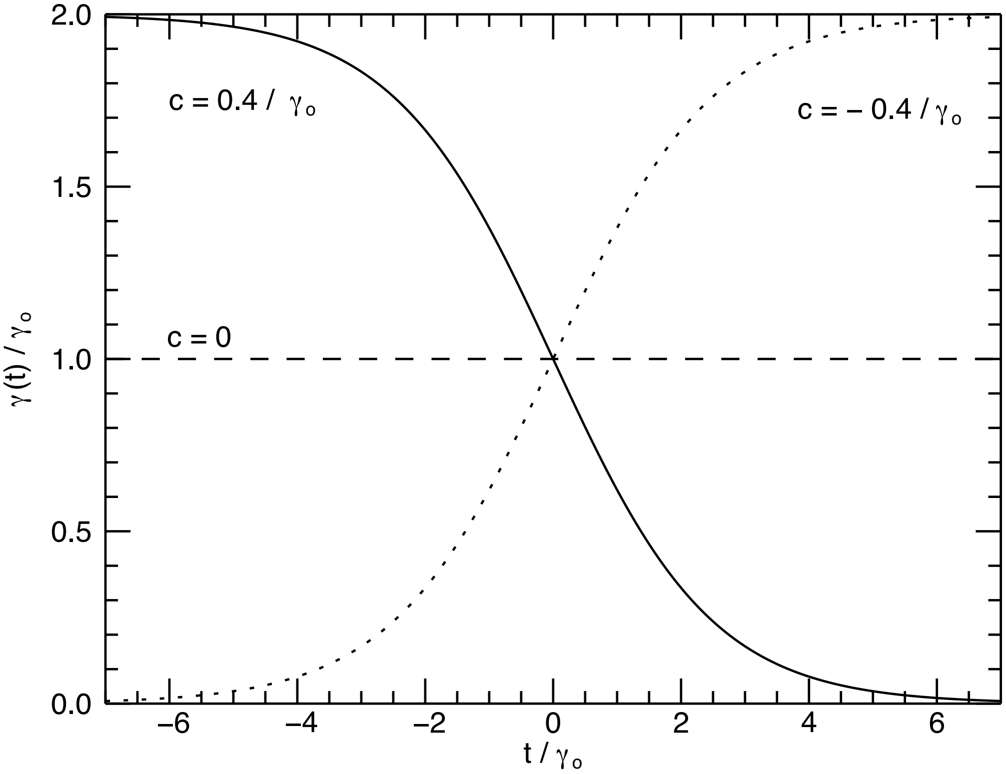

Figure 5.11: Time-dependent linewidth for asymmetric Lorentzian lineshapes for the case of $c = 0$, and $c = \pm\ 0.4/\gamma_o$.

into Eq. (5.6) and is given by

$$L_a(t) = \frac{1}{(1+e^{c(t-t_o)})} \frac{A\gamma_o}{\left[(t-t_o)^2 + \left(\frac{\gamma_o}{1+e^{c(t-t_o)}}\right)^2\right]} + B. \tag{5.10}$$

An example of the full lineshape for the case of $c = 0$ and $c = \pm 0.4/\gamma_o$ is shown in Fig. 5.12. For the case of $c = 0$, the symmetric Lorentzian lineshape is recovered. The case of $c < 0$ is weighted heavily towards later time; and the case of $c > 0$ is weighted heavily towards earlier time.

The single asymmetric function, $L_a(t)$ is useful as a first approximation to

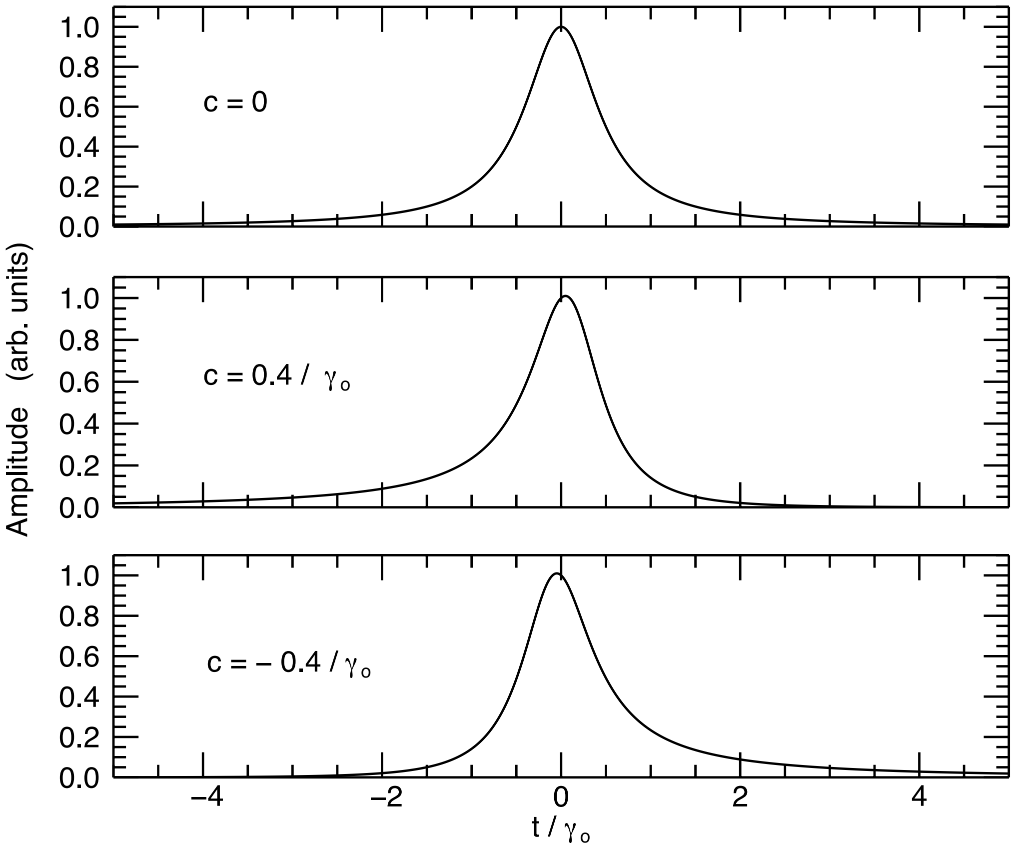

Figure 5.12: Asymmetric Lorentzian lineshapes for the case of $c = 0$, and $c = \pm\ 0.4/\gamma_o$.

the observed lineshape on the TOF detector. However, in the case of Ar^{13+} TOF detection, there is sufficient structure in the early storage time signals that it is necessary to fit the data with a sum of asymmetric Lorentzian functions. In later storage times, the charge states are sufficiently overlapped that it is again necessary to fit the TOF signal with multiple $L_a(t)$ functions in order to extract the fraction of the signal that corresponds to a particular charge state.

An example of a short storage time TOF signal for Ar^{13+} is shown in Fig. 4.18b. This signal is obtained at a storage time of 1 ms, when the charge state is entirely Ar^{13+}. It is possible to fit the data to a sum of three $L_a(t)$ functions given by

$$f_3(t) = L_{a1}(t) + L_{a2}(t) + L_{a3}(t) \tag{5.11}$$

where $L_{a1}(t)$ corresponds to the early arrival time component of the signal, $L_{a2}(t)$ corresponds to the mid-time arrival component, and $L_{a3}(t)$ corresponds to the late time arrival component. Each function $L_{ai}(t)$, has a corresponding amplitude A_i, arrival time t_{oi}, width γ_{oi}, and asymmetry parameter c_i; where the subscript i refers to component 1, 2, and 3.

The ion signal is fit using a commercial software package (IDL) which employs a Levenberg-Marquardt non-linear least squares technique described in [55]. The corresponding number of ions is obtained by integrating the fitted function, $f_3(t)$, where the expression is similar to Eq. (3.7) and is given as

$$N = \frac{1}{QG_{TOF}R_{pre}G_{pre}} \int_{t_1}^{t_2} f_3(t)\, dt \tag{5.12}$$

where the detector gain factors are determined by the hardware settings described in §3.4.2. An example of an Ar^{13+} TOF signal and corresponding fit to $f_3(t)$ is shown in Fig. 5.13. The storage time here is 1 ms and the base pressure in the trap is 8.1×10^{-10} torr. The integrated ion number obtained from the fit is 294, which is consistent with the number obtained using numerical integration with Eq. (3.7).

As the ion storage time increases, the lineshape changes such that the function $f_3(t)$ no longer reliably fits the data. This condition occurs when the early arrival peak amplitude drops to zero. Therefore, the TOF signal is fit with the sum of two $L_a(t)$ functions,

$$f_2(t) = L_{a1}(t) + L_{a2}(t) \tag{5.13}$$

where $L_{a1}(t)$ corresponds to the strong observed peak and $L_{a2}(t)$ corresponds to the long-time shoulder that continues to be observed.

An example of an Ar^{13+} TOF signal and corresponding fit to $f_2(t)$ is shown in Fig. 5.14. The storage time here is 50 ms and the base pressure in the trap is 8.1×10^{-10} torr. The integrated ion number obtained from the fit is 263, which is consistent with the number obtained using numerical integration with Eq. (3.7). One possible explanation for the observed change in the lineshape of the TOF peak may be associated with the temperature and spatial distribution of the ion cloud while in the trap. These issues will be addressed in the remaining sections of this chapter.

The cases of 1 ms storage and 50 ms storage are chosen to illustrate the ability of the asymmetric Lorentzian function to fit the observed TOF lineshape when there is a single charge state present in the trap. As the storage time increases, Ar^{13+} ions

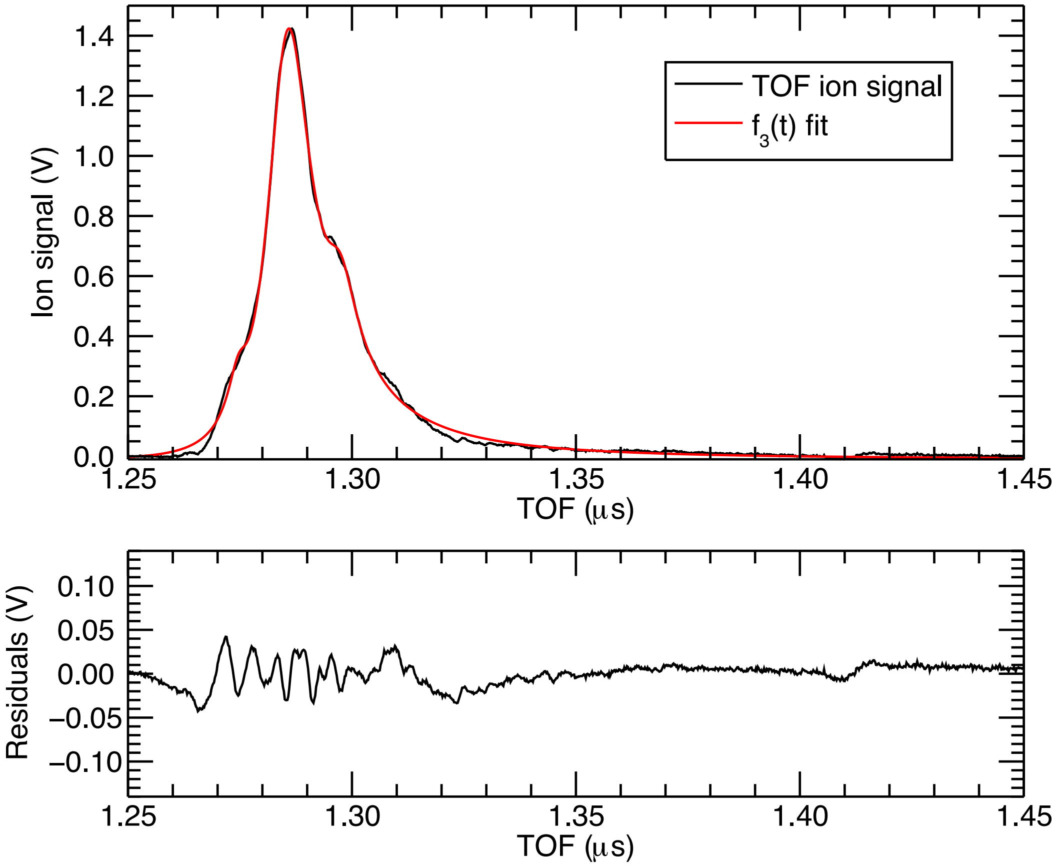

Figure 5.13: Fit of the three asymmetric Lorentzian function, $f_3(t)$, to an Ar^{13+} ion signal obtained after 1 ms of storage at a base pressure of $P = 8.1 \times 10^{-10}$ torr. The integrated number of ions obtained from the fit is 294 which is consistent with the number obtained via numerical integration of 296.

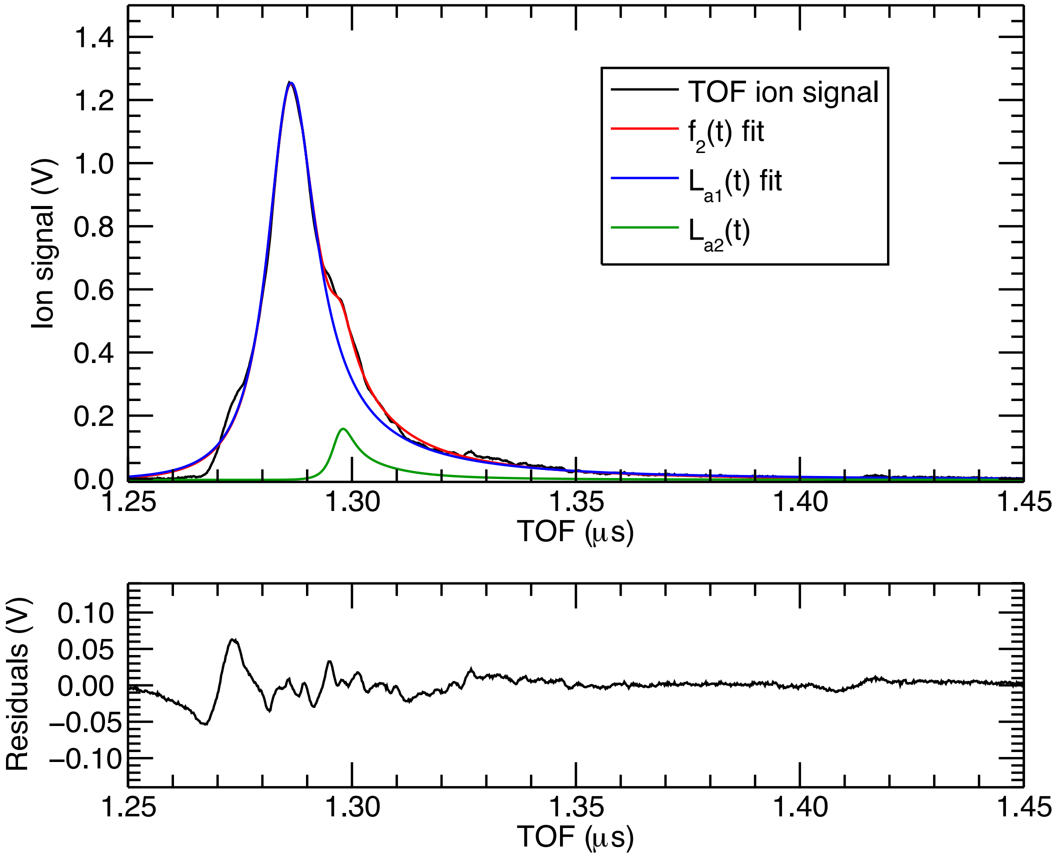

Figure 5.14: Fit of the two asymmetric Lorentzian function, $f_2(t)$, to an Ar^{13+} ion signal obtained after 50 ms of storage at a base pressure of $P = 8.1 \times 10^{-10}$ torr. The integrated number of ions obtained from the fit is 263 which is consistent with the number obtained via numerical integration of 264.

begin to undergo charge exchange reactions with the background gas in the chamber, as shown in Fig. 5.10. Fitting the TOF signal is very important between 100 ms and 1.25 s, when the background pressure is 8.1×10^{-10} torr, where a significant fraction of the ion signal is unresolved in time. An example of an ion signal with charge exchange present and a fit to the data using $f_2(t)$ (see Eq. (5.13)) is shown in Fig. 5.15. Here $L_{a1}(t)$ corresponds to Ar^{13+} ions and $L_{a2}(t)$ corresponds to Ar^{12+} ions. The ion storage time is 500 ms and the base pressure in the chamber is again 8.1×10^{-10} torr. The integrated number of ions in the Ar^{13+} peak is 114. At storage times greater than 1.25 s, the TOF peaks become sufficiently separated and the technique of integrating a fixed window in time becomes valid.

The ion storage lifetime has been measured for Ar^{13+} using the fitted peak results from $f_3(t)$ and $f_2(t)$, as well as fixed width numerical integration, where appropriate, to determine the detected ion number. An example of the ion storage lifetime for Ar^{13+} at a base pressure of 8.1×10^{-10} torr is shown in Fig. 5.16. The measured ion storage lifetime, $\tau_{loss} = 578(17)_{\mathrm{stat}}(10)_{\mathrm{syst}}$ ms, is obtained for an applied potential difference of $V_o = 30$ V and a capture float potential of $V_c = 2926$ V; here $\chi^2/\nu = 0.92$. The systematic uncertainty is estimated by performing the TOF peak integration using a fixed time window (see method in §5.1.2) and using the fitted lineshape and then comparing the results. Here the ion storage lifetime obtained with the two methods differs by 10 ms.

The trap storage lifetime can be measured as a function of the background trap pressure. An example of a measurement for Ar^{13+} is shown in Fig. 5.17. Here the applied trapping potential is $V_o = 30$ V and capture float potential is

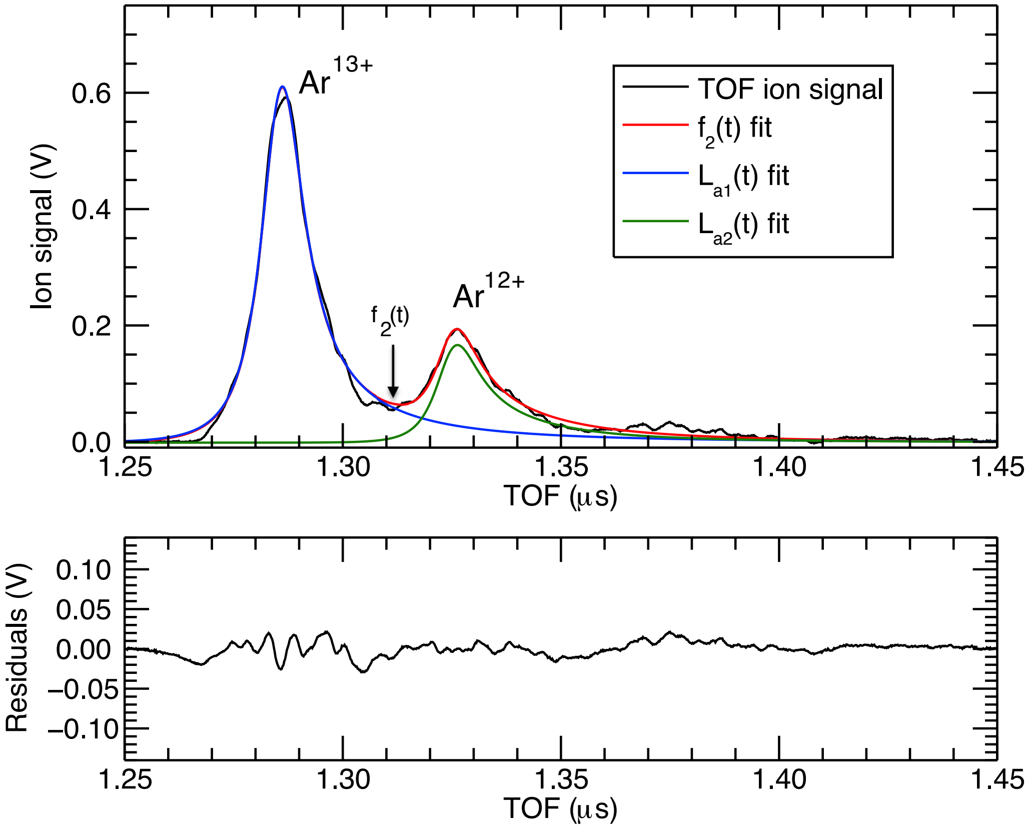

Figure 5.15: Fit of $f_2(t)$ containing two asymmetric Lorentzian functions to an Ar^{13+} and Ar^{12+} ion signal. The storage time was 500 ms and the chamber pressure was 8.1×10^{-10} torr. The integrated number of Ar^{13+} ions obtained from the component $L_{a1}(t)$ fit result is 114.

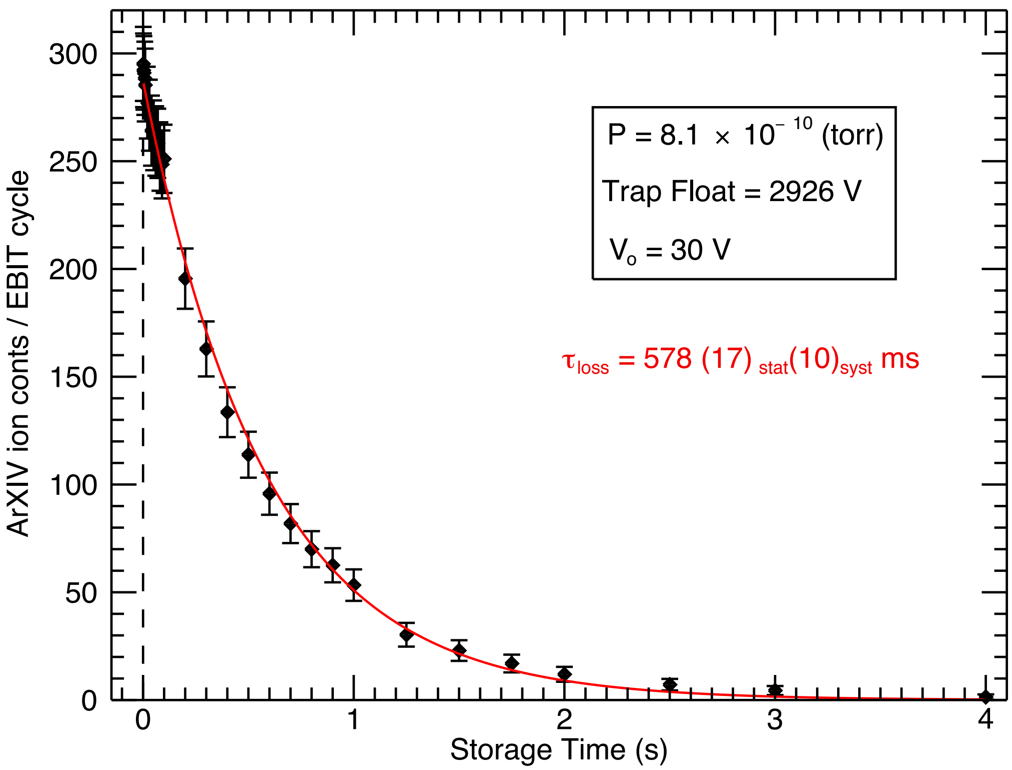

Figure 5.16: Measured storage lifetime for Ar^{13+}. The background pressure in the system was 8.1×10^{-10} torr. The measured ion storage lifetime is $\tau_{st} = 578(17)_{\mathrm{stat}}(10)_{\mathrm{syst}}$ ms.

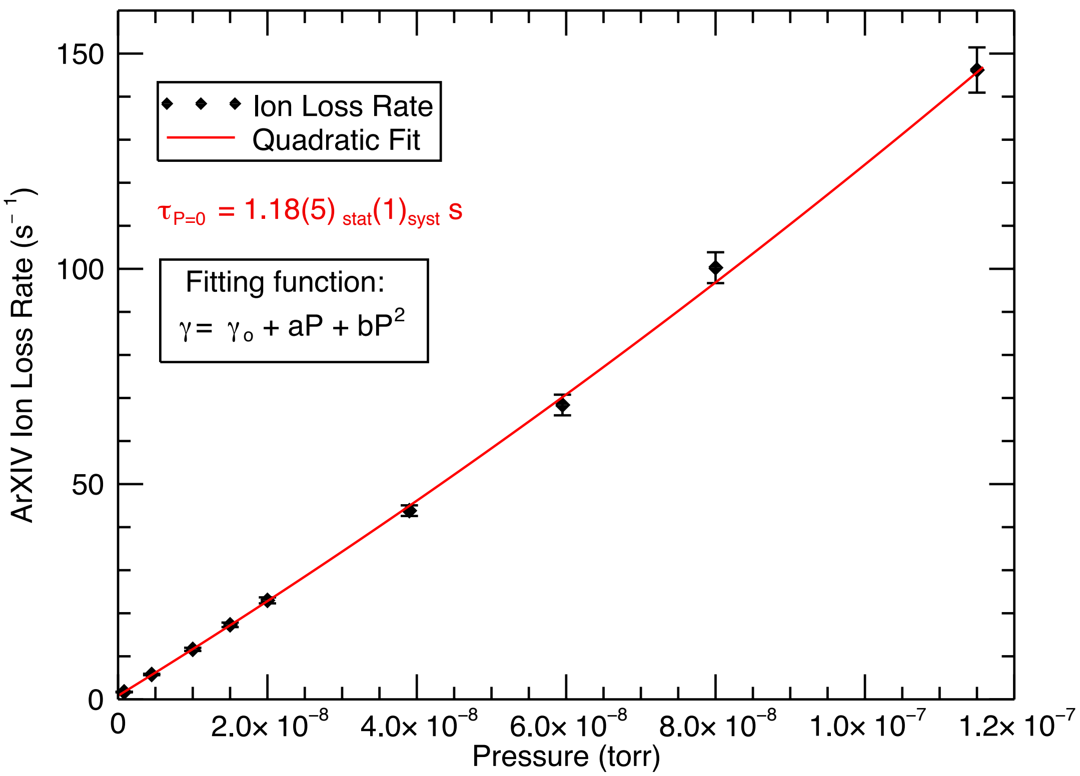

Figure 5.17: Pressure dependent ion loss measurement for Ar^{13+} storage.

$V_c = 2926$ V. The pressure-extrapolated ion loss lifetime is $\tau_{P=0} = 1.18(5)_{\mathrm{stat}}(1)_{\mathrm{syst}}$ s; here $\chi^2/\nu = 0.93$. For comparison, a linear fit yields $\chi^2/\nu = 1.20$. Again, the systematic uncertainty is estimated by comparing the result obtained using the fixed integration widow technique and the lineshape fitting technique. The inverse of the zero-pressure storage lifetime is taken to be the inherent ion cloud expansion rate due to trap instabilities that depend on ion charge-to-mass, trap imperfections, and applied trapping potential. The expansion rate is also, in principle, a function to the ion cloud temperature. The ion cloud temperature is addressed in the following section.

5.2 Temperature of captured ions

The thermal energy of captured ions, stored in the Penning trap, is of general interest for a wide range of measurements, including spectroscopic measurements on isolated ions. For example, Doppler broadening due to thermal motion of an ion can be an important source of uncertainty in precision measurements. The thermal energy of the captured ion cloud is also important for investigating ion-ion and ion-neutral collisions. In addition, the ion cloud shape and size is related to the temperature. The cloud shape is important for interpretation of the time-of-flight lineshape. This section examines the ion cloud temperature both immediately after capture, as well as the temporal evolution as a result of collisions with neutral background gas.

5.2.1 Slow ion ejection energy measurements

We are interested in the thermal energy of stored ions; however, current limitations do not allow non-destructive, in-trap measurements to be made. Since the primary detection technique used is through ejection of the stored ions to the TOF detector, we have adopted a technique developed in high-field Penning traps [14]. In high-field traps, the ion energy is measured by slowly lowering the axial potential well and correlating the arrival of ions at a detector with the applied voltage on the electrode. This method relies in part on the presence of a strong magnetic field, along the long trap axis, to ensure ions are not lost to the electrode walls as they exit the trap. In addition, in long traps made of stacks of many electrodes, the minimum of the trapping well remains fairly fixed in space, along the trap axis. In the case of the compact Penning trap, the axial magnetic field drops rapidly, inside the BEC electrode; also the potential well minimum can shift by a significant fraction of z_o when the trap is biased asymmetrically.

The ion optics for ejected ions is optimized to maximize the detected ion signal. In the interests of minimizing transport losses during the energy measurement, the ring electrode has been used to allow the ions to escape from the trap. An example of the ion arrival at the detector as a function of the ring ramp time is shown in Fig. 5.18 The ion cloud energy, 1 ms after capture, has been measured by slowly ramping the trap ring electrode voltage up, decreasing the axial potential well, and allowing ions to spill out of the trap. The transit time for an ion leaving the trap and arriving at the TOF detector is ≈ 1.2 μs. Since the ring electrode potential is

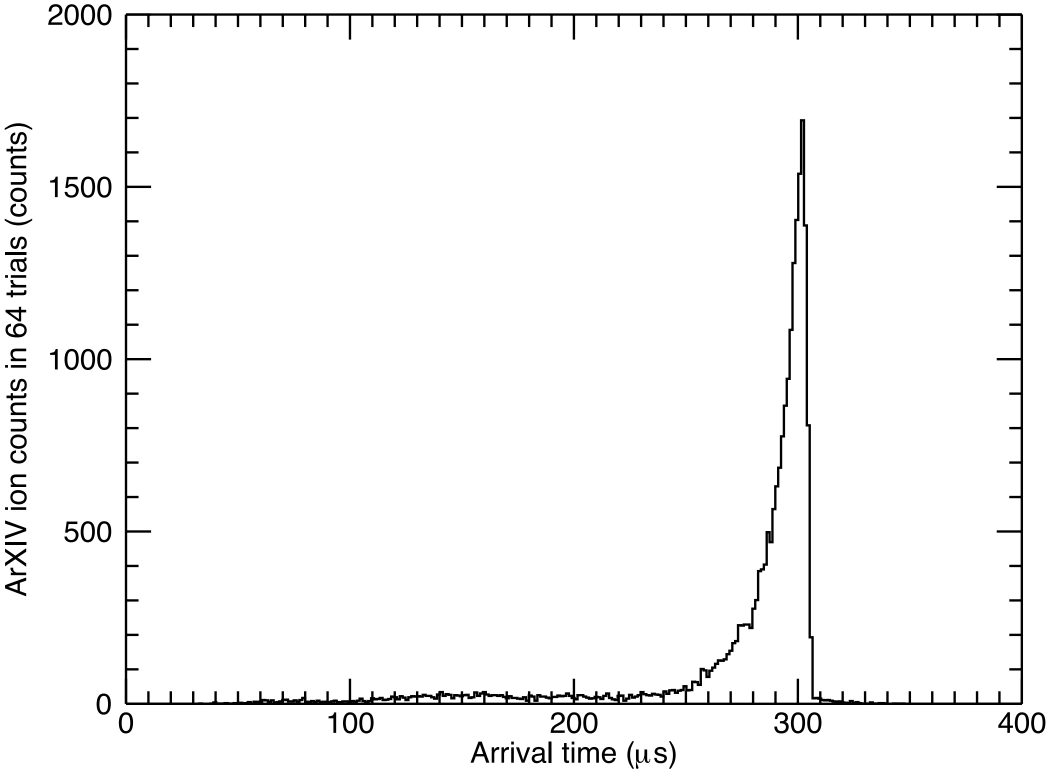

Figure 5.18: ArXIV ion arrival measurement during a slow ramp extraction.

slowly ramped at a rate of 0.1V / μs it is possible to correlate the arrival time of ions at the TOF detector with the applied voltage. The TOF detector was operated in the fully saturated event-counting mode, with a detector bias voltage of -1700 V. The detected ions were counted using a fast multichannel scalar (SRS–SR430) that was triggered to begin acquisition when the ring electrode began ramping.

The applied potential ramp is shown in Fig. 5.19. To correlate the applied potential well with the ion energy, the trap well depth is multiplied by the ion charge, Q. As illustrated in Fig. 5.14, at a storage time of 1 ms, the ion population is entirely Ar^{13+}. In order to get a reliable energy scale calibration it is necessary to measure the temperature at short storage times before charge exchange reactions take place.

The results of an ion energy measurement are shown in Fig. 5.20. Given the applied voltage on the ring and endcap electrodes, the axial well depth was calculated at each time step of the measurement. For the two-magnet trap, the actual well depth is determined to be

$$\Delta V = 0.388 V_o. \tag{5.14}$$

The calculated on-axis potential well is used to correlate the ion energy with the number of ions arriving at the TOF detector. The observed ion energy distribution has a thermal energy width of 5.5 ± 0.5 eV. This captured ion energy represents a factor of ≈ 60 reduction in the ion temperature from inside the EBIT [31]. This measurement gives the initial ion cloud temperature before any active cooling techniques have been applied to the cloud. One can expect that much colder clouds can

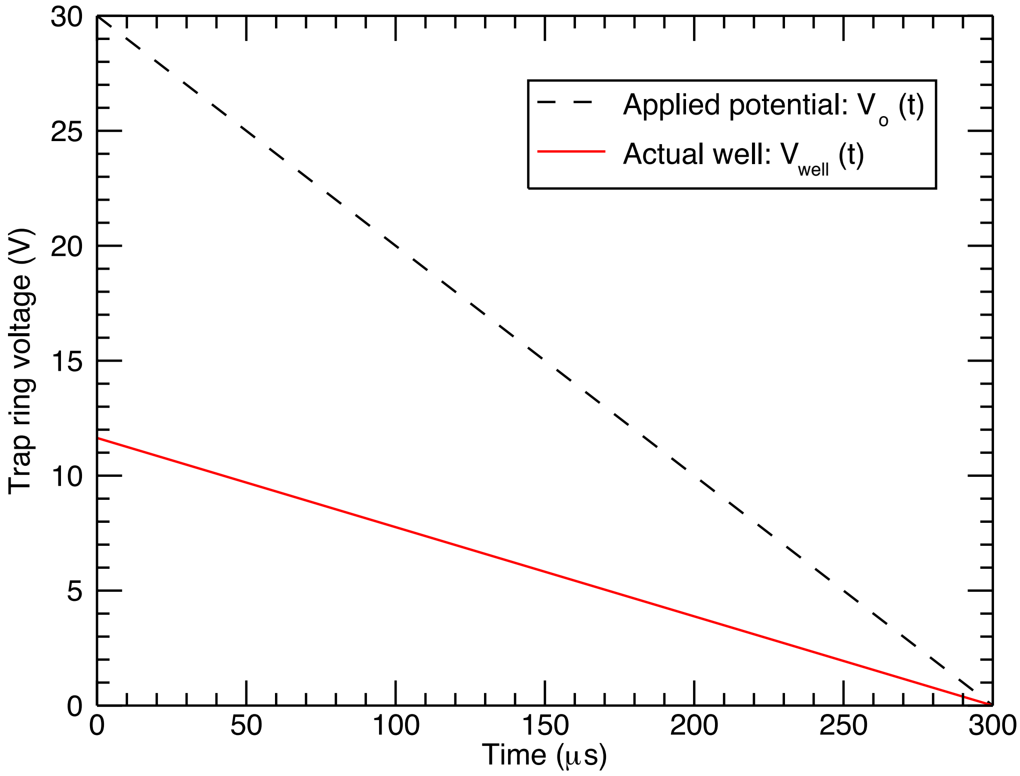

Figure 5.19: Applied axial potential $V_o(t)$ employed in slow ramp extraction and the calculated axial potential well depth, $\Delta V(t)$ ($\mathrm{V}_{\mathrm{well}}(t)$).

be achieved if evaporative or sympathetic cooling techniques are applied.

5.2.2 Buffer-gas narrowing of the TOF linewidth

The TOF linewidth contains information about the ion cloud shape and temperature. The thermodynamics of an ionized gas that influence the ion cloud shape and temperature are addressed in detail in §6.2. Intuitively, the ion cloud axial size is essentially set by the thermal energy and the trapping fields. Due to the

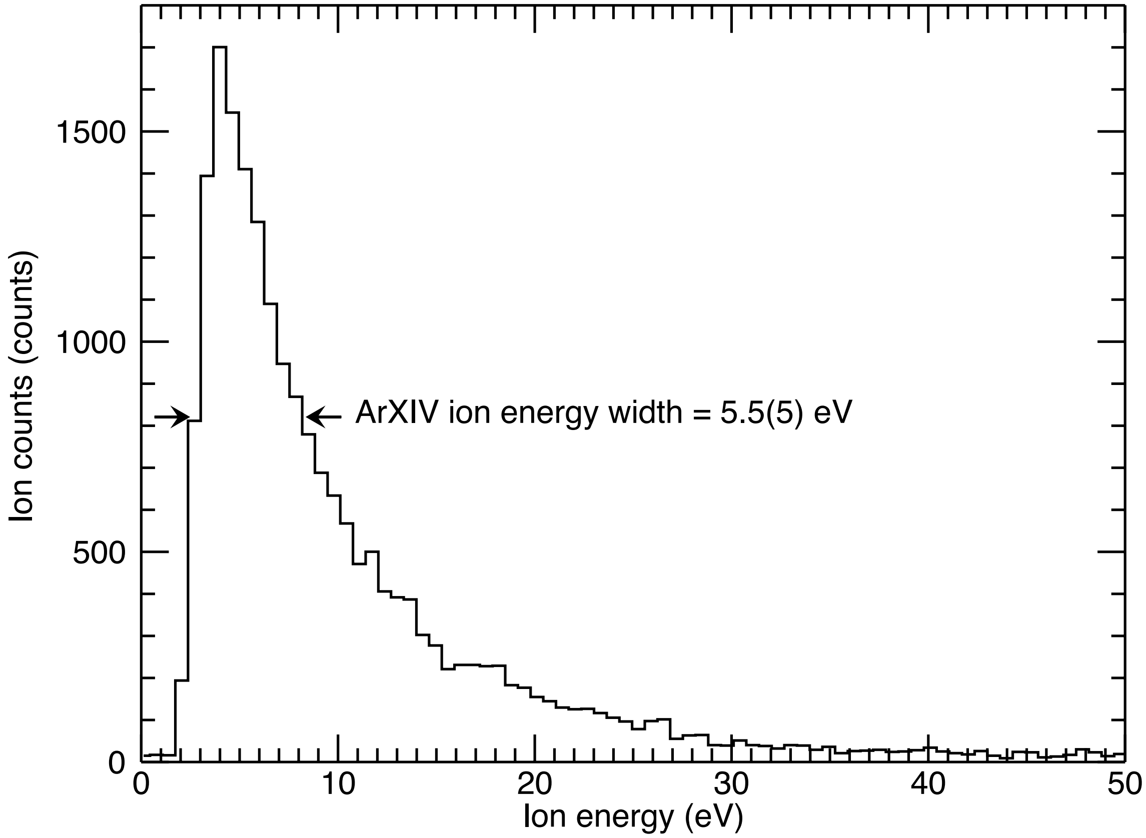

Figure 5.20: ArXVI ion temperature measurement after 1 ms of storage. The measured ion energy width is 5.5(5) eV, corresponding to a trap axial well depth of $\Delta V = 0.42$ V.

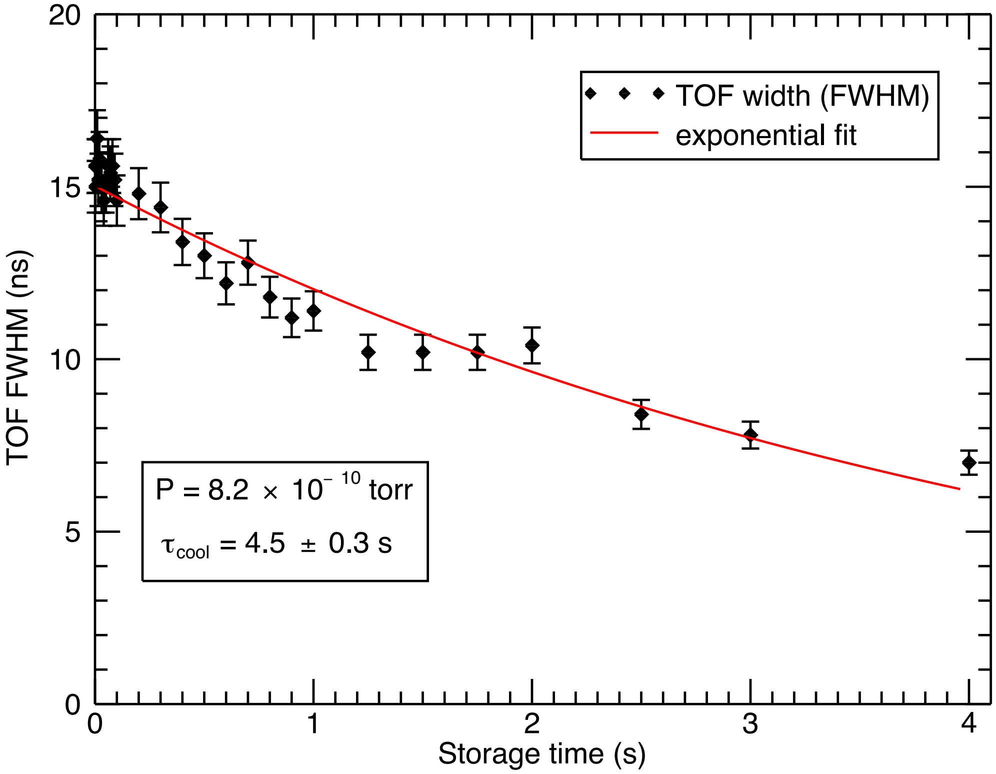

Figure 5.21: Narrowing of the Ar^{13+} TOF width as a function of time. The background gas pressure was 8.2×10^{-10} torr, with measured cooling lifetime of 4.5 ± 0.3 s.

trap axial potential well, an ion requires more energy to be located in a position farther from the trap center. A narrowing in time of the TOF width implies a cloud that is axially less extended than the captured cloud. Therefore, the narrower TOF width suggests a lower ion cloud temperature. An example of narrowing of the TOF linewidth of Ar^{13+} ions is shown in Fig. 5.21. The background gas pressure here is 8.2×10^{-10} torr. The time variation of the TOF linewidth has been fit to a single exponential function, yielding a time constant of 4.5 ± 0.3 s.

A similar phenomenon of TOF line narrowing has been observed in heavy-ion experiments in an RFQ trap [10]. In RFQ experiments, high pressure buffer gasses have been used to cool incoming ion beams and stored ion clouds through collisions with the buffer gas. If we interpret the TOF narrowing in Fig. 5.21 as buffer gas cooling, with rate Γ_c, then for the case of Ar^{13+}, $\Gamma_c = 0.22 \pm 0.01\ \text{s}^{-1}$. This cooling rate depends on the mobility of the ion, which is discussed in §5.2.3.

5.2.3 Ion mobility data

Buffer-gas cooling of trapped ions depends upon the ion mobility [71]. The ion mobility can be related to the drag force on ions in a Penning trap [72] which in turn leads to an exponential radial ion expansion rate. Ion transport theories indicate that ion mobility improves with lower temperature [73]. For a swarm of ions in the presence of a background gas with density N and temperature T, the mobility is given by [73]

$$K \equiv \frac{v_d}{E} = \frac{3q}{N}\left(\frac{\pi}{2mk_BT_{eff}}\frac{m+M}{M}\right)^{1/2}\left(\frac{1+\alpha}{\Omega^{(1,1)}(T_{eff})}\right) \tag{5.15}$$

where v_d is the ion drift velocity, E is the electric field in which the ions move, q is the ion charge, k_B is Boltzmann's constant, m is the ion mass, M is the neutral particle mass, and $\Omega^{(1,1)}(T)$ is the temperature-dependent momentum transfer collision integral [74]. The effective ion temperature, T_{eff} is given by [73]

$$3/2k_BT_{eff} = 3/2k_BT + 1/2Mv_d^2(1+\beta) \tag{5.16}$$

where α and β are correction terms which are typically smaller than 0.1 [73]. The set of ion mobility equations are solved recursively; a theoretical treatment requires knowledge of the initial conditions of the ion cloud.

Although we cannot measure the ion mobility directly, the ion cooling rate can be inferred as shown in §5.2.2, which gives the observed buffer-gas cooling rate Γ_c for Ar^{13+} as a function of injected N_2 gas pressure. To investigate the effect of ion mobility on the buffer gas cooling rate the background gas pressure has been varied over two orders of magnitude. The pressure-dependent ion cooling rate for Ar^{13+} is shown in Fig 5.22. It is obtained from the reciprocal of the fitted buffer-gas cooling time at each N_2 gas injection pressure. The pressure-dependent ion cooling rate has been fit to both a linear and quadratic function, with the quadratic fit giving a more

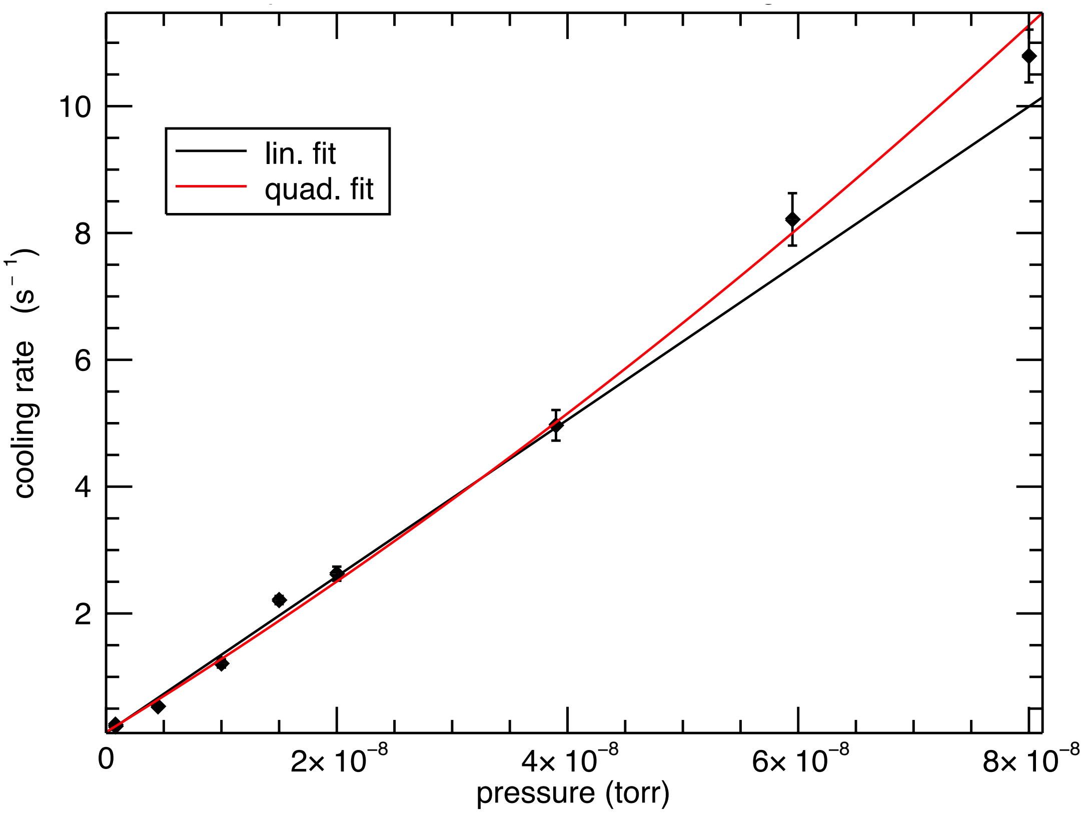

Figure 5.22: Ar^{13+} cooling rate as a function of pressure. The applied axial potential was $V_o = 30$ V.

accurate description. Here $\chi^2/\nu = 1.1$ for the quadratic fit and $\chi^2/\nu = 1.4$ for the linear fit. With the low buffer gas pressures, roughly four orders of magnitude lower than those used in RFQ experiments [10], the ion cooling rates observed here for low pressure are modest. Nevertheless, ion mobility improves with lower temperature, as Eq. (5.16) indicates. This implies that ion cloud expansion should be slower at lower temperatures. Our observations are consistent with this expectation. Figure 5.9 shows that ion cloud expansion is slower in a $\Delta V = 10$ V well depth than in a $\Delta V = 40$ V well depth; TOF analysis indicates that the ion cloud in the $\Delta V = 10$ V well is colder. A comparison of the TOF width at these two well depths is shown in Fig. 5.23. The $\Delta V = 10$ V data shows a factor of ≈ 2 reduction in the measured TOF width compared to the $\Delta V = 40$ V case. Ions in the deeper potential well ($\Delta V = 40$ V) exhibit narrowing of the TOF width similar to that shown in Fig. 5.21. Ions in the shallower potential well ($\Delta V = 10$ V) exhibit a TOF width which is essentially unchanged during storage.

5.3 Discussion

The storage lifetime, temperature, and charge state evolution have been characterized here for some ions of interest, in both the one-magnet and two-magnet Penning traps. Confinement of ions is demonstrated for a range of trapping well depths ranging from applied axial potentials of 10 V – 40 V. In these room-temperature traps, ion confinement times of ≈ 1 s have been achieved for a variety of ions, captured at beam energies ranging between 2.5 keV/Q and 4.0 keV/Q, where Q is the

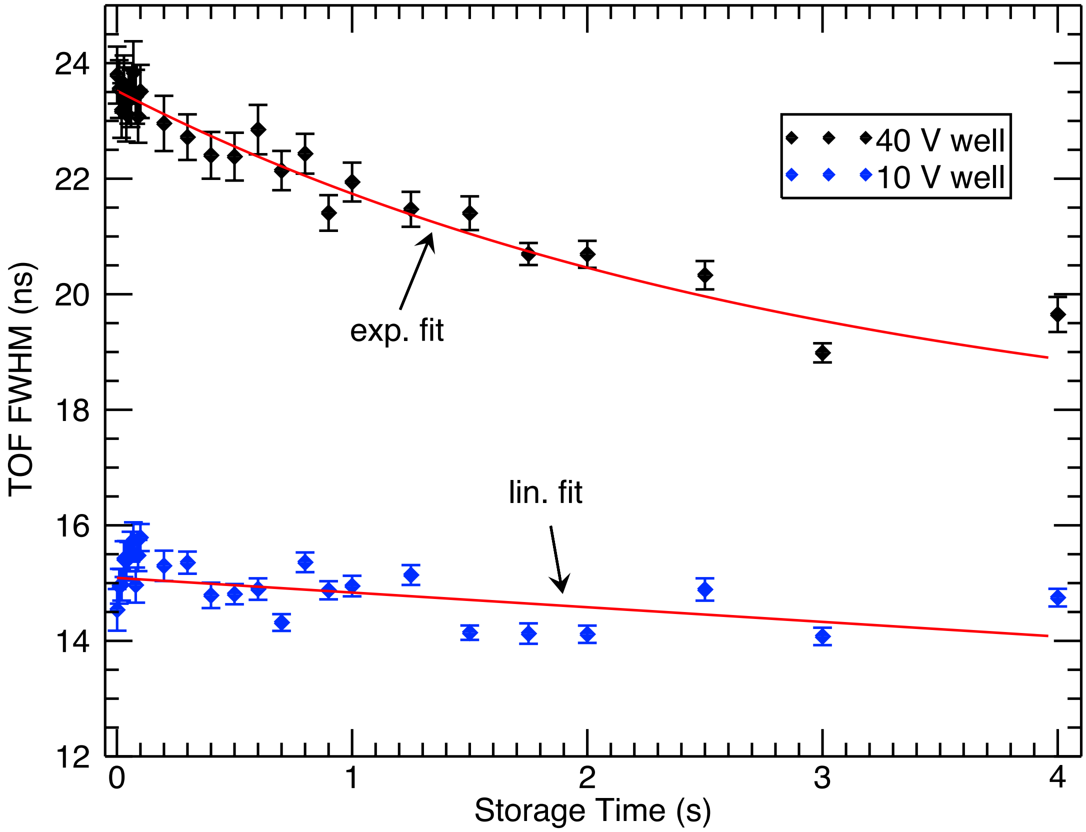

Figure 5.23: Ne^{10+} TOF width for $\Delta V = 10$ V and $\Delta V = 40$ V. Ions in the deeper potential well ($\Delta V = 40$ V) exhibit narrowing of the TOF width similar to that shown in Fig. 5.21. Ions in the shallower potential well ($\Delta V = 10$ V) exhibit a TOF width which is essentially unchanged during storage.

ion charge state.

Experiments with the one-magnet Penning trap indicate that the electrode alignment is sufficient to provide long confinement times, limited by background gas pressure. This is a major milestone for developing more sophisticated unitary Penning traps. Given the ease of construction, operation, and low cost of production, the one-magnet unitary Penning trap may find other applications in both laboratory and field-deployed instrumentation. In general, ion capture tends to be more resource intensive and technically challenging than in-trap loading of low charge state ions. The deployment of the one-magnet Penning trap at the EBIT facility at NIST has demonstrated the usefulness of unitary architecture in applications with severe space constraints.

The two-magnet trap and apparatus incorporated new features and improvements: in particular, the addition of the time-of-flight MCP detector to provide accurate ion counting and facilitate studies of the charge-state evolution inside the trap. The cases of ion capture of Ne^{10+} and Ar^{13+} have been presented in detail to illustrate the fully-resolved and unresolved TOF signals. With the ability to investigate charge-state evolution at low energy in a controlled environment, the two-magnet Penning trap apparatus could be useful in studies of interest in astronomy, collision theory, and plasma diagnostics. With further technical improvements in the high voltage control systems, operation at a lower extraction float voltage may lead to higher TOF resolution.

Before the application of any cooling technique, the temperature of Ar^{13+} ions captured in the two-Magnet Penning trap is ≈ 5.5 eV, a significant reduction in thermal energy when compared to $\approx$ 350 eV inside an EBIT ion source [31]. In short, the effective starting energy for measurements in the Penning trap has been reduced by a factor of 60. In addition to the initial thermal energy reduction from ion capture, a measurable buffer-gas cooling has been observed even for low pressures in the form of narrowing of the TOF lineshape. Initial measurements indicate collisions with residual background gas tend to narrow the TOF linewidth at a rate of $\Gamma_c \approx 0.2$ ns / s (FWHM / storage time). Further investigation into the thermal evolution of the ion cloud is necessary to extract precise cooling rates.

Chapter 6

Model of the Stored Ion Cloud

6.1 Overview

The dynamics of a single ion in a trap has been presented in Ch. 2; the thermodynamical behavior of a collection of interacting ions stored in a trap is presented in a model here. Numerical computations are compared with time-of-flight data to develop a simple model. This model provides a rough understanding of observed TOF features, a consistency check for temperature determinations, as well as ion cloud characteristics of interest in some experiments. The long-time ($\approx$ 1 s) ion cloud expansion, for example, is important in the measurement of radiative lifetimes of metastable states. In particular, the ion cloud expansion rate is included as a correction to the measured lifetime of the $^2P_{3/2}$ state in Ar^{13+}, presented in Chapter 7.

Ions loaded into the two-magnet Penning trap will undergo collisions both with each other (ion-ion) and with background gas particles (ion-neutral). The effects of ion-neutral collisions (elastic collisions, charge-exchange, etc.) on the ion storage lifetime have been investigated in Ch. 5. The ion-ion (Coulomb repulsion) interaction upon capture brings about thermal equilibrium if sufficient time has lapsed for collisions to thermalize the ion cloud. An estimate of the single species thermalization time in seconds, derived by Spitzer [75], is given by

$$t_c = \frac{11.4 A^{1/2} T^{3/2}}{n Z^4 \ln \Lambda} \tag{6.1}$$

where T is the temperature of the ion cloud in Kelvin, A is the atomic mass number, Z is the ion charge number, $\ln \Lambda$ is the Coulomb logarithm, and n is the particle density given in cm^{-3}. For ion densities of $\approx 10^4$ cm^{-3}, corresponding to roughly 300 – 1000 trapped ions in the two-magnet trap, thermalization times ranging from $t_c \approx 30$ ms to $t_c \approx 9$ ms are estimated for Ar^{13+} ion clouds with $T \approx 64,000$ K ($k_B T = 5.5$ eV). The thermalization time is short compared to the measured ion cloud expansion times presented in §5.1.3. Therefore, a model assuming thermal equilibrium can be useful for predicting ion cloud characteristics for long time scales.

6.2 Thermal Equilibrium

A numerical study of the ion cloud conditions has been carried out, to understand the shape and density of ion clouds in the two-magnet Penning trap. The analytic form of the ion cloud distribution inside the trap is not easily attainable, if at all. Therefore, numerical computations using the EQUILSOR code [76], developed by Spencer, *et. al.* have been carried out to solve for the ion cloud density distribution in the two-magnet Penning trap. The EQUILSOR code is based upon Poisson's equation

$$\nabla^2 \phi = -\frac{Q}{\epsilon_o} n(r, z) \tag{6.2}$$

where Q is the charge of the ion, and the ion cloud spatial density, $n(r, z)$ is a function of the total potential ϕ, in turn. Thus, Eq. (6.2) is a non-linear, partial differential equation for the electric potential ϕ. The thermodynamic relation between the density and the potential $\phi(r, z)$ is discussed in §6.4.

Calculations for a single ion species have been performed, since ions extracted from the NIST EBIT are charge-state selected before isolation in a Penning trap. The trap electrodes are assumed to be cylindrically symmetric, coaxial, and positioned in a region of uniform magnetic field. The ion cloud is assumed to be in thermal equilibrium. The code uses a finite difference Newton SOR (simultaneous over-relaxation) method [55] to solve for the potential and the ion density distribution. Various tests of the code have been performed including a low-temperature electron cloud calculation presented in §6.5.

When an ion cloud is in thermal equilibrim, the electrodynamics of the system – whether it behaves as a gas or a plasma – depends upon the cloud size relative to the Debye length (§6.4 Eq. (6.6)). A case of experimental interest is considered here. Based on measurements of the ion cloud temperature and the number of detected ions, Fig. 6.1 shows the computed ion distribution for Ar^{13+} at a temperature of 5.5 eV and $N = 300$, with a central density $n_o \approx 4.6 \times 10^{11}\ \mathrm{m}^{-3}$. At a temperature of 5.5 eV, the Debye length, (See Eq. (6.6)) $\lambda_D \approx 2$ mm, which is roughly the size of the ion cloud itself. Since the density is not uniform, the ion cloud size is characterized by the width of the distribution evaluated at the half height. The radial and axial dimensions of the ion cloud are referred to as r_o and z_o, respectively. The radial profile of the 300 ion cloud is shown in Fig. 6.2 (black), as well as the cases of 500, 700, and 1000 ions. Due to the high temperature and low number of particles in the ion cloud, the radial size is much smaller than the Debye length.

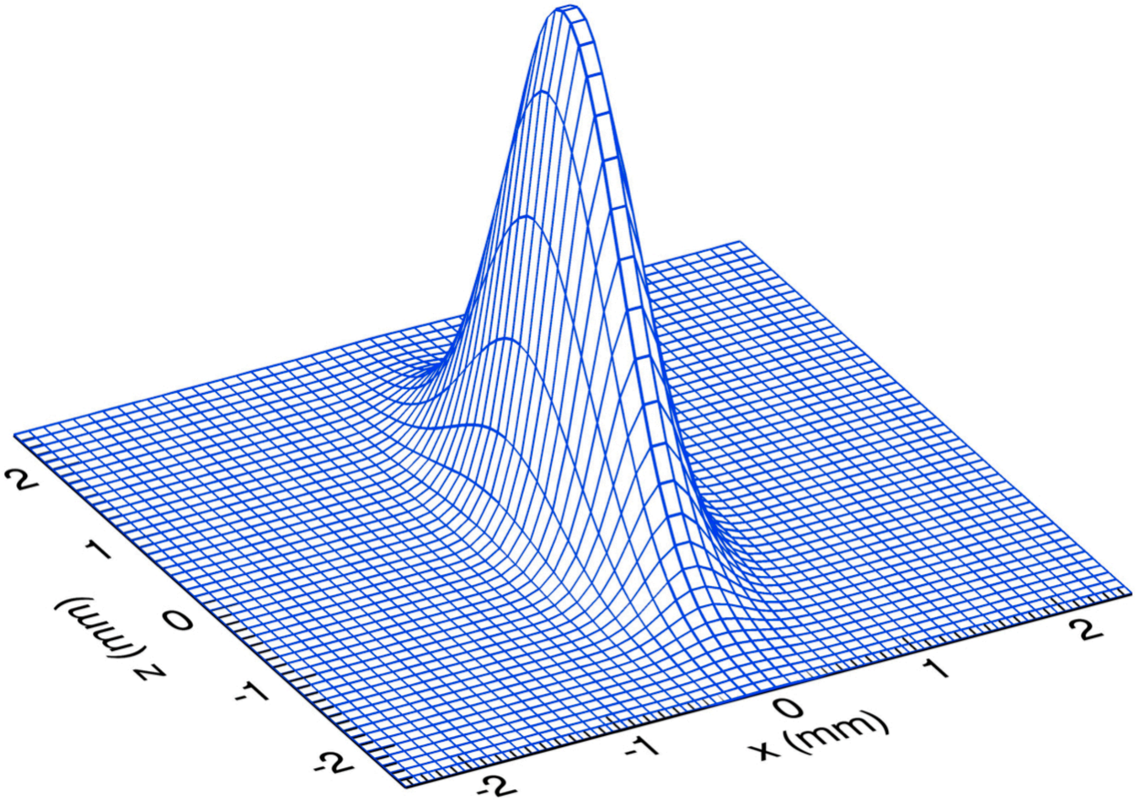

Figure 6.1: EQUILSOR computation of Ar^{13+} ion cloud density $n(r, z)$. Given an ion number $N = 300$ and cloud temperature $T = 5.5$ eV, the central density is $n_o \approx 4.6 \times 10^{11}$ m^{-3}.

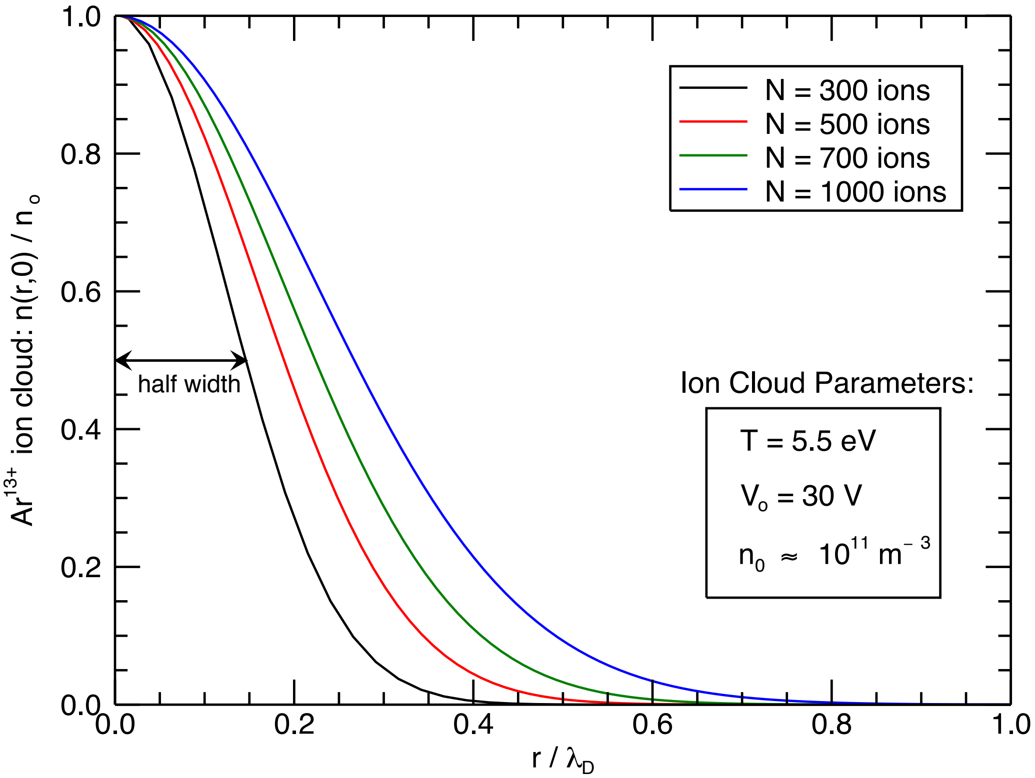

Figure 6.2: Radial distribution of Ar^{13+} ions in the two-magnet trap, calculated using the EQUILSOR code. The number of ions ranges from $N = 300$ to $N = 1000$, the central density, $n_o \approx 10^{11}$ m^{-3}, and the ion cloud temperature is $T = 5.5$ eV.

On the other hand, the corresponding axial density profile is shown in Fig. 6.3. For an applied trap voltage of $V_o = 30$ V computations yield an ion cloud aspect ratio, $\alpha \equiv z_o/r_o = 2.85$. The axial size of the ion cloud is essentially set by the temperature; for simplicity, only the case for $N = 300$ ions is shown. Here the axial ion cloud size is not much smaller than the Debye length: $\lambda_D \geq z_o$.

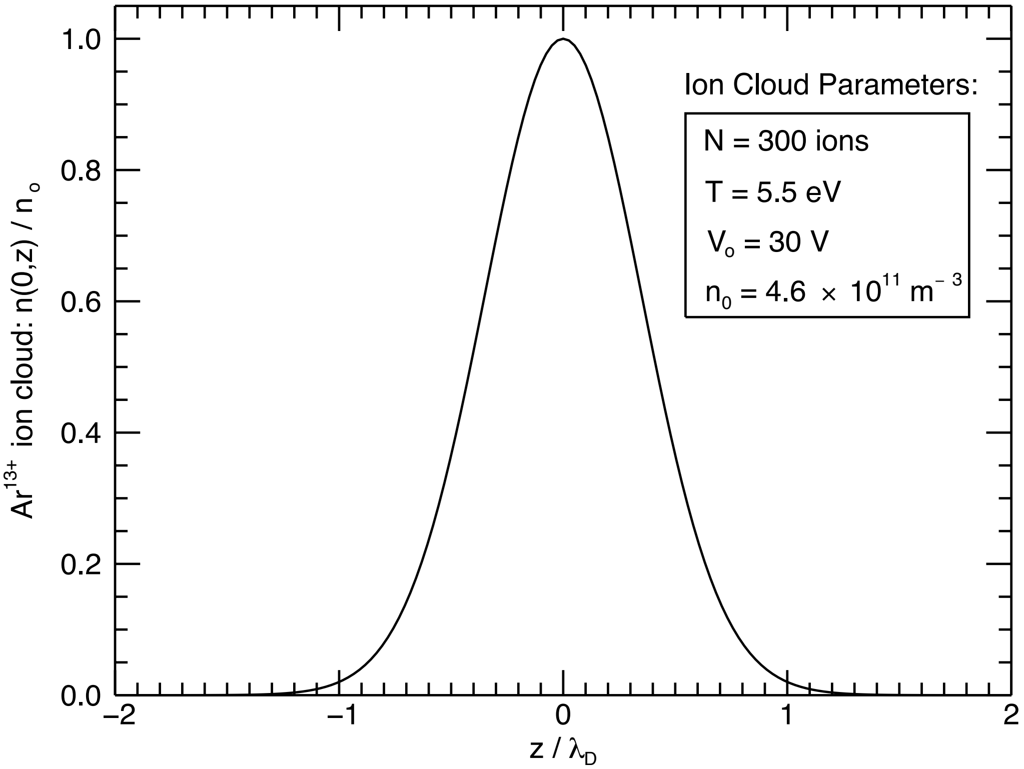

Figure 6.3: Axial distribution of Ar^{13+} ions in the two magnet trap, calculated using the EQUILSOR code. The number of ions is $N = 300$, the central density, $n_o \approx 4.6 \times 10^{11}$ m^{-3}, and the ion cloud temperature is $T = 5.5$ eV. The axial size of the ion cloud is essentially set by the temperature. Only the case for $N = 300$ ions is shown for simplicity.

6.3 Ion transport: computations and TOF data

Information about the ion cloud shape, size and temperature can be obtained by properly interpreting the TOF data obtained when ions are ejected from the trap rapidly. In principle, when the BEC electrode (Fig. 4.2) is switched quickly (≈ 50 ns), the spatial and velocity information about the stored ions dictates the ion transport to the detector and hence can be extracted from the TOF lineshape. Consider a static ion distribution in the trap, (r_1, z_1, t_1), it is possible to define a transfer function, $F_I(r : r_1, z : z_1, t : t_1)$, that maps the in-trap distribution to the detector region (r, z, t); ions are detected at time t if they arrive with coordinates (r, z) within the active area of the TOF detector. Formally, the transfer function can be written as

$$N_D(r, z, t) = \sum_{t_1} \sum_{r_1} \sum_{z_1} F_I(r : r_1, z : z_1, t : t_1) N_C(r_1, z_1, t_1) \qquad (6.3)$$

where $N_D(r, z, t)$ is the number density of ions transported to a position, r and z on the TOF detector at a time t, $N_C(r_1, z_1, t_1)$ is the ion number density in the trap as a function of the initial position and time (r_1, z_1, t_1) and can be specified by the thermal density.

In practice, $F_I(r : r_1, z : z_1, t : t_1)$ is a matrix of calculated arrival times and locations for a given initial location inside the trap. Numerical calculations of the ion transport function from the trap to the TOF detector have been performed using the BEM technique [54] and the details will be presented here. Much like the ion capture calculations presented in Ch. 4, single particle trajectories have been calculated for ions originating in the trap and being ejected to the TOF detector. Initially, the trap potentials are set in the storage condition with stored ions distributed at location r_1 and z_1. For the case of Ar^{13+}, the applied electrode potentials are specified in Table 4.1: the applied trapping potential, $V_o = 30$ V. At $t = 0$, a linear voltage ramp is applied to the BEC electrode, with a rise time consistent with the measured switching time of ≈ 50 ns. The fast switching of the BEC electrode causes the ions to leave the trap and move towards the TOF detector. The ion trajectory is integrated through the space containing the trap einzel lens, steering plate sets 2 and 3 and the RF trap / einzel lens electrodes and the TOF detector. In this way, it can be determined if an ion leaving the trap from an position r_1 and z_1 will strike the TOF detector or not, and the arrival time is computed if it strikes the active area of the detector.

A molecular dynamics (MD) type computation would provide the most detailed treatment including velocity distributions. Although feasible, MD simulations can be time-consuming even for 300 ions. To get a simple approximation, a heuristic treatment of the velocity distribution is used here. The initial kinetic energy is specified to be consistent with the measured ion temperature given by

$$KE_o(r,z) = T_c - QV(r,z) \tag{6.4}$$

where T_c is a cut-off ion energy and $V(r,z)$ is the trap potential. From this relation the velocity is also a function of (r,z) unless $QV(r,z) > T_c$, for which $KE_o(r,z)$ is ill-defined. In addition, the CPO software requires $KE_o(r,z) > 0$; therefore, in the case that $QV(r,z) > T_c$, the initial kinetic energy is arbitrarily specified as $KE_o(r,z) << T_c \approx 0$ to allow the inclusion of points in the tail of the density function that require more energy than the fitting parameter T_c allows, while ensuring that ions located near the mid-plane of the trap will have the expected kinetic energies approximated by Eq. (6.4).

Tests have been carried out to find the radial range in which ions can be detected when quickly ejected from the trap. Optimizations of the calculations required the trap space to be divided into a grid of initial r and z values ranging from $-2 < z < 2$ mm and $0.025 < r < 1$ mm with a step size of $\Delta r = \Delta z = 0.05$ mm. For simplicity, the same spatial grid is used in the BEM and EQUILSOR calculations.

An application of the calculated transfer function for the detected r_1 and z_1 positions is shown in Fig. 6.4. It gives the TOF detection field of view. The trap center is located at $z = 0$ mm and the TOF detector is located at $z = 318.859$ mm. Note that ions leaving the trap from positions closer to the BEC electrode are detected for larger initial radial positions. This effect occurs because ions that start near the BEC electrode essentially end up "riding" down the potential as the BEC is switched. As the BEC potential is changed, ions are subjected to a potential gradient across the trap which causes them to move towards the BEC electrode. Ions initially near the FEC electrode are quickly accelerated towards the back of the trap and can end up scattering outwards to the trap walls. However, ions initially near the BEC electrode tend to be moving slower when exiting the trap because the local potential is changing slowly, causing a smaller acceleration out of the trap. These ions can actually end up leaving the trap close to the trap axis, where the transport to the TOF detector is more efficient. In fact, the ions leaving the trap

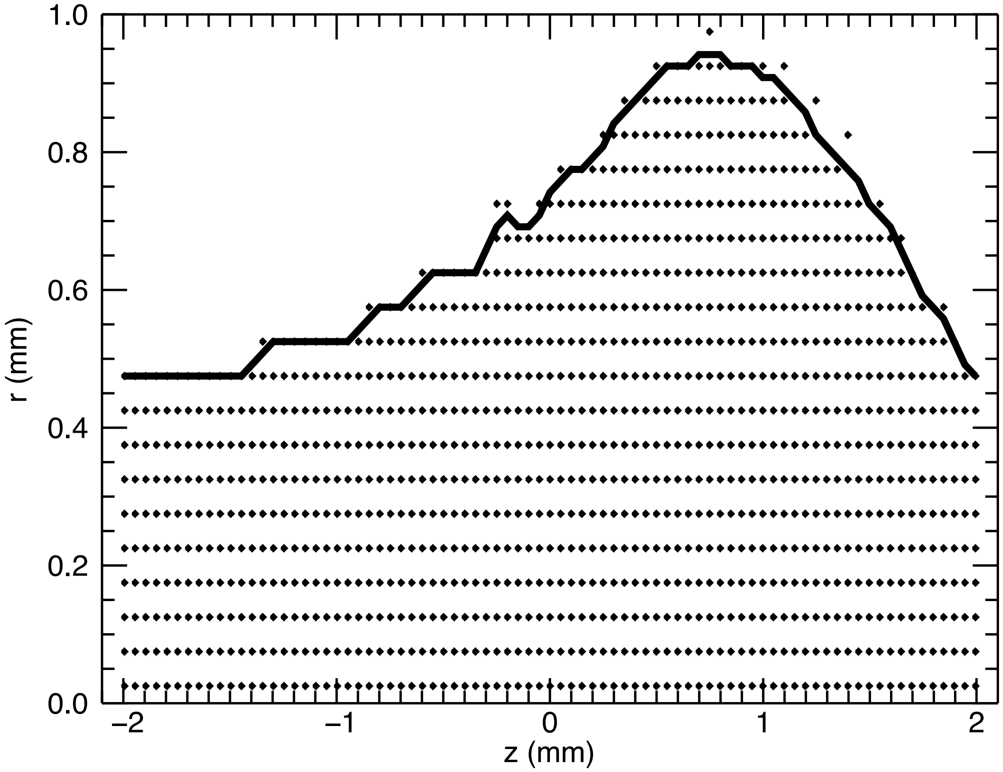

Figure 6.4: TOF detection field of view. Dots indicate initial positions for calculated ion trajectories that hit the TOF detector with $T_c = 10$ eV and a BEC ramp time of 40 ns. The solid line shows the calculated boundary of observable initial positions; a two-point running average is applied to the boundary.

from near the FEC "overtake" the ions leaving near the BEC and arrive at the detector earlier.

The calculated arrival times for each initial z_1 position in the field of view are shown in Fig. 6.5. Ions leaving the trap at positions near $z = -1$ mm arrive some tens of ns earlier than those leaving from the center of the trap. The spread in arrival times for each z_1 position is due to the spread in initial radial position in

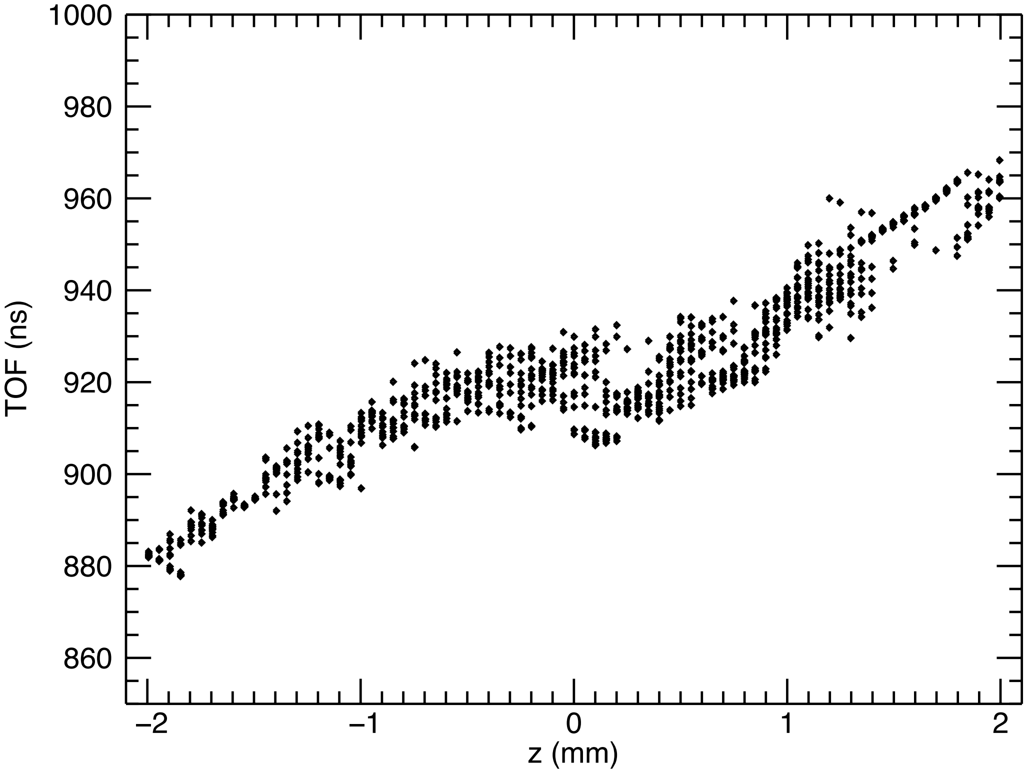

Figure 6.5: Calculated arrival times as a function of the initial z_1 in the TOF field of view, position for ions exiting the trap with $T_c = 10$ eV and a BEC ramp time of 40 ns. The multiplicity at each z_1 position reflects the radial spread.

the field of view (Fig. 6.5). The spread near $z = 0.7$ mm compared to the spread near $z = 0$ mm is a reflection of the effect described above and shown in Fig. 6.4.

Predicted TOF spectra have been obtained using the above model involving the numerical transfer function $F(r : r_1, z : z_1, t : t_1)$ and an equilibrium ion density distribution, $n(r, z)$. In order to properly weight the ion distribution to account for the cylindrical symmetry, a differential ion number, dN, given by

$$dN = n(r, z) 2\pi r dr dz \tag{6.5}$$

where dN represents the number of ions in an annular ring of height dz with inner and outer radii r and $r + dr$, respectively. The factor of 2π is obtained from the azimuthal integration over ϕ. An example of the weighted ion distribution is shown in Fig. 6.6. Convolving the weighted ion distribution with $F(r : r_1, z : z_1, t : t_1)$ yields the number of ions arriving at a time t at the detector. A histogram of the arrival times is performed to generate a computed TOF spectrum for comparison with the observed TOF lineshape. An example of a calculated TOF spectra for the case of Ar^{13+} ions with a temperature of $T = 5.5$ eV is shown in Fig. 6.7. The calculated TOF spectra uses the transfer function obtained for a 40 ns BEC ramp time and an initial velocity distribution specified by Eq. (6.4), using a cut-off parameter of $T_c = 10$ eV. The only other adjustable parameter in the final comparison is a time offset, t_{dif}, which is related to an offset in the HV pulse switch used in the experiment. There is an offset between the input trigger for the BEC dump pulse and the HV output of the pulser of ≈ 150 ns. The measurement is referenced to the TTL trigger pulse and not the actual switching of the HV output.

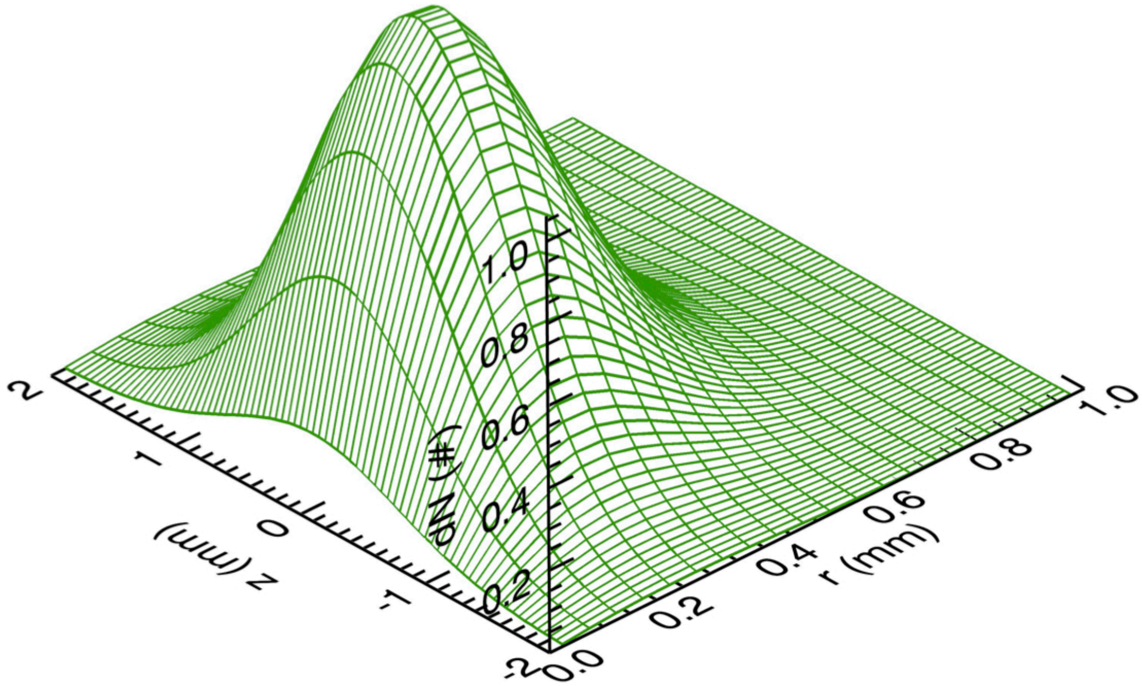

Figure 6.6: Weighted density profile, $dN = n(r,z)2\pi r dr dz$, for an Ar^{13+} ion cloud in the two magnet trap, calculated using the EQUILSOR code. The total number of ions is $N = 300$, the ion cloud temperature is $T = 5.5$ eV.

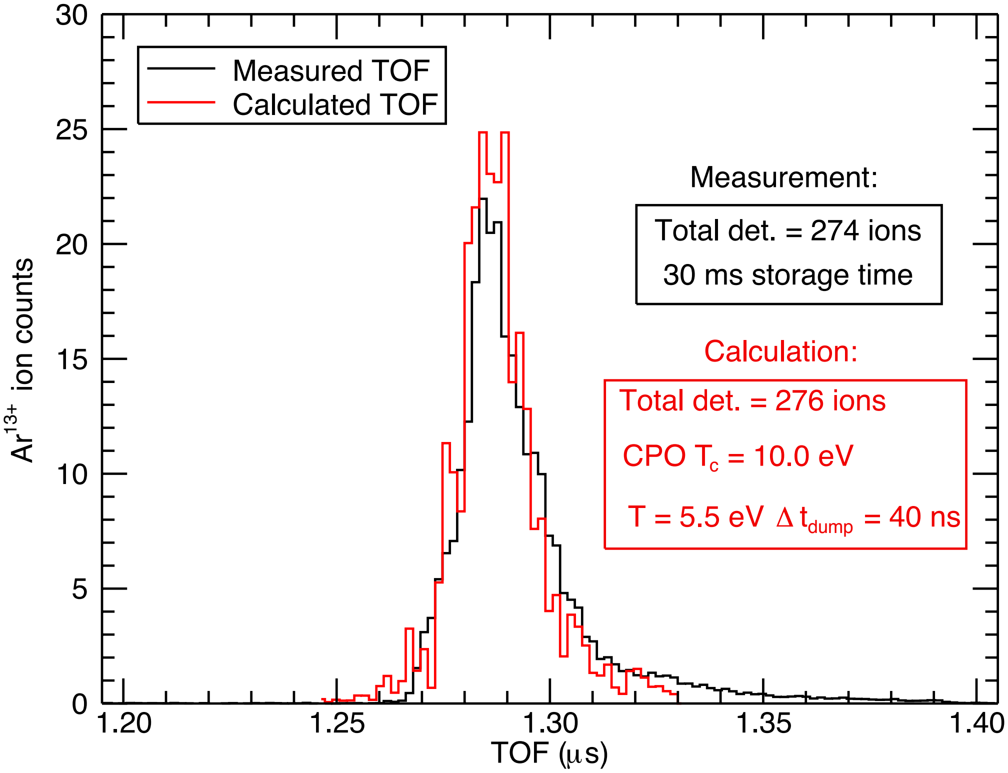

Figure 6.7: Comparison of the calculated (red) and measured (black) TOF spectra for an Ar^{13+} ion cloud in the two magnet trap, calculated using the EQUILSOR code and a measurement at 30 ms storage time. The total number of ions is $N = 300$, the ion cloud temperature is $T = 5.5$ eV. The measured signal has been re-binned in order to allow a direct comparison with the calculation.

6.4 Conditions for non-neutral plasma behavior

The velocity distribution of ions captured in the two-magnet trap corresponds to a thermal energy of ≈ 5.5 eV, about two orders of magnitude lower than typically found in an EBIT. As mentioned in §6.2, this is not sufficient for unambiguous plasma behavior, although the axial extent of the ion cloud is roughly of the same order as the Debye length. Here some general considerations are presented, with illustration that may be relevant to experiments in the near future.

Non-neutral plasmas have been well studied previously, both experimentally and theoretically. Experiments with clouds of Be^+ ions in high-field cylindrical Penning traps have seen correlated motion [77, 78]. An instructive review, by D. Dubin, on the theory of non-neutral plasmas can be found in [79], as well as the earlier work of Davison [80, 81]. The basic theoretical formalism, derived in the above sources, is briefly summarized below in a general form. The zero temperature limit is emphasized to provide a framework for future experiments in which applied cooling techniques may lower the temperature of the stored ion cloud.

An ion cloud possesses characteristics of a non-neutral plasma when either the ion density, $n(r, z)$ is high, or the temperature T is low, such that all dimensions are large compared to the Debye length λ_D. Ions in a trap interact via the Coulomb force reacting to the applied trapping fields in a way that makes the net electric field vanish inside the plasma. The distance over which this cancellation occurs is the Debye length and takes the form

$$\lambda_D = \sqrt{\frac{\epsilon_o k_B T}{n_o Q^2}} \tag{6.6}$$

where ϵ_o is the permittivity of free space (electric constant), k_B is the Boltzmann constant, Q is the ion charge, and n_o is the ion density at the center of the trap. As described in Ch. 2, for a single ion in a Penning trap, the $\mathbf{E} \times \mathbf{B}$ interaction in the trap gives rise to a magnetron motion characterized by the rotation frequency ω_m. When many ions equilibrate in the trap, the space charge interaction gives rise to a "rigid" rotation of the entire cloud at a frequency w_r.

For a single species isolated in a trap, the Hamiltonian which describes the motion of the ions, each with charge Q and mass m, is given by [79]

$$H = \sum_{i=1}^{N} \frac{1}{2} m v_i^2 + \sum_{i=1}^{N} Q\phi(\mathbf{r}_i) \tag{6.7}$$

where N is the total number of ions, v_i is the velocity of each ion, and $\phi(\mathbf{r}_i)$ is the total electric potential at the location of each ion. The trap is assumed to be cylindrically symmetric and cylindrical coordinates (r, θ, z) are used. The total electric potential, $\phi(\mathbf{r})$ is composed of the trap potential, $\phi_t(r, z)$, and the space charge potential of the ion cloud, $\phi_p(r, z)$, and is written as

$$\phi(r, z) = \phi_t(r, z) + \phi_p(r, z). \tag{6.8}$$

The canonical angular momentum of the system is conserved and is given by

$$L = \sum_{i=1}^{N} m r_i^2 \dot{\theta}_i + \frac{1}{2} Q B r_i^2 \tag{6.9}$$

where $\dot{\theta}$ is the velocity in the $\hat{\theta}$ direction. For an ion cloud in thermal equilibrium, the single particle distribution function is given by [82]

$$f = n_o \left(\frac{m}{2\pi k_B T} \right)^{3/2} \exp\left(-\frac{H_1 + \omega_r L_1}{k_B T} \right) \tag{6.10}$$

where n_o is the plasma density at the center of the trap; H_1 and L_1 are the single particle Hamiltonian and angular momentum for an ion in the trap, given by

$$H_1 = \frac{1}{2}mv^2 + Q\phi(r,z), \tag{6.11}$$

$$L_1 = mr^2\dot{\theta} + \frac{1}{2}QBr^2. \tag{6.12}$$

Substituting Eqs. (6.11) and (6.12) into Eq. (6.10), the distribution function is given by

$$f = n(r,z)\left(\frac{m}{2\pi k_B T}\right)^{3/2} \exp\left(-\frac{1}{2}m\frac{(\mathbf{v}+\omega_r r\hat{\theta})^2}{k_B T}\right) \tag{6.13}$$

where

$$n(r,z) = n_o \exp\left(-\frac{Q\phi(r,z) + \frac{1}{2}m\omega_r(\Omega-\omega_r)r^2}{k_B T}\right). \tag{6.14}$$

where Ω is the cyclotron frequency given in Eq. (2.1).

The single particle distribution function is valid when the correlated motion of the ions is small. The Coulomb coupling constant, Γ, characterizes the nearest neighbor ion-ion interaction, and is the dimensionless ratio of the Coulomb interaction energy to the thermal energy; it is defined by

$$\Gamma \equiv \frac{Q^2}{4\pi\epsilon_o a_s k_B T} \tag{6.15}$$

where a_s is the Wigner-Seitz radius, given by

$$a^3 = \frac{3}{4\pi}\frac{1}{n_o}. \tag{6.16}$$

Plasmas with $\Gamma > 1$ are considered to be strongly coupled and should exhibit correlations due to nearest-neighbor interactions. It follows that, the total angular momentum can be re-written as [79]

$$L = m(\Omega/2 - \omega_r)\int d^3\mathbf{r}\, n(r,z)r^2 = m(\Omega/2-\omega_r)N\langle r^2\rangle \tag{6.17}$$

where the thermal distribution is accounted for in the density $n(r, z)$, $\langle r^2 \rangle$ is the mean-squared plasma radius, and the total number of particles, N, is given by

$$N = \int d^3\mathbf{r} n(r, z). \tag{6.18}$$

6.5 Zero temperature limit for a single species

The strong Coulomb interaction ($\propto Q^2$) between highly-charged ions allows the plasma regime to be reached at relatively high temperatures. The highest density attainable is in this regime. It is therefore instructive to consider the description of a non-neutral plasma at very low temperatures, for which the system dimensions are much larger than λ_D. In the zero temperature limit, the density distribution of Eq. (6.14) must remain finite. Therefore, the following condition is imposed:

$$Q\phi(r, z) + \frac{1}{2} m\omega_r(\Omega - \omega_r) r^2 = 0. \tag{6.19}$$

When $\phi(r, z)$ from Eq. (6.19) is substituted into Poisson's equation (Eq. (6.2)), $n(r, z)$ becomes constant over the extent of the plasma with the relation

$$n_o = \frac{2\epsilon_o m\omega_r(\Omega - \omega_r)}{Q^2}. \tag{6.20}$$

The plasma has a well-defined boundary, and is described as a spheroid with axial and radial dimensions z_o and r_o, respectively. A schematic of the plasma dimensions and relevant coordinates are shown in Fig. 6.8. The plasma has azimuthal symmetry and cylindrical coordinates are used. The magnetic field is aligned along the z-axis, and the plasma mid-plane is centered on the r axis.

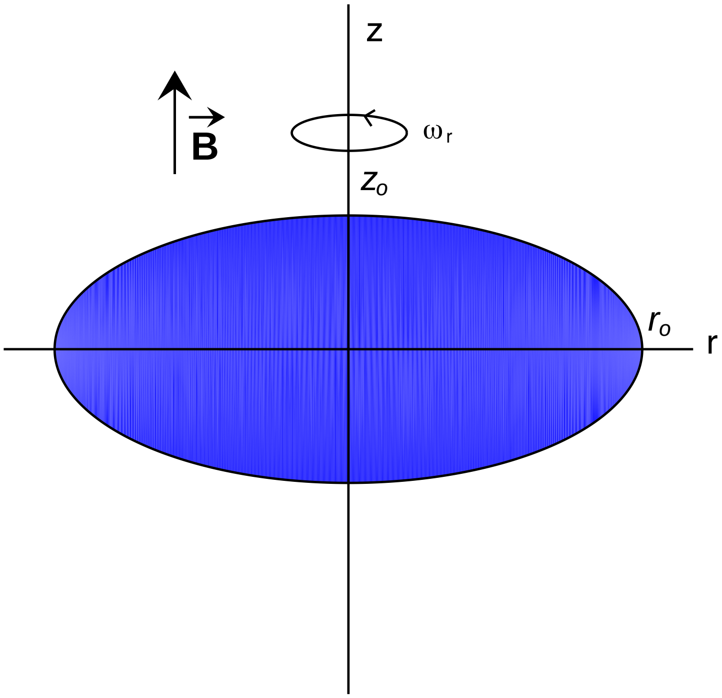

Figure 6.8: Schematic of the spheroidal plasma in the zero temperature case. Here the plasma is defined by a sharp boundary with characteristic dimensions r_o and z_o.

In addition to the rotation frequency, ω_r, the plasma can also be described by the plasma frequency, ω_p which is given in terms of the density and is related to the rotation frequency by

$$\omega_p^2 \equiv \frac{Q^2 n_o}{\epsilon_o m} = 2\omega_r(\Omega - \omega_r). \tag{6.21}$$

It is important to note that there are two allowed rotation frequencies corresponding to the same plasma frequency. This also implies that the angular momentum of the plasma is different for the two possible rotation frequencies. It is useful to define an aspect ratio, $\alpha \equiv z_o/r_o$, which describes the shape of the plasma. The aspect ratio of the plasma is related to the plasma frequency through the axial trap frequency, ω_z, introduced in Eq. (2.4) and is obtained by solving

$$\frac{\omega_z^2}{\omega_p^2} = Q_1^0\left(\frac{\alpha}{\sqrt{(\alpha^2-1)}}\right)(\alpha^2-1)^{-1} \tag{6.22}$$

where Q_l^m is the associated Legendre function of the second kind [83]. Two cases of the plasma shape are considered. When the plasma spheroid is prolate ($\alpha > 1$), Eq. (6.22) takes the form [78]

$$\frac{\omega_z^2}{\omega_p^2} = \frac{1}{\alpha^2-1}\left[\frac{u_p}{2}\ln\left(\frac{u_p+1}{u_p-1}\right) - 1\right], u_p \equiv \frac{\alpha}{(\alpha^2-1)^{1/2}}. \tag{6.23}$$

When the plasma spheroid is oblate ($\alpha < 1$), Eq. (6.22) takes the form

$$\frac{\omega_z^2}{\omega_p^2} = \frac{1}{\alpha^2-1}\left[u_o\tan^{-1}\left(\frac{1}{u_o}\right) - 1\right], u_o \equiv \frac{\alpha}{(1-\alpha^2)^{1/2}}. \tag{6.24}$$

The calculated frequency ratio $(\omega_z/\omega_p)^2$ is shown as a function of the aspect ratio α in Fig. 6.9. The plasma is spherical, $\alpha = 1$, when $(\omega_z/\omega_p)^2 \approx 0.332$. The calculated frequency ratio $(\omega_z/\omega_p)^2$ is also shown as a function of the rotation frequency ratio

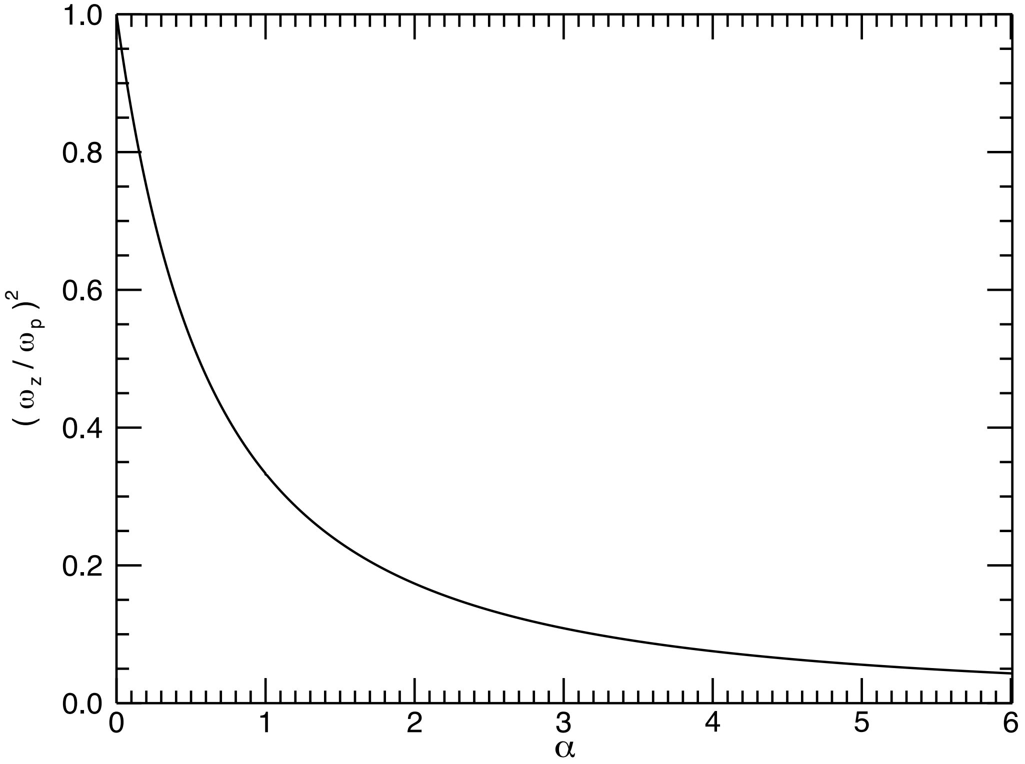

Figure 6.9: Calculated frequency ratio, Q_1^0, as a function of the aspect ratio α.

ω_r/Ω in Fig. 6.10. The plasma spheroid is oblate ($r_o > z_o$) for applied trapping potentials $V_o > 15$V, and prolate ($r_o < z_o$) when $V_o < 15$V. Since the two-magnet trap magnetic field is ≈ 0.3 T, the range of V_o which can support a symmetric, $\alpha = 1$ plasma is narrower than in the case of multi-tesla traps [78].

An interesting limit to consider is the case in which the rotation frequency is equal to half the cyclotron frequency, $\omega_r = \Omega/2$, for which the plasma reaches the maximum possible density. This is referred to as the Brillion limit [80], and the

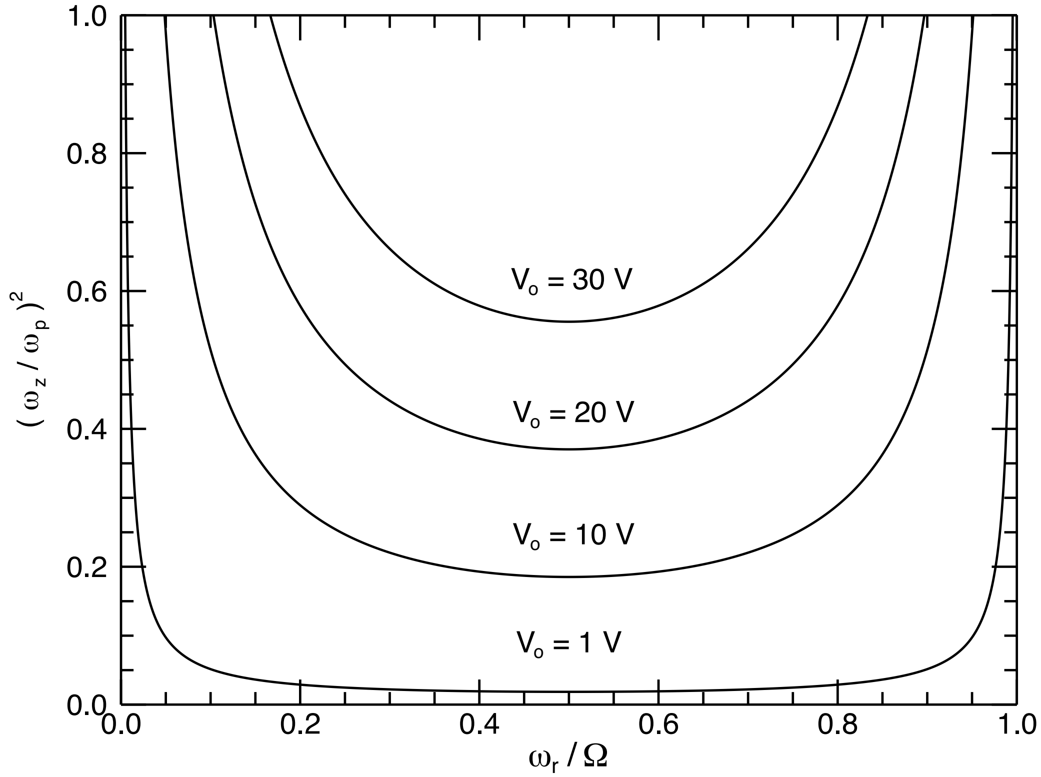

Figure 6.10: Calculated frequency ratio, Q_1^0, as a function of the rotation frequency, ω_r for the case of ArXIV in the two magnet trap. The axial potential limits the range of allowable rotation frequencies.

Brillion density

$$n_B = \frac{\epsilon_o m \Omega^2}{2Q^2} \tag{6.25}$$

describes the maximum plasma density that can be supported by the trap magnetic field. From the Brillion density, the maximum number of trapped ions can be estimated by assuming uniform density over the geometric volume of the trap. In the two-magnet Penning trap, the maximum number of Ar^{13+} ions that can be loaded in the trap is $\approx$ 14 million.

Various tests of the EQUILSOR code have been carried out and an example of a case of an electron cloud described in [81] is shown in Fig. 6.11. The density is fairly constant to about $5\lambda_D$ and then gradually decreases over a few Debye lengths, where the radial size is typically $2r_o \approx 16\lambda_D$, in agreement with the result of Davison [81]. With Fig. 6.11 for comparison, it is interesting to consider Ar^{13+} ions stored in the two magnet trap. At low temperature, the Ar^{13+} ion cloud will behave much like the electron cloud and have a fairly uniform density distribution over a radial extent of many λ_D. An example of a calculation of the ion cloud density for 1000 Ar^{13+} ions at a temperature of $T = 10$ meV and an applied potential well of $V_o = 30$ V is shown in Fig 6.12. Here the temperature is sufficiently low that the Doppler width of the 2p $^2\mathrm{P}_{1/2}$ - 2p $^2\mathrm{P}_{3/2}$ transition would be suppressed to the point that the Zeeman sub-levels can be resolved in the two-magnet trap field.

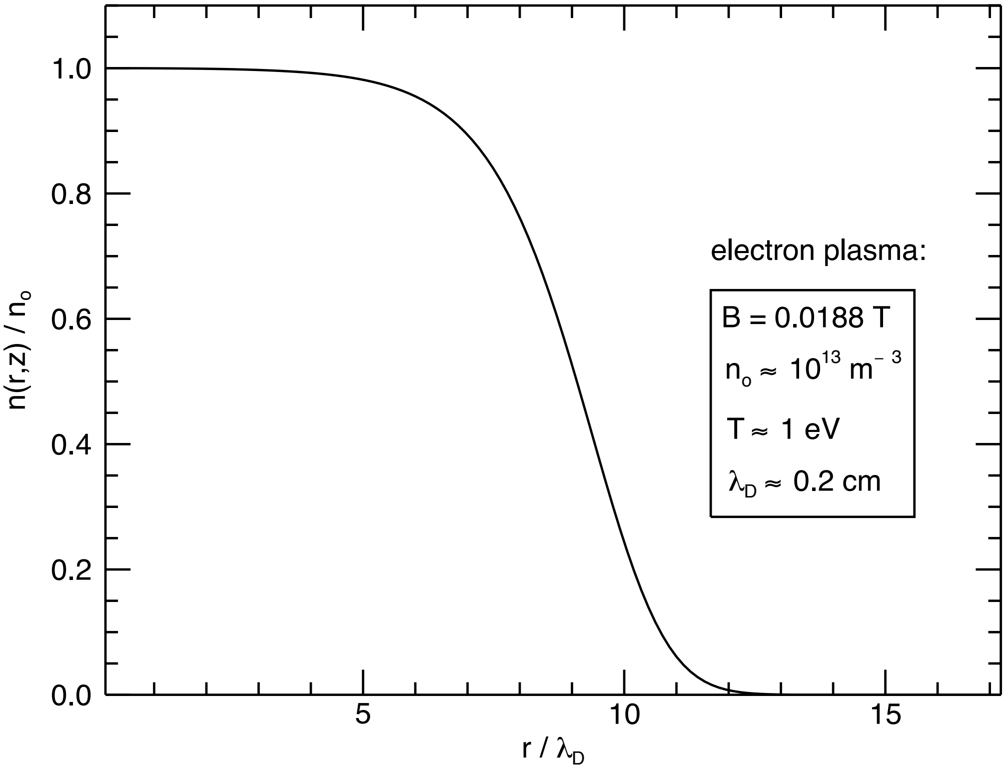

Figure 6.11: Density profile for an electron cloud calculated using the EQUILSOR code. Here the number of electrons, $N = 1000$.

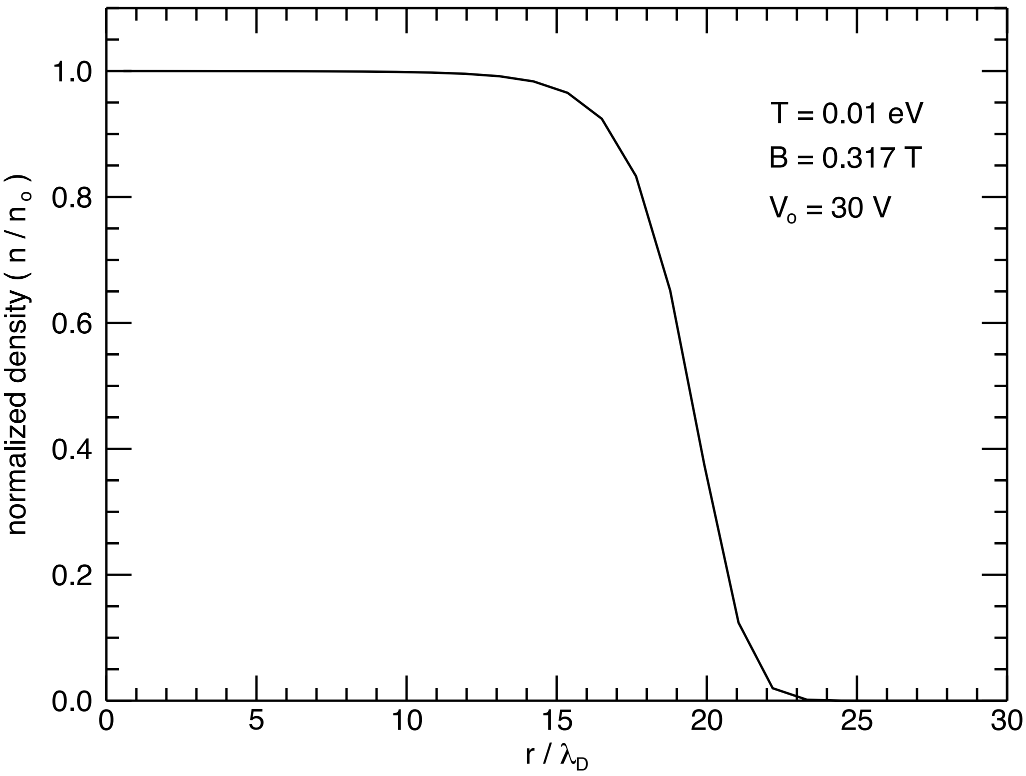

Figure 6.12: Density profile for an Ar^{13+} ion cloud in the two magnet trap, calculated using the EQUILSOR code. The number of ions is $N = 1000$ and the ion cloud temperature is $T = 10$ meV.

6.6 Discussion

A model of the stored ion cloud, assuming thermal equilibrium has been presented. In particular, the case of Ar^{13+} ions stored in the two-magnet Penning trap has been examined. In Chapter 7, results from this model are combined with fluorescence measurements of the decay of the metastable 2p $^2\mathrm{P}_{3/2}$ state in Ar^{13+} to estimate the ion cloud expansion correction to the radiative lifetime.

Ion transport calculations have been presented to model the ejection of stored ions to the detector. The ion cloud characteristics and the initial conditions used in the transfer function calculation determine the level of agreement between the calculated TOF spectra and the measured TOF spectra. Improvements in the agreement, and in the understanding of the ion cloud dynamics in the trap, could be achieved by using Monte-Carlo [55] or molecular-dynamics (MD) [84] techniques to treat the velocity spread of trapped ions more thoroughly, and to include additional ion-ion and ion-neutral scattering effects.

Simple features of a zero-temperature limit have been presented which will become important in experiments with colder highly-charged ions. At thermal energies of ≈ 0.01 eV, for example, clouds of Ar^{13+} ions will exhibit the characteristics of a non-neutral plasma.

Chapter 7

First Light: Measuring the Decay of Metastable States

A unitary Penning trap with two NdFeB magnets has been built with optical access in the mid-plane to facilitate spectroscopic measurements on captured highly-charged ions. In this chapter, the first spectroscopic study of ions stored in a unitary Penning trap is presented to demonstrate the potential of this new tool. Due to the high nuclear charge, many highly-charged ions have strong electric-dipole (E1) transitions in the UV and X-ray part of the electromagnetic spectrum; however, in some instances, the transitions of interest are in the visible regime. Some of the transitions in the visible and infrared (IR) domain are forbidden by E1 selection rules, but can occur via higher order processes, such as spin-flipping magnetic-dipole (M1) transitions. The lifetime of such metastable states are sufficiently long to survive transport from the EBIT to the two-magnet Penning trap. Extraction to a unitary Penning trap has some advantages such as the ability to capture a single charge state, leading to a simpler analysis of atomic processes. In addition, the background gas pressure can be adjusted over a range of greater than 2 orders of magnitude, and can be measured directly, allowing detailed studies of pressure-depending quenching effects and ion-neutral collision dynamics.

Observations of radiative decay from metastable states of highly-charged ions demonstrates one application of the two-magnet trap apparatus. For a “first light” experiment in the new apparatus, the case of the M1 transition in the lowest lying $1s^22s^22p$ manifold of Ar^{13+} is presented. The upper metastable $^2P_{3/2}$ state has a radiative lifetime of $\approx$ 10 ms and decays to the lower $^2P_{1/2}$ by emitting a blue ($\lambda \approx 441$ nm) photon. An overview of the history and previous measurements is presented in §7.1. The technique applied in the new Penning trap measurement including the photon counting scheme is discussed in §7.2. The decay of the $^2P_{3/2}$ state is presented in §7.3. A detailed discussion of the major systematic corrections to the observed fluorescence decay including pressure-dependent quenching effects, and a model to address slow ion cloud expansion in the trap, is shown in §7.4. Additional systematic considerations are discussed in §7.5. Finally, a preliminary result for the lifetime of the $^2P_{3/2}$ state is presented in §7.6.

7.1 Overview and history of measurements in Ar^{13+}

Boron-like Ar^{13+} is a simple atomic system that has been of interest for decades [85] because with only five electrons and a high nuclear charge, high accuracy atomic structure calculations become manageable [86]. The ground-state configuration of Ar^{13+} is $1s^22s^22p$, with the first two electronic shells closed, and a single electron in the p orbital. In addition, since the ^{40}Ar isotope has zero nuclear spin, the atomic energy levels are free of hyper-fine structure. A simplified Grotrian diagram (energy-level diagram) for the 2p state in Ar^{13+} is shown in Fig. 7.1. The 2p state is split, through spin-orbit ($\mathbf{L} \cdot \mathbf{S}$) coupling into the lower energy $^2P_{1/2}$ state and the higher energy, metastable $^2P_{3/2}$ state. A pedagogical diagram shows the orbital

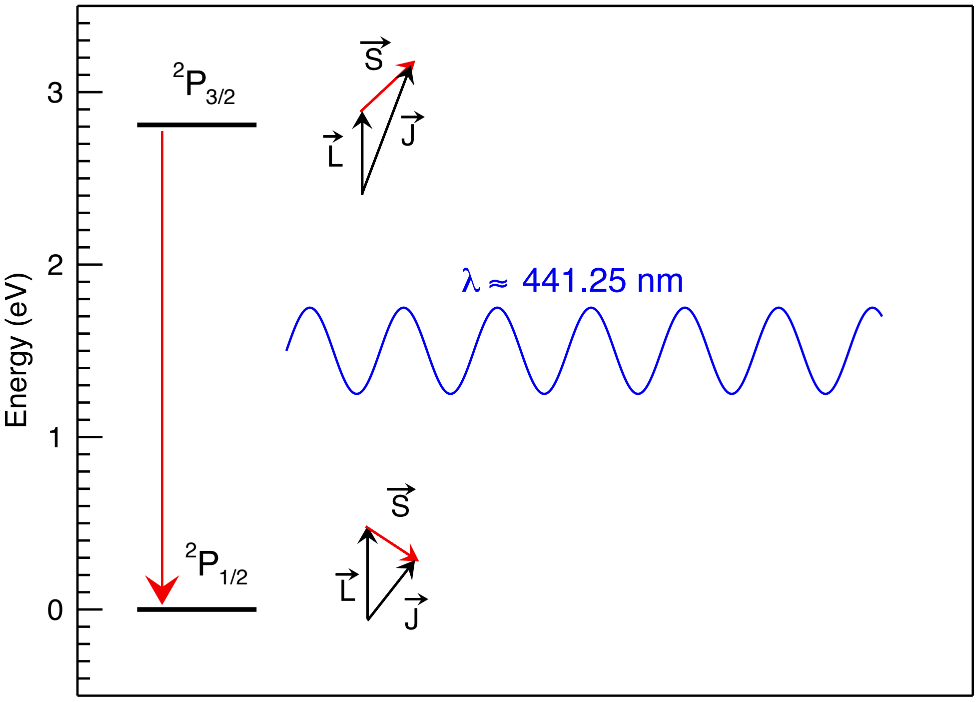

Figure 7.1: Simplified energy level diagram for the $1s^22s^22p$ state of Ar^{13+} showing the orbital angular momentum **L**, the spin angular momentum **S**, and the total angular momentum $\mathbf{J} = \mathbf{L} + \mathbf{S}$. The $J = 3/2$ state is metastable and decays to the $J = 1/2$ state via a spin-flipping M1 transition. The wavelength of the emitted photon is $\lambda \approx 441.25$ nm.

angular momentum **L**, spin angular momentum **S**, and the total angular momentum $\mathbf{J} = \mathbf{L} + \mathbf{S}$ for each state. The fine-structure splitting of the ground electronic state is $\Delta E \approx 2.81$ eV which is due largely to the Z-scaling, where $\Delta E \propto (Z\alpha)^4$.

A brief review of the theory of the Ar^{13+} transition rate follows. Fermi's golden rule, with the two parts: one proportional to the matrix element of the interaction squared and the other a phase factor, proportional to the transition energy cubed ($1/\lambda^3$), gives the general form of the transition rate. In CGS units, the transition rate is given by [87]

$$A_{if} = \frac{64\pi^4}{3h}\frac{1}{\lambda^3}\frac{S_{if}}{2J_i + 1} \tag{7.1}$$

where h is Planck's constant, λ is the transition wavelength, J_i is the total angular momentum of the upper state, and S_{if} is the transition amplitude. For a magnetic dipole (M1) transition, the transition amplitude is given in terms of the non-relativistic magnetic moment operator μ_{nr} expressed as [86]

$$\boldsymbol{\mu}_{nr} = -\mu_B(\mathbf{L} + g_e\mathbf{S}) \tag{7.2}$$

where μ_B is the Bohr magneton ($\mu_B = e\hbar/m_e c$), **L** is the orbital angular momentum operator, **S** is the spin angular momentum operator, and g_e is the electron g-factor. Therefore, the non-relativistic transition amplitude, S_{if}^{nr}, is given as [86]

$$S_{if}^{nr} = \mu_B^2 |\langle f||\mathbf{L} + g_e\mathbf{S}||i\rangle|^2. \tag{7.3}$$

Taking $g_e = 2$, and evaluating the reduced matrix element for $J_f = J_i - 1$, S_{if}^{nr} becomes [87]

$$S_{if}^{nr} = \frac{\mu_B^2}{4J_i}(L + S + J_i + 1)(L + S - J_i + 1)(J_i + S - L)(J_i + L - S). \tag{7.4}$$

For the case of $J_i = 3/2$, $L = 1$, and $S = 1/2$, $S_{if}^{nr} = 4/3\mu_B^2$. Substituting the result of Eq. (7.4) into Eq. (7.1) gives the non-relativistic $^2P_{3/2}$ - $^2P_{1/2}$ transition rate

$$A_{if}^{nr} = \frac{64}{9}\frac{\pi^4}{h}\frac{\mu_B^2}{\lambda^3}, \tag{7.5}$$

and for Ar^{13+}, $A_{if}^{nr} = 104.56$ s^{-1} [86]. This expression is a result of the angular momentum algebra, with its Z dependence absorbed in the wavelength, λ, of the transition. Given an accurate experimental transition wavelength, an accuracy of better than 1% for the transition rate has been estimated using Eq. (7.5) [86].

A number of corrections to the non-relativistic transition rate are considered in [86]. These include the use of relativistic, one-electron Dirac wave functions, ΔA_D, as well as interelectronic-interaction corrections applied using a configuration-interaction (CI) method, denoted as ΔA_{CI}, and a higher-order method, denoted as ΔA_{freq}. These corrections to the transition rate are reported as $\Delta A_D = -0.23$ s^{-1}, $\Delta A_{CI} = 0.037$ s^{-1}, and $\Delta A_{freq} = 0.0005$ s^{-1} [86]. A correction for the negative-energy excitation contribution to the transition rate is reported to be $\Delta A_{neg} = -0.0093$ s^{-1} [86]. Of these, the largest correction, ≈ 0.2 %, is due to the use of single-electron Dirac wave functions.

The largest reported theoretical correction to the transition rate arises from the single-electron QED correction to the electron g-factor. The anomalous magnetic moment of the electron gives a g_e value slightly greater than 2, and has been measured to extremely high accuracy in a high-field Penning trap [88]. The correction for g_e can be written as [86]

$$g_e = 2(1 + \kappa_e) \tag{7.6}$$

where $\kappa_e \approx \alpha/2\pi$ and $\alpha \approx 1/137$ is the fine structure constant. To leading order, the QED corrected g_e yields a magnetic moment operator of the form [86]

$$\boldsymbol{\mu}_{\boldsymbol{a}}^{\boldsymbol{nr}} = -\mu_B[\mathbf{L} + 2(1+\kappa_e)\mathbf{S}] \tag{7.7}$$

where the notation $\boldsymbol{\mu}_a^{nr}$ refers to the non-relativistic magnetic moment operator corrected for the anomalous magnetic moment of the electron. Substituting Eq. (7.7) into Eq. (7.2) gives the leading order QED corrected transition rate [86]

$$A_{if} = \frac{64}{9}\frac{\pi^4}{h}\frac{\mu_B^2}{\lambda^3}(1+4\kappa_e) \tag{7.8}$$

which for Ar^{13+} yields a correction of $4\kappa_e A_{if}^{nr} = 0.485\ \mathrm{s}^{-1}$ [86]. A final theoretical transition rate of $A_{if} = 104.85(2)\ \mathrm{s}^{-1}$ is predicted in [86]. The QED correction due to the anomalous magnetic moment of the electron is ≈ 0.46 %, which is roughly twice as large as the next largest reported correction.

The metastable lifetime of an excited state is related to the transition rate by

$$\frac{1}{\tau} = \sum_f A_{if} \tag{7.9}$$

where the sum over final states f accounts for all possible decay channels of the excited state. In the case of Ar^{13+} there is only a single decay channel from the $^2\mathrm{P}_{3/2}$ state to the $^2\mathrm{P}_{1/2}$. Therefore, the non-relativistic metastable radiative lifetime is given by

$$\tau = \frac{1}{A_{if}} \approx \frac{9}{64}\frac{h}{\pi^4}\frac{\lambda^3}{\mu_B^2}\frac{1}{1+4\kappa_e}. \tag{7.10}$$

The radiative lifetime is proportional to the cube of the transition wavelength, in principle allowing very long lived fine-structure states, even in highly-charged ions.

In addition, given the high nuclear charge, transition energies are amplified to the optical domain which makes the energy levels more robust against external perturbations.

The $^2\mathrm{P}_{3/2}$ state has been studied previously both theoretically and experimentally. Previous calculations of the radiative lifetime are presented in Table 7.1.

$\mathrm{Ar}^{13+}\ 2s^22p\ ^2\mathrm{P}_{3/2}$					
Year	Method	λ_{rep} (nm)	$\Delta\lambda$ (nm)	τ (ms)	τ_{cor} (ms)
1966	HFSCF [85]	441.1	-0.1	9.300	9.309
1979	MCDF [89]	438.69	-2.563	9.407	9.573
1983	MCBP [90]	441.31	0.0506	9.515	9.512
1986	MCDF [91]	441.44	0.187	9.360	9.348
1986	MCDF [92]	441.6(4)	0.343	9.620	9.598
1987	MCDF [93]	441.19	-0.066	9.618	9.622
1998	SS [94]	441.44	0.187	9.569	9.557
2001	RQDO [95]	441.36	0.109	9.588	9.581
2001	MCDF [96]	441.77	0.519	9.606	9.572
2003	MRCI [97]	442.11	0.851	9.615	9.560
2004	MCDF [98]	441.661	0.405	9.6015	9.5751
2005	MCDF [99]	443.44	2.184	9.714	9.571
2005	CIDFS [86]	441.38	0.128	9.538(2)	9.530
2008	CIDFS [100]	441.38	0.127	9.5376(1)	9.5294
2009	MCDF [101]	441.016	-0.239	9.5565	9.5721
2009	MRCI [102]	441.297	0.0409	9.5384	9.5357
2012	MCDF [103]	441.151	-0.105	9.565	9.572

Table 7.1: Calculated Lifetimes, τ of $\mathrm{Ar}^{13+}\ 2s^22p\ ^2P^o_{3/2}$. The reported theoretical transition wavelength, λ_{rep}, the difference from the experimental wavelength, $\Delta\lambda = \lambda_{rep} - \lambda_{exp}$, and the wavelength-corrected lifetime, τ_{cor} are presented. The calculation methods are listed as follows. HFSCF, Hartree-Fock Self-consistent Field; MCDF, Multi-Configuration Dirac-Fock; MCBP, Multi-Configuration Breit-Pauli; SS, SUPERSTRUCTURE code; RQDO, Relativistic Quantum Defect Orbital; MRCI, Mutireference Relativistic Configuration Interaction; CIDFS, Configuration Interaction Dirac-Fock-Sturm.

The year of publication, method, calculated transition wavelength, λ_{rep}, difference in the wavelength from experiment, $\Delta\lambda = \lambda_{rep} - \lambda_{exp}$, reported lifetime, τ, and wavelength-corrected lifetime, τ_{cor} are shown. Previous theoretical investigations range from entirely non-relativistic calculations relying on the calculated transition wavelength [85] to fully relativistic calculations including interelectronic-interaction and radiative corrections [102]. The calculated lifetime has varied over ≈ 5 % in the last 40 years. This is due, in large part, to the uncertainty in the transition wavelength. The most precise measurement of the transition wavelength was performed at the Heidelberg EBIT in 2006 [66], resulting in $\lambda_{exp} = 441.2556(1)$ nm. This wavelength value has been used to correct the reported lifetimes in Table 7.1. The spread in wavelength-corrected preditions is $\approx 3\%$.

Beginning in 1998, experimental investigations have produced four reported measurements of the radiative lifetime of this state thus far. A summary of previous lifetime measurements is presented in Table 7.2. The measured lifetime of the $^2P_{3/2}$ state, the ion trap type, and the year of publication are presented. Three of the four previous measurements were done inside EBIT sources, while only one previous experiment was done using extracted ions, which were captured in an elec-

Ar^{13+} $2s^2 2p$ $^2P_{3/2}$		
Lifetime (ms)	Trap Type	Year
8.7 ± 0.5	EBIT [33]	1998
9.12 ± 0.18	ECR/Kingdon [34]	1998
9.70 ± 0.15	EBIT [32]	2000
9.573(4)(5) (stat.) (syst.)	EBIT [31]	2005

Table 7.2: Measured Lifetimes of Ar^{13+}. Three of the previous measurements have been performed on EBIT ion sources, operated in the "magnetic trapping mode", and a single ion capture measurement has been done using an ECR ion source to create Ar^{13+} ions and an electrostatic Kingdon trap to capture the ions.

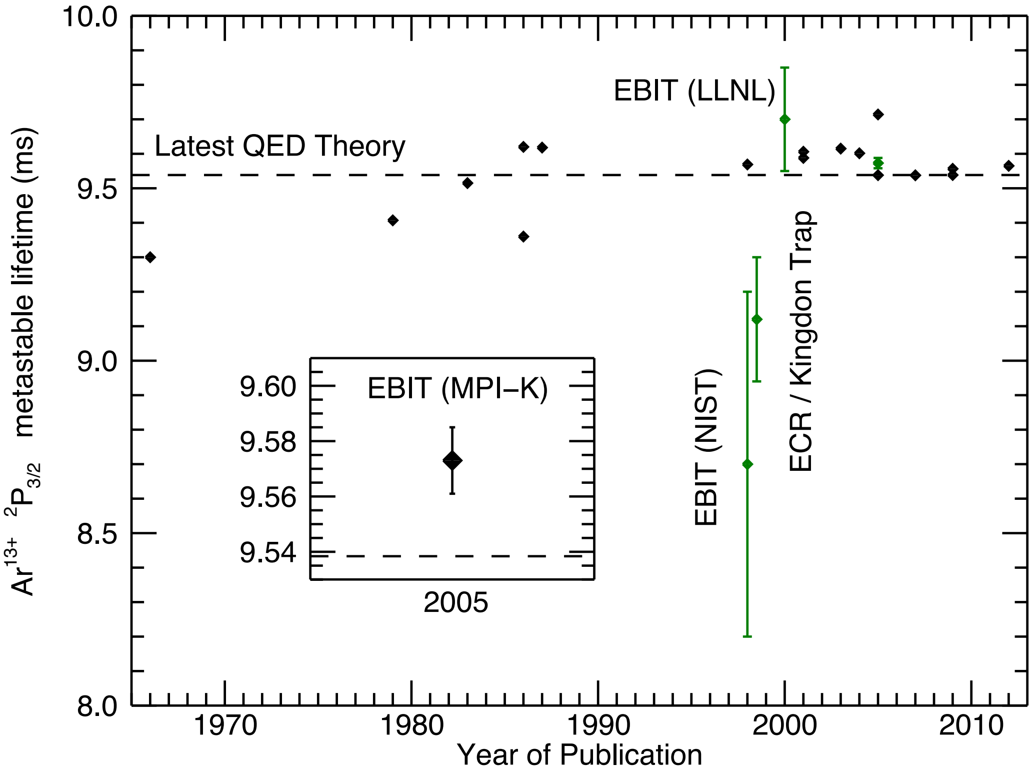

Figure 7.2: Comparison of previous measurements and theoretical values for the $^2P_{3/2}$ radiative lifetime in Ar^{13+}.

trostatic Kingdon trap connected to an ECR ion source. A comparison of previous theoretical and experimental results are shown in Fig. 7.2. The locations of the three previous in-EBIT measurements are indicated, namely: NIST (National Institute of Standards and Technology) (1998), LLNL (Lawrence Livermore National Laboratory) (2000), and MPI-K (Max Planck Institut für Kernphysik) (2005). The Kingdon trap measurement took place at the ECR ion source at the University of Nevada - Reno (USA) (1998).

Previous measurements at EBIT facilities have employed the “magnetic trapping mode” [104] in which the electron beam is turned on during a fill period to build up the charge state of interest, and then rapidly shut off while ions remain confined radially by the strong magnetic field and axially by the drift tube electric potential. Operating the EBIT in this mode allows the observation of fluorescence from trapped ions while the electron beam is off.

In contrast, an electrostatic Kingdon ion trap [105] stored ions using a negatively biased wire which is inserted into a typically grounded mesh ring electrode to create a radial potential for ion confinement. An axial potential well is superimposed via biased endcaps. The Kingdon trap used in the Ar^{13+} lifetime measurements is described in [106]. This ECR/Kingdon measurement utilized an ECR ion source which produced several μA beams of Ar^{13+} ions. The extracted ions were guided into the Kingdon trap through the wire mesh ring electrode. Upon arrival of the ions the central wire was switched quickly to apply the confining fields for ion storage.

7.2 Lifetime measurement in a unitary Penning trap

This section describes the new measurements of the 2p $^2\mathrm{P}_{3/2}$ state in Ar^{13+} carried out using the recently developed permanent magnet Penning trap described in Chapter 2 through Chapter 6. Details of the measurement technique and initial results are presented. Also discussed are a host of systematic effects including, pressure-dependent processes, such as charge exchange ion loss, as well as pressure-independent effects, such as inherent ion cloud expansion.

As illustrated in §3.4.3, the optical setup is designed to collect the photons emitted by the trapped ion cloud, focusing them on a photon counting detector. Figure 3.8 shows the details of the optical setup. An optical interference filter is used to transmit only light within a bandpass centered at $\lambda_o = 440 \pm 2$ nm with a bandwidth of 10 nm (FWHM). The transmission of the optical interference filter is ≈ 55 % at $\lambda = 441$ nm. The specified optical transmission curve of the interference filter is shown in Fig. 7.3. The strong transitions in Ar^{13+} are concentrated in the UV and X-ray domain, and there are no identified lines in the bandwidth of the filter that can be attributed to lower charge states of argon from Ar^{8+} to Ar^{12+} [107]. Therefore, the need for further filtering of the optical setup is unnecessary.

The photon detector head is made of GaAsP and is capable of performing single photon counting. The detector quantum efficiency (QE) is ≈ 40 % in the spectral region of interest. The sensor head is cooled to -20° C using a Peltier cooler, while the housing is cooled to $\approx 19°$ via thermal contact with a water-cooled aluminum mounting block. The combination of cooling the sensor head and the housing results in a measured dark count rate of $\approx 5.5\ \mathrm{s}^{-1}$. The detector converts the avalanche current to a TTL pulse which is counted by a gated multichannel scalar (MCS).

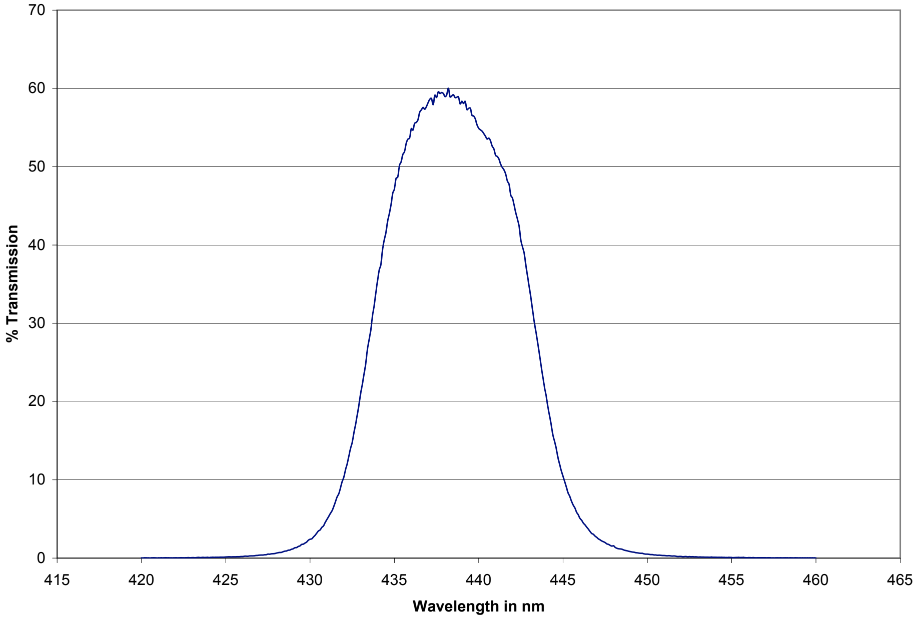

Figure 7.3: Optical transmission curve specified for the 440 nm narrow bandpass filter (Thorlabs FB441-10) used in the Ar^{13+} lifetime measurements.

7.3 Decay of the 2p $^2P_{3/2}$ state

The use of the two-magnet Penning trap to measure the Ar^{13+} 2p $^2P_{3/2}$ radiative lifetime is described here in some detail. First, Ar^{13+} ions are extracted from the EBIT and captured in the Penning trap. Upon ion capture, the MCS is gated to begin counting photons in 1 ms bins for a measurement duration (capture and storage cycle) of up to 134 ms. At the end of each such MCS measurement cycle (or “MCS pass”), ions are then ejected from the Penning trap, and the measurement cycle is repeated. A large number of passes ($\approx 140,000$) is required to observe the fluorescence decay with useful signal-to-noise ratio. A representative radiative decay curve at the base background pressure of 8.1×10^{-10} torr is shown in Fig. 7.4.

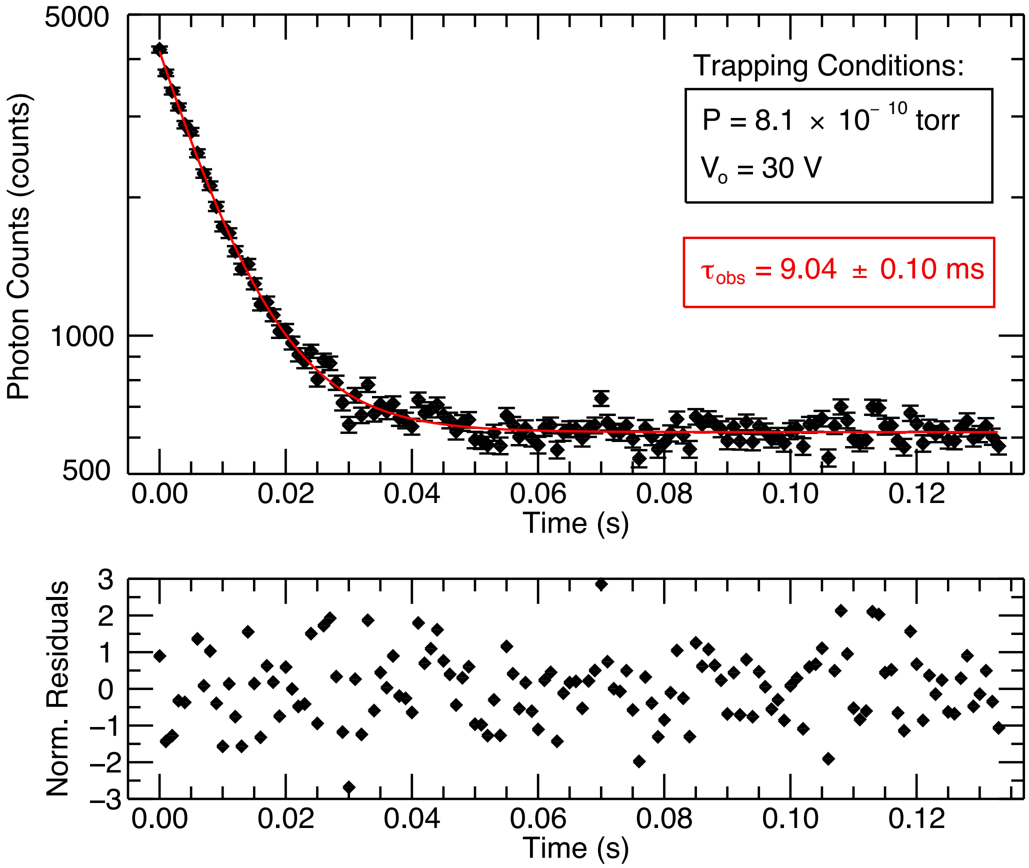

Figure 7.4: Radiative lifetime of the $^2P_{3/2}$ state of Ar^{13+} for a base background pressure of 8.1×10^{-10} torr. Top: observed fluorescence decay signal. Bottom: normalized residuals (Δ_i/σ_Δ), where Δ_i is the difference between the exponential fit result $f(t_i)$, and the measured photon data N_i, and σ_Δ is the global standard deviation of the residuals; here $\chi^2/\nu = 1.01$.

The data acquisition time was six hours, with the trapping potential $V_o = 30$ V and the trap float capture voltage $V_c = 2926$ V. The EBIT was operated in the pulsed extraction mode with an electron beam energy of 2.5 keV, electron beam current of 14.4 mA, ionization time of 76 ms, and a ballistic gas injection pressure of 5.0×10^{-5} torr. A complete list of the EBIT and Penning trap operation conditions are given in Table 4.1.

The fluorescence decay has been fit to a single exponential function given by

$$N(t) = N_o e^{-t/\tau_{obs}} + B \tag{7.11}$$

where N_o is the number of detected photons at $t = 0$, τ_{obs} is the observed fluorescence decay constant, and B is the integrated background dark count level. At base background pressure, the observed fluorescence decay constant is measured to be $\tau_{obs} = 9.04 \pm 0.10$ ms; here $\chi^2/\nu = 1.01$. An observed metastable decay rate is obtained by taking the reciprocal of the lifetime given by

$$\gamma_{obs} = \frac{1}{\tau_{obs}} \tag{7.12}$$

yielding, for the base pressure: $\gamma_{obs} = 110.57 \pm 1.19$ s^{-1}. The fitted background of $B = 616.6 \pm 2.6$ counts / time bin is consistent with the measured dark count rate integrated for 140,000 passes. The uncertainty quoted on the low pressure measurement is purely statistical. The systematic effects modifying the observed radiative lifetime are addressed in the following sections.

7.4 Major corrections

Several processes can affect the observed lifetime of the metastable $^2P_{3/2}$ state of an isolated Ar^{13+} ion. A variety of corrections have been investigated and are presented here. Quenching effects due to collisions with background gas tend to make the observed radiative lifetime shorter than the actual lifetime. This effect can be accounted for by measuring the lifetime in a series of pressures in order to extrapolate the zero-pressure result. Pressure dependent shifts in the lifetime are addressed in §7.4.1.

Ion cloud expansion and various ion loss mechanisms also tend to make the observed lifetime shorter than the actual lifetime. When ions are lost from the trap through charge-exchange, collisional losses, or cloud expansion due to trap instabilities, the population of ions in the metastable state within the optical field of view is decreased. During photon counting, it is difficult to de-couple the fluorescence decay of interest and the loss of ions from the trap or from the field of view of the detection optics. In addition, the optical field of view is generally not spatially uniform; depending on the desired level of precision, this may introduce significant sensitivity to the ion cloud shape, size, and number of ions in the trap. Therefore, ion cloud expansion within the optical field of view itself can lead to an apparent decay of the metastable state. Effects associated with ion cloud expansion and ion loss are addressed in §7.4.2 and the spatial non-uniformity of the collection optics is addressed in §7.4.3, with some consideration for the cloud shape, size, and ion number effects.

7.4.1 Pressure dependent shifts: Stern-Volmer analysis

The observed radiative lifetime can be affected by pressure-dependent quenching mechanisms such as charge exchange, and ion loss due to elastic or inelastic collisions with background gas. The principle of fluorescence quenching by background gas is discussed in detail in [108]. In the absence of quenching, the decay rate of an upper-level state takes the form

$$\frac{dN_i}{dt} = -\gamma_o N_i \tag{7.13}$$

where N_i is the ion population in the excited state and γ_o is the natural decay rate. However, in the presence of a background gas (or quencher), the Stern-Volmer description [109] yields a pressure dependent transition rate given by

$$\gamma = \gamma_o + \kappa n = \gamma_o + \alpha P \tag{7.14}$$

where n is the background particle density and κ is the rate coefficient for the quenching. Since the background gas particle density is proportional to the measured background gas pressure, γ is a function of the pressure P, where α is its rate coefficient. This relation applies to any pressure dependent process which contributes to observed fluorescence decay. The decay rate is proportional to the background gas pressure and therefore, a measurement of the decay rate as a function of pressure can be used to extract the natural decay width γ_o.

An example of the pressure-dependent transition rate is shown in Fig. 7.5. The background pressure of the two-magnet Penning trap apparatus was varied by leaking a small amount of N_2 gas into the chamber through a variable leak valve

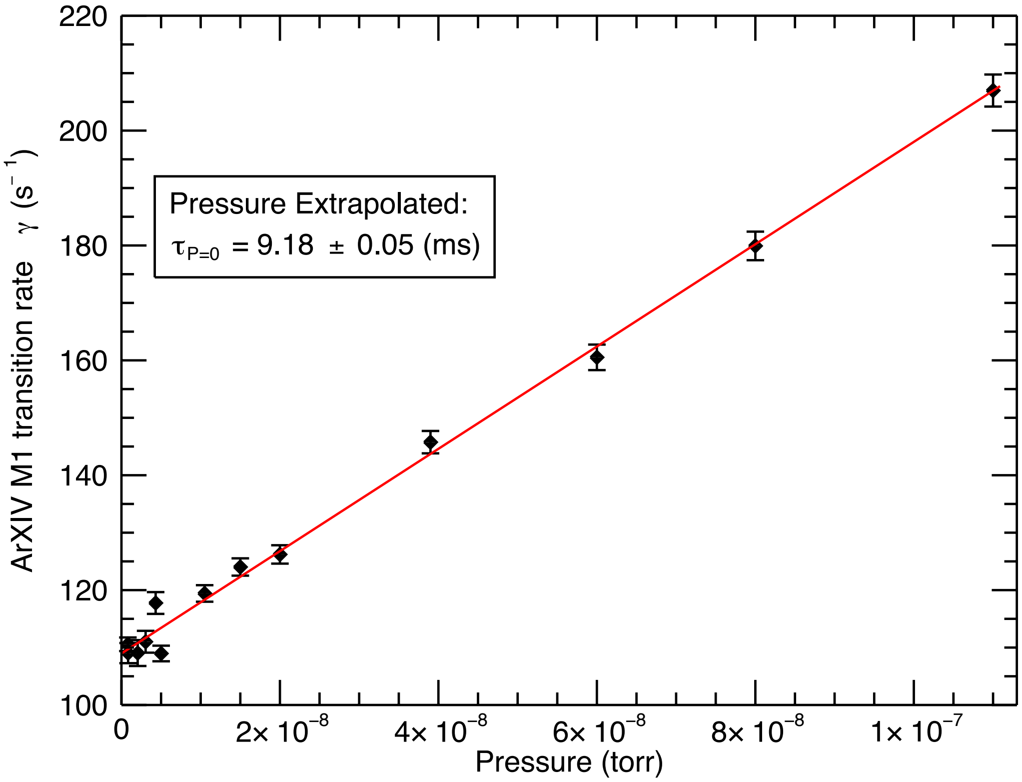

Figure 7.5: Pressure-dependence in observed radiative lifetime of the $^2P_{3/2}$ state of Ar^{13+}. Here the transition rate, γ is shown as a function of the trap background pressure. The transition rate is fitted to the linear function given in Eq. (7.14). The goodness of fit is indicated by $\chi^2/\nu = 1.04$. The quoted uncertainty (1 σ) in the pressure-extrapolated lifetime is entirely statistical.

with a sapphire seal. The pressure was measured using a cold-cathode, inverted magnetron gauge calibrated for N_2. The cold-cathode gauge was chosen because it does not emit light in the optical filter bandwidth and therefore does not contaminate the fluorescence signal. This was checked by measuring the PMT dark count rate with the gauge both on and off, to ensure that no change was observed. The background pressure was varied over two orders of magnitude in order to fully investigate pressure dependent effects. A fit of the data to Eq. (7.14) results in a zero-pressure transition rate of $\gamma_o = 108.97 \pm 0.58\ \mathrm{s}^{-1}$, corresponding to a pressure-extrapolated lifetime of

$$\tau = 9.18 \pm 0.05\,\mathrm{ms}. \tag{7.15}$$

The goodness of fit is indicated by $\chi^2/\nu = 1.04$. While the ${}^2\mathrm{P}_{3/2}$ radiative lifetime has been previously measured, and the Stern-Volmer technique has been widely used on other argon ions including charge states as high as Ar^{10+} [110], the result presented here is the first extrapolation using measurements with Ar^{13+} under various background pressures.

7.4.2 Effects due to ion cloud expansion and ion loss

Ion cloud expansion and ion loss during fluorescence measurements tend to yield a shorter than expected lifetime. Ion loss mechanisms include charge exchange and ion-neutral scattering which can alter a stable ion's trajectory causing it to leave the trap. These effects can be minimized through the pressure-dependent lifetime measurement. In addition, the inherent stability of the trap can cause ion cloud expansion leading to eventual ion loss or reduced light collection due to ion motion in the non-uniform field of view.

In various earlier experiments using a Kingdon trap [34], an ion loss correction was applied to the observed radiative lifetime given by

$$\frac{1}{\tau} = \frac{1}{\tau_{obs}} - \frac{1}{\tau_{st}} \tag{7.16}$$

where τ is the true radiative lifetime, and τ_{st} is an average ion storage lifetime, at the background pressure measured during the fluorescence observations. As already mentioned, this correction is pressure-dependent, and the storage lifetime includes both collisional ion loss processes, and ion loss due to inherent trap stability. In fact, in many earlier experiments with lower charge states of argon, an ion loss correction at zero pressure was applied to the pressure-extrapolated lifetime measurement. Here, the pressure-dependent ion storage lifetime was measured and extrapolated to get the zero-pressure ion-storage liftetime. A correction using the zero-pressure ion storage lifetime was applied as follows

$$\frac{1}{\tau} = \frac{1}{\tau_{P=0}} - \frac{1}{\tau_{ist}} \tag{7.17}$$

where $\tau_{P=0}$ is the pressure-extrapolated radiative lifetime and τ_{ist} is the zero-pressure ion storage lifetime.

The situation in the two-magnet Penning trap measurement is similar. Here τ_{ist} is related to trap misalignments which can cause ion cloud heating. The ion heating leads to radial expansion of the ion cloud which can in turn lead to ions moving out of the field of view of the PMT. If the ion cloud expands beyond the field of view of the PMT, then it can cause an apparent shortening of the radiative lifetime which is purely geometrical and independent of collisional effects. Great care has been taken to investigate the ion cloud expansion in the two magnet trap. As presented in Ch. 5, (Fig. 5.17), the Ar^{13+} ion loss has been measured as a function of the trap background pressure with a zero-pressure storage lifetime of $\tau_{ist} = 1.18 \pm 0.05$ s.

Equation (7.17) gives accurate results to the extent that the field of view of the PMT coincides with the field of view of the TOF detector. In other words, if the optical detection and the ion detection are sensitive to the same changes in the ion cloud shape and size, then applying a correction obtained by TOF detection is appropriate. However, if the PMT detection and TOF detection are not equally sensitive to ion cloud expansion, then this technique can lead to an over-correction of the measured radiative lifetime.

7.4.3 Optical Transfer Function

Similar to the ion transfer function presented in Ch. 6, an optical transfer function can also be defined for the optical setup. The definition is analogous to Eq. (6.3)

$$N_D(r,z,t) = \sum_{t_1}\sum_{r_1}\sum_{z_1} F_P(r : r_1, z : z_1, t : t_1) N_P(r_1, z_1, t_1) \tag{7.18}$$

where $N_D(r,z,t)$ is the number of photons hitting the coordinates r and z near the detector at a time t; $N_P(r_1,z_1,t_1)$ is the number of photons emitted from position and time (r_1,z_1,t_1) and is specified by the ion density and fraction of ions in the $^2\mathrm{P}_{3/2}$ metastable state. In the ideal case, the optical transfer function is spatially uniform, the detector subtends a solid angle of 4π, and the detection efficiency of all optical elements is 100 %. However, in actual experimental setups the detection solid angle is typically much less than 4π, the PMT detection efficiency is closer to 40 %, and the transfer function has spatial variation.

Ray tracing calculations have been carried out to evaluate the optical transfer function, which can be used to check the validity of the ion expansion correction to the measured radiative lifetime. The results of these calculations are presented in Fig. 7.6. It is clear that the optical transfer function is non-uniform over the trapping volume. Non-uniformity of the optical transfer function causes the photon detection to be sensitive to the ion cloud shape and size. Numerical computations of the kind introduced in Ch. 6 have been carried out to investigate the influence of both the non-uniform photon transfer function and the TOF ion expansion measurements.

Assuming that the ion density is known and that 1/2 of the trapped ions are initially in the metastable state, the photon count rate can be calculated as a function of the ion storage time. For a cloud of 500 Ar^{13+} ions, with a temperature of 5.5 eV, simulated TOF spectra have been calculated and compared with observed TOF spectra after 1 ms ion storage, taken during measurements of radiative decay at the lowest attained pressure. At such temperature, the axial size of the cloud is essentially set by the thermal energy of the ions. By adjusting the plasma radius r_p and central plasma density n_o, it is possible to generate an estimated initial cloud size. The initial cloud size corresponding to agreement with the TOF measurements is given by $r_p = 0.703$ mm, where the detected number of ions is $N_o = 296$. A

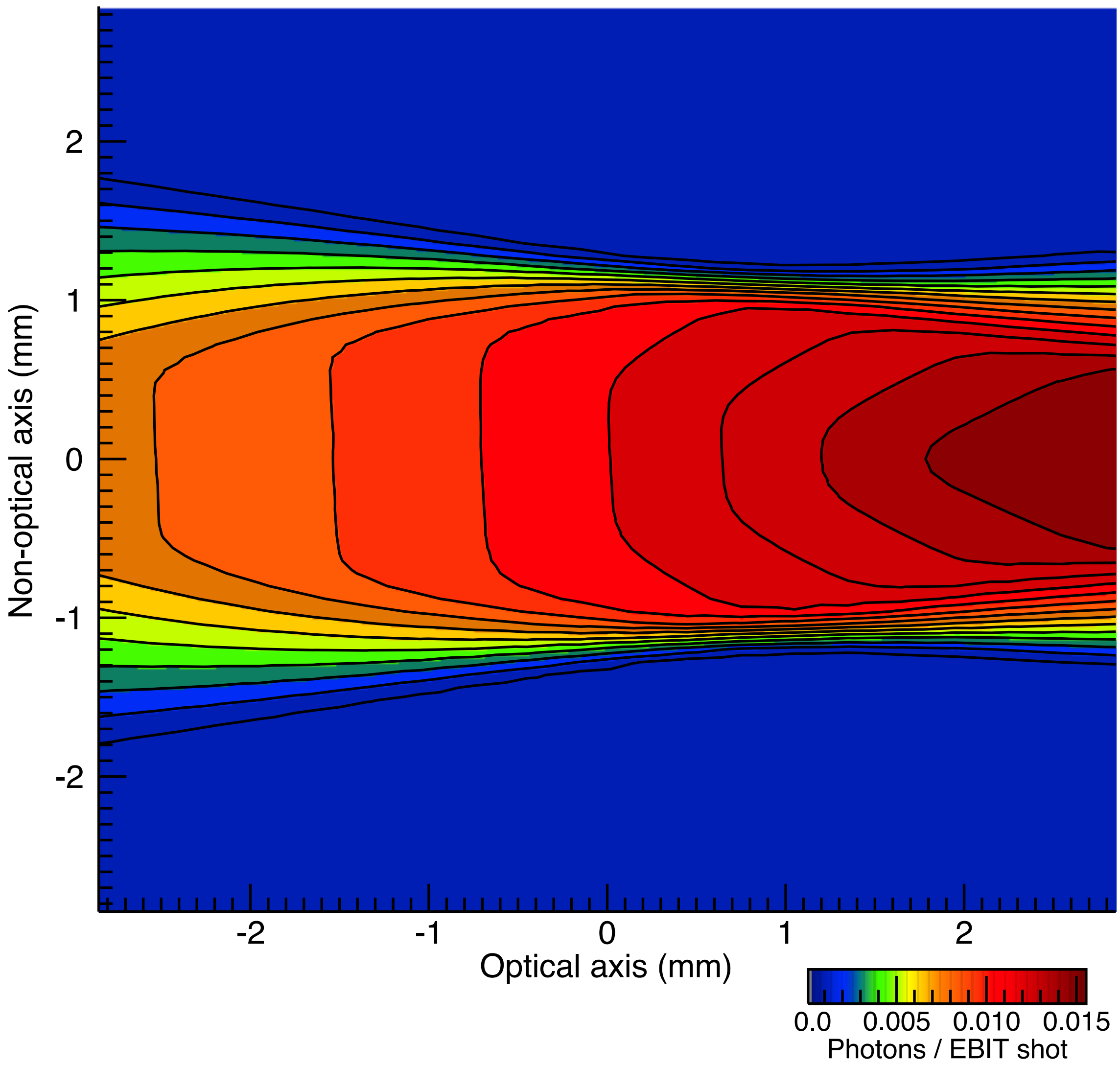

Figure 7.6: Optical transfer function for the absolute number of detected photons per MCS pass. The calculations are performed in a coordinate system which is aligned with the optical axis.

comparison of the detected photons per EBIT shot shows good agreement between the calculation and measurement at low pressure.

The EQUILSOR code can be used to estimate the ion cloud radius expansion if the zero-pressure ion loss rate has been determined. The total ion number is fixed at 500, the ion cloud radius is increased and the number of detected ions is calculated. This yields the detected ion number as a function of the ion cloud radius, $N_D(r_p)$. On the other hand, if the zero-pressure extrapolated ion loss is attributed to ion cloud expansion, then the corresponding time is calculated using

$$t = -\tau_{ist} \ln \left(\frac{N_D(r_p)}{N_o} \right) \tag{7.19}$$

where $N_D(r_p)$ is identified as the number of detected ions and τ_{ist} is the zero-pressure extrapolated ion-loss time constant. In this way, the plasma radius as a function of time $r_p(t)$ is obtained together with the photon counts per EBIT pulse as a function of time. For the case of 500 stored ions, the calculated photon counts in the initial cloud, where $r_{op} = 0.703$ mm, agrees nearly exactly with the observed photon counts / EBIT cycle.

In the "small cloud" limit, meaning that the cloud size is much smaller than the PMT field of view, the photon count rate would be constant. In addition, in the "large cloud" limit, wherein the cloud size is much larger than the PMT field of view, it is expected that the resulting photon-count decay rate would agree with the measured intrinsic ion-loss rate, interpreted as due to cloud expansion.

The comparison of the calculated and measured expansion rate allows for a more rigorous evaluation of the ion cloud size effects that could potentially shift the measured lifetime. The initial cloud size, number of ions, and fraction of ions in the metastable level have all been adjusted in order to obtain agreement with the TOF measurements and the measured photon counts per EBIT cycle of 0.27. This has been done for 300 – 1000 stored ions. The results from these calculations are presented in Table 7.3. Varying the initial size of the cloud and the fraction of ions in the metastable level allows for a constraint of the magnitude of the correction that can be applied to the zero pressure radiative lifetime. Since the metastable fraction of ions is determined by the plasma conditions inside the EBIT, it is not realistic to assume that all captured ions are initially in the excited metastable state. In fact, $\approx$ 300 ions are detected at a storage time of 1 ms which means that at least that many ions are stored in the trap. This lower limit ion number of 300, corresponds to a metastable fraction $A_{UL} = 0.75$. For comparison, in the earlier Kingdon trap measurement [34], the metastable fraction of ions exiting the ECR source was estimated to be 2/3, not much different from the 0.75 required for the case of 300 stored ions. On the other hand, the calculated ion expansion time constant of 5.65 s is longer than the measured $\tau_{ist} = 1.18$ s. This suggests that the

Calculated Ar^{13+} ion cloud expansion time in the optical field of view			
Trapped ions (N_o)	Initial cloud radius (r_{op}) (mm)	A_{UL}	Expansion time (s)
300	0.287	0.75	5.65
500	0.703	0.50	3.50
700	0.919	0.40	2.08
1000	1.15	0.30	1.45

Table 7.3: Calculated ion cloud expansion time for a given number of trapped ions and fraction in the metastable $^2\mathrm{P}_{3/2}$ state, A_{UL}.

ion cloud may be larger than the 300 ion case. As the ion number is increased, the plasma radius must be increased in order to preserve the agreement between the calculated and measured TOF signal. Adjusting the metastable fraction in order to achieve agreement with the measured photon counts gives probable ion cloud conditions that agree with experiment. The last column of Table 7.3 shows that as the number of stored ions increases, the calculated expansion rate comes into closer agreement with the measured intrinsic ion-loss rate, taken to be due to expansion.

Based on ion capture efficiency measurements and calculations presented in §4.4.1, it seems unlikely that more than 700 ions are present in the trap during lifetime measurements. An ion capture efficiency of ≈ 45% would set the limit on the number of ions at close to 700 per EBIT pulse. Ion numbers greater than 1000 would require the capture efficiency to approach 65%. The narrow timing pulse used for capture and the broad arrival pulse from the EBIT, suggest that capture efficiency greater than 45% would be rather unlikely.

7.5 Additional Systematics

A variety of additional systematic effects influencing the radiative lifetime measurement can be estimated, as discussed in the most recent in-EBIT measurement [87]. The issue of radial ion expansion and loss has been addressed in the previous section; however, axial ion losses are also possible. As shown in [87], the axial ion loss rate can be expressed as

$$\frac{d}{dt}N_{AL_i} = -\gamma_{AL}N_i \tag{7.20}$$

where N_i is the number of ions of a given charge state and γ_{AL} is given by

$$\gamma_{AL} = \frac{3}{\sqrt{2}} v_{ij} \left(\frac{e^{-\omega_i}}{\omega_i} - \sqrt{\omega_i}[\mathrm{erf}(\omega_\mathrm{i}) - 1] \right), \tag{7.21}$$

where $\mathrm{erf}(\omega_i)$ is the error function given by [83]

$$\mathrm{erf}(\omega_i) = \frac{2}{\sqrt{\pi}} \int_0^{\omega_i} e^{-t^2}\, dt, \tag{7.22}$$

and ω_i is related to the ion charge state Q_i, axial potential V, and ion temperature, T_i and is given by

$$\omega_i = \frac{Q_i e V}{k_B T_i}. \tag{7.23}$$

The quantity v_{ij} is the ion-ion Coulomb collision rate and for ions of the same mass is given by

$$v_{ij} = \sum_j \frac{4 n_j \sqrt{2\pi}}{3\sqrt{M_i}(4\pi\epsilon_o)^2} \frac{Q_i^2 Q_j^2 e^4}{(k_B T_j)^{3/2}} \ln \Lambda_{ij} \tag{7.24}$$

where n_j is the ion density of a given charge state and $\ln \Lambda_{ij}$ is the Coulomb logarithm for ion-ion collisions [111]; for only Ar^{13+} ions present in the trap, $\ln \Lambda_{ij} \approx 11$. The axial ion loss rate is estimated to be $\approx 10^{-9}$ s^{-1}, and therefore has no significance in estimating the radiative lifetime uncertainty.

A shift in the pressure-extrapolated lifetime could occur if the pressure inside the trap has an offset from the measured chamber pressure during injection of N_2. This can occur if the residual gas composition is dominated by a gas other than N_2. This shift is estimated by considering the ion loss rate data presented in §5.1.3. Since the Penning trap is a room-temperature device, it is not probable that the pressure inside the trap is lower than the measured chamber pressure. However, due to differential pumping effects and the small holes in the Penning trap it is possible that the pressure inside the trapping region is greater than the measured pressure. A positive pressure shift would cause the extrapolated ion loss rate to decrease, compared to the measured value of 1.18 ± 0.05 s. However, a pressure shift that causes an ion loss rate less than zero is not physically possible. Thus, the maximum pressure offset has be estimated from the fitted results of the ion loss data. A pressure offset of 7.98×10^{-10} torr would cause the measured ion loss rate to be consistent with zero; in this case, there would be no radial expansion of the ion cloud and no ions would be lost from the trap at zero pressure.

When a pressure offset of this size is added to the transition rate data, the resulting pressure-extrapolated lifetime is found to be $\tau = 9.24 \pm 0.05$ ms. This lifetime is consistent with the result when no pressure offset is assumed and an ion expansion correction is applied using either the TOF measured rate or the rate deduced from ion cloud modeling. A comparison of estimates for a range of pressure offsets are shown in Table 7.4. It shows that the effect of a pressure offset

Ar^{13+} $2s^22p$ $^2P_{3/2}$ Pressure offset estimates					
Pressure offset (torr)	$\tau_{P=0}$ (ms)	$\delta\tau_{P=0}$ (ms)	τ_{st} (s)	$\delta\tau_{st}$(s)	τ (ms)
-0.89×10^{-10}	9.17	0.05	1.06	0.04	9.25
zero	9.18	0.05	1.18	0.05	9.25
2.86×10^{-10}	9.20	0.05	1.84	0.14	9.25
5.0×10^{-10}	9.21	0.05	3.16	0.44	9.24
6.0×10^{-10}	9.22	0.05	4.75	1.04	9.24
7.98×10^{-10}	9.24	0.05	N/A	N/A	9.24
9.48×10^{-10}	9.25	0.05	N/A	N/A	9.25

Table 7.4: Radiative lifetime and ion storage lifetime estimates for a range of potential pressure offsets. Ion storage lifetimes that are less than zero are un-physical and are indicated with (N/A). The estimated offsets: -0.89×10^{-10} torr, 2.86×10^{-10} torr, and 9.48×10^{-10} torr correspond to residual gas compositions: pure H_2O, equal parts H_2O, N_2, H_2, and pure H_2, respectively.

in the Penning trap can shift the lifetime by no more that 0.06 ms, for offsets of order the measured base pressure, of either sign. As shown in Table 7.4, an increase in the radiative lifetime due to a pressure offset would be accompanied by a decrease in the measured ion loss correction that would be applied to the radiative lifetime. In addition, when a scaling factor of 10%, which is twice the specified gauge reproducibility, is introduced to each pressure measurement, the extrapolated radiative lifetime does not change. Any proportional shift in the pressure reading should not influence the final result; only a pressure offset is thought to have a measurable affect.

7.5.1 Angular dependence of optical transmission filter

Optical transmission filters are designed to transmit light of a specified wavelength by interference. The transmission efficiency of a filter is specified for collimated rays striking the filter front surface at normal incidence. For rays striking the filter at an angle greater than normal (0°), the peak transmission shifts to a lower wavelength [112]. We have measured the angular dependence of the peak transmission wavelength for the filters used here (Thorlabs FB440-10). An observed shift of -7.5 nm over 15° is consistent with previous measurements of dielectric optical filters [112].

The shift in the peak transmission wavelength leads to an angular dependence in the transmission efficiency at 441 nm. This angular dependence has been included in the optical model by adjusting the transmission efficiency at each incident angle.

The resulting optical transfer function is shown in Fig. 7.7. The most dramatic differences between the calculation including angular effects (Fig. 7.7) and the idealized calculation (Fig. 7.6) are the overall reduction in the photon collection efficiency, and the reduction in the effective optical field of view. This occurs because the transmission of the filter at 441 nm drops significantly as rays enter at an angle other than normal.

Interestingly, the inclusion of angular effects brings the effective optical field-of-view into closer agreement with the TOF field-of-view. This leads to calculated ion expansion times between 1.86 s for 300 stored ions and 2.63 s for 700 stored ions. These calculated expansion times are in closer agreement with the measured ion expansion time, obtained using TOF analysis, of 1.18 s. Applying the angular dependent ion cloud expansion rates to the pressure-extrapolated radiative lifetime leads to a range in the $^2P_{3/2}$ lifetime of 9.21 ms to 9.23 ms.

However, while the initial inclusion of angular effects appears to bring the ion cloud expansion rate into a narrower range than suggested in §7.4, the overall reduction of the detection efficiency introduces a new uncertainty in the calculation. The inclusion of angular effects seems to require a metastable fraction of ≈ 1 for a cloud 700 ions. In other words, all captured ions would need to be in the metastable $^2P_{3/2}$ state upon leaving the EBIT. For clouds with less than 700 ions, the metastable fraction is calculated to be greater than 1, implying that the number of ions in the trap has been underestimated. However, as mentioned earlier, this is unlikely given the number of ions entering the trap per EBIT cycle ≈ 1500 and ion capture efficiency of $\approx 40\%$ for capture of 700 ions (see §4.4.1 for details).

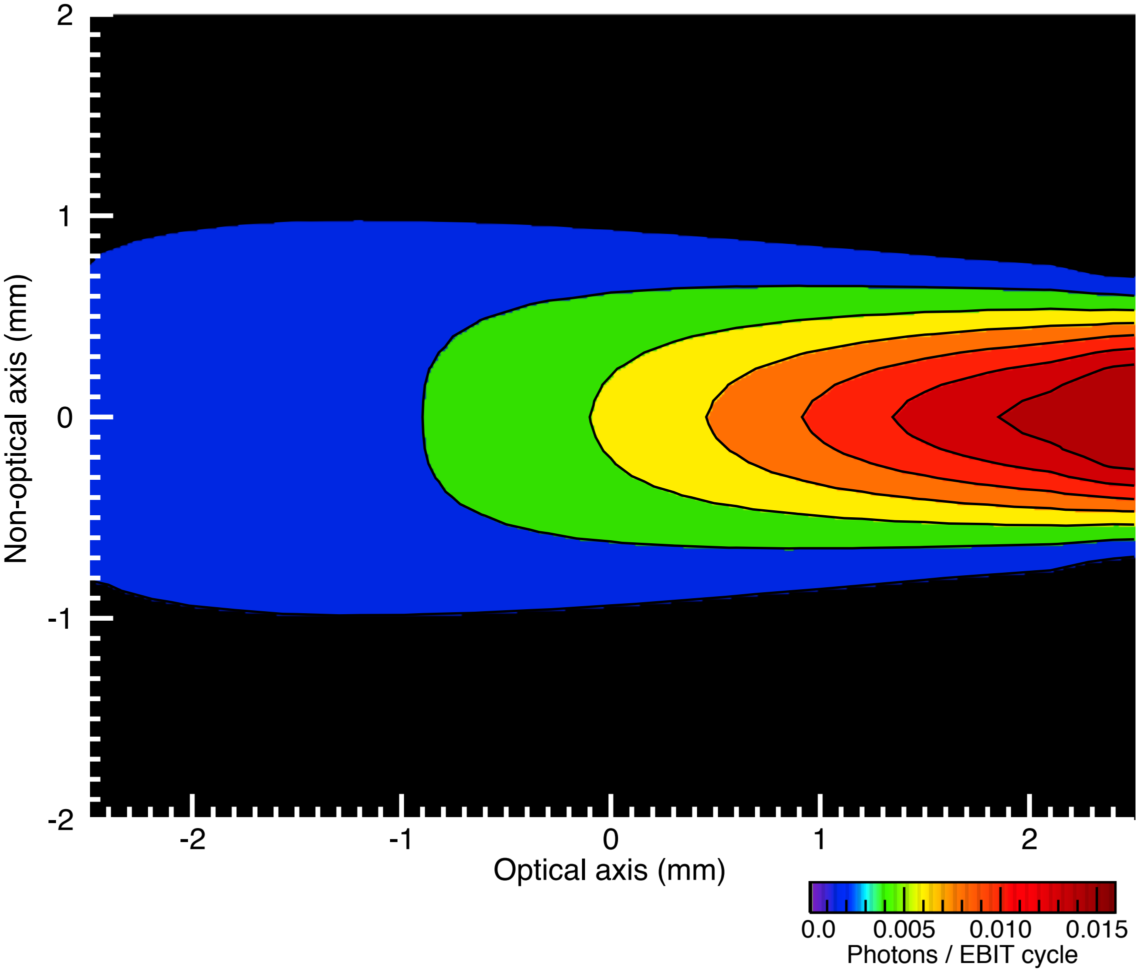

Figure 7.7: Optical transfer function for the absolute number of detected photons per MCS pass, including the angular dependence of the optical filter. The calculations are performed in a coordinate system which is aligned with the optical axis.

This lack of concordance may be due to uncertainty in the treatment of the angular dependence in the optical filter. To check the filter specification, an LED source, emitting between ≈ 400 nm and ≈ 500 nm, was imaged through a 150 μm pinhole and collimated using a 25 mm focal length lens. This approach produced a beam that was collimated over ≈ 10 cm, with a spot diameter of ≈ 1 mm. This light source was then passed through the filter and the transmitted light was collected on a fiber-fed grating spectrometer (Ocean Optics USB4000). The filter was mounted on a rotation stage, and a spectrum was taken at 1° intervals.

Due to the uncertainty in the source collimation and optical alignment, we estimate that the uncertainty in the measured angle is $\approx 1°$. In addition, an uncertainty of $\approx 2°$ comes from the numerical approximation in treating the angular spread of light rays passing through the filter and impinging upon the finite size of the photon counting head (5 mm diam). These uncertainties can cause shifts in the calculated ion cloud expansion time, thus generating uncertainty in the corrected $^2P_{3/2}$ lifetime determination. The influence of these uncertainties has been estimated by adjusting the transmission curve to reflect a range of angles. The estimated systematic uncertainty in the $^2P_{3/2}$ lifetime associated with the rough inclusion of angular effects is 0.09 ms.

7.6 Discussion: Error Budget

The radiative lifetime measurement presented here demonstrates the use of the two-magnet Penning trap in studying metastable states of isolated, highly-charged ions. The preliminary result includes corrections due to systematic effects associated with the ion cloud size, radial expansion based on the ion loss rate measurements, and properties of optical components modeled above. The various systematic effects and their contribution to the total uncertainty are presented in Table 7.5.

Ar^{13+} $2s^2 2p$ $^2P_{3/2}$ lifetime uncertainty budget	
Statistical effects:	Uncertainty (ms)
Statistics	0.05
Measured ion cloud expansion	0.003
Total statistical uncertainty	0.05
Systematic effects:	Uncertainty (ms)
Angular dependence of interference filter	0.09
Ion cloud and optical modeling	0.07
Residual gas composition and pressure offset	0.06
Measured ion cloud expansion	0.001
Axial ion loss	N/A
Cascade repopulation	N/A
Electron-impact excitation	N/A
Total systematic error estimate	0.13

Table 7.5: Uncertainty and error budget for this determination of the radiative lifetime of the Ar^{13+} $^2P_{3/2}$ metastable state.

Currently, the largest uncertainty for this determination of the Ar^{13+} $^2P_{3/2}$ radiative lifetime comes from the angular depndence of the interference filter in the optical setup, followed by uncertainties due to the ion cloud and photon collection model, which largely determines the ion expansion rate correction. The statistics of the raw data, the fitted lifetime at each pressure, and pressure inside the trap also contribute at a similar level of precision. The ion expansion rate measured using the TOF signal alone tends to lead to a larger correction than is predicted by the optical and non-neutral plasma modeling of the ion cloud in the trap. The radiative lifetime determined using the measured TOF ion cloud expansion rate is $\tau_{IL} = 9.25 \pm 0.05$ ms. The radiative lifetime determined using the smallest calculated ion cloud expansion rate, without angular effects, is $\tau_{IEP} = 9.20 \pm 0.05$ ms. When angular effects are included, the model predicts a corrected radiative lifetime between 9.21 ms and 9.23 ms. However, uncertainties associated with parameters of the optical setup used in these calculations suggest that the systematic uncertainty due to angular effects may be as large as 0.09 ms. These include the uncertainty of the transmission curve of the optical filter, as well as the uncertainties in the angular spread of incoming rays. In addition, a potential pressure offset consistent with a positive ion expansion rate sets a range on the lifetime between 9.18 ms in the case of no pressure offset and 9.24 ms in the case of a maximum allowable pressure offset. The total systematic uncertainty is determined to be 0.13 ms.

Therefore, taking the above considerations together with the uncertainties summarized in Table 7.5, the 2p $^2\mathrm{P}_{3/2}$ lifetime has been determined to be

$$\tau = 9.25(5)_{\mathrm{stat}}(^{+10}_{-3})_{\mathrm{syst}}\,\mathrm{ms}. \tag{7.25}$$

A comparison of this preliminary measurement with the previous experimental results and the current theory is shown in Fig. 7.8. Previous in-EBIT measurements have varied by $\approx 2\sigma$ (combined uncertainty), and with the exception of the first NIST in-EBIT measurement, have also differed from the Kingdon trap measurement by $\approx 2\sigma$ (combined).

The most precise reported result comes from the in-EBIT measurement performed at the Heidelberg EBIT in 2005 [31], reporting a precision of 0.1 %, which is roughly an order of magnitude more precise than all previous measurements. There, a variety of systematic investigations have been carried out in order to estimate the effect of processes such as charge-exchange ion loss, dump-induced losses, and the potential presence of "slow electrons" in the plasma [87, 113]. The in-EBIT measurement relies on a model of the plasma conditions which takes into account the presence of residual trapped electrons created in the plasma after the electron beam is turned off and the fluorescence observation begins. These trapped electrons give rise to a long-time component in the observed fluorescence decay which enters into the fitting function used to determine the radiative lifetime.

The result of using the two-magnet, unitary Penning trap to measure the Ar^{13+} $^2\mathrm{P}_{3/2}$ lifetime presented here is in mild disagreement with some of the earlier measurements and the most current theory. This preliminary result is in agreement with both the Kingdon trap measurement [34] and the NIST in-EBIT measurement [33]; it differs from the LLNL in-EBIT measurement [32] by $\approx 2.4\sigma$ (combined). The current result differs from the Heidelberg measurement by $\approx 2.9\sigma$ (combined) and $\approx 2.6\sigma$ (combined) from theory.

A unique feature of this new experiment is the application of Stern-Volmer analysis to deal with pressure-dependent quenching. Techniques applied here are similar to those which have been utilized on low charge state lifetime determinations [114]. This Stern-Volmer technique is not typically applied to measurements on highly-charged ions inside an EBIT, and has not been applied previously to the $^2\mathrm{P}_{3/2}$ state in Ar^{13+}. Since charge-exchange and ion-neutral collisions are usually the dominant sources of systematic error in determining radiative lifetimes, the

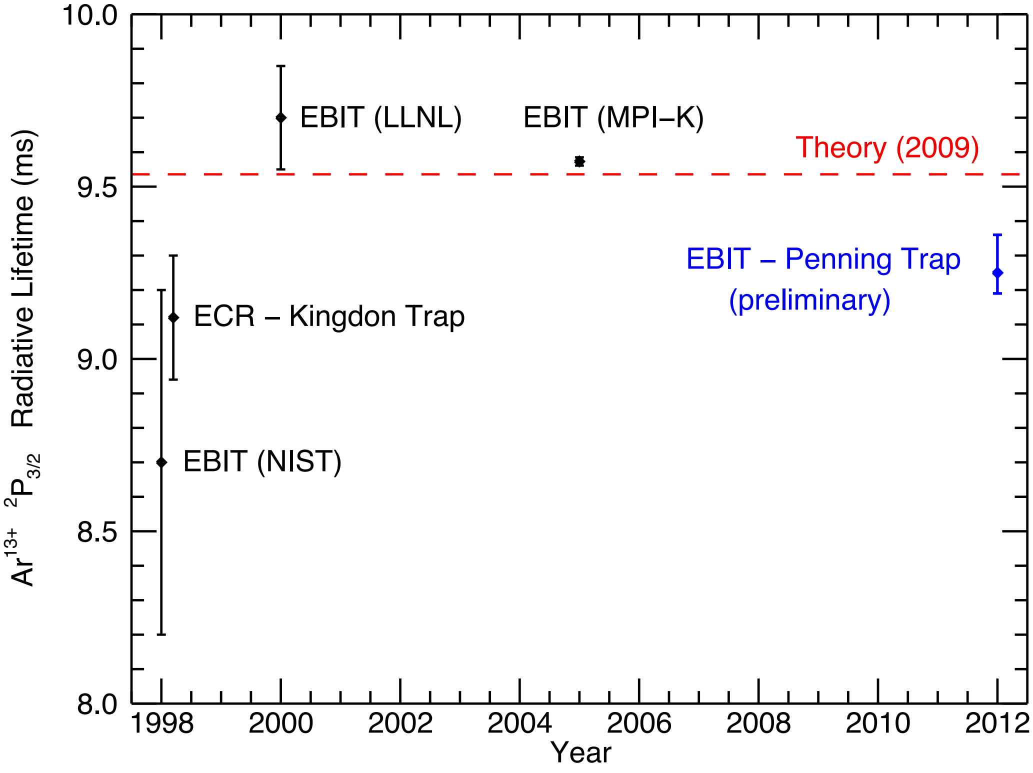

Figure 7.8: Comparison of previous measurements and theoretical values for the $^2P_{3/2}$ radiative lifetime in Ar^{13+} including the recent result from the EBIT-Penning trap experiments.

extrapolation to zero-pressure is a useful technique for experimentally accounting for these effects in a largely model-independent way.

It may be difficult to measure the radiative lifetime as a function of pressure inside an EBIT. Previously, pressure-dependent effects were investigated inside the NIST EBIT [33] by varying the gas-injection pressure. Despite changing the injection pressure over an order of magnitude, no measurable dependence in the lifetime was observed [33]. This is due in part to the fact that even though the gas injection pressure was varied widely, at the level of precision in that work, the neutral gas density in the EBIT was most likely not varied enough to produce a meaningful pressure dependence.

The current atomic structure theory [102] predicts a radiative lifetime of 9.5384 ms which is ≈ 0.4 % shorter than the Heidelberg result and ≈ 3 % longer than the preliminary result from the two-magnet Penning trap. It should be noted that while the one-electron QED corrections have been accounted for and the reported fractional uncertainty is 2×10^{-4} [86], the scatter in the wavelength-corrected theoretical predictions is ≈ 3 %.

Although studies of the systematic effects in the new Penning trap result are ongoing, there is sufficient evidence that a mild discrepancy in the value of the $^2\mathrm{P}_{3/2}$ lifetime may persist. The measurement capabilities demonstrated using the two-magnet, unitary Penning trap apparatus can be useful in enabling precision measurements on highly-charged ions. The simplicity of the unitary architecture may lead to improved measurements to provide needed corroboration of recently reported high precision lifetime measurements [35]. The ability to confine a single high charge state in a trap with easy optical access presents an opportunity to perform not only passive spectroscopic measurements, but also laser excitation to probe the physics of highly-charged ions with even greater precision.

Chapter 8

Conclusions

Unitary Penning traps, with extremely compact architecture, have been developed for capturing and storing highly-charged ions. A one-magnet Penning trap, the simplest realization using a single rare-earth magnet, has proven to be useful for capturing ions extracted at high energies from the NIST EBIT. By fully integrating the electrostatic and magnetic components, unitary Penning traps depart dramatically from the traditional architecture of a Penning trap that is typically used in conjunction with a high-field solenoid magnet operated at cryogenic temperatures. The extreme compactness and room-temperature operation of a unitary Penning trap lends itself to small instrument design for applications wherein space constraints preclude the use of high-field solenoids. Moreover, the measured trap stability resulting from the simplicity of construction illustrates the usefulness of such small traps.

A two-magnet Penning trap, with more elaborate architecture to house two NdFeB magnets that are yoked by electrical iron electrodes, was designed and built to shape the magnetic field in the trapping region and provide optical/atomic beam access to stored ions. This trap has been shown to be useful for investigations of trapped ion dynamics, collisional processes with highly-charged ions, and atomic properties of simple atoms. Notwithstanding holes for beam access, the two-magnet

Penning trap can confine ions with long storage times (of order seconds), limited primarily by collisions with the background gas. Possible future improvements to the trap include the introduction of "rotating-wall" electrodes [115, 116] to improve the intrinsic stability further.

The isolation of highly-charged ions is an important first step towards more control of atomic processes, such as synthesis of simple atomic structures for precision measurements. In fact, the new apparatus has enabled initial investigation of ion cloud dynamics, as well as a detailed characterization of the trap and ion source capabilities. The early studies presented here indicate that unitary Penning traps can open new opportunities to study highly-charged ions at lower temperatures which are rarely achievable in more traditional laboratory ion sources.

The radiative lifetime of the $^2\mathrm{P}_{3/2}$ state in B-like Ar^{13+} has been studied as the "first light" experiment using the new apparatus. A unique feature of this experiment is the measurement of the radiative lifetime as a function of background gas pressure in the apparatus. The radiative lifetime has long been in dispute, with disagreements among previous reported measurements of ≈ 5 %. In the new measurement, systematic effects including the ion cloud size and non-uniform optical field of view have been investigated using numerical models. An elaborate model was developed to estimate the uncertainty due to the ion cloud expansion in the optical field of view, an important correction to the observed radiative lifetime. Experiments with Ar^{13+} ions isolated in the two-magnet Penning trap yield a value for the $^2\mathrm{P}_{3/2}$ radiative lifetime of $\tau = 9.25(5)_{\mathrm{stat}}(^{+10}_{-3})_{\mathrm{syst}}$ ms. This preliminary result is in agreement with the previous ion capture experiment using an ECR ion source and electrostatic Kingdon trap [34], as well as the previous in-EBIT measurement at NIST [33]. This preliminary result is in mild disagreement with the recent in-EBIT result from LLNL [32] by $\approx 2.4\sigma$, combined uncertainty; it is also in mild disagreement with the recent in-EBIT result from MPI-K [31] by $\approx 2.9\sigma$, combined uncertainty, and with the current theory [102] by $\approx 2.6\sigma$, combined uncertainty. Improvements to the optical setup could reduce uncertainty associated with the angular dependence of the interference filter.

Future studies will also include the production and spectroscopic interrogation of hydrogen-like ions in circular Rydberg states, as well as other atomic systems of interest in astrophysics, atomic theory, and fundamental metrology. These investigations will be facilitated by the advances in ion capture and storage presented here.

Bibliography

[1] H.F. Beyer and V.P. Shevelko. *Introduction to the Physics of Highly Charged Ions.* Institute of Physics, 2003.

[2] J. D. Gillaspy. Highly charged ions: Topical review. *J. Phys. B*, 34:R93, 2001.

[3] U. D. Jentschura, P. J. Mohr, J. N. Tan, and B. J. Wundt. Fundamental constants and tests of theory in rydberg states of hydrogenlike ions. *Physical Review Letters*, 100(16):160404, 2008.

[4] B. Edlén. *Z. Astrophys.*, 22:30, 1942.

[5] Y. Lie. A high power radiation source in the vacuum ultraviolet. *Applied Physics A: Materials Science and Processing*, 2:297–302, 1973.

[6] S. Rifai Habbal, M. Druckmüller, H. Morgan, A. Daw, J. Johnson, A. Ding, M. Arndt, R. Esser, V. Rusin, and I. Scholl. Mapping the distribution of electron temperature and fe charge states in the corona with total solar eclipse observations. *The Astrophysical Journal*, 708(2):1650, 2010.

[7] H. R. Griem. *Principles of Plasma Spectroscopy.* Cambridge University Press, 1997.

[8] Th. Stöhlker, P. H. Mokler, F. Bosch, R. W. Dunford, F. Franzke, O. Klepper, C. Kozhuharov, T. Ludziejewski, F. Nolden, H. Reich, P. Rymuza, Z. Stachura, M. Steck, P. Swiat, and A. Warczak. $1s$ lamb shift in hydrogenlike uranium measured on cooled, decelerated ion beams. *Phys. Rev. Lett.*, 85:3109, 2000.

[9] A. Gumberidze, Th. Stöhlker, D. Banaś, K. Beckert, P. Beller, H. F. Beyer, F. Bosch, S. Hagmann, C. Kozhuharov, D. Liesen, F. Nolden, X. Ma, P. H. Mokler, M. Steck, D. Sierpowski, and S. Tashenov. Quantum electrodynamics in strong electric fields: The ground-state lamb shift in hydrogenlike uranium. *Phys. Rev. Lett.*, 94:223001, 2005.

[10] F. Herfurth, J. Dilling, A. Kellerbauer, G. Bollen, S. Henry, H.-J. Kluge, E. Lamour, D. Lunney, R.B. Moore, C. Scheidenberger, S. Schwarz, G. Sikler, and J. Szerypo. A linear radiofrequency ion trap for accumulation, bunching, and emittance improvement of radioactive ion beams. *Nucl. Inst. and Meth. A*, 469:254, 2001.

[11] F.M. Penning. *Physica*, 3:873, 1936.

[12] Z. Andjelkovic, S. Bharadia, B. Sommer, M. Vogel, and W. Nrtershuser. Towards high precision in-trap laser spectroscopy of highly charged ions. *Hyperfine Interact.*, 196:81, 2010.

[13] J. Repp, Ch. Böhm, J. R. Crespo López-Urrutia, A. Dörr, S. Eliseev, S. George, M. Goncharov, Yu. N. Novikov, C. Roux, S. Sturm, S. Ulmer, and K. Blaum. Pentatrap: A novel cryogenic multi-penning trap experiment for high-precision mass measurements on highly charged ions. *Applied Physics B: Lasers and Optics*, page 1, 2011.

[14] G. Gabrielse, X. Fei, L. A. Orozco, R. L. Tjoelker, J. Haas, H. Kalinowsky, T. A. Trainor, and W. Kells. Cooling and slowing of trapped antiprotons below 100 mev. *Phys. Rev. Lett.*, 63:1360, Aug 1989.

[15] G. Gabrielse, R. Kalra, W. S. Kolthammer, R. McConnell, P. Richerme, D. Grzonka, W. Oelert, T. Sefzick, M. Zielinski, D. W. Fitzakerley, M. C. George, E. A. Hessels, C. H. Storry, M. Weel, A. Müllers, and J. Walz. Trapped antihydrogen in its ground state. *Phys. Rev. Lett.*, 108:113002, 2012.

[16] S. Ettenauer, M. C. Simon, A. T. Gallant, T. Brunner, U. Chowdhury, V. V. Simon, M. Brodeur, A. Chaudhuri, E. Mané, C. Andreoiu, G. Audi, J. R. Crespo López-Urrutia, P. Delheij, G. Gwinner, A. Lapierre, D. Lunney, M. R. Pearson, R. Ringle, J. Ullrich, and J. Dilling. First use of high charge states for mass measurements of short-lived nuclides in a penning trap. *Phys. Rev. Lett.*, 107:272501, 2011.

[17] H. J. Kluge, K. Blaum, F. Herfurth, and W. Quint. Atomic and nuclear physics with stored particles in ion traps. *Phys. Scr.*, T104:167, 2003.

[18] M.A. Levine, R.E. Marrs, J.R. Henderson, D.A. Knapp, and M.B. Schneider. *Physica Scripta*, T22:157, 1988.

[19] J.D. Gillaspy, L.P. Ratliff, J.R. Roberts, and Endre Takács. Highly charged ions: Publications of the ebit project, 1993-2001. Special Publication 972, NIST, 2001.

[20] R. E. Lake, J. M. Pomeroy, H. Grube, and C. E. Sosolik. Charge state dependent energy deposition by ion impact. *Phys. Rev. Lett.*, 107:063202, 2011.

[21] Hiro Tawara, Endre Takács, Tibor Suta, Károly Makónyi, L. P. Ratliff, and J. D. Gillaspy. k x rays produced in collisions of bare ions with atoms: Contribution of multiple-electron transfer in kr^{36+}, ar^{18+}, and ne^{10+} + Ar collisions. *Phys. Rev. A*, 73:012704, Jan 2006.

[22] D. Schneider, D. A. Church, G. Weinberg, J. Steiger, B. Beck, J. McDonald, E. Magee, and D. Knapp. Confinement in a cryogenic penning trap of highest charge state ions from ebit. *Review of Scientific Instruments*, 65(11):3472–3478, 1994.

[23] M. Hobein, A. Solders, M. Suhonen, Y. Liu, and R. Schuch. Evaporative cooling and coherent axial oscillations of highly charged ions in a penning trap. *Phys. Rev. Lett.*, 106:013002, 2011.

[24] Joseph N. Tan, Samuel M. Brewer, and Nicholas D. Guise. Penning traps with unitary architecture for storage of highly charged ions. *Review of Scientific Instruments*, 83(2):023103, 2012.

[25] J. Sucher. Magnetic dipole transitions in atomic and particle physics: ions and psions. *Rep. Prog. Phys.*, 41:1781, 1978.

[26] C. W. Chou, D. B. Hume, J. C. J. Koelemeij, D. J. Wineland, and T. Rosenband. Frequency comparison of two high-accuracy al$^+$ optical clocks. *Phys. Rev. Lett.*, 104:070802, 2010.

[27] P. Beiersdorfer, E. Träbert, and E. H. Pinnington. *The Astrophysical Journal*, 587:836, 2003.

[28] E. Träbert. Atomic lifetime measurements with ion traps of many sizes. *Physica Scripta*, 61:257, 2000.

[29] M. S. Safronova, W. R. Johnson, and U. I. Safronova. Relativistic many-body calculations of energies of n=2 states for boronlike ions. *Phys. Rev. A*, 54:2850, 1996.

[30] V. Mäckel, R. Klawitter, G. Brenner, J. R. Crespo López-Urrutia, and J. Ullrich. Laser spectroscopy on forbidden transitions in trapped highly charged ar^{13+} ions. *Phys. Rev. Lett.*, 107:143002, 2011.

[31] A. Lapierre, U. D. Jentschura, J. R. Crespo López-Urrutia, J. Braun, G. Brenner, H. Bruhns, D. Fischer, A. J. González Martínez, Z. Harman, W. R. Johnson, C. H. Keitel, V. Mironov, C. J. Osborne, G. Sikler, R. Soria Orts, V. Shabaev, H. Tawara, I. I. Tupitsyn, J. Ullrich, and A. Volotka. *Phys. Rev. Lett.*, 95:183001, 2005.

[32] E. Träbert. *Astrophysical Journal*, 541:506, 2000.

[33] F.G. Serpa, J.D. Gillaspy, and E. Träbert. *J. Phys. B*, 31:3345, 1998.

[34] D.P. Moehs and D.A. Church. *Phys. Rev. A*, 58:1111, 1998.

[35] E. Träbert. Problems with accurate atomic lifetime measurements of multiply charged ions. *Physica Scripta*, 79(6):068101, 2009.

[36] P. J. Mohr, B. N. Taylor, and D. B. Newell. Codata recommended values of the fundamental physical constants: 2010. *Reviews of Modern Physics*, 2012. (arXiv:1203.5425v1 – To be published).

[37] Th. Udem, A. Huber, B. Gross, J. Reichert, M. Prevedelli, M. Weitz, and T. W. Hänsch. *Phys. Rev. Lett.*, 79:2646, 1997.

[38] R. Pohl and et. al. The size of the proton. *Nature*, 466:213216, 2010.

[39] J. C. DeVries. *A Precision Millimeter-Wave Measurement of the Rydberg Frequency.* PhD thesis, MIT, 2001.

[40] B J Wundt and U D Jentschura. Proposal for the determination of nuclear masses by high-precision spectroscopy of rydberg states. *J. Phys. B: At. Mol. Opt. Phys.*, 43:115002, 2010.

[41] U. D. Jentschura, P. J. Mohr, and J. N. Tan. Fundamental constants and tests of theory in rydberg states of one-electron ions. *Journal of Physics B: At. Mol. Opt. Phys.*, 43:074002, 2010.

[42] U. D. Jentschura, P. J. Mohr, J. N. Tan, and B. J. Wundt. Fundamental constants and tests of theory in rydberg states of hydrogenlike ions. *Can. J. Phys.*, 87:757, 2009.

[43] S. R. Lundeen, R. A. Komara, C. W. Fehrenbach, and B. D. DePaola. *Phys. Rev. A*, 64:052714, 2001.

[44] M. A. Gearba, R. A. Komara, S. R. Lundeen, C. W. Fehrenbach, and B. D. DePaola. *Phys. Rev. A*, 71:013424, 2005.

[45] M. R. Flannery and D. Vrinceanu. *Phys. Rev. A Rapid Cmmunications*, 68:030502(R), 2003.

[46] C. H. Storry and OTHERS. *Phys. Rev. Lett.*, 93:263401, 2004.

[47] L.S. Brown and G. Gabrielse. Geonium theory: Physics of a single electron or ion in a penning trap. *Rev. Mod. Phys.*, 58:233, 1986.

[48] V. Gomer, H. Strauss, and D. Meschede. A compact penning trap for light ions. *Applied Physics B*, 60:89–94, 1995.

[49] L. Suess, C. D. Finch, R. Parthasarathy, S. B. Hill, and F. B. Dunning. Permanent magnet penning trap for heavy ion storage. *Review of Scientific Instruments*, 73(8):2861–2866, 2002.

[50] W. K. Panofsky and M. Phillips. *Classical Electricity and Magentism, 2nd edition.* Addison-Wesley, Reading, MA, 1969.

[51] Identification of a product herein is for documentation purposes only, and does not imply recommendation or endorsement by NIST, nor does it imply that this product is necessarily the best available for the purpose.

[52] P. Campbell. *Permanent Magnet Materials and their Application.* Cambridge University Press, 1994.

[53] MMPA Standard No. 0100-00, Sec. 9.1.

[54] E. Harting and F. Read. *Electrostatic Lenses.* Elselvier Publishing Company, 1976.

[55] William Press, Saul Teukolsky, William Vetterling, and Brian Flannery. *Numerical Recipes in C*. Cambridge University Press, Cambridge, UK, 2nd edition, 1992.

[56] J. D. Gillaspy, I. N. Draganić, Yu. Ralchenko, J. Reader, J. N. Tan, J. M. Pomeroy, and S. M. Brewer. *Phys. Rev. A*, 80:010501(R), 2009.

[57] Glenn E. Holland, Craig N. Boyer, John F. Seely, J. N. Tan, J. M. Pomeroy, and J. D. Gillaspy. Low jitter metal vapor vacuum arc ion source for electron beam ion trap injections. *Review of Scientific Instruments*, 76:073304, 2005.

[58] Y.K. Kim and J.-P. Desclaux. *Phys. Rev. A*, 66:012708, 2002.

[59] A. I Pikin, C. A. Morgan, E. W. Bell, L. P. Ratliff, D. A. Church, and J. D. Gillaspy. A beam line for highly charged ions. *Rev. Sci. Instrum.*, 67:2528, 1996.

[60] L. P. Ratliff, E. W. Bell, D. C. Parks, A. I. Pikin, and J. D. Gillaspy. Continuous highly charged ion beams from the National Institute of Standards and Technology electron-beam ion trap. *Rev. Sci. Instrum.*, 68:1998, 1997.

[61] L. P. Ratliff and J. R. Roberts. Highly charged ion studies at the nist ebit. In J. Gillaspy, editor, *Trapping Highly Charged Ions: Fundamentals and Applications*, page 257. Nova Science Publishers, Hauppauge, 2001.

[62] B Leskovar. Microchannel plates. *Physics Today*, 30:42–49, 1977.

[63] J. L. Wiza. Microchannel plate detectors. *Nuclear Instruments and Methods*, 162:587, 1979.

[64] W. B. Colson, J. McPherson, and F. T. King. High-gain imaging electron multiplier. *Review of Scientific Instruments*, 44:1694–1696, 1973.

[65] M. Lampton and C. W. Carlson. Low-distortion resistive anodes for two-dimensional position-sensitive mcp systems. *Review of Scientific Instruments*, 50:1093–1097, 1979.

[66] R. Soria Orts, Z. Harman, J. R. Crespo López-Urrutia, A. N. Artemyev, H. Bruhns, A. J. González Martínez, U. D. Jentschura, C. H. Keitel, A. Lapierre, V. Mironov, V. M. Shabaev, H. Tawara, I. I. Tupitsyn, J. Ullrich, and A. V. Volotka. *Phys. Rev. Lett.*, 97:103002, 2006.

[67] K. Jousten. Thermal outgassing. *CAS - Cern Accelerator School: Vacuum Technology*, page 111, 1999.

[68] Joseph N Tan, Samuel M Brewer, and Nicholas D Guise. Experimental efforts at nist towards one-electron ions in circular rydberg states. *Physica Scripta*, 2011(T144):014009, 2011.

[69] X. Fei, R. Davisson, and G. Gabrielse. High-voltage switching for in-flight capture of kev antiprotons in a penning trap. *Review of Scientific Instruments*, 58(11):2197–2199, 1987.

[70] A. L. Stancik and E. B. Brauns. A simple asymmetric lineshape for fitting infrared absorption spectra. *Vibrational Spectroscopy*, 47:66–69, 2008.

[71] E. W. McDaniel and E. A. Mason. *The Mobility and Diffusion of Ions in Gases*. Wiley, 1973.

[72] G. Savard, St. Becker, G. Bollen, H.-J. Kluge, R.B. Moore, Th. Otto, L. Schweikhard, H. Stolzenberg, and U. Wiess. A new cooling technique for heavy ions in a penning trap. *Physics Letters A*, 158:247, 1991.

[73] H.W. Ellis, E.W. McDaniel, D.L. Albritton, L.A. Viehland, S.L. Lin, and E.A. Mason. Transport properties of gaseous ions over a wide energy range. part ii. *Atomic Data and Nuclear Data Tables*, 22:179 – 217, 1978.

[74] Larry A Viehland and E.A Mason. Gaseous lon mobility in electric fields of arbitrary strength. *Annals of Physics*, 91:499 – 533, 1975.

[75] L. Spitzer. *Physics of Fully Ionized Gases*. Interscience Publishers, 2nd edition, 1962.

[76] R. L. Spencer, S. N. Rasband, and R. R. Vanfleet. Numerical calcuation of axisymmetric non-neutral plasma equilibria. *Phys. Fluids B*, 5:4267, 1993.

[77] D.J. Wineland, J.J. Bollinger, and W.M. Itano. Laser-fluorescence mass spectroscopy. *Phys. Rev. Lett.*, 50:628–631, 1983.

[78] J.J. Bollinger, D. J. Heinzen, F. L. Moore, W.M. Itano, D.J. Wineland, and D. H. E. Dubin. Electrostatic modes of ion-trap plasmas. *Phys. Rev. A*, 48:525, 1993.

[79] Daniel H. E. Dubin and T. M. O'Neil. Trapped nonneutral plasmas, liquids, and crystals (the thermal equilibrium states). *Rev. Mod. Phys.*, 71:87–172, 1999.

[80] R. C. Davidson. *Theory of Nonneutral Plasmas*. Benjamin, 1974.

[81] R. C. Davidson. *Physics of Nonneutral Plasmas*. Addison-Wesley, 1990.

[82] L. R. Brewer, J. D. Prestage, J. J. Bollinger, W. M. Itano, D. J. Larson, and D. J. Wineland. Static properties of a non-neutral ^{9}be$^+$-ion plasma. *Phys. Rev. A*, 38:859, 1988.

[83] G. B. Arfken and H. J. Weber. *Mathematical Methods for Physicists*. Elsevier, 6th edition, 2005.

[84] S. Plimpton. Fast parallel algorithms for short-range molecular dynamics. *J. Comp. Phys.*, 117:1–19, 1995.

[85] T. K. Krueger and S. J. Czyzak. *Astrophys. J.*, 144:1194, 1966.

[86] I.I. Tupitsyn. *Phys. Rev A*, 72:062503, 2005.

[87] A. Lapierre, J. R. Crespo López-Urrutia, J. Braun, G. Brenner, H. Bruhns, D. Fischer, A. J. González Martínez, V. Mironov, C. Osborne, G. Sikler, R. Soria Orts, H. Tawara, J. Ullrich, V. M. Shabaev, I. I. Tupitsyn, and A. Volotka. *Phys. Rev. A*, 73:052507, 2006.

[88] D. Hanneke, S. Fogwell, and G. Gabrielse. New measurement of the election magnetic moment and the fine structure constant. *Phys. Rev. Lett.*, 100, 2008.

[89] K.T. Cheng, Y.K. Kim, and J.P. Desclaux. *At. Data Nucl. Data Tables*, 24:111, 1979.

[90] C.F. Fischer. *J. Phys. B*, 16:157, 1983.

[91] A.K. Bhatia, U. Feldman, and J.F. Seely. *At. Data Nucl. Data Tables*, 35:319, 1986.

[92] V. Kaufman and J. Sugar. *J. Phys. Chem. Ref. Data*, 15:321, 1986.

[93] T.R. Verhey B.P. Das and W.F. Perger. *J. Phys. B*, 20:3639, 1987.

[94] M.E. Galavís, C. Mendoza, and C.J. Zeippen. *Astron. Astrophys. Suppl. Ser.*, 131:499, 1998.

[95] E. Charro, S. Lópex-Ferrero, and I. Martín. *J. Phys. B*, 34:4243, 2001.

[96] C.Z. Dong, S. Fritzsche, B. Fricke, and W.D. Sepp. *Phys. Scr.*, T92:294, 2001.

[97] K. Koc. *J. Phys. B*, 36:L93, 2003.

[98] C. Froese Fischer and G. Tachiev. *MCHF/MCDHF Collection, Version 2, Ref. No. 27*, 2004. Available online at http://nlte.nist.gov/MCHF/. National Institute of Standards and Technology.

[99] K. M. Aggawal, F. P. Keenan, and S. Nakazaki. Energy levels and radiative rates for transitions in ar xiii, ar xiv and arxv. *Astronomy and Astrophysics*, 436:1141, 2005.

[100] A. V. Volotka, D. A. Glazov, G. Plunien, V. M. Shabaev, and I. I. Tupitsyn. Nuclear recoil effect on the magnetic-dipole decay rates of atomic levels. *Eur. Phys. J. D*, 48:167, 2008.

[101] C. Froese Fischer and G. Tachiev. *MCHF/MCDHF Collection, Version 2, Ref. No. 40*, 2009. Available online at http://nlte.nist.gov/MCHF/. National Institute of Standards and Technology.

[102] K. Koc. Relativistic multireference configuration interaction calculations of lifetime of $2s^22p\ ^2p_{3/2}$ level along boron isoelectronic sequence. *Eur. Phys. J. D*, 53:9, 2009.

[103] P. Rynkun, P. Jönsson, G. Gaigalas, and C. Froese Fischer. Energies and e1, m1, e2, m2 transition rates for states of the $2s^22p$, $2s2p^2$, and $2p^3$ configurations in boron-like ions between n ii and zn xxvi. *Atomic Data and Nuclear Data Tables*, 98:481, 2012.

[104] P. Beiersdorfer, B. Beck, St. Becker, and L. Schweikhard. *Int. J. Mass Spectrom. Ion Processes*, 157/158:149, 1996.

[105] K. H. Kingdon. A method for the neutralization of electron space charge by positive ionization at very low gas pressures. *Phys. Rev.*, 21:408–418, 1923.

[106] D. P. Moehs, D. A. Church, and R. Phaneuf. *Review of Scientific Instruments*, 69:1991, 1998.

[107] E. B. Saloman. Energy levels and observed spectral lines of ionized argon, ar ii through ar xviii. *Journal of Physical and Chemical Reference Data*, 39:033101, 2010.

[108] J. R. Lakowicz. *Principles of fluorescence spectroscopy.* Springer, 3rd edition, 2006.

[109] V. O. Stern and M. Volmer. On the quenching-time of fluorescence. *Physik. Zeitschr.*, 20:183–188, 1919.

[110] L. Yang and D.A. Church. *Phys. Rev. Lett.*, 70:25, 1993.

[111] B. M. Penetrante, J. N. Bardsley, D. DeWitt, M. Clark, and D. Schneider. Evolution of ion-charge-state distributions in an electron-beam ion trap. *Phys. Rev. A*, 43:4861–4872, 1991.

[112] S. A. Pollack. Angular dependence of transmission characteristics of interference filters and application to a tunable fluorometer. *Applied Optics*, 5:1749, 1966.

[113] A. Lapierre, J. R. Crespo Lopez-Urrutia, J. Braun, G. Brenner, H. Bruhns, D. Fischer, A. J. Gonzalez Martinez, V. Mironov, C. J. Osborne, G. Sikler, R. Soria Orts, H. Tawara, Y. Yamazaki, and J. Ullrich. Do electrons and ions coexist in an ebit? *AIP Conference Proceedings*, 793:361–371, 2005.

[114] A. G. Calamai and C. E. Johnson. Radiative lifetimes of several metastable states of doubly and triply ionized ar, kr, and xe. *Phys. Rev. A*, 45:7792, 1992.

[115] X.-P. Huang, F. Anderegg, E. M. Hollmann, C. F. Driscoll, and T. M. O'Neil. *Phys. Rev. Lett.*, 78:875, 1997.

[116] E. M. Hollman, F. Anderegg, and C. F. Driscoll. *Phys. Plasmas*, 7:2776, 2000.